



**HAL**  
open science

# Advanced bio-based epoxies and furanics thermosets – hierarchically assembled macromolecular design

Jean-Mathieu Pin

► **To cite this version:**

Jean-Mathieu Pin. Advanced bio-based epoxies and furanics thermosets – hierarchically assembled macromolecular design. Other. Université Nice Sophia Antipolis, 2015. English. NNT: 2015NICE4027. tel-01238609

**HAL Id: tel-01238609**

**<https://theses.hal.science/tel-01238609>**

Submitted on 6 Dec 2015

**HAL** is a multi-disciplinary open access archive for the deposit and dissemination of scientific research documents, whether they are published or not. The documents may come from teaching and research institutions in France or abroad, or from public or private research centers.

L'archive ouverte pluridisciplinaire **HAL**, est destinée au dépôt et à la diffusion de documents scientifiques de niveau recherche, publiés ou non, émanant des établissements d'enseignement et de recherche français ou étrangers, des laboratoires publics ou privés.

UNIVERSITE DE NICE-SOPHIA ANTIPOLIS - UFR Sciences  
Ecole Doctorale Sciences Fondamentales et Appliquées

# T H E S E

pour obtenir le titre de  
**Docteur en Sciences**  
de l'UNIVERSITE de Nice-Sophia Antipolis

Discipline : Chimie

Présentée et soutenue par

***Jean-Mathieu PIN***

Matrices thermodurcissables époxydes et furaniques biosourcées  
– conception d'assemblages macromoléculaires



Advanced bio-based epoxies and furanics thermosets –  
hierarchically assembled macromolecular design

Thèse dirigée par le Professeur *Nicolas SBIRRAZZUOLI* et  
le Maître de Conférences HDR *Alice MIJA*

Soutenance: le 15 Juin 2015

Jury :

M. Cosimo CARFAGNA	Professeur (Université de Naples Federico II, Italie)	Rapporteur
M. Ed de JONG	Docteur (Vice-Président Avantium Chemicals, Pays-Bas)	Examineur
Mme. Françoise GIULIERI	Docteur HDR (Directeur Général PIGM'Azur, Nice)	Examineur
M. Marek KOWALCZUK	Professeur (Université de Wolverhampton, Angleterre)	Rapporteur
Mme. Alice MIJA	Maître de Conférences HDR (Université de Nice-Sophia Antipolis)	Examineur
M. Patrick NAVARD	Directeur de Recherche (Ecole des Mines de Paris - CEMEF)	Examineur
Mme. Mariana PINTEALA	Directeur de Recherche (Directeur IntelCentre, Roumanie)	Rapporteur
M. Nicolas SBIRRAZZUOLI	Professeur (Université de Nice-Sophia Antipolis)	Examineur



*« Chacun de nous a son étoile. Suivons-la en nous félicitant de la voir chaque jour un peu plus loin. »*

*François Auguste Victor Grignard*

A Mémé,  
A mes Parents,  
A tonton Jacques,  
A ma Famille.

## Remerciements ~ Acknowledgments

Je voudrais en premier lieu exprimer ma plus grande gratitude et mes sincères sentiments à mes deux directeurs de thèse, le Professeur Nicolas Sbirrazzuoli et le Docteur Alice Mija, pour m'avoir donné la chance d'effectuer cette aventure doctorale. Merci Nicolas pour votre confiance, pour votre legs d'une démarche scientifique fondamentale et pour votre passion de la recherche communicative, j'ai beaucoup appris à vos côtés.

Alice, dans la vie il y a des rencontres qui vous forment, vous élèvent, merci pour votre confiance et votre amitié.

Je tiens à remercier très chaleureusement mes encadrants que sont le Docteur Nathanaël Guigo et le Docteur Luc Vincent auprès desquels j'ai beaucoup appris. Et au-delà de l'aspect scientifique, merci pour votre humour et vos qualités humaines. Nathanaël, je me souviens avec joie de nos parties de jeux de sociétés et « d'Age » endiablées ☺. Luc, il va falloir attaquer les blind-tests pour la période Baroque et Classique ☺.

I would like to kindly and deeply acknowledge Professor Cosimo Carfagna from University of Napoli Federico II, Italy, Professor Marek Kowalczyk from University of Wolverhampton, England, and Doctor Mariana Pinteala from the Petru Poni Institute, Romania, for the honor you offered me by agreeing to judge this work.

Je tiens à remercier très sincèrement le Docteur Françoise Giulieri, Directeur Général de la société PIGM'azur, avec qui j'ai eu la chance de travailler. J'admire son énergie et sa passion.

I would like to present my kind and entire acknowledgement to the Doctor Ed de Jong. I really appreciate to work under his supervision, I admire his scientific culture and envision.

Je suis très touché et tiens à remercier très respectueusement le Docteur Patrick Navard, Directeur de Recherche à l'École des Mines de Paris - CEMEF pour avoir accepté d'examiner ce travail doctoral.

Je tiens à remercier très sincèrement la Région PACA et la société Sicomin à travers la personne de M. Jean-Pierre Gros, sans qui ce travail doctoral n'aurait pas pu voir le jour. Merci pour votre aide et votre support.

Je tiens à remercier tous les jeunes Docteurs et doctorants qui ont fait de ces dernières années des souvenirs inoubliables de joies, de rires...et de musique. Merci à tous pour votre soutien, votre humour, votre gentillesse, pour ces repas interminables, pour ces

vacances mémorables à travers la France et l'Europe...bon j'arrête là ☺. Merci donc aux « anciens », je ne fais référence qu'à leur sagesse bien évidemment ! Membres fondateurs de la très honorable BIM (Biomass Investigations Materials) team, j'ai nommé les Docteurs Raffaele Zavaglia et Nicolas Bosq qui m'ont accueilli dans ce labo, il y a quelques années déjà ! Un grand merci également à tous mes actuels collègues et amis ; ci-joint leurs noms affublés de leur sobriquets ☺ : Amandine Codou (Pupuce), Docteur Matthieu Moncel (Matthiouuuu), Sébastien Barale (Sebinou), Guillaume Falco (Guigui), Docteur Lucrezia Martino (Lulu), et notre dernier venu, Jesper Van Berkel. Soit rassuré nous allons te trouver un diminutif qui te siéra à merveille ☺).

J'ai également une pensée particulière pour les stagiaires qui ont égayé notre quotidien de manière sporadique (ou boulière) : Justine, Abdou, Nadège, Ioana, Rime et...Volga qui nous a émerveillé de ses tenues chatoyantes chaque jour ☺. Merci pour votre bonne humeur !

Je remercie tout particulièrement les stagiaires Hélios et Sébastien que j'ai eu la chance d'encadrer lors de leur Master 1 et 2, respectivement. Je vous souhaite le meilleur pour la suite !

Je remercie également toute l'équipe dite « du 6<sup>ème</sup> » pour leur amitié, ainsi que mes collègues chimistes du bâtiment ☺.

I have a special thought for the people of Avantium Chemicals, Amsterdam, especially my kind office colleagues Ella, Monique and Rene. Thanks to Jo, Peter, Robert-Jan, Thomas, Sullivan, Tom, Nico, André, Meyrem, Jesper, Hajime, Ana, Stefan, Danny, Victor, Erik and all the other persons that I was lucky to meet.

Obviously special thanks to you Jan Kees from "Vesuvio" ☺, it was a real pleasure to work under your guidance, I learn a lot ! Is still not too late to open a humans hat store...!

Un grand merci également aux « French Guys » d'Avantium pour m'avoir guidé dans ce nouveau monde ☺: Jeff, Etienne, Jean-Claude et Benoît.

Thank you to welcome me so friendly!

Je tiens à remercier les enseignants du département de Chimie qui m'ont aidé pour ma première expérience professorale : Nathalie, Claire, Aurélie, Anne-Christine, Charlotte, Gaëlle, Christophe et Hervé.

Je tiens à chaleureusement remercier toutes les personnes qui m'ont aidé, et avec qui j'ai eu la chance de travailler durant cette thèse : Mme Sophie Pagnota, M. Jean-Pierre Laugier, M. Gabriel Monge, Docteur Marc Gaysinski, Docteur Lionel Massi, Docteur Georges Bossis, Docteur Jessica Alves Marins, le Docteur Franck Collas.

Je tiens à remercier tout particulièrement Alina Cristian et lui souhaite tout le bonheur du monde. Merci également à Gregg Colp, et au Docteur Nicolas Volle, à qui je souhaite le meilleur pour son aventure industrielle ! Nicolas, comme promis, j'ai pensé au vin blanc !! ☺

Ma très chère Mélissa et mon très cher Julien, ou devrais-je dire « Puccineta » et « Puccineto » depuis notre excursion en terre consacrée. ☺ Comment exprimer de manière simple, et sans verser dans une mièvrerie qui ne me correspond guère, la joie d'être votre ami. Restons sobre. Je vous aime.

J'ai une pensée pour toi Juju qui t'es exilé à Lyon pour vivre ta propre aventure ! Je te souhaite le meilleur pour la suite futur Docteur ☺ !

Pour finir je souhaite remercier toute ma famille que j'adore, Marraine, Parrain, Dédée Christian, mes cousins. J'ai une pensée émue pour toute la famille Lonjon, Tata Yvette, tonton Jacques, Manue, Laurianne, Jeff, Fred, et les nouveaux venus Eloïse, Louis et...Lilly ☺.

Merci à celle que j'admire par-dessus tout Maria-Antonia. Mes derniers mots vont à mes Parents géniaux ! Michèle et Jean-François, je vous aime, merci ...pour tout !

## Index of Abbreviations

### Chemical compounds:

2,7-DAF	2,7-diaminofluorene
2MI	2-methylimidazole
BTDA	benzophenone-3, 3', 4, 4'-tetracarboxylic dianhydride
DAPTMS	[3-(2-Aminoethylamino) propyl] trimethoxysilane
DGEBA	diglycidyl ether of bisphenol A
ECH	epichlorohydrin
ELO	epoxidized linseed oil
FA	furfuryl alcohol
FDCA	2,5-furandicarboxylic acid
FF	furfural
GLYMO	3-glycidoxypropyl-trimethoxysilane
HMF	5-hydroxymethylfurfural
HTC	hydrothermal carbon
LA	levulinic acid
MA	maleic anhydride
MAG	magnetite
MAG/GLYMO	magnetite nanoparticle functionalized with GLYMO
MF	2-methyl-furan
MHHPA	methylhexahydrophthalic anhydride
MMF	5-methoxymethylfurfural
m-Sep	magnetite-sepiolite hybride nanofiller
MTHF	2-methyl-tetrahydrofuran
PEA2000	polyetheramines: 2000 g/mol
PEA230	polyetheramines: 230 g/mol
PFA	polyfurfuryl alcohol
SA	succinic anhydride
SEP	sepiolite
SEP/DAPTMS	sepilote nanofiller functionalized with DAPTMS
TB	1,2,4-trihydrobenzen
TriEP	1,3,5-Triazine,2,4,6-tris[4-(2-oxiranylmethoxy)phenyl]
TriOH	2,4,6-Tris(p-hydroxyphenyl) triazine

### Latin abbreviations:

$C_{p0}$	heat capacity extrapolated at 0 frequency	$\text{J.g}^{-1}.\text{K}^{-1}$
DC	dangling chain	
$D_f$	mass fractal dimensions	
DFT	density functional theory	
$D_s$	surface fractal dimensions	
$E'$	Young modulus	Pa
EAC	elastically active crosslinks	
EANC	elastically active network chains	
$E_\alpha$	apparent activation energy	$\text{J.mol}^{-1}$
FPs	fractal polymers	
$G'$	elastic/storage modulus	Pa
$G''$	viscous/loss modulus	Pa
LC	liquid-crystalline	
LCERs	liquid crystalline epoxy resins	
LCT	liquid-crystalline thermoset	
$T_\alpha$	temperature (i.e. of alpha relaxation)	$^\circ\text{C}$
$\tan \delta$	damping factor	
$T_\beta$	temperature (i.e. of beta relaxation)	$^\circ\text{C}$
$T_g$	glass transition temperature	$^\circ\text{C}$
$T_\gamma$	temperature (i.e. of gamma relaxation)	$^\circ\text{C}$
$T_{g\infty}$	infinite glass temperature	$^\circ\text{C}$
TTT	time-temperature-transformations	

### Greek abbreviations:

$\alpha$	extent of conversion	
$\alpha_{\text{gel}}$	conversion degree at gelation	
$\beta$	heating rate	$^\circ\text{C.min}^{-1}$
$\Delta_r H$	reaction enthalpy	$\text{J.g}^{-1}$

# Table of Content

<b>I.</b>	<b>General introduction.....</b>	<b>15</b>
<b>II.</b>	<b>From petro-based to bio-based thermosets: a state of art.....</b>	<b>26</b>
<b>II.1.</b>	<b>Thermosets engineering .....</b>	<b>26</b>
II.1.1.	A petrosourced-polymer design hegemony .....	26
II.1.1.1.	<i>Epoxies monomers chemistry: DGEBA synthesis .....</i>	<i>27</i>
II.1.1.2.	<i>Polymerization process: cross-linkers and functionalities.....</i>	<i>29</i>
II.1.2.	The creation of a 3D architecture .....	32
II.1.2.1.	<i>Gelation phenomenon (sol-gel transition).....</i>	<i>32</i>
II.1.2.2.	<i>Glass transition and vitrification phenomena .....</i>	<i>34</i>
II.1.3.	Outstanding properties and application fields of epoxy thermosets.....	36
<b>II.2.</b>	<b>From biomass to bio-based thermosets .....</b>	<b>36</b>
II.2.1.	An historic renewable feedstock: the triglycerides oils.....	37
II.2.1.1.	<i>Composition and chemistry of vegetable oils.....</i>	<i>37</i>
II.2.1.2.	<i>Epoxidized linseed oil.....</i>	<i>39</i>
II.2.2.	A biosourced-polymer design issue from carbohydrate conversion.....	41
II.2.2.1.	<i>From the biorefinery concept to platform molecules production.....</i>	<i>41</i>
II.2.2.2.	<i>From furfuryl alcohol to polyfurfuryl alcohol.....</i>	<i>45</i>
II.2.2.3.	<i>A side-product to valorize : the humins.....</i>	<i>49</i>
<b>II.3.</b>	<b>Hierarchical advanced materials: a Nature inspiration.....</b>	<b>53</b>
II.3.1.	Bio-inspiration as strategy to design advanced materials.....	54
II.3.2.	Bottom-up approach: the chemical way .....	56
II.3.3.	Nano-objects: their diversity and versatility.....	57
II.3.3.1.	<i>2D nano-objects: example of sepiolite clay as polyvalent nanofillers .....</i>	<i>58</i>
II.3.3.2.	<i>3D nano-objects: example of magnetite as superparamagnetic nanoparticles.....</i>	<i>58</i>
II.3.4.	Hybrid organic-inorganic nanocomposites.....	60
II.3.5.	From liquid-crystalline state to macromolecular chemistry .....	62
II.3.5.1.	<i>Liquid-crystalline state: born from a molecular frustration .....</i>	<i>62</i>
II.3.5.2.	<i>Liquid-crystalline epoxy resin .....</i>	<i>65</i>
<b>III.</b>	<b>Materials and methods.....</b>	<b>82</b>
<b>III.1.</b>	<b>Structural and morphological analysis.....</b>	<b>82</b>
III.1.1.	FT-IR .....	82
III.1.2.	Mono and multi-dimensional NMR .....	82

III.1.3.	X-ray diffraction.....	82
III.1.4.	Electronic and optical microscopy .....	82
<b>III.2.</b>	<b>Thermal and mechanical analysis.....</b>	<b>83</b>
III.2.1.	Differential Scanning Calorimetry (DSC).....	83
III.2.2.	Stochastic temperature modulated DSC (TOPEM).....	84
III.2.3.	Thermogravimetric analysis (TGA) .....	86
III.2.4.	Rheometric analysis .....	86
III.2.5.	Dynamic mechanical analysis (DMA) .....	88
III.2.6.	Mechanical tests .....	88
<b>III.3.</b>	<b>Thermo-kinetic analysis.....</b>	<b>89</b>
III.3.1.	Extent of conversion and apparent activation energy.....	90
III.3.2.	Isoconversional principle and advanced kinetic methods .....	91
<b>IV.</b>	<b>From epoxidized linseed oil to bio-resins: an overall approach of epoxy/anhydride cross-linking.....</b>	<b>98</b>
<b>IV.1.</b>	<b>Epoxidized linseed oil cross-linking.....</b>	<b>98</b>
IV.1.1.	Epoxy/anhydride reactivity investigations .....	98
IV.1.1.1.	<i>The choice of cross-linker: a good compromise.....</i>	<i>98</i>
IV.1.2.	Epoxy/anhydride cross-linking mechanism .....	98
IV.1.2.1.	<i>Anionic living copolymerization mechanism.....</i>	<i>99</i>
IV.1.2.2.	<i>Homopolymerization and etherification as side reactions of cross-linking .....</i>	<i>100</i>
<b>IV.2.</b>	<b>Investigation of ELO/anhydride reactivity .....</b>	<b>100</b>
IV.2.1.	Formulation of ELO/anhydride resins.....	100
IV.2.1.1.	<i>Materials and systems presentation for a comparative study .....</i>	<i>100</i>
IV.2.1.2.	<i>Elaboration of formulations: functionalities, ratios and curing .....</i>	<i>101</i>
IV.2.2.	Investigation on epoxy/anhydride cross-linking by DSC.....	102
IV.2.3.	Investigation by FT-IR on evolution of the structure during crosslinking .....	105
<b>IV.3.</b>	<b>Physico-chemical aspects of cross-linking .....</b>	<b>108</b>
IV.3.1.	Heat capacity evolution during cross-linking: a TOPEM study.....	108
IV.3.2.	Chemorheological analysis and kinetic studies .....	109
<b>IV.4.</b>	<b>Thermo-mechanical characterisations and structure-properties relationship .....</b>	<b>112</b>
IV.4.1.	Glass and sub-glass transitions studies by dynamic mechanical analysis .....	112
IV.4.2.	Thermogravimetric analysis (TGA) .....	116
<b>IV.5.</b>	<b>Conclusions .....</b>	<b>117</b>
<b>V.</b>	<b>Valorization of bio-refinery side-stream products: combination of humins with polyfurfuryl alcohol for composites elaboration .....</b>	<b>124</b>

<b>V.1. Humins and furfuryl alcohol: the design of a furanic architecture .....</b>	<b>124</b>
V.1.1. From humins structure to green furanic strategy .....	124
V.1.2. Lignin organosolv as heterogeneous macromolecules of reference .....	125
<b>V.2. Resin formulation, composite elaboration and processability.....</b>	<b>126</b>
V.2.1. Materials .....	126
V.2.2. Humins/FA reactivity investigation by DSC.....	127
V.2.3. Elaboration of humins/FA cellulosic composite .....	128
V.2.4. Optimization parameters for resin and composite elaboration.....	129
V.2.4.1. <i>Effect of the pre-curing temperature</i> .....	126
V.2.4.2. <i>1 step vs 2 steps strategy</i> .....	127
V.2.4.3. <i>Importance of resin viscosity for impregnation</i> .....	131
<b>V.3. Structural characterization by FT-IR .....</b>	<b>132</b>
<b>V.4. Multi-comparative mechanical and morphological studies of cellulosic composite...</b>	<b>136</b>
V.4.1. Mechanical characterization .....	136
V.4.2. Morphological characterization.....	138
<b>V.5. An opening toward industry.....</b>	<b>140</b>
V.5.1. Reduction of polymerization temperature .....	140
V.5.2. Application fields .....	141
<b>V.6. Conclusions .....</b>	<b>142</b>
<b>VI. Combination of epoxidized linseed oil and furfuryl alcohol to design tailored fully bio-based material.....</b>	<b>150</b>
<b>VI.1. Epoxidized linseed oil and furfuryl alcohol: a green cationic marriage.....</b>	<b>150</b>
VI.1.1. A cationic copolymerization strategy .....	151
<b>VI.2. Investigation on ELO/FA copolymerization reactivities.....</b>	<b>152</b>
VI.2.1. Materials .....	152
VI.2.2. Investigation of reactivities by DSC.....	152
VI.2.3. FT-IR analysis of structural evolution during copolymerization .....	153
VI.2.3.1. Monomers and ELO50/FA50 unreacted mixture .....	154
VI.2.3.2. Structural evolution during ELO50/FA50 copolymerization .....	154
VI.2.4. Structural polymerization investigation by multi-dimensional NMR .....	158
VI.2.4.1. Study of ELO50/FA50 system at t=0 in regard with comonomers signals .....	158
VI.2.4.2. Study of ELO50/FA50 system at t=60 min in regard with homopolymers signals	160
<b>VI.3. Thermo-mechanical study of ELO50/FA50 thermoset material.....</b>	<b>167</b>
VI.3.1. Elaboration of resin bulk for mechanical analysis.....	167
VI.3.2. ELO/FA bio-based thermoset characterization by dynamic mechanical analysis (DMA) .....	167
VI.3.3. Tensile test experiments and fracture analysis by SEM .....	169

VI.3.4.	Thermogravimetric analysis (TGA) .....	171
<b>VI.4.</b>	<b>Conclusions .....</b>	<b>172</b>
<b>VII.</b>	<b>Anisotropic Reinforcement of Epoxy-Based Nanocomposites with Aligned Magnetite-Sepiolite Hybrid Nanofiller .....</b>	<b>178</b>
<b>VII.1.</b>	<b>Orientation of hybrid magnetic nanofiller into the epoxy thermoset .....</b>	<b>178</b>
VII.1.1.	Strategy of hybrid nanofiller preparation and elaboration of nanocomposite. ....	178
<b>VII.2.</b>	<b>Elaboration and characterization of the sepiolite hybrid nanofiller.....</b>	<b>179</b>
VII.2.1.	Materials.....	179
VII.2.2.	Synthesis of amino-modified sepiolite .....	180
VII.2.2.1.	<i>Synthesis of SEP/DAPTMS</i> .....	180
VII.2.2.2.	<i>Characterization by FT-IR, TGA and solid-NMR</i> .....	180
VII.2.3.	Synthesis and structural characterization of glymo-modified magnetite particles ....	181
VII.2.3.1.	<i>Synthesis of MAG/GLYMO</i> .....	181
VII.2.3.2.	<i>Characterization by FT-IR and TGA</i> .....	182
VII.2.4.	Preparation and characterization of magnetite-sepiolite hybrid nanofiller.....	183
VII.2.4.1.	<i>Preparation of m-SEP</i> .....	183
VII.2.4.2.	<i>Characterization by AAS, DSC, TEM and magnetization</i> .....	183
<b>VII.3.</b>	<b>Thermomechanical anisotropy of epoxy nanocomposite .....</b>	<b>185</b>
VII.3.1.	Preparation of m-sepiolite oriented fibers epoxy nanocomposite .....	185
VII.3.2.	Morphologies alignment of m-sepiolite into the epoxy matrix .....	185
VII.3.3.	Anisotropic thermomechanical properties of hybrid nanocomposite .....	186
VII.3.3.1.	<i>Nanocomposite mechanical properties as a function of frequency</i> .....	187
VII.3.3.2.	<i>Nanocomposite mechanical properties as a function of temperature</i> .....	189
VII.3.3.3.	<i>Thermal stability of hybrid epoxy nanocomposites</i> .....	190
<b>VII.4.</b>	<b>Conclusions .....</b>	<b>190</b>
<b>VIII.</b>	<b>Star-epoxy mesogens to design multifunctional materials: polymerization kinetics and fractal self-assembly .....</b>	<b>198</b>
<b>VIII.1.</b>	<b>Investigations on a new family of epoxy monomers .....</b>	<b>198</b>
VIII.1.1.	Star-epoxy mesogens as potential platform monomers to design hierarchical materials .	198
<b>VIII.2.</b>	<b>Synthesis and characterization of a star-epoxy mesogen monomer .....</b>	<b>199</b>
VIII.2.1.	Materials.....	199
VIII.2.2.	Synthesis and characterization of a star-epoxy monomer with 1,3,5-triazine core ....	199
VIII.2.2.1.	<i>2,4,6-Tris(p-hydroxyphenyl) triazine: TriaOH</i> .....	199
VIII.2.2.2.	<i>1,3,5-Triazine,2,4,6-tris[4-(2-oxiranylmethoxy)phenyl]: TriaEP</i> .....	200
VIII.2.3.	Investigations on star-epoxy monomer's mesogeneity .....	202

<b>VIII.3. Influence of supramolecular interactions on the polymerization kinetic: an example of anionic living copolymerization.....</b>	<b>203</b>
VIII.3.1. An epoxy/anhydride anisotropic network.....	203
VIII.3.2. Influence of supramolecular interactions on the polymerization kinetic.....	206
<b>VIII.4. Network morphological investigations correlated with thermomechanical properties: an example of A<sub>4</sub>B<sub>3</sub> epoxy/amine architecture .....</b>	<b>203</b>
VIII.4.1. TriaEP/2,7-DAF system: generation of an A <sub>4</sub> B <sub>3</sub> network .....	203
VIII.4.2. Morphological and thermomechanical investigations of TriaEP/2,7 DAF .....	211
<i>VIII.4.2.1. TriaEP/2,7 DAF: a fractal polymerization.....</i>	<i>211</i>
<i>VIII.4.2.2. Relationship between anisotropic architecture and thermomechanical properties</i>	<i>214</i>
<b>VIII.5. Conclusions .....</b>	<b>216</b>
<b>IX. General conclusion and perspectives.....</b>	<b>223</b>
<b>Annexes .....</b>	<b>225</b>
<b>Annexes - Français.....</b>	<b>239</b>



## **Chapter I**

### General introduction



## Chapter I: General introduction

The international context of modern society focuses the strategy of research in direction of the elaboration of materials with high properties, as illustrated in **Figure I.1**. The actual demand on technological materials is considerable and exacerbated by a competitive market. The creation of high performance materials became possible with the emergence of nanotechnology. This area which is the fruit of a transversality between physical and chemical sciences aims to control the design of structural entities at nanoscale level. Furthermore, this control allows to induce specific properties by tailoring the matter at different scales: the multi-functional materials are born.

The macromolecular science plays a key role in the design and elaboration of multi-functional materials which possess combined properties such as semi-conduction, gases adsorption or fire resistance and high mechanical properties. These materials can be found in common applications such as plastic bottles, batteries, adhesives, materials for transport or energy for instance.



**Figure I.1.** Omnipresence of polymers in our society in sectors of transport, energy, packaging, electronic, textile etc.

Today the petroleum hegemony in the conception of the advanced materials is quasi-total. However, the rarefaction of this resource, which is not renewable at human scale, impacts directly the world economy. Furthermore, the immoderate usage of petroleum by-products leads to important environmental damages. For all of these economic, environmental and geostrategic reasons, more and more countries are engaged into a transition towards a bio-economy as depicted in the **Figure I.2**.

This awareness is concretely materialised by common agreements such as the ratification of Kyoto protocol in 1997 which involved the signatory countries to a regulation of anthropic greenhouses gases. In the frame of the European Union, the REACH (Registration, Evaluation, and Authorization of Chemicals) directive has been ratified which drastically increased the legislation in terms of safety and chemicals management, according to the principle of Green Chemistry which supposes the utilization of eco-friendly chemicals and processes.<sup>1</sup>

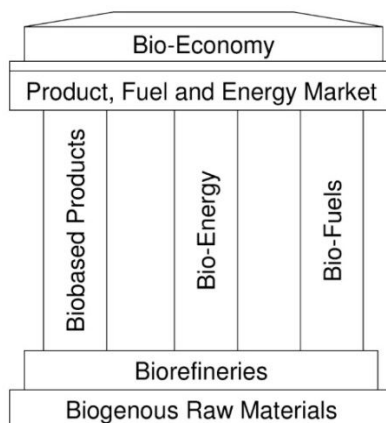


**Figure I.2.** “3-pillars” model of a bio-economy<sup>2</sup>

As seen on the **Figure I.2**, the bio-economy is based on the biogenous raw materials. Two of bio-resources recognized to have a higher potential to substitute petroleum building blocks are the biological oils and the ligno-cellulosic biomass. As a first example, we can notice the association Fimalin created in 2009 that promotes the utilization of linseed fibers and linseed oil to design performant bio-materials in term of matrix or fibers for composites elaboration. Another example is the Avantium Chemicals industry which develops news chemicals and platform building blocks and polymers from the ligno-cellulosic conversion. Avantium operates a pilot plant (24/7 since 2011) to convert carbohydrates into Alkoxymethylfurfural (RMF) compounds, further processed to a new class of furanic building blocks based on FDCA denoted as YXY. FDCA resembles the bulk chemical terephthalic acid and can be used as building blocks of polymers.

Due to their high potentials and availabilities, linseed oil and furfuryl alcohol raw materials have been chosen as precursors for the elaboration of bio-based materials in this thesis work.

<sup>1</sup> Anastas, P. T.; Warner, J. C., Green chemistry: theory and practice. Oxford university press: 2000.

<sup>2</sup> Kamm, B.; Kamm, M.; Gruber, P. R.; Kromus, S., Biorefinery Systems – An Overview. In Biorefineries-Industrial Processes and Products, Wiley-VCH Verlag GmbH: 2008; pp 1-40.

## Chapter I: General introduction

This thesis work has been co-financed by *Provence-Alpes-Côte d'Azur (PACA)* region and Sicomin Composites company that work on epoxy formulations since more than twenty years for diverse sectors such as energy or transport. This financing has been concretely supported by the Region-APO BIOECOMAT project. In agreement with the international context of transition from the actual petroleum-based economy to the bio-economy presented above, this project aims to develop new bio-based materials for eco-building or eco-transport for instance.

The purpose of BIOECOMAT project has been extended to the European project called “BIOpolymers and BIOfuels from FURan” (BIOFUR) in the frame of “Marie Curie Industry-Academia Partnerships and Pathways” (IAPP) (FP7-PEOPLE-2012-IAPP). This project was conducted by Avantium Chemicals Company, in collaboration with CNRS Laboratory in Nice France for the polymer part, and with University of Messina Italia for the catalysis part.

The principal work of this manuscript related to BIOFUR project studied the possibilities of the valorization of “humins” which are side-stream products issued from the biomass conversion during the formation of bio-based building blocks destined to generate biopolymers and biofuels. This work has been essentially conducted in Avantium Chemicals society, in Amsterdam Netherland, under the supervising of Dr. Ed De Jong, Dr. Jan C. Van der Wall and Dr. Nathanaël Guigo, during my secondment of four months from 22 July 2013 to 15 November 2013.

In agreement with BIOECOMAT and BIOFUR projects, three objectives have been defined for these doctoral investigations:

- (1) *Upgrade the knowledge on monomers behavior as precursors for the elaboration of thermosets in terms of polymerization and structure-properties correlation* **Chapter IV, VI, VIII**
- (2) *Elaboration of performant (fully) bio-based materials.* **Chapter IV, V, VI**
- (3) *Proposes original strategies to improve classical thermosets properties or to develop new ones.* **Chapter V, VII, VIII**

Thus, in conformity with these objectives, this thesis manuscript has been organized in 9 chapters, with 5 chapters of results; **Chapters IV, V, VI** for biomass concern and **Chapters VII and VIII** for advanced materials investigations:

- ◆ **Chapter I:** is an introductory part, highlighting the main objectives of this thesis work in the actual international context. The strategy of research of this study is presented.
- ◆ **Chapter II:** the bibliographic part, this chapter aims to present the major concepts which will be discussed in the following chapters. Herein, the first paragraph presents the **thermosets science**, through the chemical and physical phenomenon involved during the

cross-linking process, reliable to the creation of **tridimensional architectures**. Then the chemistry developed from biomass conversion is briefly exposed, putting in light the **epoxidized linseed oil (ELO)**, the **furfuryl alcohol (FA)** and the **humins** as preferential precursors to elaborate sustainable thermosets. The last paragraph presents fundamental approaches in order to develop bio-inspired hierarchically organized materials. These approaches concern the conception of **nanocomposites** with the elaboration of inorganic-hybrids of **sepiolite** and of **magnetite, then their combination**. Finally, the work treats about the self-organization of **mesogenic monomers** into **liquid-crystalline polymers**.

- ◆ **Chapter III:** describes the **different techniques, apparatus and methods** which have been used during this work thesis, linked to each chapter.
- ◆ **Chapter IV:** focuses on the elaboration of **epoxidized linseed oil (ELO)** thermosets, through a **comparative study between mono- and di-anhydrides as crosslinkers**. Firstly, the polymerization parameters were optimized (by DSC, rheometry, kinetics analysis) in order to generate a fully cured thermoset network. Secondly, the thermomechanical properties (DMA, TGA) have been discussed highlighting the relationship between reactivity and polymer architecture i.e. the influence of **secondary reactions like homopolymerization and etherification**.
- ◆ **Chapter V:** the principal objective of this chapter is to find a new application for **humins**, recalcitrant side-stream product. For this purpose, a **fully “furanic” strategy** has been tested with humins as functional blend for **polyfurfuryl alcohol (PFA)** resins. Humins **cellulosic composites** have been elaborated to test their ability to impregnate wood or textiles. Tensile test analysis on impregnated cellulose composites permitted to evaluate and to compare humins resins (at different weight ratios) in regard to pure PFA resin and lignin resin.
- ◆ **Chapter VI:** reports the elaboration of **fully bio-based thermosets** through the **combination** of **epoxidized linseed oil (ELO)** and **furfuryl alcohol (FA)** monomers, with the principal aim to tailor the polymer’s mechanical properties in function of monomers ratio. The cationic polymerization has been explored by FT-IR, 2D-NMR and the mechanical properties have been investigated by DMA and tensile tests.
- ◆ **Chapter VII:** proposes a strategy for the **anisotropic reinforcement** of an epoxy resin through the creation of an **original hybrid** of sepiolite grafted magnetite **orientable under a magnetic field**. The first part presents the nanofiller elaboration by a double functionalization of **sepiolite** and **magnetite**, followed by the curing of epoxy (DGEBA) **nanocomposite** under magnetic field. The second part focuses on the influence of composite nanofiller orientation (parallel, anti-parallel, and isotrope) in regard to

## Chapter I: General introduction

mechanical solicitation (DMA). This work has been done in collaboration with Dr. Jessica Alves Marins, Dr. Françoise Giulieri and Dr. Georges Bossis.

- ◆ **Chapter VIII:** is focused on the possibility to develop epoxy resins having **multi-scales organization**. For this purpose a preliminary work has been done with the design and study of a new class of epoxy monomer which possesses a star geometry and a mesogenic character capable to induce a self-organization into mesophase during the polymerization. Thus after the synthesis and characterization of this **star-epoxy mesogen**, its proclivity to generate cross-linked thermosets has been explored. Firstly, in combination with anhydride through the analysis of the influence **of supramolecular interactions** on the **polymerization kinetics**; and secondly with a di-amine as cross-linker for investigations on **network morphology by fractal development** (X-ray) in relationship with thermo-mechanical properties (TGA and DMA).
- ◆ **Chapter IX:** presents the general conclusion of this thesis work, and open the discussion to perspectives.



## Chapter II

From petro-based advanced materials to bio-based  
thermosets: state of the art



<b>II.1. Thermosets engineering</b> .....	<b>26</b>
II.1.1. A petrosourced-polymer design hegemony .....	26
II.1.1.1. <i>Epoxies monomers chemistry: DGEBA synthesis</i> .....	27
II.1.1.2. <i>Polymerization process: cross-linkers and functionalities</i> .....	29
II.1.2. The creation of a 3D architecture .....	32
II.1.2.1. <i>Gelation phenomenon (sol-gel transition)</i> .....	32
II.1.2.2. <i>Glass transition and vitrification phenomena</i> .....	34
II.1.3. Outstanding properties and application fields of epoxy thermosets.....	36
<b>II.2. From biomass to bio-based thermosets</b> .....	<b>36</b>
II.2.1. An historic renewable feedstock: the triglycerides oils.....	37
II.2.1.1. <i>Composition and chemistry of vegetable oils</i> .....	37
II.2.1.2. <i>Epoxidized linseed oil</i> .....	39
II.2.2. A biosourced-polymer design issue from carbohydrate conversion.....	41
II.2.2.1. <i>From the biorefinery concept to platform molecules production</i> .....	41
II.2.2.2. <i>From furfuryl alcohol to polyfurfuryl alcohol</i> .....	45
II.2.2.3. <i>A side-product to valorize : the humins</i> .....	49
<b>II.3. Hierarchical advanced materials: a Nature inspiration</b> .....	<b>53</b>
II.3.1. Bio-inspiration as strategy to design advanced materials.....	54
II.3.2. Bottom-up approach: the chemical way .....	56
II.3.3. Nano-objects: their diversity and versatility.....	57
II.3.3.1. <i>2D nano-objects: example of sepiolite clay as polyvalent nanofillers</i> .....	58
II.3.3.2. <i>3D nano-objects: example of magnetite as superparamagnetic nanoparticles</i> .....	58
II.3.4. Hybrid organic-inorganic nanocomposites.....	60
II.3.5. From liquid-crystalline state to macromolecular chemistry .....	62
II.3.5.1. <i>Liquid-crystalline state: born from a molecular frustration</i> .....	62
II.3.5.2. <i>Liquid-crystalline epoxy resin</i> .....	65

## II. From petro-based to bio-based thermosets: a state of art

### II.1. Thermosets engineering

Polymers can be classified considering various criteria, such as their origins, structures, stereochemistry, number of implied monomers, their connectivity manner, properties or fields of applications for instance. However a common way to discriminate the organic polymers is to make a distinction of their particular response in regard to the temperature.<sup>1</sup> Thus, polymeric materials can be classified in two categories: thermoplastics and thermosets. Thermoplastics are generally semi-crystalline polymers which possess amorphous and crystalline phases that mean they have characteristic temperatures of melting/crystallization and of glass transition. These thermoplastics are constituted by linear or ramified polymer chains and are known to be remouldable and recyclables. Thermoset materials are covalent cross-linked polymers generating a tridimensional network (this is also the case for elastomeric materials with a lower number of covalent bridges). Due to this dense cross-linked architecture, a thermoset is classically infusible, insoluble and unrecyclable, but possess very high thermo-mechanical properties that cannot generally be reached by a thermoplastic material. As exposed in the introductory part, this thesis work will focus only on thermoset polymers and composites.

This part is an introduction into the thermoset aspects referred in this thesis, taking into account the major progress and understanding of this discipline. After a brief enumeration of the most important thermoset families, the first paragraph focuses on the epoxy thermoset chemistry, from the synthesis of epoxy monomer to the polymerization mechanism. The second paragraph centers on the physico-chemistry of polymerization, from liquid to solid state, highlighting the physical events which occur during the creation of a tridimensional network, and conclude with the applications of these versatile materials.

#### II.1.1. A petrosourced-polymer design hegemony

Since the discovery of Goodyear and Hancock for the vulcanization of natural rubber in 1839, the innovation and commercialization of thermoset resins have been in a constant progression as depicted on **Table II.1** As principal thermoset examples, we can cite phenolic, urea-formaldehydes, polyurethanes, epoxy or polyimides resins. Each of these formulations has preferential domain fields such as plywood adhesive for phenolic resin, or polyurethanes foams

for construction. But epoxy resins have the particularity, due to their monomeric versatility, to cover an important range of application fields.

**Table II.1.** Evolution of thermoset science and industry<sup>2</sup>

1839	Goodyear discovered vulcanization of rubber.
1909	Baekeland granted his 'Heat and Pressure' patent for phenolic resins.
1926	Alkyd introduced. Aniline-formaldehyde introduced in U.S.
1928	Urea-formaldehyde introduced commercially.
1931	Hyde began research on organo-silicon polymers.
1933	Ellis patented unsaturated polyester resins.
1935	Henkel made melamine-formaldehyde resins.
1937	Automatic compression molding introduced commercially. Polyurethanes first produced.
1938	Melamine introduced commercially.
1939	First patent (in Germany) on epoxy.
1941	Urethane-polyester type-introduced in Germany.
1942	Dow Corning made silicone industrially.
1943	Castan's patent issued on epoxy.
1946	Polyurethane elastomers introduced.
1947	Epoxy introduced commercially.
1954	Polyurethane introduced in U.S.
1957	Urethane-polyether type-introduced in U.S.
1964	Polyimides introduced as a fabricated product.
1970s	Mobay & Bayer issued first patents on cyanate esters. Commercial development expands into 1980s.
1970s	Thermosetting polyimides expand into high-temp adhesives and composites for aerospace applications.
1980–1990s	Development of BMI & BMI copolymer commercial applications.

#### II.1.1.1. Epoxies monomers chemistry: DGEBA synthesis

This section aims to present the main strategies of epoxidation to generate epoxy “resins”. Focus will be done on the *epoxidation way by epichlorohydrin* because it is the most employed strategy to produce DGEBA (DiGlycidyl Ether of Bisphenol A) which is the most popular epoxy resin.

- ◆ *Epoxidation by epichlorohydrin (ECH)*: this strategy consists on the reaction between a hydroxyl function (mostly a phenol group) and 1-chloroprene-2-oxide called epichlorohydrin (ECH). In the **Figure II.3** is illustrated the epoxidation of the bisphenol A. Concerning the synthesis protocol, as presented in the literature, ECH is generally used in large excess or also as solvent. Then, the sodium hydroxide is usually added in aqueous or alcoholic solution.<sup>3</sup> This reaction can also be catalyzed by several salts as tetrabutylammonium bromide or zinc chloride for instance.<sup>4,5,6,7</sup> In general the involved mechanism is described as two competitive reactions between a phenate ion ( $\text{Ar-O}^-$ ) and ECH. The first one is a one-step nucleophilic substitution mechanism ( $\text{S}_{\text{N}}2$ ) with the

cleavage of C-Cl bond; the second one is a two-step mechanism associated with a ring opening of ECH by phenate ion, followed by an intramolecular cyclization ( $S_Ni$ ) of the generated alcoholate and accompanied by the release of a chlorate anion.

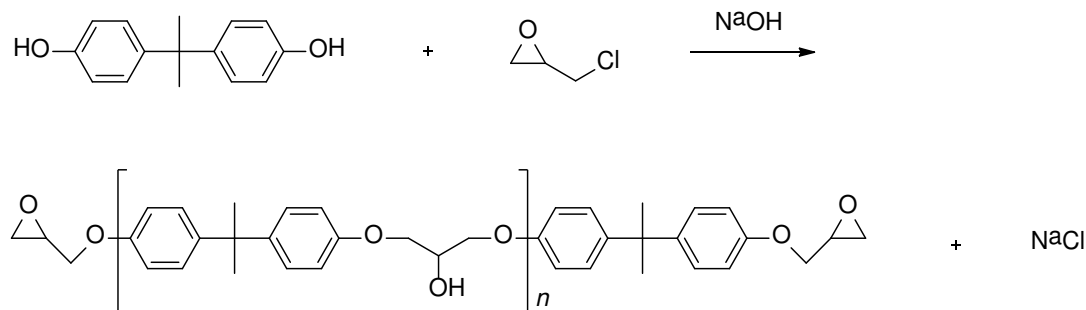


**Figure II.3.** Epoxidation reaction between bisphenol A and epichlorohydrin to generate DGEBA monomeric resin.

The advantage of this epoxidation strategy is the possibility of tailoring pre-polymer's length and molecular weight. As a result, DGEBA pre-polymer (or resin) characteristics are essentially depending on the molar ratios between epichlorohydrin / bisphenol A. Typically, the pre-polymer of DGEBA (**Figure II.3**) possess  $n$  monomeric units in the range of  $0.03 < n < 10$ . At room temperature, this DGEBA monomer is in a crystalline solid state for  $n$  close to 0, it is liquid for  $n \approx 0.5$  and vitreous for superior values of  $n$  ( in this case  $T_g \sim 40-80$  °C).<sup>8</sup> In general, the DGEBA low molecular weight ( $M_w$  around  $370 \text{ g.mol}^{-1}$ ) is used as adhesive, for encapsulation, plywood etc., while the high molecular weight (around  $1420 \text{ g.mol}^{-1}$ ) is preferred for surface coatings.<sup>9</sup>

- ◆ *Epoxidation by double bond oxidation*: this epoxidation pathway concerns the peroxidation of C-C double bonds. The protocol can differ depending on the electronic effects implying the double bond. Indeed, in the simple case of an alkyl olefin, the simple utilization of hydrogen peroxide ( $\text{H}_2\text{O}_2$ ) is enough to generate the oxiran ring. In the presence of electroattractor groups like oxygen in  $\beta$ -position of the double bond requires a stronger oxidative reagent such as *m*-chloroperbenzoic acid. The complexity of purification of epoxy monomer limits the industrial development of this way.<sup>8,10,11</sup>
- ◆ *Epoxidation via glycidyl (meth)acrylate*: this epoxidation consists on the reaction of a glycidyl (meth)acrylate with another co-monomer containing a vinyl or (meth)acrylic group by free radical polymerization.<sup>8</sup>

After this brief presentation of epoxidation strategy, in following subchapter will be presented the associated co-monomer molecules that can be used to generate cross-linked polymers.



**Figure II.4.** Epoxy/amine reactions accompanying the polymerization.

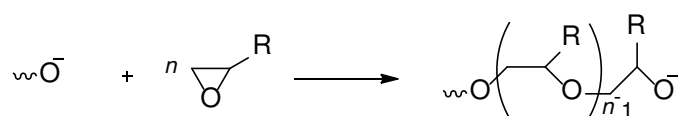
Another original reaction is that between epoxy and isocyanate groups which leads to generate also 3D networks through several competitive reactions such as trimerization forming isocyanurate rings or epoxy addition catalyzed by a nucleophilic agent forming oxazolidone ring.<sup>17</sup>

The functionality is an essential information on the proclivity of epoxy and cross-linker groups to generate covalent bonds.<sup>18</sup> These functionalities are necessary for calculating the optimal ratio of epoxy in regard to the curing agent to ensure that all the chemicals groups react. In the case of polycondensation, the functionality of epoxy function is always equal to 1. It is the same case for alcohol or mercaptan. For primary amine function, the functionality is equal to 2 in regard with the previously described reactivity; it is important to take into account both the attack of the primary and of the secondary amine.<sup>3,19</sup>

◆ *Chain-growth polymerizations:*

- *Homopolymerization:* Self-reaction of epoxy group can also be induced by thermal or by catalytic inductions of either nucleophilic or electrophilic species as illustrated in **Figure II.5**. The commonly used initiator, also called “catalytic” curing agent, include imidazoles, tertiary amines, or ammonium salts for anionic chain polymerization. The active species which provokes the propagation is then an alkoxide. Lewis acids like boron trifluoride complexes, complexes aromatic salts of triarylsulfonium, etc. are generally used for cationic chain polymerizations. In this case the active species is an ozonium. This latent catalysis is initiated by decomposition reaction of Lewis acid which can be operated by thermal or UV treatment.<sup>20,21</sup> These catalyzed chain propagations lead to relative low molecular mass value, due to several chain transfer and complex termination steps.<sup>21</sup>

**Anionic homopolymerization**



**Cationic homopolymerization**

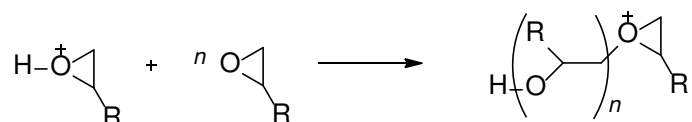
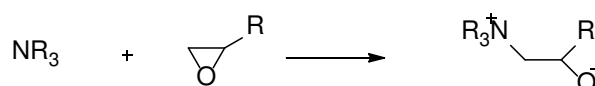


**Figure II.5.** Catalysed anionic and cationic epoxy homopolymerization.

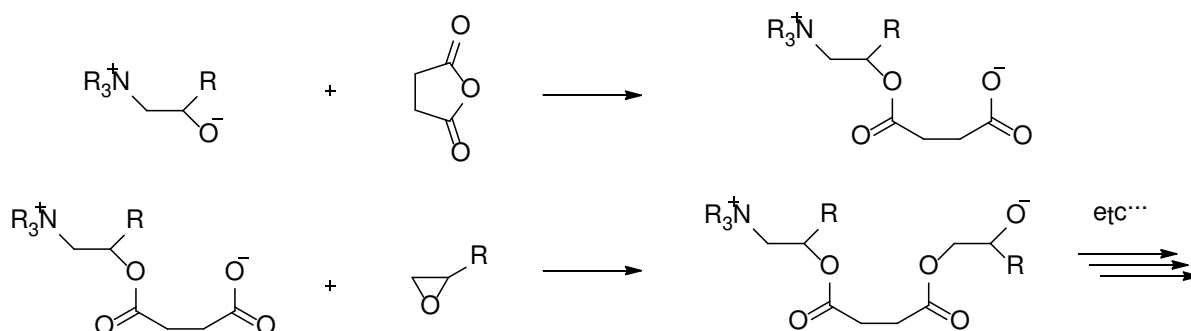
- *Copolymerization:* besides polyadditions, epoxy group can polymerize via chain copolymerizations with cyclic anhydride or carboxylic acid catalyzed by Lewis bases. The case of carboxylic acids is particular because it can undergo polyaddition or copolymerization, depending of the utilization of a Lewis base as catalyst or not. Notice that reaction with carboxylic acid is always accompanied by several secondary reactions.<sup>22</sup> The mechanism of chain copolymerization has been explored and discussed by Matějka et al.<sup>23</sup> and Leukel et al.<sup>24</sup> highlighting a strictly alternant mechanism called “living anionic copolymerization” in analogy with biological system. Indeed, this kind of polymerization should avoid all chain transfer and termination reactions. However the question that flows about the catalyst regeneration is still under debate.<sup>25</sup> The mechanism presented in **Figure II.6** consists on an initiation step with the formation of a zwitterion that contains an ammonium and an alkoxide anion. This generated alkoxide reacts immediately with an anhydride group leading to the formation of a carboxylate anion as described in **Figure II.6 (b)**. Then, the resulting carboxylate active center can react with another oxiran ring, generating a new alkoxide as active center and thus connecting epoxy and anhydride in a strictly alternate manner.<sup>23</sup>

### Living Anionic Copolymerization

a) Initiation mechanism



b) Alternating anionic propagation mechanism

**Figure II.6.** Epoxy/anhydride mechanism catalysed by a tertiary amine: living anionic copolymerization.

In regard with the presented mechanism of epoxy/anhydride reaction, the functionality of each epoxy and mono-anhydride groups are equal to 2. This presentation is not exhaustive due to the large variety of cross-linkers and catalysis so each mechanism related to specific formulation will be presented directly in the concerned chapter.

### II.1.2. The creation of a 3D architecture

The formation of a 3D polymer network requires at least a global functionality larger than 2 for the starting components. This is a necessary condition but often not sufficient to reach the creation of a tridimensional skeleton.<sup>26</sup> Knowing that, the below section aims to focus on the general criteria for obtaining a tridimensional architecture, and on the definition of critical transformations that can occur during the formation of an epoxy network i.e. gelation and vitrification.

#### II.1.2.1. Gelation phenomenon (sol-gel transition)

##### ◆ General features of network formation:

The overall cross-linking process should be schematized as follows: initially a combination of monomeric precursors react together, in function of their functionalities and reactivities, generating macromolecular units. This group of molecules having a particular distribution of molecular weights are constitutive of the “sol” that means the soluble part of the system undergoing crosslinking. At a higher extent of crosslinking conversion, with the continuous growing of “sol” molecular weight and polydispersity, the connections between units increase until the formation of an infinite path of bonds allowing the formation of an unique giant macromolecular structure that percolates the reaction medium. According to Flory's<sup>27</sup> theory, this phenomenon is function of a given system, occurring at a definite conversion, and called “gelation”. This insoluble macromolecule, characterized by its immiscibility, is called “gel” and can be conceptually divided in several substructures which can be active and react with the free monomeric/sol units achieving the crosslinking.<sup>26</sup>

As depicted in **Figure II.7** the macromolecular gel could be described as a combination of following substructures:

- *Dangling Chains (DC)*: correspond to a substructure which is singly bonded to the main chain skeleton. DC proportion cannot be directly determined, but their influence and size can be correlated with dynamic mechanical properties. Indeed, their relaxations

distributions are different in comparison with those of EANCs or sol molecule: they don't participate to the network cohesion.<sup>28,29</sup>

- *Elastically Active Network Chains (EANC)*: correspond to linear branched chain composed by monomeric/precursor units localized between two elastic active crosslink. According to the Flory-Erman theory,<sup>26,30</sup> the quantity of EANC in a polymer network can be associated to an equilibrium modulus, and thus should be measured, due to the retractive force generated by EANC in response to an external stretching force.
- *Elastically Active Crosslinks (EAC)*: are the branch points which determine the skeleton network shape. They are composed by three or more bonds,<sup>26</sup> and define the limit of EANC molecular weight  $M_c$  (without DC consideration) which can be calculated for instance by branching theories described by Krakovsky et al.<sup>31</sup>

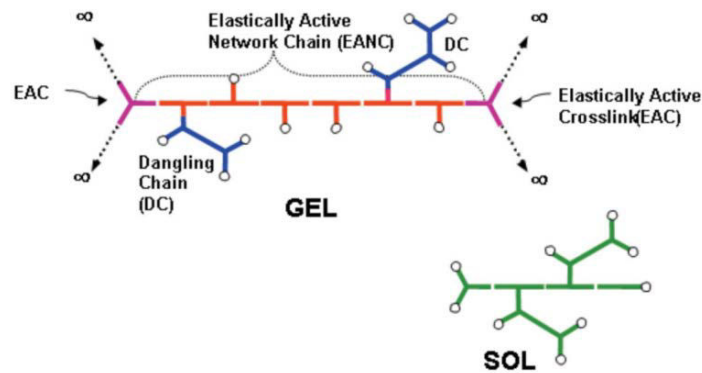


**Figure II.7.** Sol and gel substructure of a cross-linked network beyond gelation.<sup>32</sup>

In comparison with the linear polymers, less experimental techniques are available for cross-linked networks, thus is the reason of development of theoretical methods concerning network formation. These theories permit a better understanding and correlation between precursors structure and chemistry, and are able to predict the network evolution and the corresponding properties.

◆ *Theoretical description of cross-linking and network formation*: the methods usually used to describe network growing could be discriminated in three groups, taking into account the possible intra or inter-reactivities:

- *Statistical methods*: are based on the probability of distribution of monomeric/precursors associations and growing as function of their intrinsic functionalities and reactivities.<sup>32,33,34,35</sup>

- *Kinetic methods*: are based on the kinetic equations for describing the distribution evolution of molecules during the polymerization.<sup>36</sup> The apparent activation energy could be resumed as a set of differential equations taking into account the size, reactivities, steric hindrance and diffusivity of molecules groups.<sup>26</sup>
- *Simulation and modelling in finite 3D space*: these methods take into account the main interactions such as chemical reactivities and molecular physical interactions in space. However, the integration of molecular structure dynamics into the simulation algorithm is still the major problem. Thus, these simulations does not reflect the real polymerization dynamics, because generated bonds are fixed in the space between lattice sites during the entire crosslinking process.<sup>37,38,39,40</sup>

The principal characteristics of the network formation can be summarized in five points:<sup>32</sup>

- ◆ The evolution of the molecular weight before gelation
- ◆ The critical time and conversion until the formation of infinite structure i.e. the gel, that can be determinated theoretically or with the help of rheology (**section III.2.4.**)
- ◆ The degree of transformation of finite (soluble) part of the system, commonly called “sol”, into the infinite structure called “gel”
- ◆ The evolution of the molecular weight of the sol
- ◆ The evolution of the viscoelastic properties of the medium during the cross-linking.

The evolution of viscosity is very important because it is reliable to another physical phenomenon called “vitrification” which has a strong influence on the reactivity during latter stages of reaction.

### *II.1.2.2. Glass transition and vitrification phenomena*

The glass transition temperature ( $T_g$ ) is an important characteristic of polymeric materials, reliable to a drastic variation of heat capacity ( $C_p$ ) and of mechanical properties of the material. The  $T_g$  is defined as a temperature domain of transition from glassy to viscoelastic state during heating the material. The knowledge of this critical temperature is important for applications, because it conditions the mechanical properties of the material at a given temperature, and also

is essential for the elaboration of the tridimensional network. Indeed, during the process of thermoset crosslinking, a phenomenon called “vitrification” may occur if the  $T_g$  is equal or becomes higher than the reaction temperature. This phenomenon corresponds to a transition from a liquid to a glassy state and provokes a decrease of molecular motions. It can be observed for isothermal or non-isothermal curing processes and can occur before or after gelation. Indeed, it is important to notice that gelation and vitrification are considered as independent events. In term of processability, the knowledge of vitrification temperature is very important because the polymerization kinetic decreases drastically in the glassy state. This effect is considered as very relevant with an increase of the difference between glass transition temperature and reaction temperature ( $T_g - T$ ). When this difference reaches 20-30°C, the reaction is considered as stopped.<sup>19</sup> Concerning the  $T_g$  evolution during polymerization, its value increases with conversion because of the increase of molar mass in the pre-gel state and of the crosslink density in the post-gel state.

In order to summarize all the concepts presented above, the Time-Temperature-Transformations (TTT) diagram developed for thermosetting systems by Gillham<sup>41</sup> presents the transitions between the different states and phenomena taking place during the crosslinking, (**Figure II.8**). This diagram represents also three critical temperatures of glass transition noted  $T_{g0}$ ,  $T_{g\text{ gel}}$  and  $T_{g\infty}$  that are associated with the glass transition of precursors, the temperature of coincidence between gelation and vitrification and finally the glass transition of the fully cross-linked network.

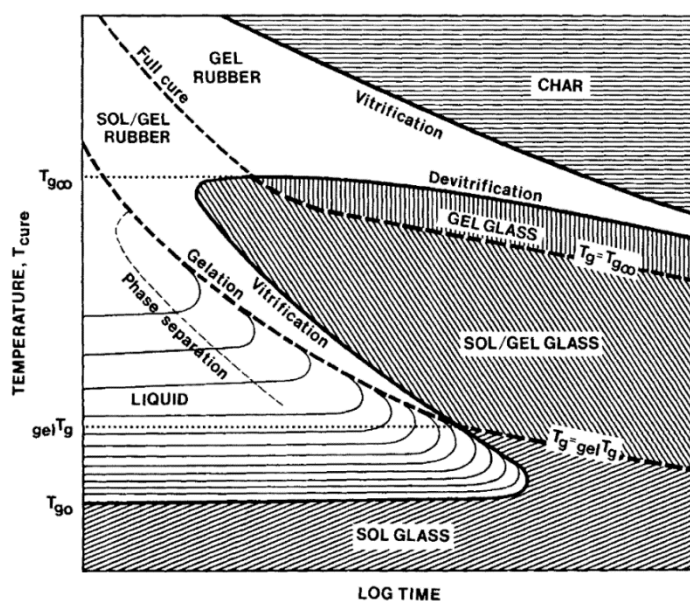


**Figure II.8.** Time-Temperature-Transformations (TTT) diagram<sup>41</sup>

### II.1.3. Outstanding properties and application fields of epoxy thermosets

The resulting cross-linked epoxy networks exhibit outstanding properties which can be reliable to numerous applications such as adhesives, coatings, insulating materials, matrix for advanced composites, etc. A wide variety of industries is associated to these applications such as aerospace, defence, construction, energy or transport. These myriad of applications are linked with the versatility of epoxy resins. Indeed, industrials are able to elaborate tailored formulations for targeted properties. The main advantages of epoxy, explaining their success, are summarized below:<sup>19</sup>

- ◆ No emission of volatile compounds during the polymerization.
- ◆ Flexibility in term of selection of monomer/co-monomer allowing to obtain variety of polymers from rubbers, low  $T_g$ , to high  $T_g$  materials.
- ◆ Versatility in terms of utilization and combinations of different polymerization chemistry in order to respond to the processability demand.
- ◆ Low coefficient of expansion during crosslinking.
- ◆ High adhesivity due to the polar groups generally present in the network.
- ◆ Possibility to introduce different modifiers in the epoxy matrix, in order to promote targeted properties like toughness or to generate new one, like optical anisotropy by addition of liquid-crystal droplet as an example.

Today the physico-chemistry of cross-linked networks is confronted to new challenges as the design of thermosets issued from bio-based synthons with equivalent properties and profitability as petro-based homologues in accordance with the European REACH directives, as presented in the introduction part.

## II.2. From biomass to bio-based thermosets

The term biomass is associated with several definitions, however, according to an US strategy program of development<sup>42,43</sup>, we can define the term “biomass” as: “any organic matter that is available on a renewable or recurring basis (excluding old-growth timber), including dedicated energy crops and trees, agricultural food and feed crop residues, aquatic plants, wood and wood residues, animal wastes and other waste materials.” In the present investigation on bio-based thermosets, we are interested in two different feedstocks: the first category concerns the lipids,

especially the vegetable oils and the second category is reliable to the lignocellulosic feedstock, more particularly on carbohydrates conversion into furanic compounds.

## II.2.1. An historic renewable feedstock: the triglycerides oils

### II.2.1.1. Composition and chemistry of vegetable oils

These recent years have been the theatre of the renewal of biological oils utilization because of the growing interest of industry for sustainable resources, inspired by the political awareness about the transition to a “green” economy. Biological oils, composed by a mix of triglycerides, are known to be one of the best candidates as renewable raw materials to design chemicals and bio-polymers as illustrated in **Figure II.9**. That is explained by its competitive cost due to their abundance and availability renewing at human scale; but also due to its biodegradability and low toxicity.<sup>44,45</sup>

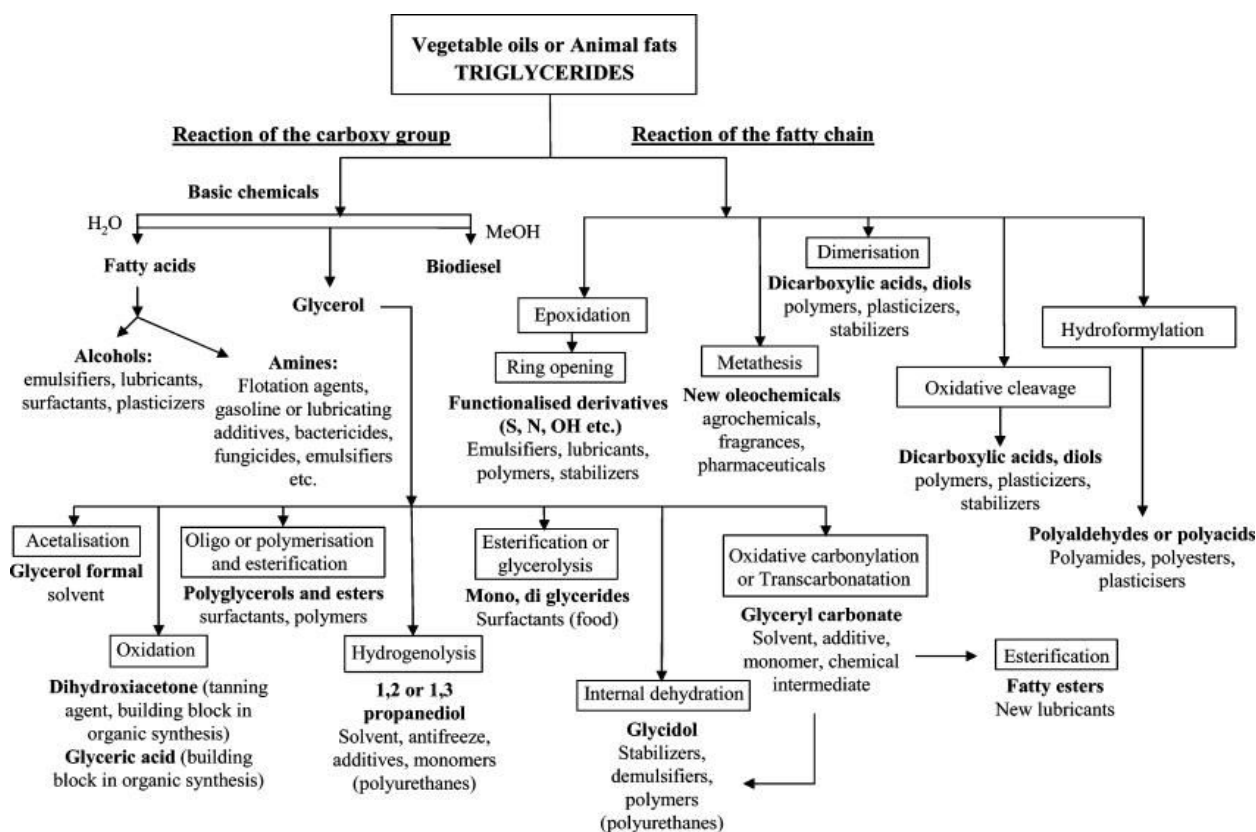


**Figure II.9.** Chemical ways associated with the production of valuable products from fats and oils.<sup>46</sup>

Triglycerides lipids are liquids at room temperature and are constituted by glycerol and fatty acids revealing a three-arms structure of tri-esters (**Figure II.10**). The most common triglycerides constitutive fatty acids are describe on **Table II.2**, and represent 94 to 96% of the triglycerides oils moieties in weight.<sup>47</sup> **Table II.3** summarizes the chemical structures and properties of the principal vegetable oils. The average number of double bonds per triglyceride and the iodine value (amount of iodine that reacts with the double bonds for 100g of vegetable oil) is an indication of vegetable oils reactivity.

**Table II.2.** Main fatty acids and their structures<sup>48</sup>

Fatty acid	Formula	Structure
Caprylic	$C_8H_{16}O_2$	
Capric	$C_{10}H_{20}O_2$	
Lauric	$C_{12}H_{24}O_2$	
Myristic	$C_{14}H_{28}O_2$	
Palmitic	$C_{16}H_{32}O_2$	
Palmitoleic	$C_{16}H_{30}O_2$	
Stearic	$C_{18}H_{36}O_2$	
Oleic	$C_{18}H_{34}O_2$	
Linoleic	$C_{18}H_{32}O_2$	
Linolenic	$C_{18}H_{30}O_2$	
$\alpha$ -Eleostearic	$C_{18}H_{30}O_2$	
Ricinoleic	$C_{18}H_{34}O_3$	
Vernolic	$C_{18}H_{32}O_3$	

**Table II.3.** Chemical properties and fatty acids composition of common vegetable oils<sup>48</sup>

Vegetable oil	Double bonds	Iodine value/mg per 100 g	Fatty acid (%)				
			palmitic	stearic	oleic	linoleic	linolenic
Palm	1.7	44-58	42.8	4.2	40.5	10.1	-
Olive	2.8	75-94	13.7	2.5	71.1	10.0	0.6
Groundnut	3.4	80-106	11.4	2.4	48.3	31.9	-
Rapeseed	3.8	94-120	4.0	2.0	56.0	26.0	10.0
Sesame	3.9	103-116	9.0	6.0	41.0	43.0	1.0
Cottonseed	3.9	90-119	21.6	2.6	18.6	54.4	0.7
Corn	4.5	102-130	10.9	2.0	25.4	59.6	1.2
Soybean	4.6	117-143	11.0	4.0	23.4	53.3	7.8
Sunflower	4.7	110-143	5.2	2.7	37.2	53.8	1.0
<b>Linseed</b>	<b>6.6</b>	<b>168-204</b>	<b>5.5</b>	<b>3.5</b>	<b>19.1</b>	<b>15.3</b>	<b>56.6</b>

The linseed oil particularly, presents an exceptional ability to polymerize because it contains the higher degree of double bonds due to its higher amount of linolenic acid. That makes a

natural good candidate to chemicals modifications on some reactive sites as C=C double bonds, ester groups, allylic positions or  $\alpha$ -carbonyl position, as showed on **Figure II.10**. Indeed, in addition to glycerol and fatty acids, which separately are considered as high valuable molecules,<sup>46</sup> triglyceride itself can be modified in many ways to obtain new chemicals and monomers.<sup>49</sup> One of this modification is well known to generate very high valued molecules: the epoxidized oils.<sup>50</sup>

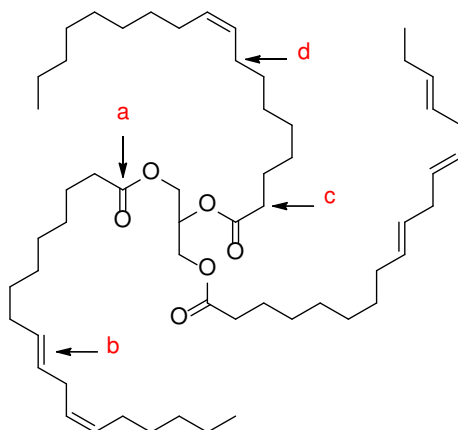


**Figure II.10.** Triglyceride molecule with their different positions for chemical modification: (a) the ester groups, (b) the double bonds, (c) the  $\alpha$ -carbonyl positions, (d) the allylic positions.<sup>51</sup>

#### II.2.1.2. Epoxidized linseed oil

Due to the high reactivity and versatility of the epoxide groups, the epoxidation strategy has been explored through different pathways in order to generate functional triglyceride derivatives. The **Figure II.11** describes 2 examples of epoxidation strategy:

- ◆ The most employed strategy in industry is commonly called Prileshajev epoxidation<sup>52</sup> and consists in the formation *in situ* of a peracid by the action of hydrogen peroxide on organic acid (acetic or formic) in presence of a strong Bronsted acid ( $\text{H}_2\text{SO}_4$  typically).<sup>53</sup> The utilization of strong acids in the process presents several disadvantages associated with a poor selectivity, necessity of neutralization, and an equipment resistant to corrosion. This kind of catalysts can also provide side-reactions such as the opening of oxiran in presence of water leading to the formation of hydroxyl and then of the oligomers through ether linkages. However, the typical conversion of double bonds into epoxy groups reaches 90 % with a selectivity around 75-85 %.<sup>54</sup>
- ◆ Greener epoxidation strategies have been investigated using lipase-catalyzed chemoenzymatic oxidation. An example of experimental conditions is given by the work

of Tellez et al.<sup>55</sup> as illustrated in **Figure II.11**. This strategy presents several advantages in regard with Prileshajev process such as a neutral pH environment and the formation of stable hydroperoxides from fatty acid, i.e. without utilization of acetic acid or strong Bronsted acid catalysts. Enzymes employment contributes to a higher regio-, stereoselectivity and an important selectivity/conversion avoiding side-reactions.<sup>54</sup>

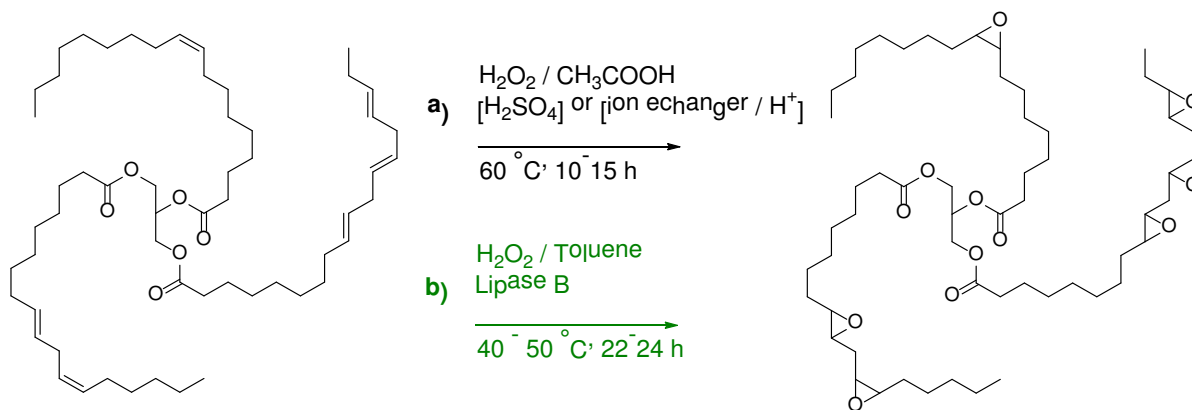


**Figure II.11.** Examples of strategies for vegetable oil epoxidation: a) Prileshajev method<sup>52,56</sup> b) enzymatic way.<sup>55</sup>

Epoxidized oils are considered as high potential intermediates for thermosets elaboration. In the same mode as olefin biological oils, epoxidized oils could play as platform molecules to develop new chemicals or monomers by ring opening with amines, alcohols, acids,  $\text{CO}_2$  etc.<sup>50,57</sup> These chemical transformations are reliable to a myriad of applications such as thermosets, polyurethane foams, coatings, adhesive resins, inks, matrix for composites, lubricants and so on.<sup>54,58</sup> Concerning the epoxidized vegetable oils for the elaboration of thermosets, researches focused, in the last years, on the development of new polymers with low-toxicity and low migration plasticizers for a greener phthalate substitution.<sup>59,60</sup>

Another important contribution relates with their capacity to scavenge acidic groups through catalytic degradation by the conversion of the formed cation radicals or excited diradicals into allylic structures that can start the growth of new polyene sequences in the conventional way.<sup>61</sup> These properties legitimate the utilization of epoxidized vegetable oils not only as co-monomers but also as monomers. This purpose has been developed in few studies treating petro- and bio-based cross-linkers covering essentially topics which concern formulation or thermo-mechanical properties but not the polymerization physico-chemistry linked to the network morphology and properties.<sup>8</sup> As an example, important progresses have been done by Boquillon et al.<sup>62</sup> for anhydride formulations. This interesting screening study establish the effective catalysis of imidazole derivatives,<sup>63</sup> and highlights the poor catalytic action of

classical tertiary amines such as N,N-dimethylbenzylamine. Several mono-anhydrides have been used as cross-linkers giving materials with good range of thermo-mechanical properties from  $T_g = 34.5\text{ °C}$  to  $157\text{ °C}$ . The contribution of Carter et al.<sup>64</sup> and Supanchaiyamat et al.<sup>65</sup> can be noticed concerning the formulation with carboxylic di-acid hardeners.

## II.2.2. A biosourced-polymer design issue from carbohydrate conversion

### II.2.2.1. From the biorefinery concept to platform molecules production

Despite of fatty acid and lipids seen below in **section II.2.1** biomass can be associated with lignocellulosic feedstock. The **Figure II.12** describes the structure of plant cell walls which is mainly constituted by three biomacromolecules with specific functions and structures: lignin, cellulose and hemicellulose. These three biomacromolecules are self-assembled at different scales forming a hierarchized architecture which corresponds to the secondary wall of plant cells. Indeed, these secondary walls are organized by base units called “micelles” which are constituted by elementary fibers of cellulose coated by hemicellulose and glued together by lignin matrix. The self-assembly of these micelles forms microfibrils which are linked also together to give macrofibrils.<sup>66,67</sup>

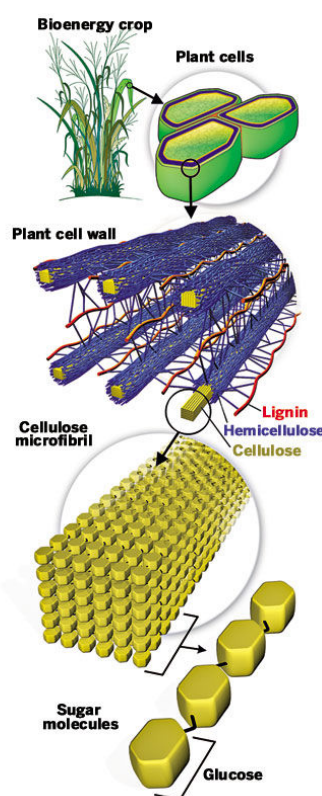


**Figure II.12.** Structural representation of plant cell walls.<sup>68</sup>

Concerning its chemical structure, the native lignin is an amorphous thermoset possessing a very complex structure<sup>69</sup> constituted by mostly three principal units: *p*-coumaryl, coniferyl and sinapyl alcohol.<sup>70,71</sup> The ratio between these units is variable, depending on the plant nature.<sup>72</sup> Cellulose has been discovered by the French chemist Anselme Payen in 1837 during his work on wood.<sup>73</sup> Therefore, Payen found in wood glucose molecules by extraction, the most plentiful organic compound on earth,<sup>74</sup> as a decomposition product of a substance which is going to turn out to be cellulose as depicted in **Figure II.12**. Cellulose is a linear homopolymer constituted by D-glucopyranose units linked via  $\beta$ -bonds in 1,4-positions.<sup>75</sup> This macromolecule that can contain until 3000 units of D-glucopyranose presents a fibrous structure provided by hydrogen bondings self-assemblies. The association of elementary fibers (composed by around 30 linear chains) gives the “micelles” described above. After cellulose, the hemicellulose is the most abundant polysaccharide on earth,<sup>76</sup> but its structure is even more complex. Indeed, hemicellulose is a branched polymer constituted by a mix of units containing a plethora of C<sub>5</sub> sugars like xylose or arabinose but also of C<sub>6</sub> sugars such as glucose, mannose and so on, the ratio between these sugars depending on the plant variety.<sup>77,78</sup>

Due to this diversity and structure complexity, the utilization of lignocellulosic biomass for applications as biofuels or for building-block chemicals generation requires the extraction and purification of these raw materials: this is the biorefinery domain. The separation of lignin/cellulose/hemicellulose biomacromolecules is a complex process, generally accomplished by hydrolysis. As an example, cellulose extraction is realized by enzymatic hydrolysis, giving glucose molecules while the extraction of lignin and/or hemicellulose is achieved by acidic or basic hydrolysis. Biomass constituents don't possess the same stability in regard to the pH environment. This difference in stability allows to separate or directly to hydrolyze the native hemicellulose or lignin.<sup>79</sup>

Herein, the resulting pentoses (xylose...) or hexoses (glucose, mannose...) sugars issued from hydrolyzed hemicellulose can undergo a cascade of reactions to generate a myriad of green platform molecules as seen in **Figure II.13**.<sup>46</sup> Carbohydrates have been particularly focused because they are considered as the most important natural alternative resource of carbon in regard to oil and coal.<sup>80</sup> The principal reactions involved in the process of sugars conversion are described below:

- ◆ Fermentative conversion of carbohydrate into several acids like lactic, succinic, glutamic but also into ethanol, butanol, or CO<sub>2</sub>.<sup>46,81,82</sup>

- ◆ Hydrogenolysis reactions which result in the cleavage of C-C and C-O bonds of carbohydrates by hydrogen and allow direct access to valuable chemicals such as alkanes, alcohols and polyols like methanol, glycerol or erythritol<sup>83</sup>
- ◆ Dehydration reactions of carbohydrates into a great variety of furan derivatives compounds such as 5-hydroxymethylfurfural (HMF) or furfural (FF) and levulinic acid.<sup>80</sup>

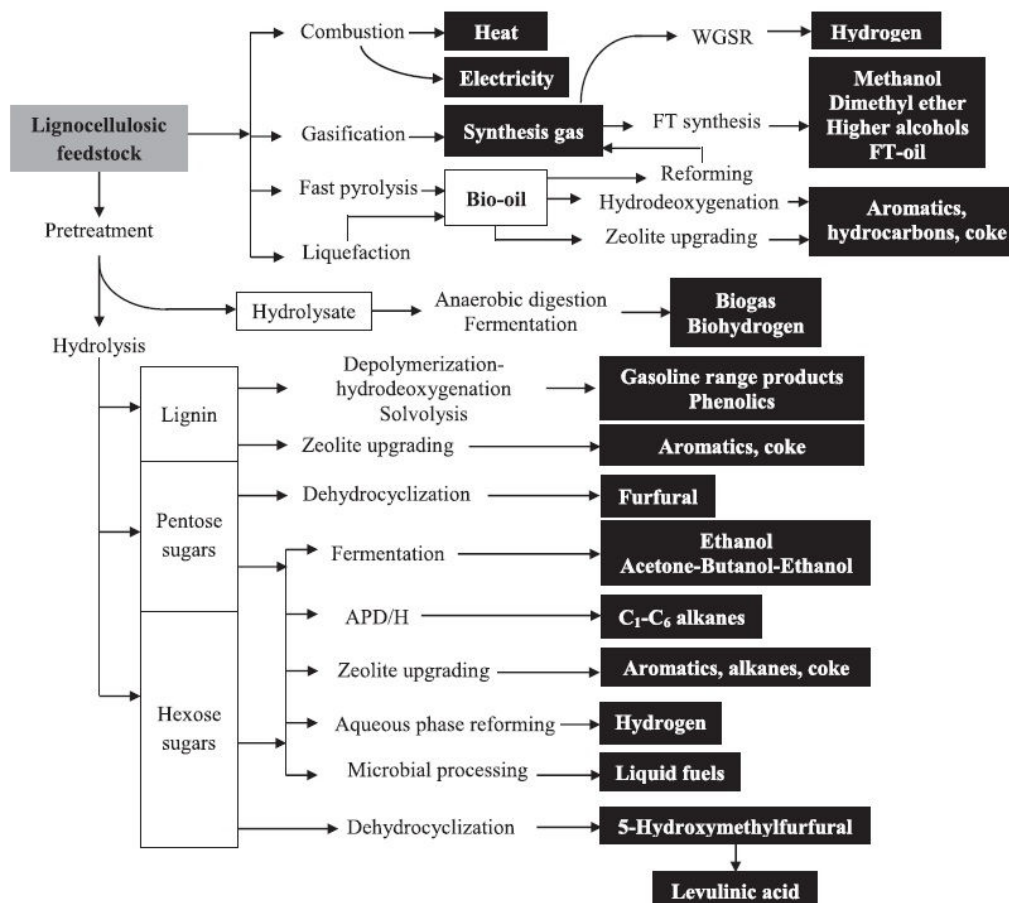


**Figure II.13.** Potential production routes for biorefinery from lignocellulosic feedstock.<sup>84</sup>

This last strategy of dehydration pathways has required much effort and attention these last decades, particularly in the case of furanic compounds considered to have a great potential for the design of fuels and chemicals. Indeed, a recent review of Bozell et al.<sup>85</sup> revisits the famous classification of US Department of Energy<sup>86</sup>, describing the high potential of 5-hydroxymethylfurfural (HMF) and furfural (FF) as the “Top10 +4” interesting compounds.

- ◆ One of the principal versatile building block is the HMF which possess a high potential demand.<sup>46</sup> Despite of its current cost, it is considered as “sleeping giant”<sup>87</sup> because of this high proclivity to generate new green building block as illustrated in **Figure II.14**. As an example, in polymer domain, 2,5-furandicarboxylic acid (FDCA) is able to replace

terephthalic, isophthalic, or adipic acids in the design of polyamides, polyesters, and polyurethanes.<sup>88</sup>

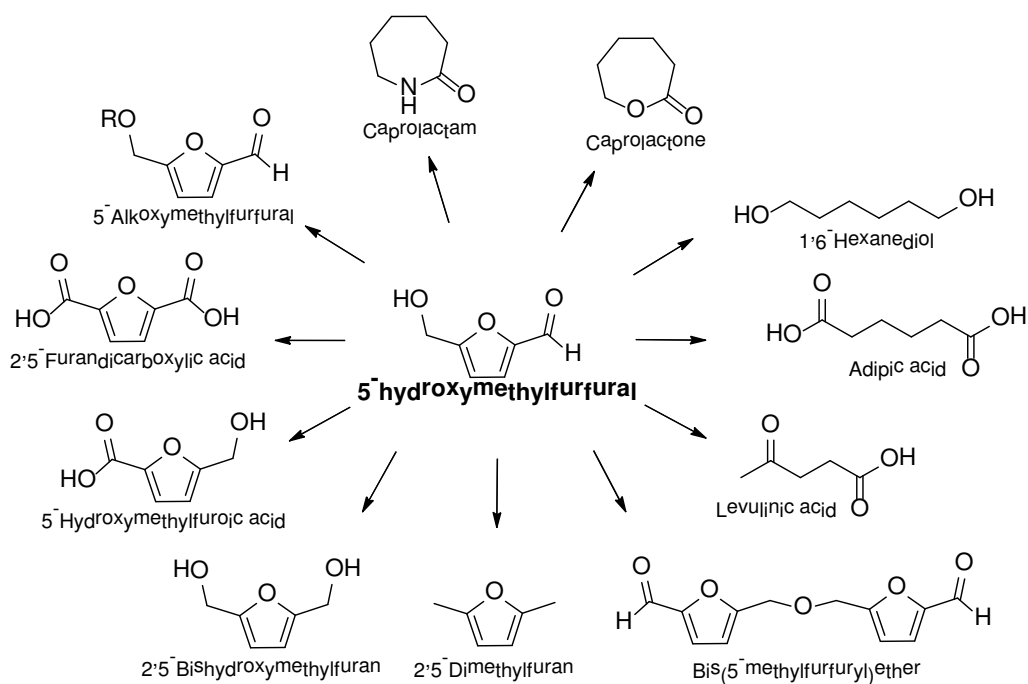


**Figure II.14.** Building block molecules issued from 5-hydroxymethylfurfural (HMF) as chemical platform.<sup>80</sup>

- ◆ The furfural (FF) represents also a very important building block issued from biorefinery being the precursor of several high potential molecules as seen in **Figure II.15**. It is obtained from pentose (mostly xylose) through a hydrolysis under acidic catalysis undergoing a triple dehydration.<sup>46</sup>

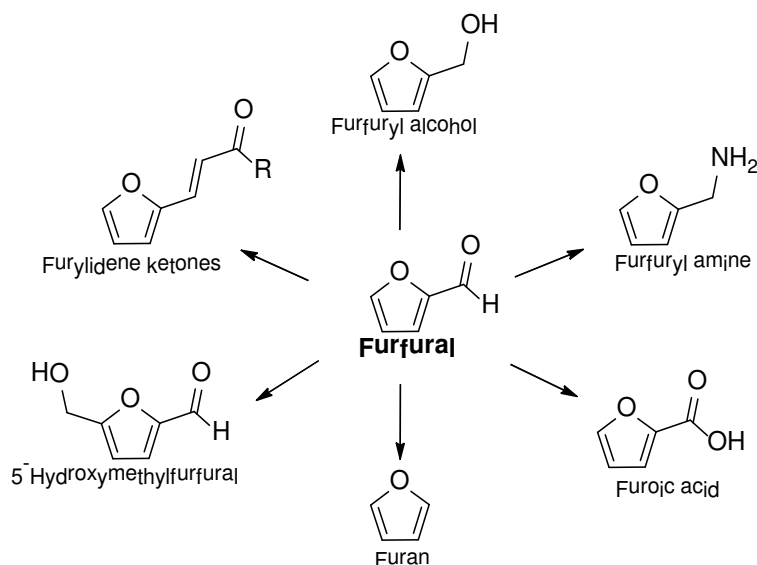


**Figure II.15.** Primary products directly synthesized from furfural.<sup>46</sup>

One of the most important building blocks generated by FF is the furfuryl alcohol (FA) because this compound has found a multitude of industrial applications presented in the next section. Industrially, FA is directly obtained by catalytic hydrogenation of furfural (FF) via two possible ways of reduction in vapour or in liquid phase. As the liquid phase way requires high pressures and temperatures, these drastic experimental conditions favour the generation of side-products. In vapour phase, the possibility to use a catalyst increases the selectivity. After 50 years of utilizations of Adkins catalysts (CuCr-based catalysts), today the utilization of Cu/MgO or Pt/TiO<sub>2</sub>/SiO<sub>2</sub> for instance are preferred because of their low toxicity. Also, some alloys of Fe-Ni-B, Mo-Co-B can be used for furfural hydrogenation. These two examples present a yield of 100% for a temperature of 373 K and a pressure of 1 MPa.<sup>46</sup>

#### II.2.2.2. From furfuryl alcohol to polyfurfuryl alcohol

Besides its great potential as renewable “building block”, the furanic ring of furfuryl alcohol (FA) possess a very peculiar chemical behaviour, which is often different from their thiophene or pyrrole homologues. Indeed, its dienic character is more marked while furan heterocycle possess a lower aromaticity.<sup>89</sup> Concerning FA stereochemistry, Barsberg et al.<sup>90</sup> have shown the preponderance of two conformers on a total of five at room temperature. This assertion, has been completed by the work of Araujo-Andrade et al.<sup>91</sup> who have fruitfully explored the energy barrier for FA conformational isomerization, highlighting *in fine* three stable conformations instead of five.

In term of physical properties, we can notice:

- Melting point = -29°C
- Boiling point = 170°C (1 atm)
- Density = 1.1285 (at 20°C)
- Dipole moment = 1.9 D

Associated to the furan moieties the presence of hydroxymethyl increases the FA hydrophilicity which allows its miscibility in various organic solvents (ether, ketone), but also in water. As a result, FA is commonly used as wetting agent or as solvent<sup>89,92</sup> and co-solvent.<sup>93</sup> The FA has mostly a reactivity close to classical primary alcohols, which concern oxidation, esterification, etherification, etc.<sup>92</sup> The FA furan ring reactivity has been exhaustively investigated for the design of new generations of ligno-cellulosic biofuels. Indeed, catalytic hydrogenation reactions lead to produce promising gasoline components as 2-methyl-furan (MF) and 2-methyl-tetrahydrofuran (MTHF).<sup>94</sup>

Concerning the FA behaviour into acido-basic media: it is relatively stable under basic environment, while it forms a highly reactive carbenium ion under acidic conditions. Indeed, in dilute acid media, the furanic ring opens and produces levulinic acid.<sup>95,96</sup> This is a possible way to make the bridge towards the production of aliphatic green building-blocks like ethyl levulinate as preferential precursor for instance.<sup>97</sup> Under strong acidic catalysts effect, FA polymerizes into PolyFurfuryl Alcohol (PFA).

The polymerization of FA has been investigated under different conditions of catalysis:

- Mineral acids: phosphoric acid<sup>98</sup>, sulphuric acid<sup>99</sup>
- Organic acids: *p*-toluene sulfonic acid,<sup>100,101</sup> maleic anhydride,<sup>98,102,103</sup> trifluoroacetic acid<sup>104</sup>
- Lewis acids: TiCl<sub>4</sub>,<sup>105</sup> SnCl<sub>4</sub>,<sup>105</sup> ZnCl<sub>2</sub><sup>106</sup> and iodine<sup>107,108</sup>

The FA polymerization proceeds via a complex mechanism which can be mostly discriminated in two steps.

- The first step, under acid catalysis, consists in the condensation of a hydroxymethyl group on the C<sub>5</sub> position to another FA ring associated with dehydration.<sup>92</sup> In consequence of this condensation reaction, as illustrated by **Figure II.16 (a)**, furan rings are connected by methylene linkages generating linear oligomers and prepolymers.<sup>109</sup> We could mention that the formation of dimethylene ether link could also occur (by a head to head condensation). Nevertheless, this structure tends to revert to methylene links after the loss of formaldehyde.<sup>89</sup> As illustrated by **Figure II.16 (b)**, chromophores with highly conjugated sequences are generated by successive releases of hydride and proton.<sup>89,105</sup>

- Then, in the second step the linear oligomers will submit cross-linking via two possible pathways:

- ◆ Electrophilic substitutions of conjugated sequences illustrated in **Figure II.16 (c)** have been proposed by Maciel et al.<sup>110,111</sup> and studied further by some authors.<sup>101,108</sup> Montero et al.<sup>112</sup> highlighted a preferential electrophilic attack on the C<sub>6</sub> instead of C<sub>8</sub> or C<sub>9</sub> positions.
- ◆ Diels-Alder (DA) cycloadditions occur as proposed by Choura et al.<sup>105</sup> between the furan rings (diene) and the dihydrofuranic cycles (dienophile) (**Figure II.16 (d)**); the authors argued this mechanism by a deep study based on model molecules.

Overall FA cross-linking has been investigated by liquid chromatography (LC)<sup>107</sup> or gel permeation chromatography (GPC)<sup>99</sup>, revealing a complex mechanism. However, these techniques are limited by the physico-chemical modifications inherent to crosslinking as seen in **section II.1.2**. The major associated problems are the decrease of the medium polarity and the high increase of the polymer viscosity during the polycondensation and specially during cross-linking.

To overcome these problems, DSC has been used as an adapted technique, because the measure of heat flow variation give information correlated with the entire range of polymerization. Herein, the first investigations based on DSC data using *classical* kinetic methods have been done by Milkovic et al.<sup>100</sup> in the 80s revealing a multi-step mechanism varying with both temperature and extend of cure. It is necessary to mention that in the case of complex mechanisms, the *classical* empirical kinetic methods based on a reaction model are not relevant. In order to have an overall understanding of polymerization process, Guigo et al.<sup>103</sup> have used advanced isoconversional methods giving access to the apparent activation energy calculated for each extend of conversion, without the need of a reaction model for the polymerization mechanism. This “model-free” method exposed on **section III.1.**, associated to rheological data and applied to the PFA cross-linking, has been very powerful to discriminate each variation of apparent activation energy during entire polymerization process, and supplying another contribution on reactivity understanding of polycondensation and cross-linking.

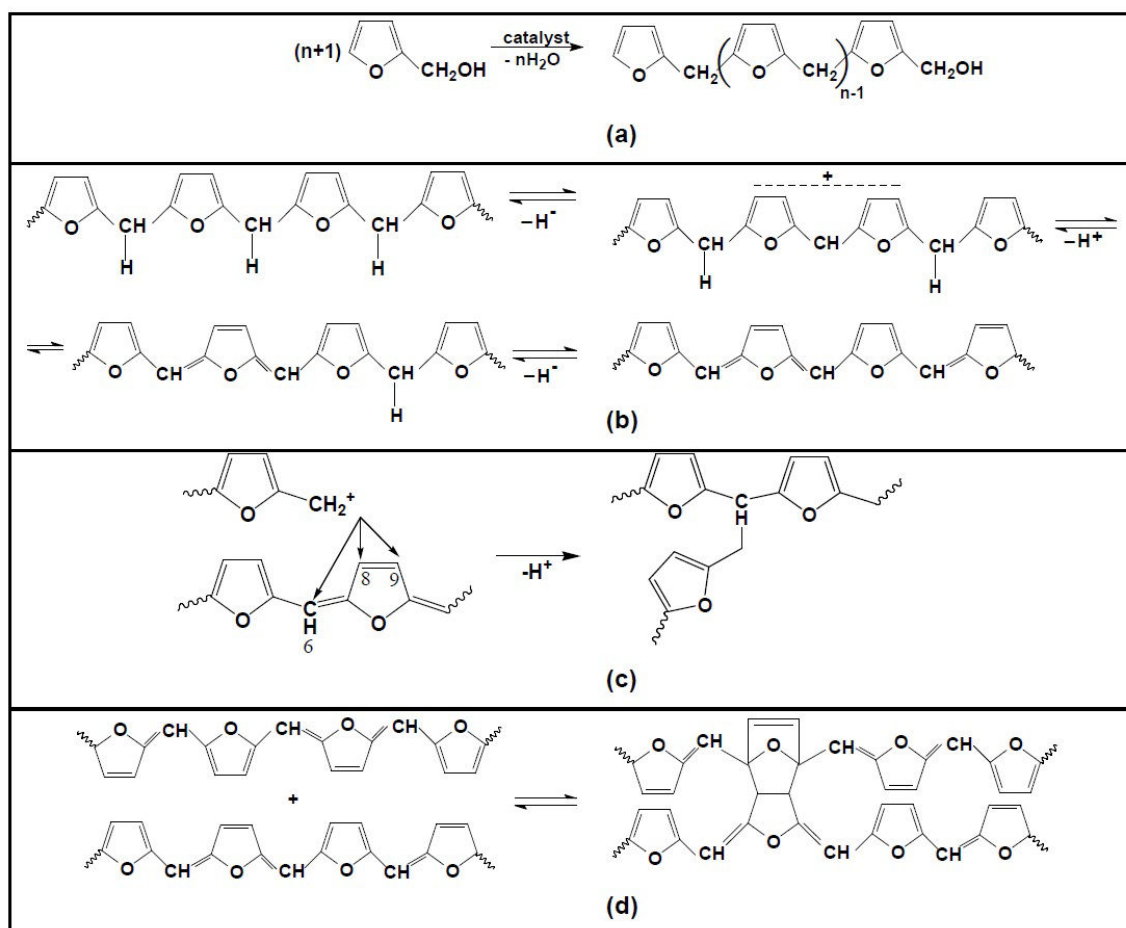


**Figure II.16.** Oligomerization and prepolymerization through acid catalyzed condensation (a); formation of conjugated sequences (b); cross-linking by electrophilic substitution (c); cross-linking by Diels-Alder cycloadditions (d).<sup>113</sup>

The elaboration of PFA represents today the principal industrial utilization of FA, the obtained resin having numerous applications:

- For wood industry, as stabilizers<sup>114</sup> and adhesives<sup>115,116</sup>
- As binders<sup>117</sup> for several applications like porous materials for methane storage<sup>118</sup>
- For corrosion and fire resistant materials<sup>89,106,119</sup>
- For sand consolidation to produce cores and moulds for foundries<sup>120,121</sup>

The PFA is also considered as preferential precursor for the elaboration of advanced material like carbon electrodes,<sup>122</sup> carbon nanospheres,<sup>123</sup> membranes for gas separation<sup>124</sup> or water desalination<sup>125</sup> for instance. PFA can be also carbonized to generate nanocomposites or defined micro and nanostructures.<sup>126,127,128,129,130</sup>

Finally in term of safety, while the FA monomer presents certain cytotoxicity<sup>131</sup> and neurotoxicity<sup>132</sup>, the PFA pre-polymers and the fully condensed material present lower hazard. That legitimates why the physico-chemical knowledge of the polymerization, in terms of enthalpy, kinetics and their occurrence reveals a high significance for industrial production.

## II.2.2.3. A side-product to valorize : the humins

As previously mentioned in the **section II.2.2.1**, the production of green building blocks such as HMF, FF or levulinic acid (LA) is always accompanied by the generation of heterogeneous macromolecules, provided by carbohydrates dehydration and degradations, commonly called “humins” (**Figure II.17**).

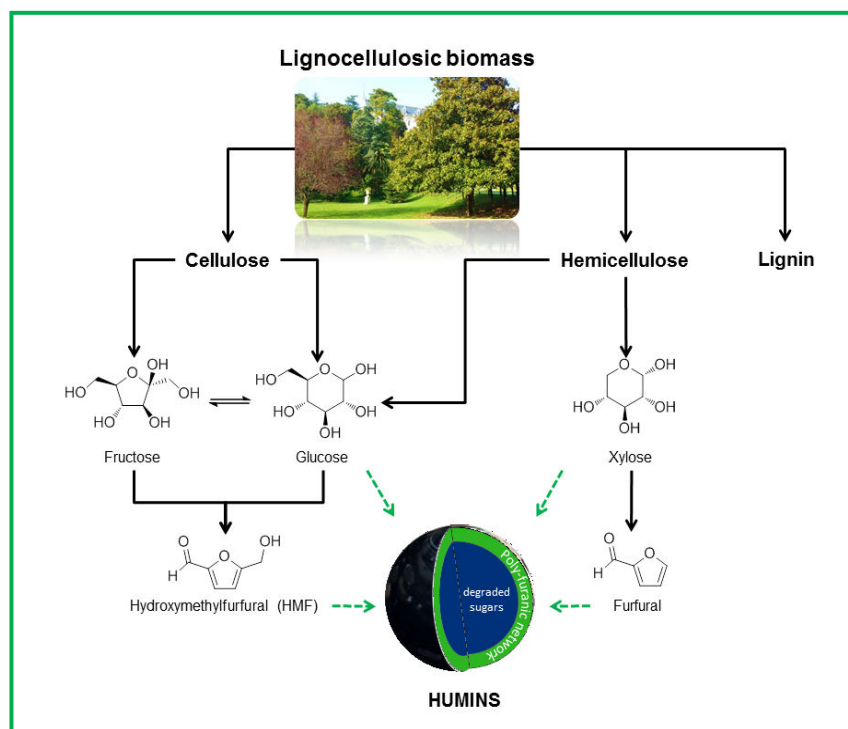


**Figure II.17.** Humins by-product formation from the lignocellulosic biomass conversion

The management of this side-stream product is a current challenge of first priority for the economic viability of biorefinery. Indeed, Hoang et al.<sup>133</sup> in a very recent paper, make an exhaustive summary of humins yields for the production of HMF/FF/LA from different bio-derived (poly)saccharides. The yield range of humins conversion is generally found from around 4 % to 50 %. For all envisaged strategies until now, the production of humins has been reported. To illustrate this fact, two different examples have been taken from the literature:

- ◆ From D-Glucose source, catalysis with both liquid or solid acids have been done in ionic liquids as solvents, giving humins ratio between 7 % to 21 %.<sup>134</sup>
- ◆ From cellulose, catalysis with mineral sulfate acid in biphasic system H<sub>2</sub>O/THF gives humins yields from 7 % to 40 %.<sup>135</sup>

These two recent examples show that whatever the sugar substrate, or the experimental conditions, (catalysis, solvent, or physico-chemicals parameters such as temperature and pressure) humins are always present on the final products. This established fact underlines the

increasing necessity to develop knowledge on the formation of humins and on their potential use as valuable product, to answer to the problematic of biorefinery efficiency.<sup>136</sup>

◆ *Humins-like materials: HydroThermalCarbon (HTC)*

Most of the knowledge of humins or humins-like materials comes from HydroThermal Carbon (HTC) which is prepared from carbohydrates, or biomass, under a hydrothermal treatment. The difference from the humins provided by the conversion of carbohydrates into HMF/FF/LA, HTC are generated without any acidic catalyst.<sup>136,137,138,139</sup> HTC exhibits the morphology of spherical particles that could be generated by the putative mechanism of condensation between sugars and furanic moieties provided by cellulose dehydration. The resulting proposed architecture consists in a core-shell structure with an hydrophilic polyaromatic shell and a less dense core, according to Sevilla et al.<sup>137,138</sup> and Yao et al.<sup>140</sup> As an alternative suggestion, the group of Baccile et al.<sup>139</sup> proposed through advanced <sup>13</sup>C solid NMR investigations, a furan-rich structure of HTC which is mostly linked on  $\alpha$  or  $\beta$  positions by aliphatic linkages. This study on various pentose- and hexose-derived HTC highlights also the presence of LA, physically adsorbed and trapped between the polymer chains. The authors concluded that the HTC provided by C<sub>5</sub> sugars contains more furanic moieties than their C<sub>6</sub> sugars homologues. This result implies that different structure will be produced, according with the feedstock.<sup>141,142</sup> This important difference in terms of morphology and structure can be also reliable to the processing parameters. As an illustration, the amount of HTC increases with the temperature, the conversion and the concentration on (poly)saccharides.<sup>137,138</sup>

◆ *Humins definition and investigations*

In many aspects, the behavior and structure of humins issued from bio-refinery are close to HTC. Some studies highlight the variability in term of particles size and chemical structure, which strongly dependent on feedstock and processing parameters.<sup>136</sup> First of all, we need to properly define the humins, which is not easy considering its structure variation with the feedstock source and with experimental conditions. Herein, the elemental analysis illustrated by van Krevelen diagram depict the oxygen/carbon atomic ratio in the range of 0.30 to 0.40 and that of hydrogen/carbon in the range of 0.65 to 0.80.<sup>136</sup> Macroscopically humins have the aspect of shiny bitumen, with a high viscosity, depending on its degree of condensation (**Figure II.18**).



**Figure II.18.** Humins produced by Avantium company pilot plant.

Two approaches have been explored in the literature to answer to the following major questions: how humins are formed? What are the structures of humins? And which are the parameters influencing their structures and growing?

- ◆ The first approach, proposed by Patil et al.,<sup>143,144</sup> concern the humins formation and their growing mechanism, with the help of FT-IR, HPLC and molecular modelling. For that purpose, they were interested on the conversion of HMF into levulinic acid (LA) and formic acid, which generate humins by parallel reactions. The resulting observations in term of selectivity suggest that humins are derived from HMF and not from LA or formic acid. This assertion is in good agreement with the mechanism proposed by Horvat et al.<sup>95</sup> who explained the formation of humins from 2,5-dioxo-6-hydroxy-hexanal, which is itself provided by HMF. The humins FT-IR spectra confirm that humins furanic moieties are derived from HMF furan ring. Moreover, the authors confirm the presence in humins structure of the hydroxyl groups from HMF but interestingly are missing the associated carbonyl groups from HMF aldehyde functions. These results could be a proof of the postulated humins growing via aldol addition/condensation of HMF with 2,5-dioxo-6-hydroxy-hexanal. Accompanied to this primary route of humins growing, another possible way could be associated to 1,2,4-trihydrobenzen (TB), which is a minor product formed during the conversion of HMF from carbohydrate dehydration.<sup>145</sup> Indeed, the addition of TB during glucose acidic conversion provokes an increase on humins yield. This clearly exhibits the TB as a potential cause for humins growing and cross-linking.<sup>136</sup> All of these assumptions underscore the complexity of the growing mechanism, including also the role of other side-products generated during the carbohydrate conversions and intervening on humins formation.
- ◆ A second approach is based on structural elucidations through the work of van Zandvoort et al.<sup>136</sup> using a deep investigation on elemental analysis, FT-IR, solid state <sup>13</sup>C NMR, and TGA pyrolysis/GC-MS techniques. The obtained results confirm mostly a furanic

structure with alcohol, acid, ketone and aldehyde functional groups, as summarized in **Figure II.19** by structure models proposed from glucose and xylose feedstock. The humins morphology observed by SEM could be described as an agglomerate of spherical particles of around 3-5  $\mu\text{m}$  diameter. However, the humins obtained from xylose present more furanic groups, instead of aliphatic chains, leading to the formation of more condensed humins. That could be explained by the C<sub>5</sub> free position of furfural which can be a direct source for the cross-linking on furan moieties.

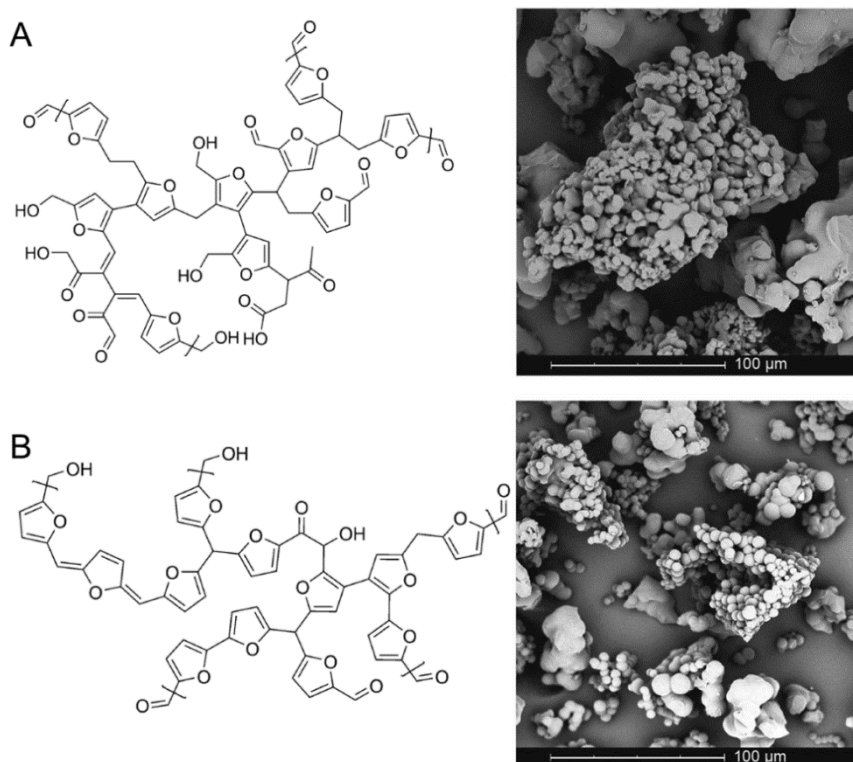


**Figure II.19.** Proposed structure of idealized humins provided by glucose (A) and xylose (B) conversion.<sup>136</sup>

Humins should be considered as a “living” material, with an architecture which can be modulated by several experimental conditions, such as thermal treatment, as illustrated by the analysis of condensable volatile fractions issued from humins degradation (**Figure II.20**).<sup>133</sup> These volatile compounds can be classified in six families as depicted in **Figure II.20**. The main results is the formation of (poly)aromatics and phenols above 400 °C, thus revealing that a complex succession of reactions occur during heating. All these mechanisms need to be deeply understood to target specific structures in order to create new products with higher value.

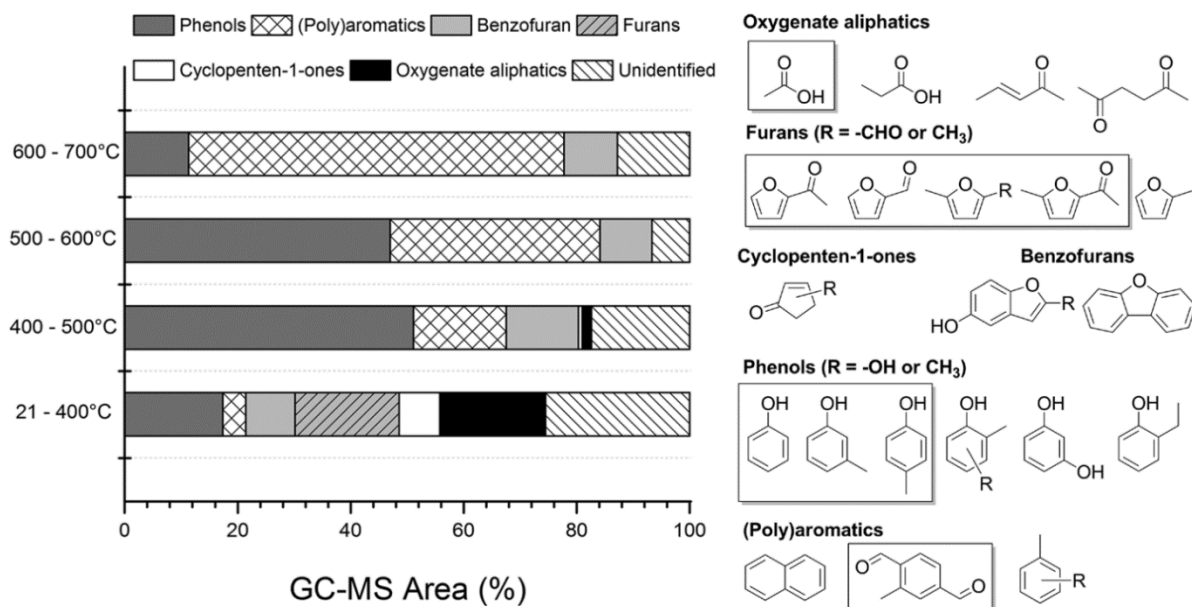


**Figure II.20.** Representative compounds released during the volatilisation stage of idealized humins issued from glucose. Chemical structures embedded in frame are those identified in the 1-step pyrolysis experiment from RT to 700 °C.<sup>133</sup>

Indeed, one of the challenges for biorefineries future can be summarized in one question: What we can do with this humins? Nowadays, humins are mostly considered as a combustible to supply heat and power back into the sugar conversion process. Another approach to transform humins into higher value-added products has been investigated by Hoang et al.<sup>133,146</sup> with the production of syngas and hydrogen by catalytic gasification.

### II.3. Hierarchical advanced materials: a *Nature* inspiration

One of the first example of biomimetism concept materialisation has been investigated by Leonardo Da Vinci.<sup>147</sup> This concept in the frame of a scientific approach could be envisaged gradually, in three steps. The first step is the observation of a natural phenomenon; the second is about its study, to understand the mechanisms that provoke and have an influence on it, in order to crystallize these collected information into fundamental knowledge. Finally, the third step is about the transposition of this knowledge to respond to a concrete needing. An illustration of this biomimetism concept is illustrated in **Figure II.21**. Leonardo Da Vinci begins by the observation of flying bird, then to study their moving in the sky and their anatomy and proportion in order to correlated physical morphology with their capacity to fly. In a last step, he transposed this knowledge to an higher scale with the creation of a *macchina* to make Human capable to fly.

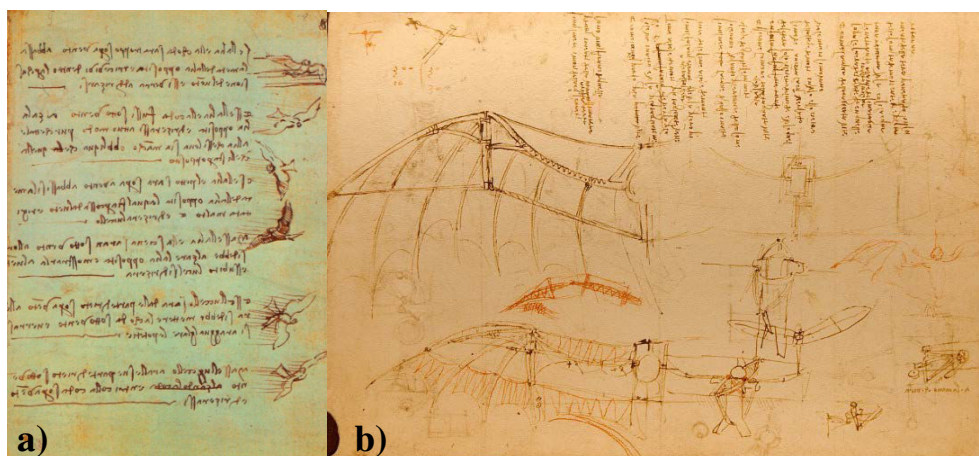


**Figure II.21.** Extracts folios of Leonardo Da Vinci works from *Codice sul volo degli uccelli* a)<sup>148</sup> and from *Codex Atlanticus* b)<sup>149</sup>.

### II.3.1. Bio-inspiration as strategy to design advanced materials

Today the scientific community approach is similar to that proposed by Leonardo Da Vinci and still presents a great interest into natural structure and phenomenon as illustrated the recent scientific journal cover page in **Figure II.22**.



**Figure II.22.** Cover page on nacre theme from *Angewandte Chemie International Edition* journal,<sup>150</sup> and on spider silk from *Nature* journal<sup>151</sup>

The example of natural nacre as hierarchical structured material will be briefly described as bio-inspiration to design materials with outstanding properties. This example is illustrated in **Figure II.23** with a scheme presenting the hierarchical assembling of nacre structure associated to SEM micrographs at each scale.

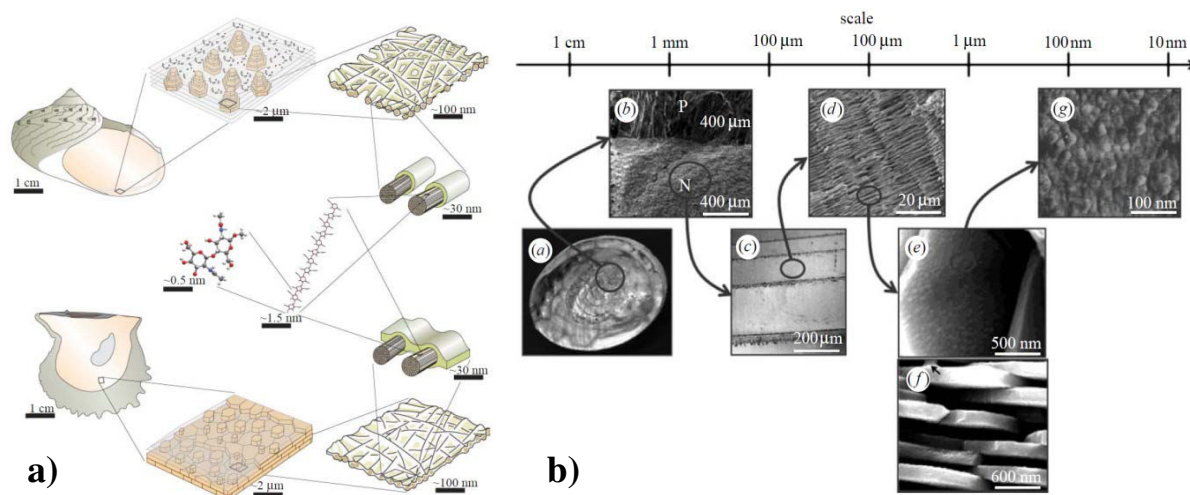


**Figure II.23.** Scheme of nacre hierarchical structure from chitin molecule for gastropods (top) and bivalves (bottom) a)<sup>152</sup> and SEM investigation highlighting its hierarchical organization b)<sup>153</sup>

Nacre structure could be schematically summarized as a “brick and mortar” layered architecture alternatively stacked with two dimensional aragonite calcium carbonate platelets: that corresponds to a material volume of 95%. The other 5% in volume corresponds to one-dimensional assembling of nanofibrillar chitin and protein, and to the interaction between proteins and aragonite platelets.<sup>154</sup> In term of mechanical properties, Jackson et al.<sup>155</sup> study shows a Young’s modulus and a tensile strength of around 70 GPa and 170 MPa for dry samples, respectively. The work of fracture is about 350 - 1240 J/m<sup>2</sup> in function of the degree of hydration. For the sake of comparison, the constitutive building block takes separately: monolithic CaCO<sub>3</sub> exhibit a work of fracture which is 3000 times inferior in comparison to the hierarchized composite nacre material.<sup>156</sup> Cheng et al.<sup>157</sup> explain this fact in one resumed sentence: “*The extraordinary properties of natural nacre are attributed to the synergistic toughening effects from the different building blocks and interface interactions.*”

The mimic design of this kind of architectures with simpler building block in order to reach these impressive properties is thus very attractive. This ambition was made possible by recent progress in all the fields of chemistry. Indeed, since the 19<sup>th</sup> century, organic chemistry investigations aim to develop a large panel of reactions which give access to the creation of an infinity of new building blocks. Then the assemblage of these building blocks into controlled architectures via physical recognition process, made the design of hierarchically ordered materials possible, this is the domain of the supramolecular chemistry.<sup>158</sup>

### II.3.2. Bottom-up approach: the chemical way

As seen on **Figure II.24** the exploration of “nanoworld” should be envisaged in two pathways. Historically, the first way has been explored by physicians who developed the concept of nanoscience. Firstly with the attractive conviction to observe new physical properties at nanoscale and secondly through the prism of micro-electronic evolution. Indeed, electronic science since its beginning follows a strong proclivity to the miniaturization. This evolution is empirically describes by the Moore law which plans a components performance multiplied by ten each two years. However, the law will be probably not verifying for the “nano-electronic” because of “nanoworld” should be assimilated as a frontier between two universes: a first one, macroscopic, described by classical mechanic laws, and a second one, atomic, governed by the quantum mechanics laws.

Economic perspectives in this domain are considerable, which explain an important focus of the research on the miniaturization of microprocessor toward “nanoprocessor” by the extrapolation of microelectronic techniques: this is the domain of the mesoscopic physics. This research way has been baptized “top-down” because of its directional approach.<sup>159,160,161</sup>

The second way consists on the symmetric directional approach called “bottom-up” which apprehend the nanoscale from atomic scale with the spontaneous recognition of building-blocks which possess the capacity to self-organization into more complex architectures. This definition is on the competence domains of chemistry and more particularly of supramolecular chemistry.

The elaboration of nanomaterials starting from nanoparticles represents the final objective of the bottom-up way, with the main goal to discover news pathways for tailoring the matter in terms of properties.<sup>161,162</sup> In the following sections, definitions and classifications relative to nano-objets (or nanoparticules) and nanomaterials will be clarify, then a specific example of supramolecular recognition process will be presented, when the liquid-crystalline state meet the macromolecular science.

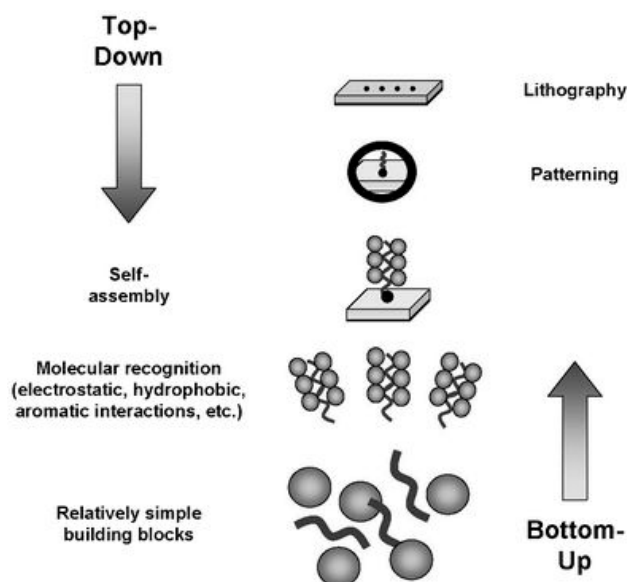


**Figure II.24.** Comparison of self-assembly process by top-down and bottom-up ways.<sup>162</sup>

### II.3.3. Nano-objects: their diversity and versatility

Nanoparticles or nano-objects synthesis should be the first step in the nanomaterials conception. These nano-objects could be discriminate by several manners: in function of their organic or inorganic character or theirs properties for instance, or considering their nanometric dimensions as seen on **Figure II.25**. Thus nano-objects could have one nanometric dimension such as montmorillonite clay sheet (thickness), two nanometric dimensions such as carbon nanotube (diameter of the filament) or three such as macromolecules or clusters. In the following **sections** of **II.3.3.1.** and **II.3.3.2.**, we will focus on the nano-objects that will be used in the manuscript.

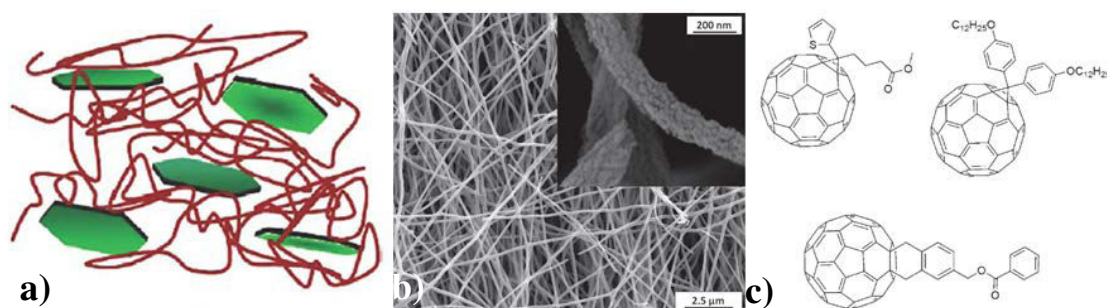


**Figure II.25.** Examples of nano-objects with one nanometric dimension: exfoliated montmorillonite clay a)<sup>163</sup>, two nanometric dimensions: nanofilament obtained after ceramization of polyacrylonitrile in Al precursor solution b)<sup>164</sup>, three nanometric dimensions: variety of C<sub>60</sub> fullerene used in solar cells c)<sup>165</sup>

### II.3.3.1. 2D nano-objects: example of sepiolite clay as polyvalent nanofillers

Sepiolite is a crystalline hydrated magnesium silicate natural clay presenting a needle-like aspect with length dimensions of 0.5-5  $\mu\text{m}$  and a cross section of around 20-50 nm as seen on **Figure II.26**. This nanofiller structure is organized in continuous two-dimensional talc like tetrahedral sheets and discontinuous octahedral sheets, exhibiting a regular nanoporosity organized in rectangular-shape channels with a porous cross-section of 11.5  $\text{\AA}$  x 3.7  $\text{\AA}$ .<sup>166</sup> This architecture is built from unit cells which present the ideal composition of  $\text{Mg}_8\text{Si}_{12}\text{O}_{30}(\text{OH})_4(\text{OH}_2)_4 \cdot 8\text{H}_2\text{O}$  where 4 and 8  $\text{H}_2\text{O}$  are respectively associated to coordinated and zeolitic water molecules.<sup>166,167</sup>

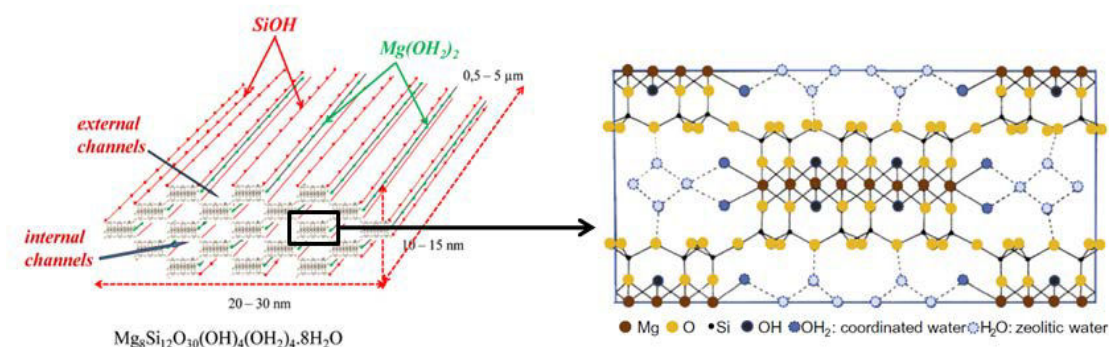


**Figure II.26.** Scheme representing sepiolite nanofiller.<sup>168,169</sup>

These previously described physico-chemicals structural information can be reliable to numerous of very interesting properties such as adsorption, encapsulation<sup>168,170,171</sup> (high specific surface area of around 300  $\text{m}^2 \cdot \text{g}^{-1}$ ) or flame retardant<sup>172</sup> for instance. These properties associated to a modulus of  $E=180 \text{ GPa}$ <sup>173</sup> for a sepiolite fiber, to abundance and to a relative low cost make sepiolite nanofillers as attractive nanoparticles platform as blend for thermoplastic,<sup>174</sup> elastomeric<sup>175</sup> or thermoset<sup>176</sup> polymers in order to design nanocomposites with higher and new properties. Furthermore, the silanol groups on sepiolite external surface present an easy way to functionalize this nanofiller using silane chemistry in particular. This strategy has been investigated in particular to improve the compatibility between polymeric matrix and the nanofiller.<sup>177,178,179</sup>

### II.3.3.2. 3D nano-objects: example of magnetite as superparamagnetic nanoparticles

The literature describes several procedures for the synthesis of magnetite nanoparticles ( $\text{Fe}_3\text{O}_4$ ) such as: the thermal decomposition of Fe(III) chelate in presence of hydrazine;<sup>180</sup> the hydrolysed Fe(II) salt decomposition assisted by sonication and thermal treatment<sup>181</sup> or  $\text{Fe}(\text{acac})_3$  in presence of stabilizing amphiphilic molecules in high temperature organic liquid phase.<sup>182</sup> In this manuscript the utilized method gives magnetite nanoparticles with a size diameter of around 12 nm. The resulting nanoparticles are obtained by the co-precipitation of ferrous and ferric entities in aqueous media, as exhibited the reaction (1) in **Figure II.27**.<sup>183</sup> Concomitantly to this principal reaction, several secondary reactions could occur in function of different experimental conditions.

The magnetite nanoparticle is very sensible to oxidation and thus, in the presence of air, could form  $\text{Fe}(\text{OH})_3$  or maghemite ( $\gamma\text{-Fe}_2\text{O}_3$ )<sup>184</sup> as respectively exposed in the reactions (2) and (3). The presence of  $\text{O}_2$  in water could also provokes the formation of  $\text{Fe}^{3+}$  species by oxidation of  $\text{Fe}^{2+}$  through the reaction (4), thus this enriched environment of  $\text{Fe}^{3+}$  leads to the generation of  $\text{Fe}(\text{OH})_3$  and ( $\gamma\text{-Fe}_2\text{O}_3$ ) through the pathways (5) and (6) respectively. Notice that  $\text{Fe}^{3+}$  could also generates, in certain pH condition, goethite ( $\alpha\text{-FeOOH}$ ) *via* reaction (7) and (8). Despite of these possible secondary reactions, the precise control of experimental conditions leads to form magnetite particles.<sup>185</sup>

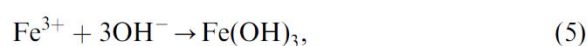
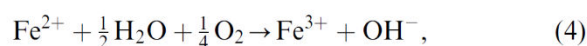
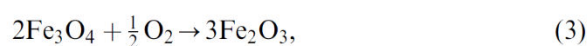
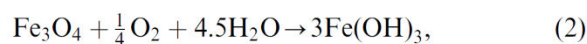
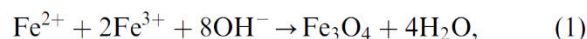


**Figure II.27.** Synthesis of magnetite nanoparticles in regard to the possible secondary reactions.<sup>185</sup>

Concerning the magnetic properties, magnetite macroscopic material presents a ferromagnetic behavior. At microscale this magnetism is expressed through anisotropy reliable to the presence of a polydomain into the material. The local spontaneous magnetization of each of these called Weiss domains is different, respecting the conditions for that global magnetic moment of the material equal to zero.

At the scale of very small particles such as nanoparticles, Néel<sup>186,187</sup> has shown a particular magnetic state, which will be called superparamagnetic behavior. Contrarily to the microscopic particle, the nanoparticle possesses only a monodomain at this dimension, which imply a possible spontaneous change in the magnetization in function of temperature. The average time between two changes of magnetization is called Néel time relaxation. Without application of an external magnetic field, if the time used to measure the magnetization of these particles is much higher than the Néel relaxation time, the magnetization appears null. In this case, the particle is in a superparamagnetic state. In other words, in this state, an external magnetic field can magnetize the particles as it is the case for paramagnetic materials. However, the magnetic susceptibility (that means the proclivity of a material to be magnetized under the action of an external magnetic excitation) of superparamagnetics is much higher than classical paramagnetic materials.<sup>188</sup> Experimentally, the magnetization of the material is commonly given by the saturation magnetization curve.

Various and numerous of high potential applications of these magnetite, or functionalized magnetite nanoparticles could be found in the literature. We can cite a study which combines the aspect of magnetite nanoparticle as potential medicine co-vectors associated to hyperthermia treatment by magnetic excitation for the cancer therapy.<sup>189</sup> Also for the elaboration of sensors,<sup>190</sup> or as supports for heterogeneous catalysis etc...<sup>191,192,193</sup>

### II.3.4. Hybrid organic-inorganic nanocomposites

The impressive variety of nanomaterials/nanocomposites could be discriminate considering different factors such as the mode of nano-objects assembly in the matrix<sup>161</sup> according to their organic or inorganic character, or by nature of interactions between the nanoparticle and the matrix. This last classification is very relevant because is directly reliable to properties. Thus, if the interactions between the matrix and the nanoparticle are “weak” (hydrogen, van der Waals, or ionic bonds), the nanomaterial will be constitutive of the *class I*, however if the connections are “strong” (covalent or iono-covalent bonds), the nanomaterial will be considerate as member of *class II*.<sup>194</sup>

As seen on the **section II.3.1**, the performance of *natural* materials is associated with the synergy between each component of the architecture, often between organic and inorganic entities. Thus, hybrid organic-inorganic nanomaterials are good candidates for the elaboration of hierarchically organized structures, as depicted the **Figure II.28**, because its offer the diversity of the mineral chemistry, and the flexibility of organic chemistry.

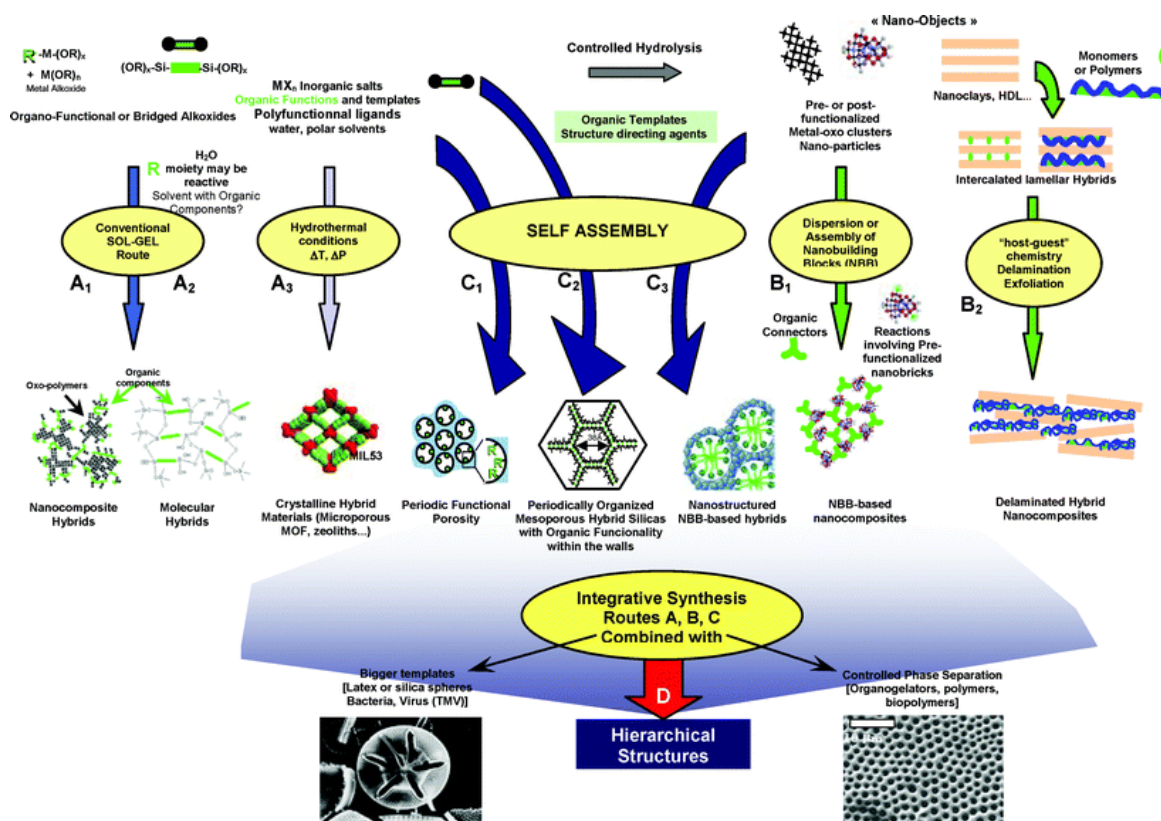


**Figure II.28.** Scheme of the main routes for the elaboration of organic-inorganic nanocomposites.<sup>194</sup>

As an illustration, linked to the example provided by the **Figure II.22** and **Figure II.23**, a synthetic nacre bio-mimetic material has been elaborated by Wang et al.<sup>195</sup> This hybrid organic-inorganic nanocomposite hydrogel consists on a system associating a poly(*N*-isopropylacrylamide) (PNIPAM) and a nanoclay (Laponite XLG) in order to form hydrogel films. The details of *N*-isopropylacrylamide (NIPAM) polymerization initiated by 2,2'-diethoxyacetophenone (DEOP) and the resulting architecture are illustrated in **Figure II.29**. The resulting nacre-like structure gels are capable to large deformations (740–1200%), associated to values of 1.54–43.2 MPa for Young modulus. These last results correspond to the highest values reported for polymeric hydrogels until now. They are comparable with that of natural hydrogels, such as biological cartilage<sup>196</sup> or cornea for instance.<sup>197</sup> These impressive results could be imputable to the hierarchically organized structure at nano- and microscale. In the same case like natural nacre, this *class I* nanocomposites (because of the hydrogen bonding between nanoclay and polymer), exhibits a synergic effect involved by the stiffness given by the nanoclay associated with the dissipative ability provided by PNIPAM.

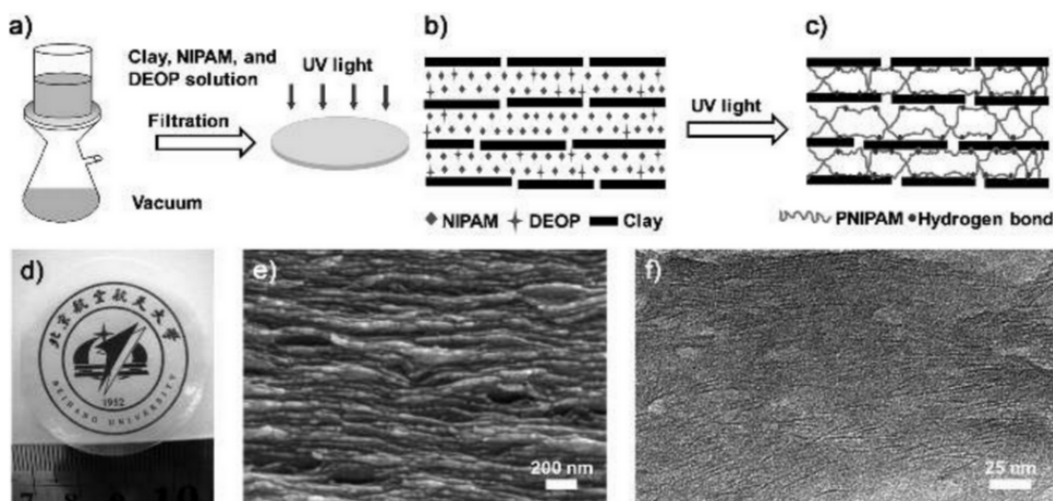


**Figure II.29.** Process of NIPAM-clay nanocomposite film elaboration a); assembled structure with precursors before polymerization b) resulting proposed model of layered assembly after polymerization c); macroscopic structure of the resulting film d); dry film morphology obtain from SEM e) TEM micrographs showing the stacking between nanoclay and polymer layer f)<sup>195</sup>

### II.3.5. From liquid-crystalline state to macromolecular chemistry

#### II.3.5.1. Liquid-crystalline state: born from a molecular frustration

Liquid-crystalline state introduced by Friedrich Reinitzer<sup>198</sup>, Otto Lehmann<sup>199</sup> et al. during the 19<sup>th</sup> century could appear in the case of certain pure molecules, supramolecules, or in multicomponent systems during their transitions from solid to liquid state.<sup>200,201</sup> This also called “mesomorphic state” is now commonly admitted as a new state of matter that possesses an hybrid behavior between the solid (crystal) and the liquid state. That is translated by a molecular order at short and medium distances, with absence of order at long distances (the case for a crystal), and a capacity to flow as a liquid.<sup>202,203</sup>

The liquid-crystalline state is born from a self-organization into mesophases of mesogen entities that possess a structural/chemical antagonism, leading to the segregations of the entities moieties which possess a similar character (such as hydrophilic). These mesophases are sensible to different stimuli like temperature (thermotrope), concentration in multicomponent system (lyotrope). Mesogen molecules possess the capacity of orientation in a preferential direction, under an external field like electric, magnetic, or a mechanical stress. Concerning the thermotropic mesogens, these entities can be structurally reliable to a “rigid” core linked by a flexible segment. Thus in term of chemistry the rigid core is generally obtain *via* C<sub>6</sub> aromatic moieties and the flexible segments are provided by aliphatic moieties.<sup>204</sup> The type of mesophase architectures is dependent on the mesogen core geometry. Herein, as schematically

depicted in **Figure II.30**, a rod-like (calamitic) or disc-like (discotic) geometry<sup>205,206,207</sup> of the mesogen core lead to generate various kind of mesophases with different degree of order: only orientational for nematic mesophase, orientational and positional for smectic or columnar mesophase. We can also notice the cholesteric mesophase with chiral mesogen core,<sup>208,209</sup> and the bent-core or “banana-shape” (curve rod-like shape) as mesogenic core which lead to form original mesophase.<sup>210</sup>

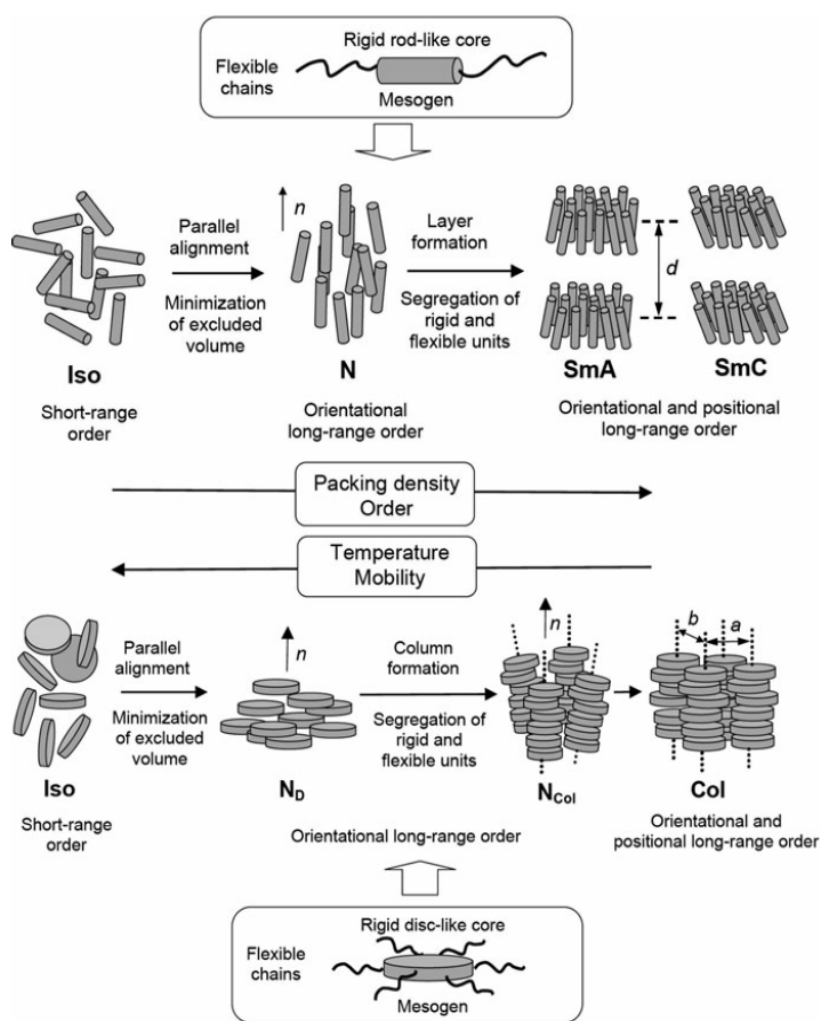


**Figure II.30.** Self-organization of disc-like molecules (bottom) and rod-like molecules (top) in mesophase, with the abbreviations: *Iso* for isotropic liquid state; *N* for nematic mesophase; *SmA* for smectic A mesophase, *SmC* for smectic C tilted mesophase and *Col* columnar phase.<sup>211,212</sup>

In addition to these *conventional* mesogens which are defined from a shape-anisotropic rigid core associated to flexible chains, the research focused these last years on the elaboration of *non-conventional* mesogens. These mesogens could present a multiarms structure as star-like, or dendritic-like for instance, and don't only possess an anisotropic-shape of the core unit, but have also the capacity to self-assembly in liquid-crystalline phases through driving forces of

nanosegregation, chemically or physically induced.<sup>213,214,215,216</sup> An example of supramolecular star-like design, is representing by the *Hekate* supramolecular family exposed in **Figure II.31** and highlighting the myriad of possibility of tailoring the final properties. This example can be enlarged in term of applications in materials science and biology fields as shown in **Figure II.32**.<sup>217</sup>

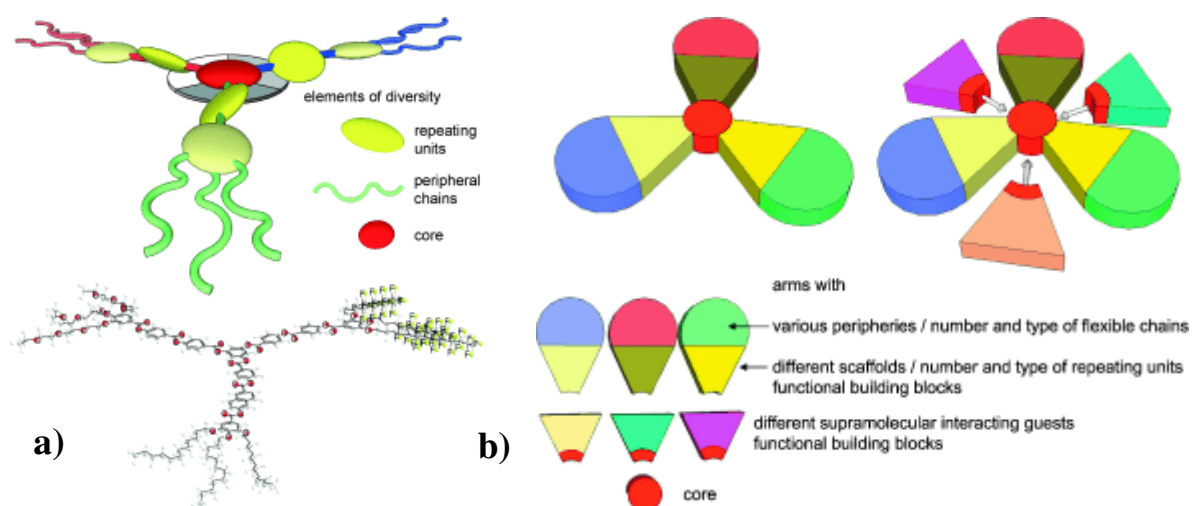


**Figure II.31.** *Hekate* model structure a) tailored possibilities of mesogen supramolecule b).<sup>213</sup>

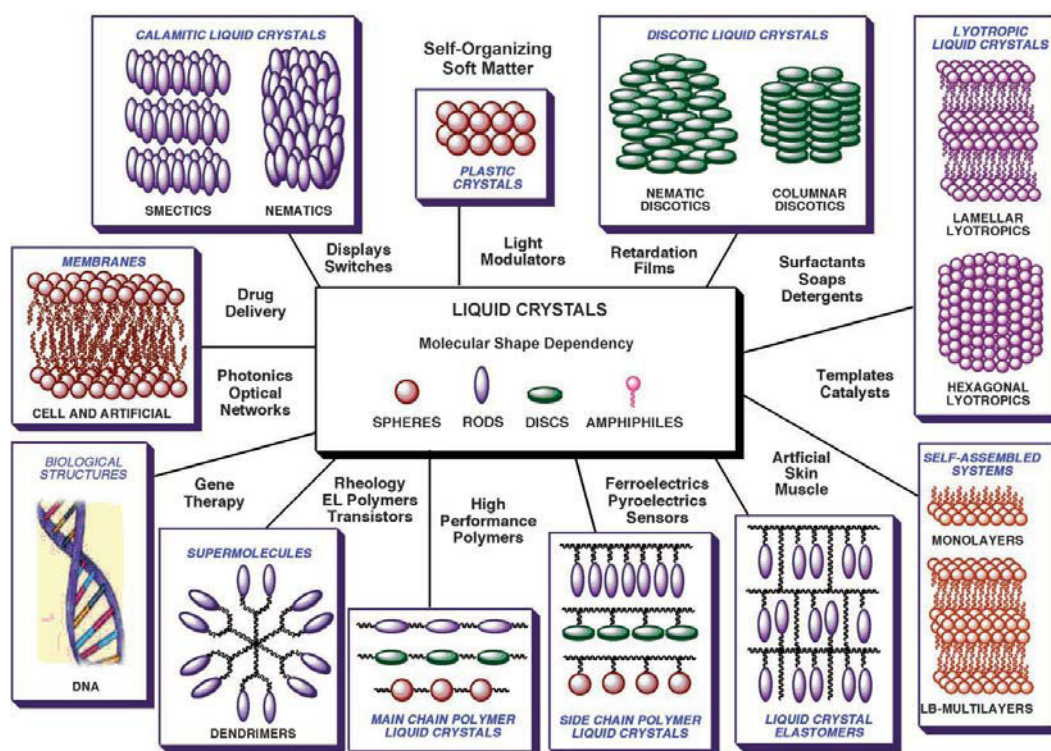


**Figure II.32.** Liquid crystals classes reliable to their self-assembled structures and their applications in function of the molecular shape.<sup>218</sup>

### *II.3.5.2. Liquid-crystalline epoxy resin*

During an allocution in 1975 de Gennes<sup>219</sup> suggested the possibility of cross-linking in mesomorphic phase, associate to the putative high potential of these anisotropic networks in term of discontinuity in the stress-strain in response to an external solicitation for instance.<sup>220</sup> Since this precursor theoretical work, a growing interest of the scientific community<sup>221,222,223</sup> was directed on this new science area which combined liquid-crystalline self-assembly and macromolecular engineering. This marriage permitted to create a new class of polymers: the liquid-crystalline thermoset (LCT).<sup>224</sup>

As seen on **section II.1.** due to this various chemistry, versatility, and outstanding properties, epoxy resins are ideal candidates to generate an anisotropic cross-linked network. This way has been investigated at the beginning of nineties by Ober et al.,<sup>225,226</sup> Carfagna et al.<sup>227,228,229</sup>, Jahromi et al.<sup>230</sup> with the aim of understanding the behavior of polymerization reaction in liquid-crystalline state, and to discover new properties of the anisotropic networks. A new subclass of LCT is born, the Liquid Crystalline Epoxy Resins (LCERs).

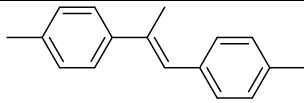
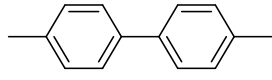
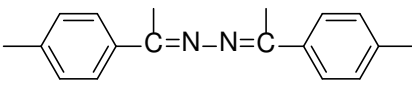
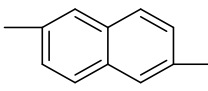
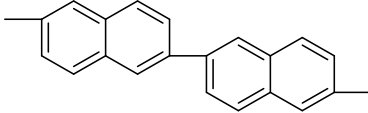
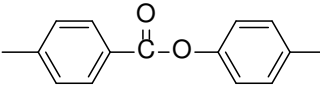
The first step of the creation of this kind of networks consists on the synthesis of an epoxy monomer, generally associated to the rigid mesogenic core moiety (**section II.3.5.1.**), which have a mesogenic or proto-mesogenic (being able to induce a mesomorphism by association with another component) character.

The most common synthetic strategy employed was the creation of the rigid core by the reaction of a phenol derived and then the epoxidation of the resulting “core” of these two phenol moiety by epichlorohydrine as explained in **section II.1.1.1.** The **Table II.4** shows some examples of the rod-like rigid cores which has been epoxidized and studied in the literature until now.

In combination with the epoxy monomers, the choice of the cross-linkers is the key of the self-assembly design, considering the functionality of both epoxide and cross-linker, which depends

on the polymerization reactivity reliable to the chemical functions such as carboxylic acid, anhydride acid, alcohol or amine for instance, as seen on **section II.1.1.2**.

**Table II.4.** Examples of epoxy monomers mesogens studied in the literature<sup>224,231</sup>

Epoxy monomer mesogen core	References
	6,232,233,234,235,236
	6,233,237,238,239,240
	228
	233
	229
	6,233,237,230
	5,7,241,242

The chemical structure of cross-linker is also very important, especially in the case of proto-mesogenic monomers. Therefore, the length, the aromaticity or the hydrophobic/hydrophilic balance are to take into account for the design of network morphology.<sup>3,19</sup> As an example, the classical rod-like anisotropic networks are tribute of supramolecular interactions, provided by  $\pi$ - $\pi$  stacking, hydrogen bonding of secondary groups from polymerization or from designed cross-linkers.<sup>226,243</sup> Some studies also highlighted the important contribution of alkyl moieties as entropic reservoir for mesophase design.<sup>244</sup>

The cross-linking induce the formation of an anisotropic network which is characterized by the presence of polydomains (their size are reliable to the type of mesophase but are still at microscale order); each domain presents a different preferential directional orientation.<sup>236</sup> However, as seen above in the case of classical liquid-crystals, is possible to induce a preferential orientation in order to switch to a kind of monodomain with the application of an external electric<sup>245</sup> or magnetic field<sup>246</sup> during polymerization. The increase of order is also possible by application of a mechanical stress like a shear.<sup>241</sup> The anisotropic networks have interesting applications because of their higher mechanical properties in regard to their

homologues, amorphous epoxy resins, or as materials for optic domain, in particular with the case of cholesteric “frozen” phase.<sup>231</sup>

1. Pascault, J.-P.; Sautereau, H.; Verdu, J.; Williams, R. J., *Thermosetting polymers*. CRC Press: 2002; Vol. 64.
2. Dodiuk, H.; Goodman, S. H., *Handbook of thermoset plastics*. William Andrew: 2013.
3. Henry Lee, K. N., *Handbook of epoxy resins*. Mc Graw-Hill Book Company ed.; 1982.
4. Mikroyannidis, J. A., Epoxides bearing azomethine linkages. *Polymer International* **1991**, *25* (2), 91-97.
5. Mititelu-Mija, A.; Cascaval, C. N., Liquid Crystalline Epoxy Azomethine Thermoset. *High Performance Polymers* **2007**, *19* (2), 135-146.
6. Mormann, W.; Bröcher, M., “Liquid crystalline” thermosets from 4,4'-bis(2,3-epoxypropoxy)biphenyl and aromatic diamines. *Macromolecular Chemistry and Physics* **1996**, *197* (6), 1841-1851.
7. Mormann, W.; Bröcher, M.; Schwarz, P., Mesogenic azomethine based diepoxides – monomers for the synthesis of “liquid crystal” thermoset networks. *Macromolecular Chemistry and Physics* **1997**, *198* (11), 3615-3626.
8. Auvergne, R.; Caillol, S.; David, G.; Boutevin, B.; Pascault, J.-P., Biobased Thermosetting Epoxy: Present and Future. *Chemical reviews* **2013**, *114* (2), 1082-1115.
9. Tomi, P. Etudes thermocinétiques et physico-chimiques pour la caractérisation d'une résine époxy thermodurcie. Université de Nice, 1988.
10. Stevens, C. L.; Tazuma, J., Epoxyethers. V. The Reaction of Perbenzoic Acid with Vinyl Ethers. *Journal of the American Chemical Society* **1954**, *76* (3), 715-717.
11. Royals, E. E.; Harrell, L. L., Oxygenated Derivatives of d- $\alpha$ -Pinene and d-Limonene. Preparation and Use of Monoperphthalic Acid1. *Journal of the American Chemical Society* **1955**, *77* (12), 3405-3408.
12. Schechter, L.; Wynstra, J.; Kurkky, R., Ind Eng Chem 1956, 48, 94. *CrossRef, Web of Science® Times Cited 181*.
13. Gough, L.; Smith, I., A gel point method for the estimation of overall apparent activation energies of polymerization. *Journal of Applied Polymer Science* **1960**, *3* (9), 362-364.
14. Smith, I. T., The mechanism of the crosslinking of epoxide resins by amines. *Polymer* **1961**, *2*, 95-108.
15. Tanaka, Y.; Mika, T., Epoxide curing reactions. *Epoxy Resins* **1973**, 135-238.
16. Vyazovkin, S.; Sbirrazzuoli, N., Mechanism and Kinetics of Epoxy–Amine Cure Studied by Differential Scanning Calorimetry. *Macromolecules* **1996**, *29* (6), 1867-1873.
17. Delebecq, E.; Pascault, J.-P.; Boutevin, B.; Ganachaud, F., On the Versatility of Urethane/Urea Bonds: Reversibility, Blocked Isocyanate, and Non-isocyanate Polyurethane. *Chemical reviews* **2013**, *113* (1), 80-118.
18. Galy, J.; Sabra, A.; Pascault, J. P., Characterization of epoxy thermosetting systems by differential scanning calorimetry. *Polymer Engineering & Science* **1986**, *26* (21), 1514-1523.
19. Pascault, J.-P.; Williams, R. J., *Epoxy polymers*. John Wiley & Sons: 2009.
20. Bednarek, M.; Kubisa, P.; Penczek, S., Polymerization of propylene oxide by activated monomer mechanism-kinetics. *Die Makromolekulare Chemie* **1989**, *15* (S19891), 49-60.
21. Matějka, L.; Chabanne, P.; Tighzert, L.; Pascault, J., Cationic polymerization of diglycidyl ether of bisphenol A. *Journal of Polymer Science Part A: Polymer Chemistry* **1994**, *32* (8), 1447-1458.
22. Madec, P.-J.; Maréchal, E., Kinetics and mechanisms of polyesterifications II. Reactions of diacids with diepoxides. In *Analysis/Reactions/Morphology*, Springer: 1985; pp 153-228.
23. Matějka, L.; Lövy, J.; Pokorný, S.; Bouchal, K.; Dušek, K., Curing epoxy resins with anhydrides. Model reactions and reaction mechanism. *Journal of Polymer Science: Polymer Chemistry Edition* **1983**, *21* (10), 2873-2885.
24. Leukel, J.; Burchard, W.; Krüger, R.-P.; Much, H.; Schulz, G., Mechanism of the anionic copolymerization of anhydride-cured epoxies – analyzed by matrix-assisted laser desorption ionization time-of-flight mass spectrometry (MALDI-TOF-MS). *Macromolecular Rapid Communications* **1996**, *17* (5), 359-366.
25. Steinmann, B., Investigations on the curing of epoxides with phthalic anhydride. *Journal of applied polymer science* **1990**, *39* (9), 2005-2026.

26. Dušek, K.; Dušková-Smrčková, M., Network structure formation during crosslinking of organic coating systems. *Progress in Polymer Science* **2000**, *25* (9), 1215-1260.
27. Flory, P. J., *Principles of polymer chemistry*. Cornell University Press: 1953.
28. Dusek, K., Size of network chains. *Macromolecules* **1984**, *17* (4), 716-722.
29. Dušek, K.; Ilavský, M., Characterization of network structure by branching theory and correlation with viscoelastic properties. In *Relaxation in Polymers*, Springer: 1989; pp 26-34.
30. Flory, P. J., Theory of elasticity of polymer networks. The effect of local constraints on junctions. *The Journal of Chemical Physics* **1977**, *66* (12), 5720-5729.
31. Krakovský, I.; Havránek, A.; Ilavský, M.; Dušek, K., Dependence of viscoelastic spectrum width on the structure of model imperfect networks prepared by endlinking. *Colloid and Polymer Science* **1988**, *266* (4), 324-332.
32. Dušek, K.; Dušková-Smrčková, M., Modeling of Polymer Network Formation from Preformed Precursors. *Macromolecular Reaction Engineering* **2012**, *6* (11), 426-445.
33. Gordon, M., Good's theory of cascade processes applied to the statistics of polymer distributions. *Proc. Roy. Soc. (London)* **1962**, *268* (Ser. A), 240-59.
34. Tanaka, Y.; Stanford, J. L.; Stepto, R., Interpretation of Gel Points of an Epoxy–Amine System Including Ring Formation and Unequal Reactivity: Reaction Scheme and Gel-Point Prediction. *Macromolecules* **2012**, *45* (17), 7186-7196.
35. Dušek, K.; Dušková-Smrčková, M.; Huybrechts, J.; Ďuračková, A., Polymer Networks from Preformed Precursors Having Molecular Weight and Group Reactivity Distributions. Theory and Application. *Macromolecules* **2013**, *46* (7), 2767-2784.
36. Šomvářsky, J.; Dušek, K.; Smrčková, M., Kinetic modelling of network formation: Size-dependent static effects. *Computational and Theoretical Polymer Science* **1998**, *8* (1), 201-208.
37. Pakula, T., Static and dynamic properties of computer simulated melts of multiarm polymer stars. *Computational and Theoretical Polymer Science* **1998**, *8* (1–2), 21-30.
38. Pakula, T.; Vlassopoulos, D.; Fytas, G.; Roovers, J., Structure and Dynamics of Melts of Multiarm Polymer Stars. *Macromolecules* **1998**, *31* (25), 8931-8940.
39. Fitzgerald, B. W.; Lentzakis, H.; Sakellariou, G.; Vlassopoulos, D.; Briels, W. J., A computational and experimental study of the linear and nonlinear response of a star polymer melt with a moderate number of unentangled arms. *The Journal of chemical physics* **2014**, *141* (11), 114907.
40. Polanowski, P.; Jeszka, J. K.; Matyjaszewski, K., Synthesis of star polymers by “core-first” one-pot method via ATRP: Monte Carlo simulations. *Polymer* **2014**, *55* (10), 2552-2561.
41. Gillham, J. K., Formation and properties of thermosetting and high Tg polymeric materials. *Polymer Engineering & Science* **1986**, *26* (20), 1429-1433.
42. President, U., Developing and promoting biobased products and bioenergy. *Executive order* **1999**, *13101*, 13134.
43. Congress, U. In *Biomass research and development act of 2000*, US Congress, Washington, DC, 2000.
44. Erhan, S. Z., *Industrial uses of vegetable oils*. AOCS Press Champaign: 2005.
45. Lu, Y.; Larock, R. C., Novel Polymeric Materials from Vegetable Oils and Vinyl Monomers: Preparation, Properties, and Applications. *ChemSusChem* **2009**, *2* (2), 136-147.
46. Corma, A.; Iborra, S.; Velty, A., Chemical routes for the transformation of biomass into chemicals. *Chemical reviews* **2007**, *107* (6), 2411-2502.
47. Seniha Güner, F.; Yağcı, Y.; Tuncer Erciyes, A., Polymers from triglyceride oils. *Progress in Polymer Science* **2006**, *31* (7), 633-670.
48. Xia, Y.; Larock, R. C., Vegetable oil-based polymeric materials: synthesis, properties, and applications. *Green Chemistry* **2010**, *12* (11), 1893.
49. Gandini, A., Polymers from Renewable Resources: A Challenge for the Future of Macromolecular Materials. *Macromolecules* **2008**, *41* (24), 9491-9504.
50. Petrović, Z. S., Polymers from Biological Oils. *Contemporary Materials* **2010**, *1* (1), 39-50.
51. Loureiro, N. P. D. Furfuryl-functionalized soybean oil derivatives: synthesis and polymerization. Universidade de Aveiro, 2010.
52. Formo, M., Miscellaneous oil and fat products. *Bailey's Industrial Oil and Fat Products* **1982**, *2*, 343.
53. Petrović, Z. S.; Zlatanić, A.; Lava, C. C.; Sinadinović-Fišer, S., Epoxidation of soybean oil in toluene with peroxyacetic and peroxyformic acids—kinetics and side reactions. *European Journal of Lipid Science and Technology* **2002**, *104* (5), 293-299.

54. Vlček, T.; Petrović, Z., Optimization of the chemoenzymatic epoxidation of soybean oil. *J Amer Oil Chem Soc* **2006**, *83* (3), 247-252.
55. Téllez, G. L.; Viguera-Santiago, E.; Hernández-López, S., Characterization of linseed oil epoxidized at different percentages. *Superficies y vacío* **2009**, *22* (1), 5-10.
56. Rüschen Klaas, M.; Warwel, S., Complete and partial epoxidation of plant oils by lipase-catalyzed perhydrolysis I. *Industrial Crops and Products* **1999**, *9* (2), 125-132.
57. Luo, Q.; Liu, M.; Xu, Y.; Ionescu, M.; Petrović, Z. S., Thermosetting Allyl Resins Derived from Soybean Oil. *Macromolecules* **2011**, *44* (18), 7149-7157.
58. Wu, X.; Zhang, X.; Yang, S.; Chen, H.; Wang, D., The study of epoxidized rapeseed oil used as a potential biodegradable lubricant. *J Amer Oil Chem Soc* **2000**, *77* (5), 561-563.
59. Fenollar, O.; Garcia-Sanoguera, D.; Sanchez-Nacher, L.; Lopez, J.; Balart, R., Effect of the epoxidized linseed oil concentration as natural plasticizer in vinyl plastisols. *J Mater Sci* **2010**, *45* (16), 4406-4413.
60. Fenollar, O.; Garcia-Sanoguera, D.; Sánchez-Nácher, L.; López, J.; Balart, R., Characterization of the curing process of vinyl plastisols with epoxidized linseed oil as a natural-based plasticizer. *Journal of Applied Polymer Science* **2012**, *124* (3), 2550-2557.
61. Starnes, W. H.; Ge, X., Mechanism of autocatalysis in the thermal dehydrochlorination of poly (vinyl chloride). *Macromolecules* **2004**, *37* (2), 352-359.
62. Boquillon, N.; Fringant, C., Polymer networks derived from curing of epoxidised linseed oil: influence of different catalysts and anhydride hardeners. *Polymer* **2000**, *41* (24), 8603-8613.
63. Fedoseev, M. S.; Derzhavinskaya, L. F.; Strel'nikov, V. N., Curing of epoxy-anhydride formulations in the presence of imidazoles. *Russian Journal of Applied Chemistry* **2010**, *83* (8), 1408-1412.
64. Carter, D.; Stansfield, N.; Mantle, R.; France, C.; Smith, P., An investigation of epoxidised linseed oil as an alternative to PVC in flooring applications. *industrial crops and products* **2008**, *28* (3), 309-319.
65. Supanchaiyamat, N.; Shuttleworth, P. S.; Hunt, A. J.; Clark, J. H.; Matharu, A. S., Thermosetting resin based on epoxidised linseed oil and bio-derived crosslinker. *Green Chemistry* **2012**, *14* (6), 1759.
66. Bailey, I. W., Cell wall structure of higher plants. *Industrial & Engineering Chemistry* **1938**, *30* (1), 40-47.
67. Chafe, S.; Wardrop, A., Microfibril orientation in plant cell walls. *Planta* **1970**, *92* (1), 13-24.
68. Steen, E. J.; Kang, Y.; Bokinsky, G.; Hu, Z.; Schirmer, A.; McClure, A.; del Cardayre, S. B.; Keasling, J. D., Microbial production of fatty-acid-derived fuels and chemicals from plant biomass. *Nature* **2010**, *463* (7280), 559-562.
69. Hammel, K., Fungal degradation of lignin. *Driven by nature: plant litter quality and decomposition* **1997**, 33-45.
70. Whetten, R.; Sederoff, R., Lignin biosynthesis. *The Plant Cell* **1995**, *7* (7), 1001.
71. Dien, B. S.; Miller, D. J.; Hector, R. E.; Dixon, R. A.; Chen, F.; McCaslin, M.; Reisen, P.; Sarath, G.; Cotta, M. A., Enhancing alfalfa conversion efficiencies for sugar recovery and ethanol production by altering lignin composition. *Bioresource technology* **2011**, *102* (11), 6479-6486.
72. Jolivet, C.; Guillet, B.; Karroum, M.; Andreux, F.; Bernoux, M.; Arrouays, D., Les phénols de la lignine et le <sup>13</sup>C, traceurs de l'origine des matières organiques du sol. *Comptes Rendus de l'Académie des Sciences-Series IIA-Earth and Planetary Science* **2001**, *333* (10), 651-657.
73. Adler, E., Lignin chemistry—past, present and future. *Wood science and technology* **1977**, *11* (3), 169-218.
74. Hon, D. N.-S., Cellulose: a random walk along its historical path. *Cellulose* **1994**, *1* (1), 1-25.
75. Viëtor, R. J.; Mazeau, K.; Lakin, M.; Perez, S., A priori crystal structure prediction of native celluloses. *Biopolymers* **2000**, *54* (5), 342-354.
76. Saha, B. C., Hemicellulose bioconversion. *Journal of Industrial Microbiology and Biotechnology* **2003**, *30* (5), 279-291.
77. Sun, R.; Tomkinson, J.; Ma, P.; Liang, S., Comparative study of hemicelluloses from rice straw by alkali and hydrogen peroxide treatments. *Carbohydrate Polymers* **2000**, *42* (2), 111-122.
78. Sun, J.; Sun, X.; Sun, R.; Su, Y., Fractional extraction and structural characterization of sugarcane bagasse hemicelluloses. *Carbohydrate Polymers* **2004**, *56* (2), 195-204.
79. Sun, R. C.; Tomkinson, J., Characterization of hemicelluloses obtained by classical and ultrasonically assisted extractions from wheat straw. *Carbohydrate Polymers* **2002**, *50* (3), 263-271.

80. van Putten, R. J.; van der Waal, J. C.; de Jong, E.; Rasrendra, C. B.; Heeres, H. J.; de Vries, J. G., Hydroxymethylfurfural, a versatile platform chemical made from renewable resources. *Chemical reviews* **2013**, *113* (3), 1499-597.
81. Wolin, M.; Miller, T. L., Carbohydrate fermentation. *Human Intestinal Microflora* **2012**, 147-165.
82. Lee, S. Y.; Park, J. H.; Jang, S. H.; Nielsen, L. K.; Kim, J.; Jung, K. S., Fermentative butanol production by clostridia. *Biotechnology and Bioengineering* **2008**, *101* (2), 209-228.
83. Ruppert, A. M.; Weinberg, K.; Palkovits, R., Hydrogenolysis Goes Bio: From Carbohydrates and Sugar Alcohols to Platform Chemicals. *Angewandte Chemie International Edition* **2012**, *51* (11), 2564-2601.
84. Maity, S. K., Opportunities, recent trends and challenges of integrated biorefinery: Part I. *Renewable and Sustainable Energy Reviews* **2015**, *43* (0), 1427-1445.
85. Bozell, J. J.; Petersen, G. R., Technology development for the production of biobased products from biorefinery carbohydrates-the US Department of Energy's "Top 10" revisited. *Green Chemistry* **2010**, *12* (4), 539-554.
86. Werpy, T.; Petersen, G.; Aden, A.; Bozell, J.; Holladay, J.; White, J.; Manheim, A.; Eliot, D.; Lasure, L.; Jones, S. *Top value added chemicals from biomass. Volume 1-Results of screening for potential candidates from sugars and synthesis gas*; DTIC Document: 2004.
87. Bicker, M.; Kaiser, D.; Ott, L.; Vogel, H., Dehydration of d-fructose to hydroxymethylfurfural in sub- and supercritical fluids. *The Journal of Supercritical Fluids* **2005**, *36* (2), 118-126.
88. Moreau, C.; Belgacem, M.; Gandini, A., Recent Catalytic Advances in the Chemistry of Substituted Furans from Carbohydrates and in the Ensuing Polymers. *Topics in Catalysis* **2004**, *27* (1-4), 11-30.
89. Gandini, A.; Belgacem, M. N., Furans in polymer chemistry. *Progress in Polymer Science* **1997**, *22* (6), 1203-1379.
90. Barsberg, S.; Berg, R. W., Combined Raman Spectroscopic and Theoretical Investigation of Fundamental Vibrational Bands of Furfuryl Alcohol (2-furanmethanol). *The Journal of Physical Chemistry A* **2006**, *110* (30), 9500-9504.
91. Araujo-Andrade, C.; Gómez-Zavaglia, A.; Reva, I. D.; Fausto, R., Conformers, Infrared Spectrum and UV-Induced Photochemistry of Matrix-Isolated Furfuryl Alcohol. *The Journal of Physical Chemistry A* **2012**, *116* (9), 2352-2365.
92. Dunlop, A.; Peters, F., The Furans, Reinhold Publ. Corp., New York **1953**, 447.
93. Morawski, P.; Letcher, T. M.; Naicker, P. K.; Domanska, U., Liquid-Liquid Equilibria for Mixtures of (Furfuryl Alcohol+ an Aromatic Hydrocarbon+ an Alkane) at T= 298.15 K. *Journal of Chemical & Engineering Data* **2002**, *47* (6), 1453-1456.
94. Lange, J.-P.; van der Heide, E.; van Buijtenen, J.; Price, R., Furfural—A Promising Platform for Lignocellulosic Biofuels. *ChemSusChem* **2012**, *5* (1), 150-166.
95. Horvat, J.; Klaić, B.; Metelko, B.; Šunjić, V., Mechanism of levulinic acid formation. *Tetrahedron letters* **1985**, *26* (17), 2111-2114.
96. Lange, J.-P.; Van De Graaf, W. D., Process for the conversion of furfuryl alcohol into levulinic acid or alkyl levulinate. Google Patents: 2007.
97. Lange, J. P.; van de Graaf, W. D.; Haan, R. J., Conversion of furfuryl alcohol into ethyl levulinate using solid acid catalysts. *ChemSusChem* **2009**, *2* (5), 437-441.
98. Wewerka, E., An investigation of the polymerization of furfuryl alcohol with gel permeation chromatography. *Journal of Applied Polymer Science* **1968**, *12* (7), 1671-1681.
99. Mokoena, T.; Ddamba, W.; Keikotlhaile, B., Gel permeation chromatography study of the kinetics of condensation of furfuryl alcohol in THF solution. *South African Journal of Chemistry* **1999**, *52* (1), 2-7.
100. Milkovic, J.; Myers, G. E.; Young, R. A., Interpretation of curing mechanism of furfuryl alcohol resins. *Cellulose chemistry and technology* **1979**.
101. Principe, M.; Ortiz, P.; Martínez, R., An NMR study of poly(furfuryl alcohol) prepared with p-toluenesulphonic acid. *Polymer International* **1999**, *48* (8), 637-641.
102. Philippou, J.; Zavarin, E., Differential scanning calorimetric and infra-red spectroscopic studies of interactions between lignocellulosic materials, hydrogen peroxide, and furfuryl alcohol. *Holzforschung-International Journal of the Biology, Chemistry, Physics and Technology of Wood* **1984**, *38* (3), 119-126.

103. Guigo, N.; Mija, A.; Vincent, L.; Sbirrazzuoli, N., Chemorheological analysis and model-free kinetics of acid catalysed furfuryl alcohol polymerization. *Physical chemistry chemical physics : PCCP* **2007**, *9* (39), 5359-66.
104. González, R.; Martínez, R.; Ortiz, P., Polymerization of furfuryl alcohol with trifluoroacetic acid: the influence of experimental conditions. *Die Makromolekulare Chemie* **1992**, *193* (1), 1-9.
105. Choura, M.; Belgacem, N. M.; Gandini, A., Acid-Catalyzed Polycondensation of Furfuryl Alcohol: Mechanisms of Chromophore Formation and Cross-Linking. *Macromolecules* **1996**, *29* (11), 3839-3850.
106. Sugama, T.; Kukačka, L., Effect of zinc-levulinic acid chelate compounds formed in furfuryl alcohol polymer concrete. *J Mater Sci* **1982**, *17* (7), 2067-2076.
107. González, R.; Rieumont, J.; Figueroa, J. M.; Siller, J.; González, H., Kinetics of furfuryl alcohol polymerisation by iodine in methylene dichloride. *European polymer journal* **2002**, *38* (2), 281-286.
108. González, R.; Figueroa, J. M.; González, H., Furfuryl alcohol polymerisation by iodine in methylene chloride. *European polymer journal* **2002**, *38* (2), 287-297.
109. Moreau, C.; Belgacem, M. N.; Gandini, A., Recent catalytic advances in the chemistry of substituted furans from carbohydrates and in the ensuing polymers. *Topics in Catalysis* **2004**, *27* (1-4), 11-30.
110. Maciel, G. E.; Chuang, I.-S.; Myers, G. E., Carbon-13 NMR study of cured furfuryl alcohol resins using cross polarization and magic-angle spinning. *Macromolecules* **1982**, *15* (4), 1218-1220.
111. Chuang, I. S.; Maciel, G. E.; Myers, G. E., Carbon-13 NMR study of curing in furfuryl alcohol resins. *Macromolecules* **1984**, *17* (5), 1087-1090.
112. Montero, A. L.; Montero, L. A.; Martínez, R.; Spange, S., Ab initio modelling of crosslinking in polymers. A case of chains with furan rings. *Journal of Molecular Structure: THEOCHEM* **2006**, *770* (1-3), 99-106.
113. Guigo, N. Biomass based materials: polymers, composites and nano-hybrids from furfuryl alcohol and lignin. Université de Nice-Sophia Antipolis, 2008.
114. Alfred J, S., Dimensional Stabilization of Wood with Furfuryl Alcohol Resin. In *Wood Technology: Chemical Aspects*, AMERICAN CHEMICAL SOCIETY: 1977; Vol. 43, pp 141-149.
115. Belgacem, M. N.; Gandini, A., Furan-based adhesives. *Handbook of Adhesive Technology* **2003**, 615-634.
116. Dao, L. T.; Zavarin, E., Chemically activated furfuryl alcohol-based wood adhesives. I. The role of furfuryl alcohol. *Holzforschung-International Journal of the Biology, Chemistry, Physics and Technology of Wood* **1996**, *50* (5), 470-476.
117. Toriz, G.; Arvidsson, R.; Westin, M.; Gatenholm, P., Novel cellulose ester-poly (furfuryl alcohol)-flax fiber biocomposites. *Journal of applied polymer science* **2003**, *88* (2), 337-345.
118. Machnikowski, J.; Kierzek, K.; Lis, K.; Machnikowska, H.; Czepirski, L., Tailoring Porosity Development in Monolithic Adsorbents Made of KOH-Activated Pitch Coke and Furfuryl Alcohol Binder for Methane Storage†. *Energy & Fuels* **2010**, *24* (6), 3410-3414.
119. Varbanov, S.; Borissov, G., Furfuryl-containing tertiary phosphine oxides and polymers based on some of them. *European polymer journal* **1984**, *20* (2), 185-189.
120. Oliva-Teles, M. T.; Delerue-Matos, C.; Alvim-Ferraz, M. C. M., Determination of free furfuryl alcohol in foundry resins by chromatographic techniques. *Analytica chimica acta* **2005**, *537* (1), 47-51.
121. Schmitt, C., Polyfurfuryl alcohol resins. **1974**.
122. Ozaki, J.-i.; Mitsui, M.; Nishiyama, Y.; Cashion, J. D.; Brown, L. J., Effects of Ferrocene on Production of High Performance Carbon Electrodes from Poly(furfuryl alcohol). *Chemistry of Materials* **1998**, *10* (11), 3386-3392.
123. Ju, M.; Zeng, C.; Wang, C.; Zhang, L., Preparation of Ultrafine Carbon Spheres by Controlled Polymerization of Furfuryl Alcohol in Microdroplets. *Industrial & Engineering Chemistry Research* **2014**, *53* (8), 3084-3090.
124. Dong, Y.-R.; Nishiyama, N.; Egashira, Y.; Ueyama, K., H<sub>2</sub>-Selective Carbon Membranes Prepared from Furfuryl Alcohol by Vapor-Phase Synthesis. *Industrial & Engineering Chemistry Research* **2006**, *46* (12), 4040-4044.
125. He, L.; Li, D.; Zhang, G.; Webley, P. A.; Zhao, D.; Wang, H., Synthesis of Carbonaceous Poly(furfuryl alcohol) Membrane for Water Desalination. *Industrial & Engineering Chemistry Research* **2010**, *49* (9), 4175-4180.
126. Yi, B.; Rajagopalan, R.; Foley, H. C.; Kim, U. J.; Liu, X.; Eklund, P. C., Catalytic Polymerization and Facile Grafting of Poly(furfuryl alcohol) to Single-Wall Carbon Nanotube:

- Preparation of Nanocomposite Carbon. *Journal of the American Chemical Society* **2006**, *128* (34), 11307-11313.
127. Zhang, X.; Solomon, D. H., Carbonization Reactions in Novolac Resins, Hexamethylenetetramine, and Furfuryl Alcohol Mixtures. *Chemistry of Materials* **1999**, *11* (2), 384-391.
128. Zheng, H.-Y.; Zhu, Y.-L.; Teng, B.-T.; Bai, Z.-Q.; Zhang, C.-H.; Xiang, H.-W.; Li, Y.-W., Towards understanding the reaction pathway in vapour phase hydrogenation of furfural to 2-methylfuran. *Journal of Molecular Catalysis A: Chemical* **2006**, *246* (1), 18-23.
129. Zarbin, A. J.; Bertholdo, R.; Oliveira, M. A., Preparation, characterization and pyrolysis of poly (furfuryl alcohol)/porous silica glass nanocomposites: novel route to carbon template. *Carbon* **2002**, *40* (13), 2413-2422.
130. Gaefke, C.; Botelho, E.; Ferreira, N.; Rezende, M., Effect of furfuryl alcohol addition on the cure of furfuryl alcohol resin used in the glassy carbon manufacture. *Journal of applied polymer science* **2007**, *106* (4), 2274-2281.
131. Sujatha, P., Monitoring cytotoxic potentials of furfuryl alcohol and 2-furyl methyl ketone in mice. *Food and chemical toxicology* **2008**, *46* (1), 286-292.
132. Savolainen, H.; Pfäffli, P., Neurotoxicity of furfuryl alcohol vapor in prolonged inhalation exposure. *Environmental research* **1983**, *31* (2), 420-427.
133. Hoang, T. M. C.; van Eck, E. R. H.; Bula, W. P.; Gardeniers, J. G. E.; Lefferts, L.; Seshan, K., Humins based by-products from biomass processing as a potential carbonaceous source for synthesis gas production. *Green Chemistry* **2015**.
134. Chidambaram, M.; Bell, A. T., A two-step approach for the catalytic conversion of glucose to 2,5-dimethylfuran in ionic liquids. *Green Chemistry* **2010**, *12* (7), 1253-1262.
135. Shi, N.; Liu, Q.; Zhang, Q.; Wang, T.; Ma, L., High yield production of 5-hydroxymethylfurfural from cellulose by high concentration of sulfates in biphasic system. *Green Chemistry* **2013**, *15* (7), 1967-1974.
136. van Zandvoort, I.; Wang, Y.; Rasrendra, C. B.; van Eck, E. R.; Bruijninx, P. C.; Heeres, H. J.; Weckhuysen, B. M., Formation, molecular structure, and morphology of humins in biomass conversion: influence of feedstock and processing conditions. *ChemSusChem* **2013**, *6* (9), 1745-58.
137. Sevilla, M.; Fuertes, A. B., Chemical and structural properties of carbonaceous products obtained by hydrothermal carbonization of saccharides. *Chemistry-A European Journal* **2009**, *15* (16), 4195-4203.
138. Sevilla, M.; Fuertes, A. B., The production of carbon materials by hydrothermal carbonization of cellulose. *Carbon* **2009**, *47* (9), 2281-2289.
139. Baccile, N.; Laurent, G.; Babonneau, F.; Fayon, F.; Titirici, M.-M.; Antonietti, M., Structural Characterization of Hydrothermal Carbon Spheres by Advanced Solid-State MAS <sup>13</sup>C NMR Investigations. *The Journal of Physical Chemistry C* **2009**, *113* (22), 9644-9654.
140. Yao, C.; Shin, Y.; Wang, L.-Q.; Windisch, C. F.; Samuels, W. D.; Arey, B. W.; Wang, C.; Risen, W. M.; Exarhos, G. J., Hydrothermal Dehydration of Aqueous Fructose Solutions in a Closed System. *The Journal of Physical Chemistry C* **2007**, *111* (42), 15141-15145.
141. Titirici, M.-M.; Antonietti, M.; Baccile, N., Hydrothermal carbon from biomass: a comparison of the local structure from poly- to monosaccharides and pentoses/hexoses. *Green Chemistry* **2008**, *10* (11), 1204-1212.
142. Falco, C.; Perez Caballero, F.; Babonneau, F.; Gervais, C.; Laurent, G.; Titirici, M.-M.; Baccile, N., Hydrothermal Carbon from Biomass: Structural Differences between Hydrothermal and Pyrolyzed Carbons via <sup>13</sup>C Solid State NMR. *Langmuir : the ACS journal of surfaces and colloids* **2011**, *27* (23), 14460-14471.
143. Patil, S. K. R.; Lund, C. R. F., Formation and Growth of Humins via Aldol Addition and Condensation during Acid-Catalyzed Conversion of 5-Hydroxymethylfurfural. *Energy & Fuels* **2011**, *25* (10), 4745-4755.
144. Patil, S. K. R.; Heltzel, J.; Lund, C. R. F., Comparison of Structural Features of Humins Formed Catalytically from Glucose, Fructose, and 5-Hydroxymethylfurfuraldehyde. *Energy & Fuels* **2012**, *26* (8), 5281-5293.
145. Luijkx, G. C. A.; van Rantwijk, F.; van Bekkum, H., Hydrothermal formation of 1,2,4-benzenetriol from 5-hydroxymethyl-2-furaldehyde and d-fructose. *Carbohydrate Research* **1993**, *242* (0), 131-139.

146. Hoang, T. M. C.; Lefferts, L.; Seshan, K., Valorization of Humin-Based Byproducts from Biomass Processing—A Route to Sustainable Hydrogen. *ChemSusChem* **2013**, *6* (9), 1651-1658.
147. Arasse, D., *Léonard de Vinci: le rythme du monde*. Fernand Hazan: 2002.
148. Vinci, L. d. s. P. d., Codice sul volo degli uccelli. 1505.
149. Vinci, L. d. s. P. d., Codex Atlanticus. 1478-1518.
150. Wang, J.; Lin, L.; Cheng, Q.; Jiang, L., Inside Cover: A Strong Bio-Inspired Layered PNIPAM–Clay Nanocomposite Hydrogel (Angew. Chem. Int. Ed. 19/2012). *Angewandte Chemie International Edition* **2012**, *51* (19), 4494-4494.
151. Cranford, S. W.; Tarakanova, A.; Pugno, N. M.; Buehler, M. J., Nonlinear material behaviour of spider silk yields robust webs. *Nature* **2012**, *482* (7383), 72-76.
152. Cartwright, J. H.; Checa, A. G., The dynamics of nacre self-assembly. *Journal of the Royal Society Interface* **2007**, *4* (14), 491-504.
153. Luz, G. M.; Mano, J. F., Biomimetic design of materials and biomaterials inspired by the structure of nacre. *Philosophical Transactions of the Royal Society of London A: Mathematical, Physical and Engineering Sciences* **2009**, *367* (1893), 1587-1605.
154. Wegst, U. G. K.; Bai, H.; Saiz, E.; Tomsia, A. P.; Ritchie, R. O., Bioinspired structural materials. *Nat Mater* **2015**, *14* (1), 23-36.
155. Jackson, A. P.; Vincent, J. F. V.; Turner, R. M., *The Mechanical Design of Nacre*. 1988; Vol. 234, p 415-440.
156. Meyers, M. A.; Lin, A. Y.-M.; Chen, P.-Y.; Muyco, J., Mechanical strength of abalone nacre: Role of the soft organic layer. *Journal of the Mechanical Behavior of Biomedical Materials* **2008**, *1* (1), 76-85.
157. Cheng, Q.; Duan, J.; Zhang, Q.; Jiang, L., Learning from Nature: Constructing Integrated Graphene-Based Artificial Nacre. *ACS Nano* **2015**, *9* (3), 2231-2234.
158. Lehn, J. M. In *Perspectives in chemistry: From supramolecular chemistry towards adaptive chemistry*, 8e Colloque Franco – Roumain de Chimie Appliquée, ENSCM, Montpellier, France, ENSCM, Montpellier, France, 2014.
159. Wautelet, M., et coll., «*Les Nanotechnologies*,» *Book Dunod* **2003**.
160. Lahmani, M.; Bréchnignac, C.; Houdy, P., Les Nanosciences: Tome 2. *Nanomatériaux et nanochimie*. Belin **2006**.
161. Corriu, R.; Nguyễn, T.-A.; Nguyễn, T. A., *Chimie moléculaire, sol-gel et nanomatériaux*. Editions Ecole Polytechnique: 2008.
162. Gazit, E., Self-assembled peptide nanostructures: the design of molecular building blocks and their technological utilization. *Chemical Society Reviews* **2007**, *36* (8), 1263-1269.
163. Kurecic, M.; Smole, M. S., *Polymer Nanocomposite Hydrogels for Water Purification*. 2012.
164. Tony, G.; Vincent, S.; Samuel, B.; Catherine, J.; Xavier, J.; Rodica, C.; Gabriel, F.; Arnaud, B., AlN hollow-nanofilaments by electrospinning. *Nanotechnology* **2015**, *26* (8), 085603.
165. Thompson, B. C.; Fréchet, J. M. J., Polymer–Fullerene Composite Solar Cells. *Angewandte Chemie International Edition* **2008**, *47* (1), 58-77.
166. Rautureau, M.; Tchoubar, C., Structural analysis of sepiolite by selected area electron diffraction; relations with physico-chemical properties. *Clays and Clay Minerals* **1976**, *24* (1), 43-49.
167. Brauner, K.; Preisinger, A., Struktur und Entstehung des Sepioliths. *Tschermaks min u petr Mitt* **1956**, *6* (1-2), 120-140.
168. Volle, N.; Challier, L.; Burr, A.; Giulieri, F.; Pagnotta, S.; Chaze, A.-M., Maya Blue as natural coloring fillers in a multi-scale polymer-clay nanocomposite. *Composites Science and Technology* **2011**, *71* (15), 1685-1691.
169. Volle, N.; Giulieri, F.; Burr, A.; Pagnotta, S.; Chaze, A. M., Controlled interactions between silanol groups at the surface of sepiolite and an acrylate matrix: consequences on the thermal and mechanical properties. *Materials Chemistry and Physics* **2012**, *134* (1), 417-424.
170. Giustetto, R.; Wahyudi, O.; Corazzari, I.; Turci, F., Chemical stability and dehydration behavior of a sepiolite/indigo Maya Blue pigment. *Applied Clay Science* **2011**, *52* (1–2), 41-50.
171. Giustetto, R.; Seenivasan, K.; Bonino, F.; Ricchiardi, G.; Bordiga, S.; Chierotti, M. R.; Gobetto, R., Host/Guest Interactions in a Sepiolite-Based Maya Blue Pigment: A Spectroscopic Study. *The Journal of Physical Chemistry C* **2011**, *115* (34), 16764-16776.
172. Liu, Y.; Zhao, J.; Deng, C.-L.; Chen, L.; Wang, D.-Y.; Wang, Y.-Z., Flame-retardant effect of sepiolite on an intumescent flame-retardant polypropylene system. *Industrial & Engineering Chemistry Research* **2011**, *50* (4), 2047-2054.

173. Chen, B.; Evans, J. R., Elastic moduli of clay platelets. *Scripta materialia* **2006**, *54* (9), 1581-1585.
174. Tartaglione, G.; Tabuani, D.; Camino, G.; Moisisio, M., PP and PBT composites filled with sepiolite: morphology and thermal behaviour. *Composites Science and Technology* **2008**, *68* (2), 451-460.
175. Bokobza, L.; Burr, A.; Garnaud, G.; Perrin, M. Y.; Pagnotta, S., Fibre reinforcement of elastomers: nanocomposites based on sepiolite and poly(hydroxyethyl acrylate). *Polymer International* **2004**, *53* (8), 1060-1065.
176. Zheng, Y.; Zheng, Y., Study on sepiolite-reinforced polymeric nanocomposites. *Journal of Applied Polymer Science* **2006**, *99* (5), 2163-2166.
177. Franchini, E.; Galy, J.; Gérard, J.-F., Sepiolite-based epoxy nanocomposites: Relation between processing, rheology, and morphology. *Journal of Colloid and Interface Science* **2009**, *329* (1), 38-47.
178. Tartaglione, G.; Tabuani, D.; Camino, G., Thermal and morphological characterisation of organically modified sepiolite. *Microporous and Mesoporous Materials* **2008**, *107* (1-2), 161-168.
179. Gómez-Avilés, A.; Darder, M.; Aranda, P.; Ruiz-Hitzky, E., Functionalized Carbon-Silicates from Caramel-Sepiolite Nanocomposites. *Angewandte Chemie International Edition* **2007**, *46* (6), 923-925.
180. Sapieszko, R. S.; Matijević, E., Preparation of well-defined colloidal particles by thermal decomposition of metal chelates. I. Iron oxides. *Journal of Colloid and Interface Science* **1980**, *74* (2), 405-422.
181. Vijayakumar, R.; Koltypin, Y.; Felner, I.; Gedanken, A., Sonochemical synthesis and characterization of pure nanometer-sized Fe<sub>3</sub>O<sub>4</sub> particles. *Materials Science and Engineering: A* **2000**, *286* (1), 101-105.
182. Sun, S.; Zeng, H., Size-Controlled Synthesis of Magnetite Nanoparticles. *Journal of the American Chemical Society* **2002**, *124* (28), 8204-8205.
183. Harris, L. A.; Goff, J. D.; Carmichael, A. Y.; Riffle, J. S.; Harburn, J. J.; St. Pierre, T. G.; Saunders, M., Magnetite Nanoparticle Dispersions Stabilized with Triblock Copolymers. *Chemistry of Materials* **2003**, *15* (6), 1367-1377.
184. Kim, D.; Zhang, Y.; Voit, W.; Rao, K.; Muhammed, M., Synthesis and characterization of surfactant-coated superparamagnetic monodispersed iron oxide nanoparticles. *Journal of Magnetism and Magnetic Materials* **2001**, *225* (1), 30-36.
185. Yamaura, M.; Camilo, R.; Sampaio, L.; Macedo, M.; Nakamura, M.; Toma, H., Preparation and characterization of (3-aminopropyl) triethoxysilane-coated magnetite nanoparticles. *Journal of Magnetism and Magnetic Materials* **2004**, *279* (2), 210-217.
186. Néel, L., Influence des fluctuations thermiques sur laimantation de grains ferromagnétiques tres fins. *Comptes Rendus Hebdomadaires Des Seances De L Academie Des Sciences* **1949**, *228* (8), 664-666.
187. Néel, L., Théorie du traînage magnétique des ferromagnétiques en grains fins avec applications aux terres cuites. *Ann. géophys* **1949**, *5* (2), 99-136.
188. Dormann, J., Le phénomène de superparamagnétisme. *Revue de Physique Appliquée* **1981**, *16* (6), 275-301.
189. Ito, A.; Kuga, Y.; Honda, H.; Kikkawa, H.; Horiuchi, A.; Watanabe, Y.; Kobayashi, T., Magnetite nanoparticle-loaded anti-HER2 immunoliposomes for combination of antibody therapy with hyperthermia. *Cancer Letters* **2004**, *212* (2), 167-175.
190. Rossi, L.; Quach, A.; Rosenzweig, Z., Glucose oxidase-magnetite nanoparticle bioconjugate for glucose sensing. *Analytical and Bioanalytical Chemistry* **2004**, *380* (4), 606-613.
191. Hu, A.; Yee, G. T.; Lin, W., Magnetically Recoverable Chiral Catalysts Immobilized on Magnetite Nanoparticles for Asymmetric Hydrogenation of Aromatic Ketones. *Journal of the American Chemical Society* **2005**, *127* (36), 12486-12487.
192. Schätz, A.; Reiser, O.; Stark, W. J., Nanoparticles as Semi-Heterogeneous Catalyst Supports. *Chemistry – A European Journal* **2010**, *16* (30), 8950-8967.
193. Ge, J.; Huynh, T.; Hu, Y.; Yin, Y., Hierarchical Magnetite/Silica Nanoassemblies as Magnetically Recoverable Catalyst-Supports. *Nano Letters* **2008**, *8* (3), 931-934.
194. Sanchez, C.; Julian, B.; Belleville, P.; Popall, M., Applications of hybrid organic-inorganic nanocomposites. *Journal of Materials Chemistry* **2005**, *15* (35-36), 3559-3592.
195. Wang, J.; Lin, L.; Cheng, Q.; Jiang, L., A Strong Bio-Inspired Layered PNIPAM-Clay Nanocomposite Hydrogel. *Angewandte Chemie* **2012**, *124* (19), 4754-4758.

196. Bellucci, G.; Seedhom, B., Mechanical behaviour of articular cartilage under tensile cyclic load. *Rheumatology* **2001**, *40* (12), 1337-1345.
197. Zeng, Y.; Yang, J.; Huang, K.; Lee, Z.; Lee, X., A comparison of biomechanical properties between human and porcine cornea. *Journal of biomechanics* **2001**, *34* (4), 533-537.
198. Reinitzer, F., Contributions to the understanding of Cholesterol. *Monatshefte für Chemie (Wien)* **1888**, *9*, 421.
199. Lehmann, O., Über fließende krystalle. *Z. phys. Chem* **1889**, *4*, 462-472.
200. Sluckin, T. J.; Dunmur, D. A.; Stegemeyer, H., Crystals that flow. *Liquid Crystals Series Taylor & Francis: London* **2004**.
201. Tschierske, C., Micro-segregation, molecular shape and molecular topology - partners for the design of liquid crystalline materials with complex mesophase morphologies. *Journal of Materials Chemistry* **2001**, *11* (11), 2647-2671.
202. Brown, G. H.; Shaw, W. G., The Mesomorphic State - Liquid Crystals. *Chemical reviews* **1957**, *57* (6), 1049-1157.
203. De Gennes, P.-G.; Prost, J., *The physics of liquid crystals*. Clarendon press Oxford: 1993; Vol. 23.
204. Demus, D.; Goodby, J. W.; Gray, G. W.; Spiess, H. W.; Vill, V., *Handbook of Liquid Crystals, Low Molecular Weight Liquid Crystals I: Calamitic Liquid Crystals*. John Wiley & Sons: 2011.
205. Chandrasekhar, S.; Sadashiva, B. K.; Suresh, K. A., Liquid crystals of disc-like molecules. *Pramana - J Phys* **1977**, *9* (5), 471-480.
206. Kumar, S., Self-organization of disc-like molecules: chemical aspects. *Chemical Society Reviews* **2006**, *35* (1), 83-109.
207. Bisoyi, H. K.; Kumar, S., Discotic nematic liquid crystals: science and technology. *Chemical Society Reviews* **2010**, *39* (1), 264-285.
208. Reddy, R. A.; Tschierske, C., Bent-core liquid crystals: polar order, superstructural chirality and spontaneous desymmetrisation in soft matter systems. *Journal of materials chemistry* **2006**, *16* (10), 907-961.
209. Tamaoki, N., Cholesteric Liquid Crystals for Color Information Technology. *Advanced materials* **2001**, *13* (15), 1135-1147.
210. Hideo, T.; Yoichi, T., Bent-Core Liquid Crystals: Their Mysterious and Attractive World. *Japanese Journal of Applied Physics* **2006**, *45* (2R), 597.
211. Tschierske, C., Liquid crystal engineering - new complex mesophase structures and their relations to polymer morphologies, nanoscale patterning and crystal engineering. *Chemical Society Reviews* **2007**, *36* (12), 1930-1970.
212. Bellini, T.; Tschierske, C., *Liquid crystals: materials design and self-assembly*. Springer Science & Business Media: 2012; Vol. 318.
213. Lehmann, M., Star mesogens (hekates)--tailor-made molecules for programming supramolecular functionality. *Chemistry* **2009**, *15* (15), 3638-51.
214. Kölbel, M.; Beyersdorff, T.; Cheng, X. H.; Tschierske, C.; Kain, J.; Diele, S., Design of Liquid Crystalline Block Molecules with Nonconventional Mesophase Morphologies: Calamitic Bolaamphiphiles with Lateral Alkyl Chains. *Journal of the American Chemical Society* **2001**, *123* (28), 6809-6818.
215. Kölbel, M.; Beyersdorff, T.; Sletvold, I.; Tschierske, C.; Kain, J.; Diele, S., Design of New Mesogenic Block Molecules: Formation of Columnar Mesophases by Calamitic Bolaamphiphiles with Lateral Lipophilic Substituents. *Angewandte Chemie International Edition* **1999**, *38* (8), 1077-1080.
216. Abraham, S.; Paul, S.; Narayan, G.; Prasad, S. K.; Rao, D. S. S.; Jayaraman, N.; Das, S., Observation of a Chiral Smectic Phase in Azobenzene-Linked Bolaamphiphiles Containing Free Sugars. *Advanced Functional Materials* **2005**, *15* (10), 1579-1584.
217. Kato, T.; Mizoshita, N.; Kishimoto, K., Functional liquid-crystalline assemblies: self-organized soft materials. *Angewandte Chemie International Edition* **2006**, *45* (1), 38-68.
218. Goodby, J. W.; Saez, I. M.; Cowling, S. J.; Gortz, V.; Draper, M.; Hall, A. W.; Sia, S.; Cosquer, G.; Lee, S. E.; Raynes, E. P., Transmission and amplification of information and properties in nanostructured liquid crystals. *Angewandte Chemie* **2008**, *47* (15), 2754-87.
219. De Gennes, P., Physique moleculaire. *CR Acad. Sci. B* **1975**, *281*, 101.
220. De Gennes, P., Possibilites offertes par la reticulation de polymeres en presence d'un cristal liquide. *Physics Letters A* **1969**, *28* (11), 725-726.

221. Strzelecki, L.; Liebert, L., Synthèse et polymérisation de nouveaux monomères mésomorphes. *Bull, Soc. Chim. Fr* **1973**, *2*, 597.
222. Finkelmann, H.; Kock, H. J.; Rehage, G., Investigations on liquid crystalline polysiloxanes 3. Liquid crystalline elastomers—a new type of liquid crystalline material. *Die Makromolekulare Chemie, Rapid Communications* **1981**, *2* (4), 317-322.
223. Broer, D. J.; Hikmet, R. A.; Challa, G., In-situ photopolymerization of oriented liquid-crystalline acrylates, 4. Influence of a lateral methyl substituent on monomer and oriented polymer network properties of a mesogenic diacrylate. *Die Makromolekulare Chemie* **1989**, *190* (12), 3201-3215.
224. Carfagna, C.; Amendola, E.; Giamberini, M., Liquid crystalline epoxy based thermosetting polymers. *Progress in Polymer Science* **1997**, *22* (8), 1607-1647.
225. Barclay, G.; Ober, C. K.; Papatthomas, K.; Wang, D., Liquid crystalline epoxy thermosets based on dihydroxymethylstilbene: Synthesis and characterization. *Journal of Polymer Science Part A: Polymer Chemistry* **1992**, *30* (9), 1831-1843.
226. Barclay, G.; Ober, C., Liquid crystalline and rigid-rod networks. *Progress in polymer science* **1993**, *18* (5), 899-945.
227. Carfagna, C.; Amendola, E.; Giamberini, M.; Filippov, A.; Bauer, R., Curing kinetics of liquid-crystalline epoxy resins. *Liquid Crystals* **1993**, *13* (4), 571-584.
228. Carfagna, C.; Amendola, E.; Giamberini, M.; Filippov, A. G., Liquid-crystalline epoxy resins: a glycidyl-terminated benzaldehyde azine cured in the nematic phase. *Macromolecular Chemistry and Physics* **1994**, *195* (1), 279-287.
229. Carfagna, C.; Amendola, E.; Giamberini, M., Liquid crystalline epoxy resins containing binaphthyl group as rigid block with enhanced thermal stability. *Macromolecular Chemistry and Physics* **1994**, *195* (7), 2307-2315.
230. Jahromi, S.; Lub, J.; Mol, G. N., Synthesis and photoinitiated polymerization of liquid crystalline diepoxides. *Polymer* **1994**, *35* (3), 622-629.
231. Douglas, E. P., Liquid Crystalline Thermosets. In *Encyclopedia of Polymer Science and Technology*, John Wiley & Sons, Inc.: 2002.
232. Earls, J. D.; Hefner Jr, R. E.; Puckett, P. M., Mesogenic epoxy compounds. Google Patents: 1993.
233. Giamberini, M.; Amendola, E.; Carfagna, C., Lightly crosslinked liquid crystalline epoxy resins: The effect of rigid-rod length and applied stress on the state of order of the cured thermoset. *Macromolecular Chemistry and Physics* **1997**, *198* (10), 3185-3196.
234. Amendola, E.; Carfagna, C.; Giamberini, M.; Pisaniello, G., Curing reactions of a liquid crystalline epoxy resin based on the diglycidyl ether of 4,4'-dihydroxy- $\alpha$ -methylstilbene. *Macromolecular Chemistry and Physics* **1995**, *196* (5), 1577-1591.
235. Giamberini, M.; Amendola, E.; Carfagna, C., Curing of a rigid rod epoxy resin with an aliphatic diacid: an example of a lightly crosslinked liquid crystalline thermoset. *Macromolecular Rapid Communications* **1995**, *16* (2), 97-105.
236. Ortiz, C.; Kim, R.; Rodighiero, E.; Ober, C. K.; Kramer, E. J., Deformation of a Polydomain, Liquid Crystalline Epoxy-Based Thermoset. *Macromolecules* **1998**, *31* (13), 4074-4088.
237. Mormann, W.; Bröcher, M., Liquid crystalline thermosets (LCT) from diaromatic mesogenic diepoxides and aromatic diamines: synthesis and phase behaviour of model compounds and intermediate structures. *Polymer* **1998**, *39* (25), 6597-6603.
238. Punaichetch, P.; Ambrogi, V.; Giamberini, M.; Brostow, W.; Carfagna, C.; D'Souza, N. A., Epoxy+ liquid crystalline epoxy coreacted networks: II. Mechanical properties. *Polymer* **2002**, *43* (3), 839-848.
239. Vincent, L.; Mija, A.; Sbirrazzuoli, N., Liquid crystalline and isotropic epoxy thermosets: Mechanism and kinetics of non-isothermal degradation. *Polymer Degradation and Stability* **2007**, *92* (11), 2051-2057.
240. Mititelu, A.; Hamaide, T.; Novat, C.; Dupuy, J.; Cascaval, C. N.; Simionescu, B. C.; Navard, P., Curing kinetics of liquid-crystalline epoxy resins with inverse reactivity ratios. *Macromolecular Chemistry and Physics* **2000**, *201* (12), 1209-1213.
241. Mija, A.; Navard, P.; Peiti, C.; Babor, D.; Guigo, N., Shear induced structuration of liquid crystalline epoxy thermosets. *European Polymer Journal* **2010**, *46* (6), 1380-1387.

242. Castell, P.; Serra, A.; Galià, M.; Giamberini, M.; Carfagna, C., Anisotropic thermosets from liquid-crystalline azomethynic epoxy resins and primary aromatic diamines. *Journal of Polymer Science Part A: Polymer Chemistry* **2003**, *41* (1), 1-12.
243. Harada, M.; Ando, J.; Hattori, S.; Sakurai, S.; Sakamoto, N.; Yamasaki, T.; Masunaga, H.; Ochi, M., In-situ analysis of the structural formation process of liquid-crystalline epoxy thermosets by simultaneous SAXS/WAXS measurements using synchrotron radiation. *Polymer Journal* **2012**, *45* (1), 43-49.
244. Sorai, M.; Saito, K., Alkyl chains acting as entropy reservoir in liquid crystalline materials. *Chemical record* **2003**, *3* (1), 29-39.
245. Körner, H.; Shiota, A.; Bunning, T. J.; Ober, C. K., Orientation-On-Demand Thin Films: Curing of Liquid Crystalline Networks in ac Electric Fields. *Science* **1996**, *272* (5259), 252-255.
246. Benicewicz, B. C.; Smith, M. E.; Earls, J. D.; Priester, R. D.; Setz, S. M.; Duran, R. S.; Douglas, E. P., Magnetic Field Orientation of Liquid Crystalline Epoxy Thermosets. *Macromolecules* **1998**, *31* (15), 4730-4738.



## **Chapter III**

### Materials and methods



<b>III.1. Structural and morphological analysis.....</b>	<b>82</b>
III.1.1. FT-IR .....	82
III.1.2. Mono and multi-dimensional NMR .....	82
III.1.3. X-ray diffraction.....	82
III.1.4. Electronic and optical microscopy .....	82
<b>III.2. Thermal and mechanical analysis.....</b>	<b>83</b>
III.2.1. Differential Scanning Calorimetry (DSC).....	83
III.2.2. Stochastic temperature modulated DSC (TOPEM).....	84
III.2.3. Thermogravimetric analysis (TGA) .....	86
III.2.4. Rheometric analysis .....	86
III.2.5. Dynamic mechanical analysis (DMA) .....	88
III.2.6. Mechanical tests .....	88
<b>III.3 Thermo-kinetic analysis.....</b>	<b>89</b>
III.3.1. Extent of conversion and apparent activation energy.....	90
III.3.2. Isoconversional principle and advanced kinetic methods .....	91

### III. Materials and methods

#### III.1. Structural and morphological analysis

##### III.1.1. FT-IR

FT-IR technique has been used in this thesis work for characterization of products of synthesis and to investigate the evolution of polymeric structures before and after curing reactions. For this purpose, a Perkin Elmer Spectrum BX II spectrophotometer was employed in attenuated total reflectance (ATR) mode using a diamond crystal (**Chapters IV, V, VI, VIII**) and a Perkin-Elmer Paragon 1000 spectrometer with a diffuse reflection infrared device (Eurolabo Minidiff plus diffuse reflectance device) (**Chapter VII**).

##### III.1.2. Mono and multi-dimensional NMR

1D and 2D liquid state NMR have been employed to follow the polymerization between ELO and FA (**Chapter VI**), and for the characterization of synthesized monomers (**Chapter VIII**). For that,  $^1\text{H}$  NMR and  $^{13}\text{C}$  NMR investigations were recorded in  $\text{DMSO-}d_6$  with a Bruker AVANCE I instrument with direct probe working at 500.23 MHz for  $^1\text{H}$  and 125.75 MHz for  $^{13}\text{C}$ . The residual solvent signal at 2.50 ppm has been used as standard reference.

In order to highlight the sepiolite functionalization (**Chapter VII**), solid-state nuclear magnetic resonance spectra ( $\text{NMR}^{29}\text{Si/MAS}$ ) of the samples were recorded on a VARIAN spectrometer, operating at 400 MHz, 7.05 T and 4.51 s. Spectrometer was employed with a rotation speed of 5 kHz, 7 minutes of contact time and pulse interval 60 s. The chemical shifts were referenced to tetramethylsilane (TMS) as external standard, the spectrum being recorded after 1000 accumulations during 18 hours.

##### III.1.3. X-ray diffraction

The wide angle X-ray scattering (WAXS) measurements (**Chapter VIII**) have been realized with the PANalytical *X'PERT* Pro diffractometer using a standard copper anode source ( $\lambda = 1,54060 \text{ \AA}$ ).

##### III.1.4. Electronic and optical microscopy

The fracture morphologies of polymer samples (**Chapters V, VI and VIII**) were investigated by scanning electron microscopy (SEM) using a JEOL 6700F microscope equipped with a field

emission gun. The electron beam voltage was fixed to 1 kV. The samples were mounted on the microscope studs using silver colloidal paste and sputter coated with gold palladium.

Transmission electron microscopy (TEM) was carried out on a JEOL 1400 microscope, operated at an accelerating voltage of 100 kV. The TEM micrographs of the sepiolite fibers (**Chapter VII**) were recorded from a drop of a diluted suspension, which was deposited on a copper grid of 300 mesh covered by amorphous carbon. In the case of the polymer composites, the samples were cut in sections of about 80 nm thickness, using a RMC power tome X ultramicrotome equipped with a diamond knife and the films were collected onto 300 mesh copper grids.

The dispersions of m-SEP in epoxy resin without curing agent (**Chapter VII**), and the liquid-crystalline birefringence of polymer (**Chapter VIII**) were observed by optical microscopy in polarized light using a ZEISS microscope with a heating regulated device.

### III.2. Thermal and mechanical analysis

The picture in **Figure III.33** exhibits a panoramic view of analysis laboratory, with DSC, Flash DSC, DMA, rheometer, TGA-GC/MS, optical microscope equipment and so on. Most of these apparatus will be presented on the following section, associated to the referenced chapters.



**Figure III.33.** Presentation of the thermal analysis laboratory

#### III.2.1. Differential Scanning Calorimetry (DSC)

Differential scanning calorimetry (DSC) is a quantitative thermal analysis used since the beginning of 1960.<sup>1</sup> DSC is a powerful device commonly used to appreciate the reactivity by the measure of released heat flow during chemical reaction or also to measure polymers physical properties for instance, such as melting, crystallisation, glass transition temperature, phase

transitions, purity, crystallinity etc. DSC principle is based on the measurement of heat flow difference between a reference pan and a sample pan. Two type of DSC exist: power compensation DSC<sup>2</sup> where the sample and the reference are heated independently in two microfurnaces or heat flux DSC where both of pans are heated with the same temperature program. In this thesis work, we only used the heat flux DSC. Generally the two used crucibles are identical, thus the resulting heat flow corresponds to the response of the sample itself composed of both so called “latent” and “sensible” heat flow:

$$\Phi (T, t) = \frac{dQ}{dt} = mC_p\beta + m\Delta_rH \frac{d\alpha}{dt}$$

Equation 1

With  $m$  the sample mass,  $\beta$  the heating rate and  $C_p$  the specific heat capacity which is temperature dependant for a definite structure.  $\Delta_rH$  corresponds to the enthalpy of the considered thermal event and  $\alpha$ , the extent of conversion. The first equation term ( $mC_p\beta$ ) is associated to the sensible heat flow which is reliable to the heating rate, while the second term corresponds to the latent heat flow that depends on the kinetics of the physico-chemical process.

DSC measurements were carried out on a Mettler-Toledo DSC 1 equipped with STAR<sup>®</sup> software. This apparatus has a very high sensitivity due to its heat-flux ceramic sensor FRS5 (with 56 thermocouples Au-Au/Pd). Temperature and enthalpy calibrations were performed by using indium ( $T_m = 156.56$  °C) and zinc ( $T_m = 419.52$  °C) standards. Integrations of DSC peaks were done using a linear baseline. Samples of about 15 mg were placed in 40  $\mu$ L aluminium crucibles (**Chapters IV, VII, VIII**) and in 30  $\mu$ L stainless steel sealed pans to avoid evaporation (**Chapters V and VI**).

### III.2.2. Stochastic temperature modulated DSC (TOPEM)

Advanced DSC techniques started with the temperature modulated DSC (TMDSC) in 1993.<sup>3,4</sup> This technique is based on a superimposition of a periodic modulated temperature on the classical DSC temperature program. The periodic modulation should be imposed by a step function (Stepscan DSC) or with the help of a sinusoidal function (MDSC). The resulting heat flow measured can be treated by a Fourier transform to obtain the average total heat flow ( $\phi_{tot}$ ) which can be decomposed in a “reversing” ( $\phi_{rev}$ ) and “non-reversing” ( $\phi_{non-rev}$ ) components.  $\phi_{rev}$  characterises reversible processes on the range of time and temperature of perturbation. That corresponds to transition of first or second order such as melting or glass transition (pseudo

second order transition). A *contrario* non-reversing processes on the range of time and temperature of perturbation such as cold crystallizations or chemical reactions for instance are characterized by  $\phi_{non-rev}$ . However TMDSC present several limitations reliable to experimental parameters that are linked to heat transfer (very low sample mass), the necessity to make blank, sample measurements, and the limitation to one frequency. In order to avoid these limitations Schawe et al.<sup>5</sup> from Mettler-Toledo proposed a new method in DSC, called TOPEM<sup>®</sup>. In this technique, the superimposed program consists on a stochastic perturbation temperature program. Thus, the temperature program in function of time can be written as follow:

$$T(t) = T_0 + \beta_u t + \delta T(t)$$

**Equation 2**

Where  $\delta T(t)$  is the pulse amplitude which is alternately positive or negative and its application time can vary randomly in a fixed windows. Thus the heating rate derived from this stochastic temperature program is given by:

$$\beta(t) = dT/dt = \beta_u + d(\delta T(t))/dt$$

**Equation 3**

The resulting signal is treated by a Laplace transform to obtain the three components  $\phi_{tot}$ ,  $\phi_{rev}$ ,  $\phi_{non-rev}$  (notice that in this case, instead of sinusoidal TMDSC,  $\phi_{non-rev}$  is calculated independently and not deduced from the difference between  $\phi_{tot}$  and  $\phi_{rev}$ ). The stochastic perturbation give also access to the “quasi static” heat capacity obtained by extrapolation to zero-frequency. So, with only one TOPEM experiment, the complex part from the heat capacity is available for a range of frequency.

$$C_p^* = C_p' + iC_p''$$

**Equation 4**

The  $C_p'$  is the heat capacity in phase with the heating rate while  $C_p''$  corresponds to the out of phase counterpart. Herein, this technique is particularly interesting to study thermoset cross-linking because of the possible dissociation of the heat flow into non-reversing component corresponding to the polymerization reaction and into reversing component attributed to vitrification/devitrification phenomenons.<sup>6,7,8</sup>

TOPEM<sup>®</sup> measurements, investigated in the **Chapter IV**, were conducted at an underlying heating rate of 1 °C min<sup>-1</sup> with a scanning temperature ranging from 0°C to 300°C. The amplitude was fixed at ± 0.25 °C for all the modulated experiments. The period of pulses were ranging from 15 to 30 s. To evaluate the heat flow response of each system in function of stochastic modulation temperature different calculation parameters were applied. For ELO/MHHPA curing system the parameters of calculation windows are: width about 360 s, shift

of calculation windows 10 s, and width of smoothing windows 140s. For ELO/BTDA these parameters are: 120 s, 10 s, 90 s.

### III.2.3. Thermogravimetric analysis (TGA)

Thermogravimetric measurements were carried out on a TGA 851<sup>e</sup> from Mettler-Toledo. The microbalance has a precision of  $\pm 0.1 \mu\text{g}$  (**Figure III.34**). Samples of about 10 mg were placed into 70  $\mu\text{L}$  alumina pans. To characterize thermal stability of the thermosets the samples were heated at  $10 \text{ }^\circ\text{C}\cdot\text{min}^{-1}$  from  $25^\circ\text{C}$  to  $900^\circ\text{C}$  under nitrogen or air gas flow of  $50 \text{ mL}\cdot\text{min}^{-1}$  (**Chapter IV, VI, VIII**) and at  $7 \text{ }^\circ\text{C}\cdot\text{min}^{-1}$  under nitrogen flow of  $50 \text{ mL}\cdot\text{min}^{-1}$  (**Chapter VII**).

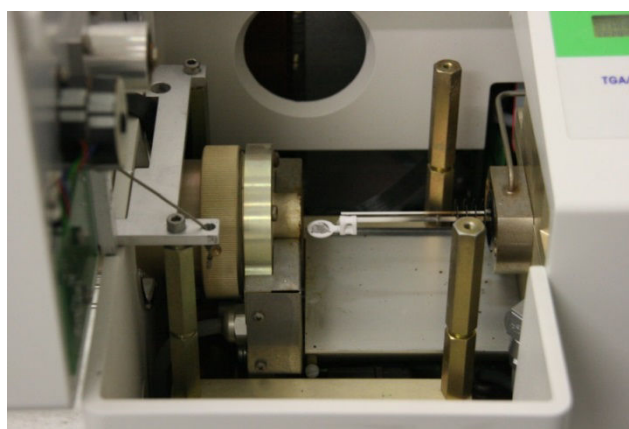


**Figure III.34.** TG microbalance from TGA 851<sup>e</sup>.

### III.2.4. Rheometric analysis

As seen on **section II.1.2.**, the formation of a tridimensional network is accompanied by high variations of viscosity (generally increase) from liquid to solid state. Rheometry is thus a preferential technique to study this kind of systems; the following section would to briefly introduce the apparatus and associated concepts.

When a system exhibits an ideal viscous behaviour in response to an external solicitation (Newtonian liquid), it exists a linear relation between the viscosity and the shear stress.

$$\tau = \eta \cdot \frac{d\gamma}{dt}$$

**Equation 5**

Where  $\tau$  is associated to the shear stress (Pa),  $\eta$  is the viscosity ( $\text{Pa}\cdot\text{s}^{-1}$ ) and  $\frac{d\gamma}{dt}$  the shear rate ( $\text{s}^{-1}$ ).

Low molecular weight liquids such as water, solvents or oils, demonstrate generally Newtonian behavior. Thus their viscosity are not dependent on the rate and duration of the shear load.

As the reverse, ideal elastic solid are described by the Hooke's law:

$$\tau = G \cdot \gamma$$

**Equation 6**

Where  $G$  corresponds to the shear modulus (Pa) that can be reliable to some structural information of the material such as network cohesion and rigidity. Indeed, higher is the rigidity and higher will be the shear modulus value. The particularity of viscoelastic materials such as thermoset is to present both viscous and elastic behaviour. These behaviours can be followed during the cross-linking by dynamic shear rheometry. In dynamic shear rheometry, the stress  $\tau(t)$  imposed to the sample follows a sinusoidal variation, function of time:

$$\tau(t) = \tau_A \cdot \sin(\omega \cdot t)$$

**Equation 7**

Where  $\tau_A$  corresponds to the stress amplitude and  $\omega$  the oscillation frequency ( $\text{rad}\cdot\text{s}^{-1}$ ). As result, the measured response (deformation)  $\gamma(t)$  can be described as follow:

$$\gamma(t) = \gamma_A \cdot \sin(\omega \cdot t + \delta)$$

**Equation 8**

Where  $\delta$  is the shift angle (rad with  $0 < \delta < \pi/2$ ). Thus the relation between  $\tau$  and  $\gamma$  in function of time is given by:

$$G^*(\omega) = \frac{\tau(t)}{\gamma(t)} = G' + iG''$$

**Equation 9**

Where  $G^*(\omega)$  is the complex shear modulus and can be dissociated into two components: a real ( $G'$ ) and an imaginary ( $G''$ ) part.  $G'$ , commonly called storage modulus, defines the material elastic response and is associated to the deformation energy stored by the sample (is a reversible process). While  $G''$ , called loss modulus, reflects the viscous response and represent the deformation energy used by the sample (is an irreversible process). Thus the rapport between the elastic and viscous components is given by:

$$\tan \delta = \frac{G''}{G'}$$

**Equation 10**

Where  $\tan \delta$  is called damping factor or loss factor. This value, measured in function of time or temperature, gives substantial information relative to the network formation such as gelation or vitrification that may occur during cure or  $\alpha$ -relaxation which could be related to the glass transition. Indeed, gelation point is commonly taken as the point where  $\tan \delta = 1$  (i.e. when  $G''$  and  $G'$  crossover).

The chemorheological behavior of epoxy/anhydride curing mixtures (**Chapter IV**) was followed using a Bohlin C-VOR rheometer. Complex viscosity, storage modulus ( $G'$ ) and loss modulus

( $G''$ ) were measured by oscillatory shear experiments. The measurements were operated on plate-plate geometries (25 mm diameter and 1 mm gap) with strain convection heating. The tests were carried out by heating the mixtures from 30 to 230°C with a rate of 1 °C min<sup>-1</sup>. The frequency was 1 Hz on auto stress mode with a deformation of 0.5%. For the **Chapter V**, an Anton Paar MCR 102 rheometer was used to measure the furanic resins viscosities in shear mode (0.1 to 10Hz) with parallel plate - plate geometries (15 mm diameter and 1 mm gap).

### III.2.5. Dynamic mechanical analysis (DMA)

For the **Chapters IV, VI, VIII**, DMA measurements were conducted using a TT DMA Triton Technology apparatus (**Figure III.35**), in tensile mode on specimens having free dimensions of 20x4x1.5 mm<sup>3</sup>. The tests were carried out by heating the samples from -150 to 300°C at 1°C min<sup>-1</sup> with a 1Hz oscillating stress. Concerning the **Chapter VII**, experiments were performed on a dynamic mechanical thermal Analyzer DMTA (Q800 from TA Instruments Inc.) equipped with a Clamp Single Cantilever, at a fixed frequency of 1 Hz, strain = 0.1 %, with a heating rate of 3 °C/min from -100° C to 120° C. With the same equipment, experiments were performed at room temperature and range frequency 0.1-100 Hz to determine the flexural modulus. In a similar way as presented in the above section for rheometry, the loss ( $E''$ ), storage ( $E'$ ) Young moduli and damping factor ( $\tan \delta = E''/E'$ ) were determined. The  $T_\alpha$  transition was assigned as the temperature of maximum of loss factor peak combined with the  $E'$  drop and the peak of  $E''$ .



**Figure III.35.** TT DMA Triton Technology apparatus

### III.2.6. Mechanical tests

The testing machine allows studying the ultimate properties of a given material, putting in light, for instance, plasticity or elasticity characteristics until break. As an example, the **Figure III.36**

illustrates the strategy adopted in the **Chapter V** that links the mechanical behavior to the compatibility between resin and cellulose fibers.

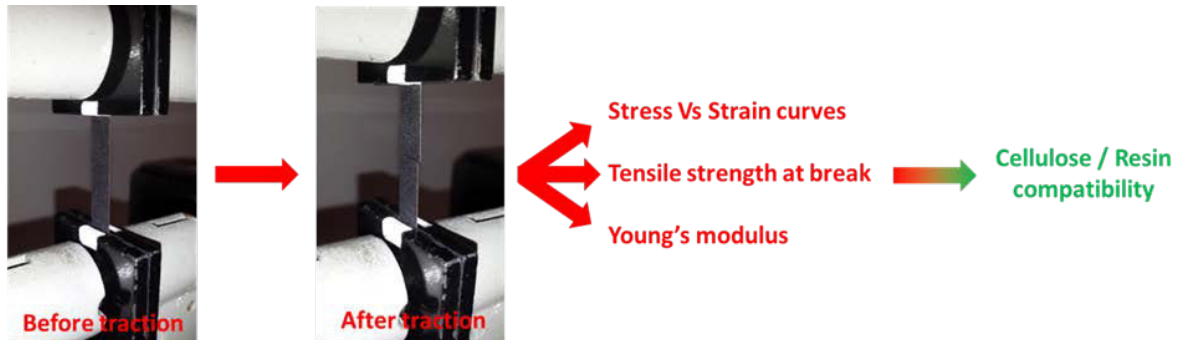


**Figure III.36.** Tensile test on cellulosic composites elaborated on **Chapter V**.

In tensile test, the resulting modulus called Young modulus ( $E'$ ) is obtained by the ratio between the stress ( $\sigma$ ) on the deformation ( $\varepsilon$ ) with:

$$\varepsilon = \frac{l}{l_0} = 1 + \frac{\Delta l}{l_0}$$

**Equation 11**

$$\sigma = \frac{F}{S}$$

**Equation 12**

Where  $S$  represents the sample section (width x thickness) and  $l$  the length. According to these equations, the samples need to be measured precisely. Then, after the correct sample positioning between clamps, testing machine can measure the strength ( $F$ ) applied to the sample as a function of the sample elongation  $\Delta l$ . The stress-strain curves were recorded at room temperature on an Instron 5565 (**Chapter V**) and on a Testwell 112.10 kN (**Chapter VI**) with a crosshead speed of 2 mm.min<sup>-1</sup>. After curing and demolding ELO/PFA thermosets have been cut using a Charly Robot milling machine into rectangular specimens of around 80 x 11 x 2 (length x width x thickness) mm, while the impregnated cellulose composites were cut into strips of around 100 x 10 x 0.25 (length x width x thickness) mm. The length between the clamps was fixed at 40 mm. For each material, the average values and standard deviations of Young's modulus and tensile strength were calculated from seven measurements.

### III.3. Thermo-kinetic analysis

The advanced isoconversional method proposed here allows to calculate the apparent activation energy  $E_\alpha$ , based on thermoanalytical data, for each extent of conversion  $\alpha$ , in a model “free” way. Indeed, this demarche is the reverse of classical investigation with kinetic models: in our case the resulting energy dependency evolution opens the discussion to determine which kind of mechanism could occur.

### III.3.1. Extent of conversion and apparent activation energy

When a physico-chemical transition or a chemical reaction occurs under the effect of temperature, the extent of conversion at time  $t_i$ ,  $\alpha_i$  is defined as the ratio between the heat quantity  $\Delta H_i$  exchanged at time  $i$  and the total quantity of heat  $\Delta H_{tot}$  exchanged during the transition or the reaction.

$$\alpha_i = \frac{\Delta H_i}{\Delta H_{tot}} = \frac{\int_{t_1}^{t_i} (dH/dt)_i dt}{\int_{t_1}^{t_2} (dH/dt)_i dt}$$

**Equation 13**

In this expression,  $\alpha_i$  represents the extend of conversion value at the instant  $i$ ,  $(dH / dt)_i$  represents the heat flow measured at time  $t_i$ ,  $t_1$  and  $t_2$  are respectively associated to the first and second integration bounds of the thermal event. Thus, the heat flow rate is a function of time  $(dH / dt)$  and proportional to the total heat  $(\Delta H_{tot})$  exchanged at the reaction rate  $(d\alpha / dt)$ :

$$\frac{dH}{dt} = \Delta H_{tot} \frac{d\alpha}{dt} = \Delta H_{tot} k(T) f(\alpha)$$

**Equation 14**

With  $k(T)$  the rate constant,  $T$  the temperature and  $f(\alpha)$  the mathematical function associated to the reaction mechanism. Then, the relation between the temperature and the rate constant is given by Arrhenius equation:

$$k(T) = A e^{-E/RT}$$

**Equation 15**

So, we can re-write **Equation 2** as follow:

$$\frac{d\alpha}{dt} = A e^{-E/RT} f(\alpha)$$

**Equation 16**

With  $A$  the pre-exponential factor,  $E$  the activation energy, and  $R$  the molar gas constant. For non-isothermal measurements, the dependency in time should be substituted by the temperature, considering the constant heating rate  $\beta$  imposed to the sample:

$$\frac{d\alpha}{dT} = \frac{A}{\beta} e^{-E/RT} f(\alpha)$$

Equation 17

With  $\beta = dT / dt$  is the heating rate.

### III.3.2. Isoconversional principle and advanced kinetic methods

The isoconversional principle stipulates that for a given extent of conversion  $\alpha$ , the reaction rate is only function of temperature.<sup>9</sup> Starting from this postulate, several methods have been developed to calculate an apparent activation energy  $E_\alpha$  from thermoanalytical data (see **section III.3.1**). Several differential or integral isoconversional methods such as Friedman,<sup>10</sup> Ozawa,<sup>11</sup> Flynn and Wall<sup>12</sup> methods are commonly used. The advantage of these methods that use several (generally 3-5) experiments performed at different heating rates, is to give a value of  $E_\alpha$  without any assumption on the reaction mechanism involved during the reaction (i.e.  $f(\alpha)$  is not included in the calculus of  $E_\alpha$ ). However these techniques present diverse problems such as sensibility to noise, or approximation for equation solving. To overcome these drawbacks, Sbirrazzuoli and Vyazovkin<sup>13,14,15,16</sup> have developed new methods based on a numerical integration described below.

These methods are applicable for  $n$  experiments realized with either isothermal or non-isothermal program  $T_i(t)$ . For each  $\alpha$  value,  $E_\alpha$  is determined as the energy value which minimizes the following function:

$$\Phi(E_\alpha) = \sum_{i=1}^n \sum_{j \neq i}^n \frac{J[E_\alpha, T_i(t_\alpha)]}{J[E_\alpha, T_j(t_\alpha)]}$$

Equation 18

With :

$$J[E_\alpha, T_i(t_\alpha)] \equiv \int_{t_{\alpha-\Delta\alpha}}^{t_\alpha} \exp\left[\frac{-E_\alpha}{RT_i(t)}\right] dt$$

Equation 19

The value of  $J$  function described above is calculated by trapezoidal rule. For each value of  $\alpha$  the minimization of  $\Phi(E_\alpha)$  is evaluated, thus the activation energy dependency can be determined on all the conversion process.<sup>17,18,19</sup> The apparent activation energy calculated by this model “free” isoconversional method can be associated to both chemical reactions and physical

transitions such as curing, thermal degradation, crystallization, glass transition or vitrification for instance. This method is particularly interesting and powerful to describe multi-step processes such as cross-linking polymerization, highlighting the preponderant physico-chemical process (*cf.* section II.1.2.) at a defined extent of conversion. The objective is to be able to, *in fine*, associate apparent activation energy variation to a change on the rate limiting step during the polymerization. Indeed, because of the complexity inherent to the polymeric transformations from liquid to solid state classical chromatographic techniques are unfortunately most often not suitable.<sup>9,20,21,8</sup>

Isoconversional methods can be applied to all type of data issue from thermal analysis such as DSC, TGA, DMA or rheometry for instance. Specialized softwares were developed to treat any kind of thermoanalytical data.<sup>22,23</sup> The extent of conversion  $\alpha$  can be calculated as a function of time or temperature  $T$ , and the resulting apparent activation energy  $E_\alpha$  as a function of  $T$  or  $\alpha$ . Notice that each value of  $E_\alpha$  is associated to an average temperature value computed over the  $i$  temperatures used in the calculation. 3-5 temperatures are generally used in isothermal mode or 3-5 heating/cooling rates (or any temperature program) in nonisothermal mode.<sup>24</sup> Thus, for a given  $\alpha$  corresponds an average temperature  $\bar{T}_\alpha$  that makes possible to interpret the activation energy dependency with temperature  $E_\alpha = f(\bar{T}_\alpha)$ .

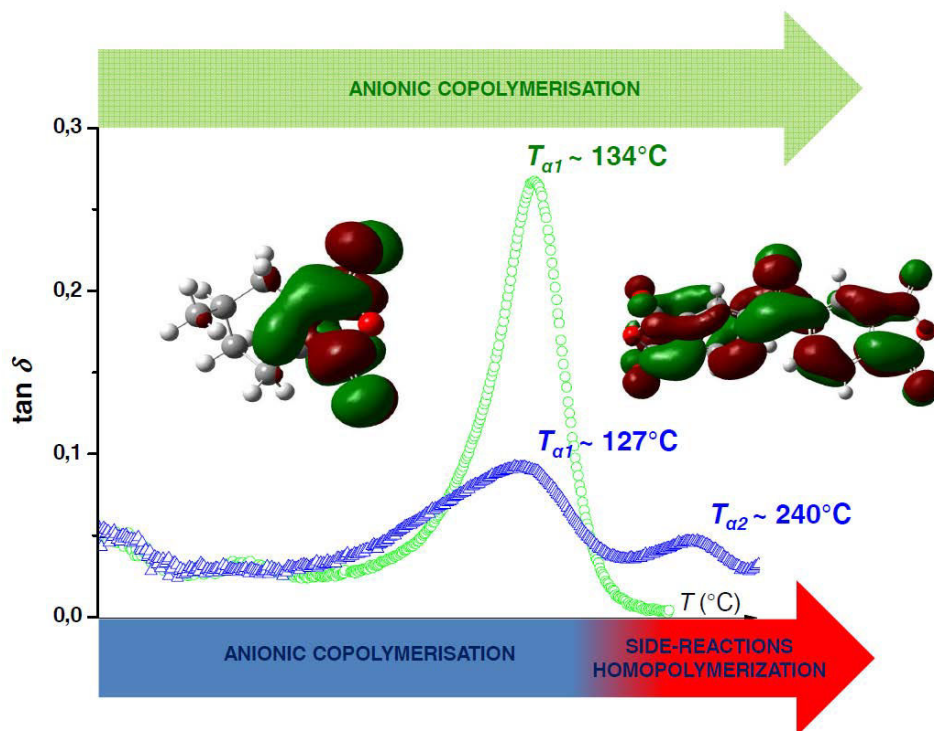
1. Schick, C., Differential scanning calorimetry (DSC) of semicrystalline polymers. *Analytical and bioanalytical chemistry* **2009**, 395 (6), 1589-1611.
2. Watson, E.; O'Neill, M.; Justin, J.; Brenner, N., A Differential Scanning Calorimeter for Quantitative Differential Thermal Analysis. *Analytical Chemistry* **1964**, 36 (7), 1233-1238.
3. Reading, M., Modulated differential scanning calorimetry—a new way forward in materials characterization. *Trends Polym. Sci* **1993**, 1 (8), 248-253.
4. Reading, M.; Luget, A.; Wilson, R., Modulated differential scanning calorimetry. *Thermochimica Acta* **1994**, 238, 295-307.
5. Schawe, J.; Hütter, T.; Heitz, C.; Alig, I.; Lellinger, D., Stochastic temperature modulation: a new technique in temperature-modulated DSC. *Thermochimica Acta* **2006**, 446 (1), 147-155.
6. Fraga, I.; Montserrat, S.; Hutchinson, J. M., TOPEM, a new temperature modulated DSC technique. *Journal of thermal analysis and calorimetry* **2007**, 87 (1), 119-124.
7. Hutchinson, J. M.; Shiravand, F.; Calventus, Y.; Fraga, I., Isothermal and non-isothermal cure of a tri-functional epoxy resin (TGAP): A stochastic TMDSC study. *Thermochimica Acta* **2012**, 529, 14-21.
8. Sbirrazzuoli, N.; Vyazovkin, S.; Mititelu, A.; Sladic, C.; Vincent, L., A Study of Epoxy-Amine Cure Kinetics by Combining Isoconversional Analysis with Temperature Modulated DSC and Dynamic Rheometry. *Macromolecular Chemistry and Physics* **2003**, 204 (15), 1815-1821.
9. Sbirrazzuoli, N.; Girault, Y.; Elégant, L., Simulations for evaluation of kinetic methods in differential scanning calorimetry. Part 3—peak maximum evolution methods and isoconversional methods. *Thermochimica acta* **1997**, 293 (1), 25-37.
10. Friedman, H. L. In *Kinetics of thermal degradation of char-forming plastics from thermogravimetry. Application to a phenolic plastic*, Journal of Polymer Science Part C: Polymer Symposia, Wiley Online Library: 1964; pp 183-195.
11. Ozawa, T., Kinetic analysis of derivative curves in thermal analysis. *Journal of Thermal Analysis and Calorimetry* **1970**, 2 (3), 301-324.
12. Flynn, J. H.; Wall, L. A., A quick, direct method for the determination of activation energy from thermogravimetric data. *Journal of Polymer Science Part B: Polymer Letters* **1966**, 4 (5), 323-328.
13. Sbirrazzuoli, N.; Girault, Y.; Elégant, L., Simulations for evaluation of kinetic methods in differential scanning calorimetry. Part 1. Application to single-peak methods: Freeman-Carroll, Ellerstein, Achar-Brindley-Sharp and multiple linear regression methods. *Thermochimica acta* **1995**, 260, 147-164.
14. Vyazovkin, S., Advanced isoconversional method. *Journal of thermal analysis and calorimetry* **1997**, 49 (3), 1493-1499.
15. Vyazovkin, S.; Sbirrazzuoli, N., Isoconversional method to explore the mechanism and kinetics of multi-step epoxy cures. *Macromolecular rapid communications* **1999**, 20 (7), 387-389.
16. Vyazovkin, S.; Sbirrazzuoli, N., Isoconversional Kinetic Analysis of Thermally Stimulated Processes in Polymers. *Macromolecular Rapid Communications* **2006**, 27 (18), 1515-1532.
17. Sbirrazzuoli, N.; Vincent, L.; Vyazovkin, S., Comparison of several computational procedures for evaluating the kinetics of thermally stimulated condensed phase reactions. *Chemometrics and Intelligent Laboratory Systems* **2000**, 54 (1), 53-60.
18. Sbirrazzuoli, N.; Vyazovkin, S., Learning about epoxy cure mechanisms from isoconversional analysis of DSC data. *Thermochimica Acta* **2002**, 388 (1), 289-298.
19. Sbirrazzuoli, N.; Mititelu-Mija, A.; Vincent, L.; Alzina, C., Isoconversional kinetic analysis of stoichiometric and off-stoichiometric epoxy-amine cures. *Thermochimica acta* **2006**, 447 (2), 167-177.
20. Vyazovkin, S.; Sbirrazzuoli, N., Mechanism and Kinetics of Epoxy-Amine Cure Studied by Differential Scanning Calorimetry. *Macromolecules* **1996**, 29 (6), 1867-1873.
21. Vyazovkin, S.; Sbirrazzuoli, N., Effect of viscosity on the kinetics of initial cure stages. *Macromolecular Chemistry and Physics* **2000**, 201 (2), 199-203.
22. Sbirrazzuoli, N., Is the Friedman method applicable to transformations with temperature dependent reaction heat? *Macromolecular Chemistry and Physics* **2007**, 208 (14), 1592-1597.
23. Sbirrazzuoli, N., Determination of pre-exponential factors and of the mathematical functions  $f(\alpha)$  or  $G(\alpha)$  that describe the reaction mechanism in a model-free way. *Thermochimica Acta* **2013**, 564, 59-69.

### Chapter III: Materials and methods

24. Vyazovkin, S.; Burnham, A. K.; Criado, J. M.; Pérez-Maqueda, L. A.; Popescu, C.; Sbirrazzuoli, N., ICTAC Kinetics Committee recommendations for performing kinetic computations on thermal analysis data. *Thermochimica Acta* **2011**, 520 (1), 1-19.

## Chapter IV

From epoxidized linseed oil to bio-resins: an overall approach of epoxy/anhydride cross-linking



**Keywords:** biorenewable resources, copolymerization, epoxidized vegetal oils, reaction mechanism, structure-properties relationship



<b>IV.1. Epoxidized linseed oil cross-linking</b> .....	<b>98</b>
IV.1.1. Epoxy/anhydride reactivity investigations .....	98
IV.1.1.1. <i>The choice of cross-linker: a good compromise</i> .....	98
IV.1.2. Epoxy/anhydride cross-linking mechanism .....	98
IV.1.2.1. <i>Anionic living copolymerization mechanism</i> .....	99
IV.1.2.2. <i>Homopolymerization and etherification as side reactions of cross-linking</i> .....	100
<b>IV.2. Investigation of ELO/anhydride reactivity</b> .....	<b>100</b>
IV.2.1. Formulation of ELO/anhydride resins .....	100
IV.2.1.1. <i>Materials and systems presentation for a comparative study</i> .....	100
IV.2.1.2. <i>Elaboration of formulations: functionalities, ratios and curing</i> .....	101
IV.2.2. Investigation on epoxy/anhydride cross-linking by DSC.....	102
IV.2.3. Investigation by FT-IR on evolution of the structure during crosslinking .....	105
<b>IV.3. Physico-chemical aspects of cross-linking</b> .....	<b>108</b>
IV.3.1. Heat capacity evolution during cross-linking: a TOPEM study .....	108
IV.3.2. Chemorheological analysis and kinetic studies .....	109
<b>IV.4 Thermo-mechanical characterisations and structure-properties relationship</b> .....	<b>112</b>
IV.4.1. Glass and sub-glass transitions studies by dynamic mechanical analysis .....	112
IV.4.2. Thermogravimetric analysis (TGA) .....	116
<b>IV.5. Conclusions</b> .....	<b>117</b>

## **IV. From epoxidized linseed oil to bio-resins: an overall approach of epoxy/anhydride cross-linking**

### **IV.1. Epoxidized linseed oil cross-linking**

This work proposes an overall approach to elaborate biobased thermosets by deep correlations between the choice of copolymerization monomers (renewable sources, structure, reactivity) with the control of thermokinetic aspects of polymerization in order to obtain maximal conversions even during physical transitions such as gelation or vitrification. Then, this study aims to correlate the evolution of reactive functions with the viscoelastic properties during network formation until gelled or vitrified solid state, through a comparative study of epoxy/anhydride network.

#### **IV.1.1. Epoxy/anhydride reactivity investigations**

The final properties of epoxy thermoset networks depend on the nature and functionality of epoxy monomers and of their comonomers or curing agents. ELO is a very interesting monomer because of its low volatility, high resistance to solvents and low migration tendency.<sup>1</sup>

##### *IV.1.1.1. The choice of cross-linker: a good compromise*

To cure epoxies, amines and carboxylic acid anhydrides are the most commonly used hardeners. Comparing to epoxy/amines networks, epoxy/anhydride products have higher glass transition temperatures, low shrinkages and stresses. In this work we propose the analysis of triglyceride based epoxy/anhydrides systems as possible candidates to develop new formulations with optimized elaboration cycles through a global approach structures vs. properties. A first objective consisted in the selection of principal requirements applied to the curing agents. With the aim to avoid very toxic hardeners we have used anhydrides, which are less toxic than amines and which release cyanhydric acid by thermal decomposition. Also, the curing agents have to be compatible with the structure of ELO in terms of functionality, miscibility and melting point. Therefore, the chemical and structural aspects of ELO/hardener reagents generating the three dimensional matrix were rationalized with the purpose to design a more stable, compacted architecture with reinforced chains interactions. The hardener functionality was varied in order to study its influence on reactivity and on final properties.

#### **IV.1.2. Epoxy/anhydride cross-linking mechanism**

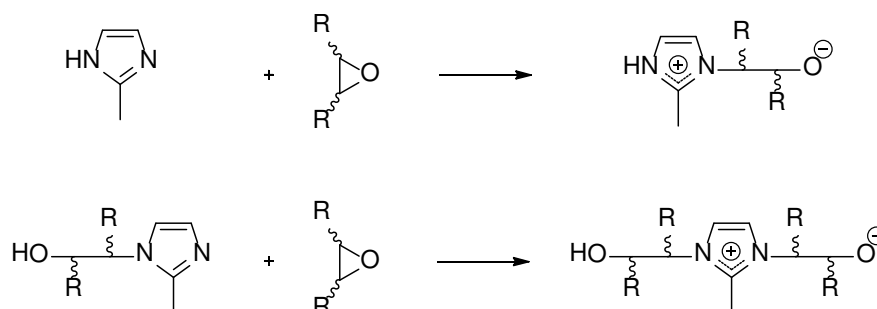
Transformation of low molecular weight molecules into polymers is based on chemical interactions (cross-linking) between epoxy functions and hardening agents. Secondary reactions such as homopolymerization thermally or catalytically induced are to be considered. Acidic anhydrides are ones of the most employed epoxy curing agents.

#### IV.1.2.1. Anionic living copolymerization mechanism

Acid anhydrides are industrially employed as epoxy hardeners, in combination with an initiator. In these reactions both the epoxide and the anhydride ring are difunctional. Strong Lewis bases like tertiary amines or imidazoles are used as initiators for the anhydride/epoxy reactions. The 2-methylimidazole (2MI) Lewis base conducts to best cured networks in epoxy/fatty diacid systems, in comparison with 1-methyl imidazole, triethylamine, 1,8-diazabicyclo [5.4.0]undec-7-ene (DBU) or dimethylaminopyridine.<sup>2</sup>

The acid anhydride/epoxy reaction progresses via a chain-wise polymerization,<sup>3,4</sup> in comparison to the stepwise scenery of the amine/epoxy crosslinking (**Figure IV.37**).

#### 1/ Initiation



#### 2/ Anionic propagation

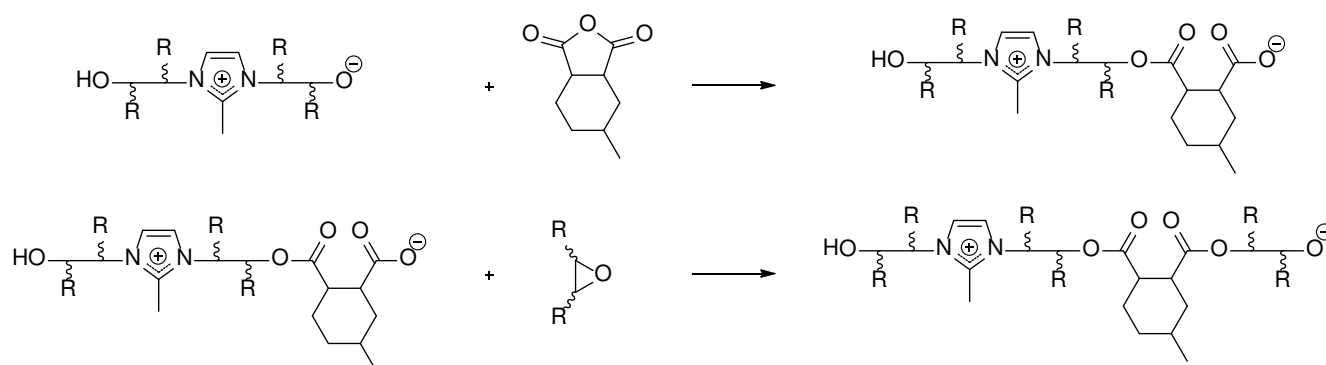


**Figure IV.37.** Mechanism of epoxy/anhydride reactions initiated by 2-methylimidazole

The 2MI initiates the reaction by opening the epoxy ring and generating a hydroxylated adduct.<sup>5</sup> This adduct gives the particularity and the force of initiation since, compared with the DGEBA,

in ELO/anhydride systems lack the -OH groups which initiate the opening of oxiranes ring. Then, a zwitterion is formed which contains a quaternary nitrogen cation and an active oxyanion. Besides, the formed oxyanion attacks quickly an anhydride ring. A new active site appears: a carboxylate anion, ester considered to be the initiator of the chain-wise polymerization. Propagation occurs through a strictly alternating copolymerization anionic mechanism according to Dusek et al.,<sup>6</sup> as shown in Figure 2. The amount of Lewis base initiator determines the number of active sites. These initiating species react with epoxy rings, leading to alkoxide species, which again attacks the cyclic anhydride. The strictly alternating copolymerization forming polyesters has been confirmed by several studies.<sup>7</sup>

#### IV.1.2.2. Homopolymerization and etherification as side reactions of cross-linking

As illustrated in **Figure IV.38**, side-reactions, as homopolymerization and etherification have also to be considered in presence of imidazole initiator, at high temperatures. Attention must be paid to the living character of the epoxy/anhydride copolymerization, very sensible to the impurities. The literature<sup>8,9</sup> proposes possible mechanisms of termination or chain transfer, also with reactions involving the regeneration of tertiary amine. The latter can initiate new chains.

#### Side reactions:

-Homopolymerization



-Etherification

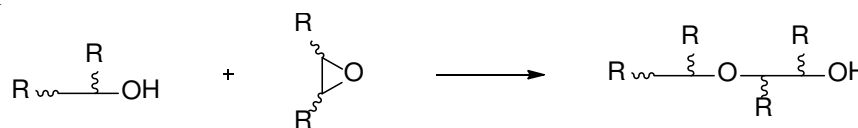


**Figure IV.38.** Side-reactions occurring during curing in excess of epoxy

## IV.2. Investigation of ELO/anhydride reactivity

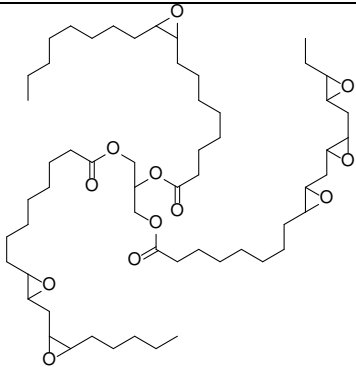
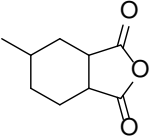
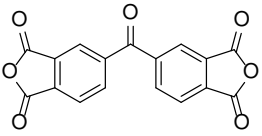
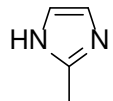
### IV.2.1. Formulation of ELO/anhydride resins

#### IV.2.1.1. Materials and systems presentation for a comparative study

A commercially available biobased epoxy molecule was obtained from Akcros Chemicals Ltd. It is an epoxidized linseed oil (ELO) which is a viscous-liquid at room temperature having a

viscosity of about 1200 mPa.s. ELO has a molecular weight of about 980 g.mol<sup>-1</sup> and contains about 5.5 epoxy groups, on average, per triglyceride. Methyl hexahydrophthalic anhydride (MHHPA) was selected for its reactivity, for being one of the most common anhydride used in industry, for the fact that it is liquid and miscible with ELO at room temperature and for its short chain rigid structure. Benzophenone 3, 3', 4, 4'-tetracarboxylic dianhydride (BTDA) has been chosen because it can lead to thermosets with high thermal and mechanical properties. Both anhydrides have 96% purity, being obtained from Sigma-Aldrich. The activation of epoxy/anhydride reaction was produced using 2-methylimidazole (2MI) as initiator, with 99% purity, also supplied from Sigma-Aldrich. Formula of all reagents and their characteristics are summarized in **Table IV.5**.

**Table IV.5.** Structural formula and characteristics of reactants

Name	Chemical Formula	Molar mass (g.mol <sup>-1</sup> )	Melting point (°C)	Functionality
Epoxidized linseed oil (ELO)		950	-	Matrix <b>5.5</b>
Methylhexahydrophthalic anhydride (MHHPA)		168.19	-	Hardener <b>2</b>
Benzophenone-3, 3', 4, 4'-tetracarboxylic dianhydride (BTDA)		322.23	220	Hardener <b>4</b>
2-Methylimidazole (2MI)		82.1	142	Initiator

#### IV.2.1.2. Elaboration of formulations: functionalities, ratios and curing

As seen in **section II.1.1.2**, epoxy and anhydride groups are bifunctional<sup>10</sup> considering the

anionic copolymerization reactivity reported by Matejka et al.<sup>3</sup> and Leukel et al.<sup>4</sup> To prepare epoxy/anhydride reaction mixtures the stoichiometric ratio R can be defined as:

$$R = \text{epoxy groups} / \text{anhydride groups}$$

Formulations were done considering  $R = 1/0.8$  and also  $1/0.5$ , so in epoxy excess in accord with the literature.<sup>11,12</sup> A default of anhydride was required considering that copolymerization cannot be complete because of the steric hindrance and of the high increase in viscosity. Finally, ratios of  $1/0.8$  for ELO/MHHPA and  $1/0.5$  for ELO/BTDA systems were chosen. The epoxy/dianhydride ratio has been determined by mixtures processability, and also by the early gelation during the polymerization.<sup>12</sup> In order to obtain homogeneous mixtures, curing samples were prepared by adding the hardener agent to ELO previously melted to  $100^{\circ}\text{C}$ . 2MI finely crushed grounded was introduced as initiator to this initial mixture, at 0.9% in weight, at room temperature. To highlight the importance of the side-reactions in ELO/BTDA system, two kinds of networks have been prepared: ELO/BTDA1 (crosslinking considering in majority the copolymerization temperature interval) and ELO/BTDA2 (post-cure reactions which suppose homopolymerization and etherification).

Thermosets were obtained by applying a curing and post-curing temperature program, according to the following thermal analysis. Reactions have been conducted during 2h at  $120^{\circ}\text{C}$  then 2h at  $160^{\circ}\text{C}$  for MHHPA and BTDA1, followed by a post-curing during 2h at  $180^{\circ}\text{C}$  for MHHPA and for 1h at  $230^{\circ}\text{C}$  for BTDA2. The infinite glass transition temperatures ( $T_{g,\infty}$ ) of these materials were determined by DMA measurements. The DSC heating of the cured samples did not show any residual heat release.

#### IV.2.2. Investigation on epoxy/anhydride cross-linking by DSC

DSC was applied to study the thermodynamic and kinetic aspects of the epoxy/anhydride polymerization. This technique offers rich information concerning thermal events accompanying epoxy thermo-curing. **Figure IV.39** shows the evolution of heat flow in function of temperature through the polymerization of ELO with the mono- and di-anhydride, at different heating rates. As seen in this figure, mainly exothermal events are present, and were attributed to sign of epoxy/anhydride reactions.

The principal mechanism is an alternating co-polyesterification by the reaction of an epoxy group with an anhydride group. Moreover the polyesterifications are accompanied at high temperatures by homopolymerization and etherification, which are known to be promoted in the

case of an anhydride default. However, it is not possible to fully separate from this DSC data the two reactions that are concomitants, especially at high temperature.

In **Figure IV.39** it can be seen that the thermoanalytical curves have distinct shapes for each ELO/anhydride system. In the case of ELO/MHHPA, heat flow follows a single exothermal peak, corresponding to the epoxy/anhydride copolymerization.

A different, more complex, behavior emerges for the curing of ELO/BTDA: two exothermal peaks succeed. The first event occurs in the same range of temperature as the ELO/monoanhydride reaction and has a higher enthalpy of reaction than that of the second peak (

**Table IV.6**). This event corresponds mainly to the alternating epoxy/anhydride copolymerization.

At higher temperatures, side reactions such as homopolymerizations or etherifications are favoured for systems with an excess of epoxy. Thus, the second exotherm mainly results from side reactions implying the epoxy groups in presence of imidazole initiator and in default of anhydride.

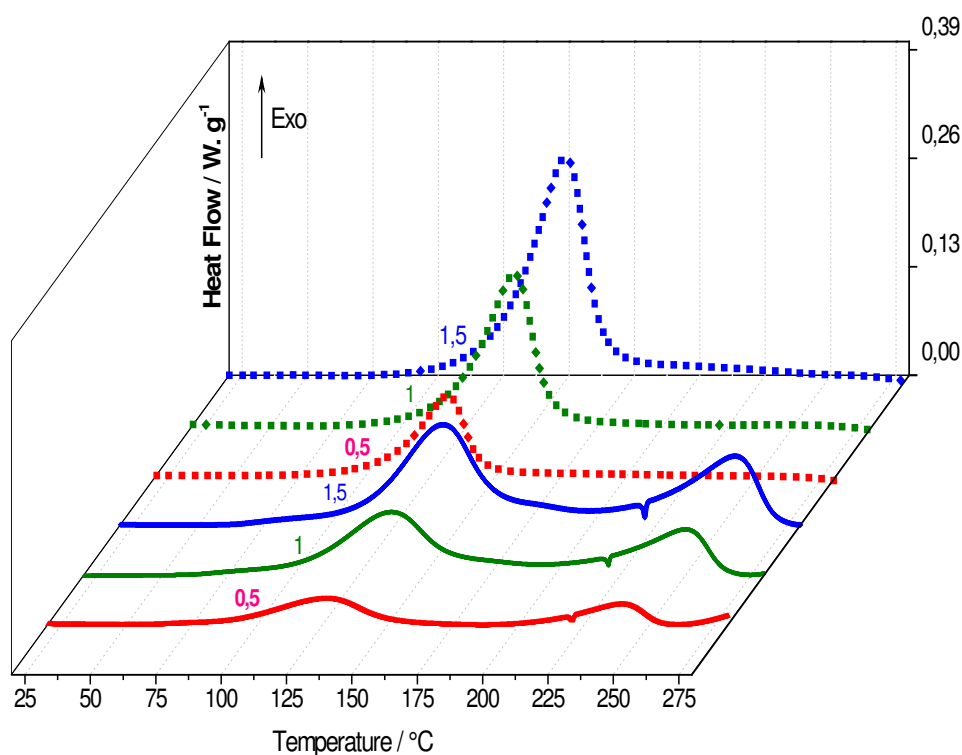


**Figure IV.39.** Dynamic DSC thermoanalytical curves showing the heat release during reactions of ELO/MHHPA (dotted lines) and ELO/BTDA (solid lines). The heating rate of the experiments (in  $^{\circ}\text{C}\cdot\text{min}^{-1}$ ) is indicated on each curve

**Table IV.6.** Reaction enthalpy ( $\Delta_r H$ ), temperature interval of reaction and peak maximum temperature ( $T_{peak}$ ) as a function of heating rate (for ELO/MHHPA and ELO/BTDA curing systems)

	$\beta /$ $^{\circ}\text{C}\cdot\text{min}^{-1}$	$\Delta_r H /$ $\text{J}\cdot\text{g}^{-1}$		$T_{peak} / ^{\circ}\text{C}$ and reaction interval	
		1 <sup>st</sup> peak	2 <sup>nd</sup> peak	1 <sup>st</sup> peak	2 <sup>nd</sup> peak
MHHPA	0.5	$297 \pm 4$	-	$131 \pm 1$ (62-213)	-
	1	$293 \pm 4$	-	$143 \pm 1$ (69-220)	-
	1.5	$301 \pm 4$	-	$149 \pm 1$ (74-229)	-
BTDA	0.5	$163 \pm 2$	$84 \pm 1$	$127 \pm 1$ (47-187)	$239 \pm 1$ (192-260)
	1	$163 \pm 2$	$91 \pm 1$	$137 \pm 1$ (54-195)	$250 \pm 1$ (198-273)
	1.5	$163 \pm 2$	$95 \pm 1$	$143 \pm 1$ (61-201)	$255 \pm 1$ (202-280)

As observed in **Figure IV.39** and in

**Table IV.6** the thermokinetic parameters of cure are very different when ELO react with MHHPA or with BTDA. Besides, we can notice the presence of two exotherms during curing, the first one occurring at lower temperature demonstrating a lower reaction enthalpy for ELO/BTDA (about  $163 \text{ J}\cdot\text{g}^{-1}$ ) than for ELO/MHHPA (about  $293 \text{ J}\cdot\text{g}^{-1}$ ). It is important to notice that this value remains the same whatever the heating rate is. The small endothermic peak at about  $221^{\circ}\text{C}$  is attributed to the melting of a small amount of solid BTDA that still remains in the mixture (always presents, even at lower ratio of 0.4 or 0.3 in dianhydride).

To investigate the second ELO/BTDA exotherm, TGA analysis has been performed (**Figure IV.47**). The results show that thermal degradation starts to become significant at  $T \sim 280^{\circ}\text{C}$  which is much higher than the temperature of the end of the second DSC exothermic peak observed in **Figure IV.39** for ELO/BTDA system. This indicates that the second DSC peak is not linked to

thermal degradation. To confirm this hypothesis, DSC thermograms of ELO/MHHPA/2MI with a ratio of 0.5 in MHHPA and 0.9% in weight of 2MI were realized and illustrated in **Figure IV.40**.

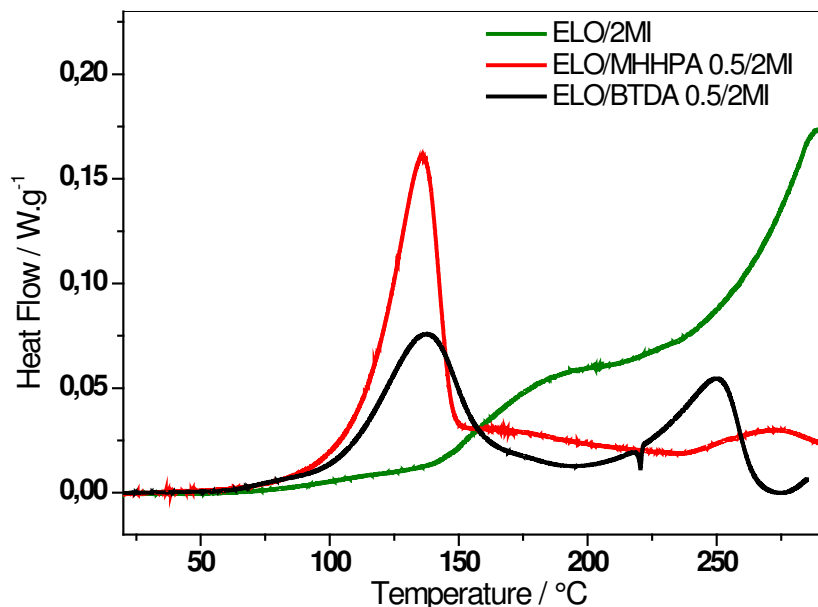


**Figure IV.40.** DSC thermograms at  $1^{\circ}\text{C}\cdot\text{min}^{-1}$ .

Two major thermal events are observed for this system at around 135 and 270°C. A measurement was also performed with the neat resin (ELO) and catalyst (2MI) alone without hardener. Two thermal events appear in this case in the same temperature range at around 170°C and 270°C in the thermogram of ELO/2MI.

These results are in good agreement with a previous study on epoxy/amine systems where it was shown that etherifications start to play an important role above 220-230°C.<sup>13</sup> These results confirm the hypothesis of side-reactions occurring at high temperature for ELO/MHHPA and for ELO/BTDA systems.

### IV.2.3. Investigation by FT-IR on evolution of the structure during crosslinking

A comparative structural study by FT-IR spectroscopy between initial monomers, their resin mixtures and the corresponding cured thermosets is presented in **Figure IV.41**. Infrared analyses reveal significant structural changes during crosslinking.

Characteristic of ELO structure is the absorption of ether peak due to internal oxiran rings at  $818\text{ cm}^{-1}$  which decrease in thermoset spectrum. A strong carbonyl stretch of triglyceride esters at  $1732\text{ cm}^{-1}$  exhibits a gradual increase in intensity and shifts to lower frequencies at  $1728\text{ cm}^{-1}$  for ELO/MHHPA thermoset. New peaks appear at  $1160\text{ cm}^{-1}$  usually associated with ester, respectively with C=O and C–O stretching vibrations from ester moieties provided by copolymerizations.

The ELO/MHHPA (**Figure IV.41 (a)**) resin mixture exhibits intense axial deformation carbonyl C=O bands of MHHPA anhydride function at  $1860$  and  $1780\text{ cm}^{-1}$ . After crosslinking, in the spectrum of ELO/MHHPA cured thermoset these bands disappear completely, sign of consumption of anhydride MHHPA functions.

Also, for ELO/MHHPA cured thermosets a broad band develops in intensity in interval  $3200\text{--}3600\text{ cm}^{-1}$  assigned with formation of –OH functions from carboxylic acid of inherent dangling mono-acid chains.

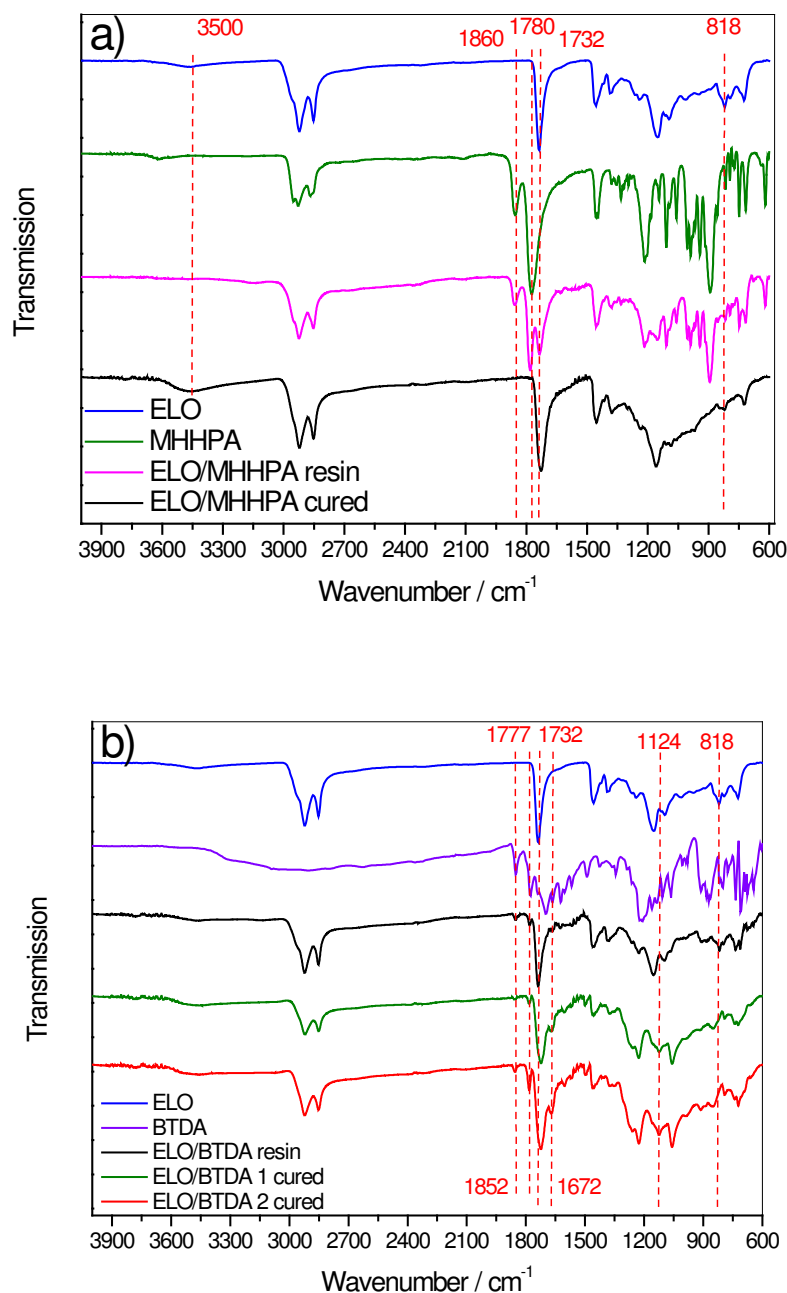


**Figure IV.41.** FT-IR spectra of (a) ELO/MHHPA system and (b) ELO/BTDA systems

Proofs of evolution of structure in the ELO/BTDA system during copolymerization and complementary side-reactions are given in spectra of **Figure IV.41 (b)**. BTDA spectrum presents characteristic carbonyl vibrations bands at  $1852\text{ cm}^{-1}$  and  $1777\text{ cm}^{-1}$  associated to the C=O of cyclic anhydride stretching vibration. The peak at  $1700\text{ cm}^{-1}$  could correspond to the carbonyl stretch of the di-aromatic ketone. The peaks series around  $1600\text{ cm}^{-1}$  and  $1500\text{ cm}^{-1}$  are generally attributed to the benzoic C=C stretch and the C–O stretch of anhydride moieties at  $1225\text{ cm}^{-1}$ . FT-IR spectrum of ELO/BTDA1 cured resin shows the same profile as ELO/MHHPA thermoset: the ester characteristic peak at  $1732\text{ cm}^{-1}$  due to the copolymer

polyester network. The decrease of the peak of oxiran ring stretch at  $818\text{ cm}^{-1}$  confirms also the consumption of epoxy functions during ELO/BTDA copolymerization.

**Figure IV.41 (b)** shows that ELO/BTDA1 and ELO/BTDA2 spectra are very similar, but some apparitions or variations of peaks intensity could be highlighted. The presence of C=O anhydride vibrations at  $1852\text{ cm}^{-1}$  and  $1777\text{ cm}^{-1}$  in the spectrum of ELO/BTDA2 cured thermoset could be assigned with the reformation of some anhydride groups since both mentioned specific carbonyl stretch anhydrides are present.

New absorptions peaks at  $1672\text{ cm}^{-1}$  and  $1124\text{ cm}^{-1}$  appear in the ELO/BTDA1 and ELO/BTDA2 spectra, which is not present on ELO or BTDA spectra. It could correspond respectively to the stretch of some carboxylic acid and to the C—O stretching of aliphatic ether, generated by side-reactions, which is always concomitant with copolymerization. The increase of aliphatic ether vibration at  $1124\text{ cm}^{-1}$  in ELO/BTDA2 spectrum, corroborated with the decrease of oxiran peak at  $818\text{ cm}^{-1}$  could be a proof of occurrence of interepoxy side-reactions during the second heating.

### IV.3. Physico-chemical aspects of cross-linking

A proper knowledge of all phenomena occurring during crosslinking is essential for the processing of thermosets. The increase of the molecular weight of the polymer with conversion provokes important evolution of viscosity, from a liquid to a solid state. Physical phenomena like gelation and vitrification contribute to the increase in viscosity to a high degree. The consequences are dramatic for the resulting material because all these transformations (especially vitrification) could block the ultimate conversions. The identification of these physical transitions is of great importance (**section II.1.2.**), because, at this stage, the reaction generally changes from a kinetically to a diffusion controlled regime.<sup>14</sup>

#### IV.3.1. Heat capacity evolution during cross-linking: a TOPEM study

In addition to regular DSC investigations, the reactions of ELO with the two anhydrides were studied by stochastically temperature modulated DSC (TOPEM<sup>®</sup>). The evaluation was made on the heat flow response to this modulation. TOPEM<sup>®</sup> technique gives access to the reversing and non-reversing components of the heat flow over the temperature modulation. For curing of thermosets, these components can generally be associated with reversible and non-reversible thermal events, such as vitrification and polymerization reaction. Stochastically modulated DSC

data allows getting information at different frequencies in a single experiment. Then, it is the sole DSC technique that makes possible to get quasi-static heat capacity  $C_{p0}$  variation during cure. Examination of **Figure IV.42 (a)** shows that vitrification of ELO/MHHPA can be identified by a decrease on the  $C_{p0}$  curve near 145°C.<sup>15</sup> During vitrification the molecular mobility of the chains decreases, the network matrix becoming more compact which results in a  $C_p$  decrease. When the reacting system is continuously heated, chemical reactions can be progressively reactivated because the curing temperature becomes higher than the vitrification temperature of the system. Thus at 160°C the  $C_{p0}$  value starts to re-increase and devitrification can be estimated to occur near 180°C.

For the ELO/BTDA system in **Figure IV.42 (b)**, the vitrification appears close to the maximum of the reaction rate as a smaller sigmoidal variation of  $C_{p0}$  at about 135°C. When the system vitrifies, the reaction rate drops dramatically. This suggests that at this stage the reaction is mainly controlled by the diffusion of polymer chains. At about 220°C an abrupt change in  $C_{p0}$  is observed, in form of a first order transition. This sharp peak of heat capacity can be attributed to a melting of some unreacted BTDA, which confirms the assessment previously drawn with conventional DSC. Another thermal event is observed at ~256°C appearing by a sigmoidal increase of  $C_{p0}$  that could be attributed to the devitrification.

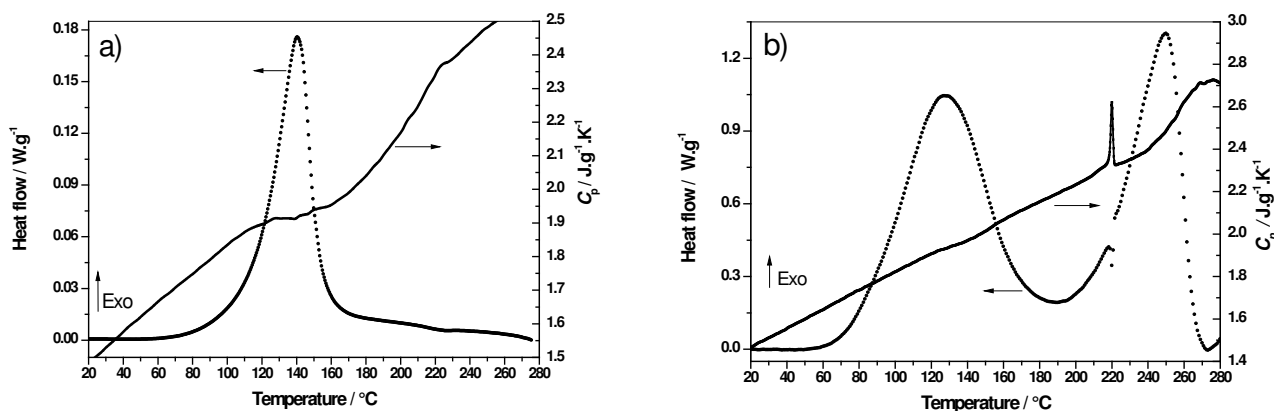


**Figure IV.42.** Deconvoluted TOPEM<sup>®</sup> thermograms: total heat flow (dotted line) and  $C_{p0}$  (solid line) during dynamic curing of (a) ELO/MHHPA and (b) ELO/BTDA systems

### IV.3.2. Chemorheological analysis and kinetic studies

Chemorheological studies permit also to identify the physical phenomena that accompany network formation, i.e. gelation and vitrification. To obtain an overview of the overall reticulation process, thermokinetic studies are combined with rheometric data. Kinetic calculations were performed by using an advanced isoconversional method applied to the DSC non-isothermal data, already presented **section III.1.**

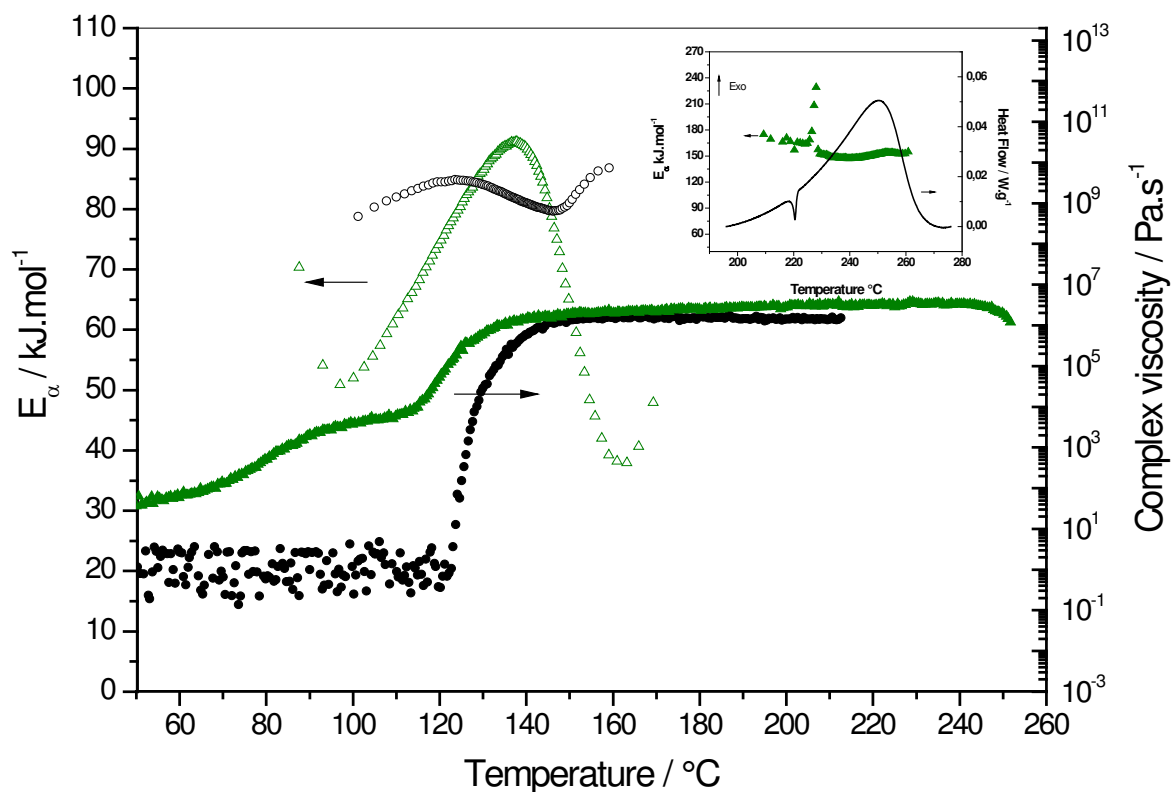


**Figure IV.43.** Evolution of  $E_a$  and complex viscosity with temperature by rheological data during dynamic cure of ELO/MHHPA (black symbols) and ELO/BTDA (green symbols) systems. In insert: DSC data for ELO/BTDA scanning at  $1^\circ\text{C}\cdot\text{min}^{-1}$  and evolution of  $E_a$  vs temperature

In **Figure IV.43** are represented the associated results of the kinetic calculations and of the rheometric data to describe the evolution of the apparent activation energy and complex viscosity during ELO/anhydrides reticulations.

It is not surprising to observe a complex evolution of apparent activation energy ( $E_a$ ) vs. temperature for both systems under curing, which can be interpreted as the existence of multi-step kinetics (mechanisms). Four stages describe the state of mixture during ELO/MHHPA curing. In the first stage (25-120°C) the mixture is in a liquid state with an initial low viscosity of about  $1\text{Pa}\cdot\text{s}^{-1}$ . This stage may correspond to the formation of active species which will initiate the copolymerization, in agreement with **Figure IV.37**; it is also correlated with the beginning of copolymerization propagation. During this stage the molar mass of epoxy-anhydride copolyester increases, as a consequence viscosity of media reaches  $\sim 12.5\text{Pa}\cdot\text{s}^{-1}$ .

The second stage (120-140°C) corresponds to the gelation, at about 123°C, when  $E_a$  increases up to  $85\text{kJ}\cdot\text{mol}^{-1}$ . Then  $E_a$  decreases in the gelled state, due to the transition from a chemical control to a diffusion control (movement of long chains), in agreement with previous work obtained for

epoxy-amine cure.<sup>13,14</sup>

At higher conversion (140-150°C), the increase of viscosity retards or inhibits the chemical reactions attributed to a restricted molecular mobility.  $E_a$  reaches a value of about 80 kJ.mol<sup>-1</sup> associated with the vitrification at 147°C observed by a plateau of viscosity. This value is also in good agreement with TOPEM<sup>®</sup> results that show the presence of a sigmoidal variation of  $C_{p0}$  near 145°C. In the latter stage (>150°C), due to heating, chemical reactions start again, mainly the homopolymerizations at high temperature and degree of conversions. In this stage  $E_a$  increases slightly from 80 to 87 kJ.mol<sup>-1</sup>. Indeed, for this system the side-reactions occur between chains situated in near proximity. This explains that the energetic barrier is low, in comparison with the values generally found for homopolymerizations or etherifications.<sup>16</sup>

In comparison, the ELO/BTDA system shows a higher viscosity. BTDA is a solid product, so the mixture has an initial viscosity, around 40 Pa. s<sup>-1</sup> until the reaction reaches 60°C. In the 60-90°C temperature interval the zwitterion species being formed start the copolymerization reactions;  $E_a$  decreases to from ~70 to 51 kJ.mol<sup>-1</sup>. Then, while the temperature increases from 90 to 115°C a continuous increase of viscosity and of apparent activation energy  $E_a$  is observed. This stage can be associated with the alternating copolymerization which produces a slightly increase of the viscosity during heating to 100°C (**Figure IV.43**). At this temperature a small plateau is reached with a viscosity about 3.7 kPa.s<sup>-1</sup>.

In the next stage (115-140°C) the gelation phenomena occurs at about 117°C and finally the gelled state is reached with a viscosity of about 9.7 kPa.s<sup>-1</sup>. At about 140°C is reached the maximum of  $E_a$  at about 91 kJ.mol<sup>-1</sup>, in good connection with the maximum of reaction rate (curve not presented here).

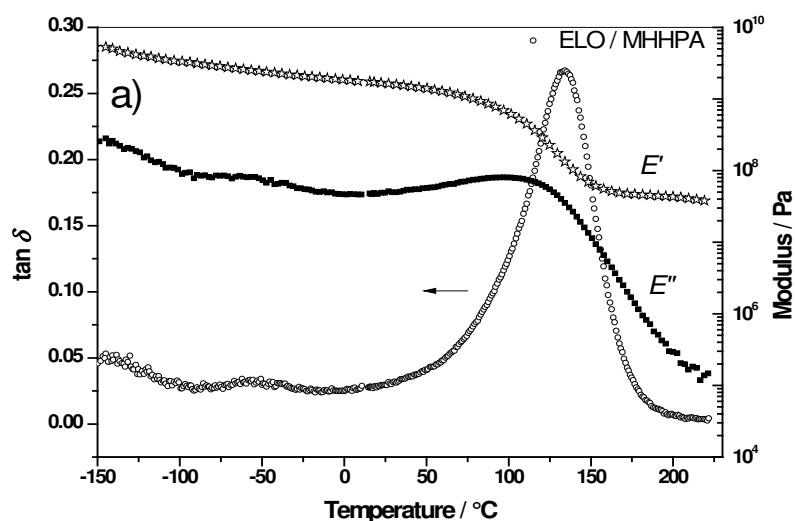
In the temperature interval 140-160°C a dramatic decrease of  $E_a$  occurs, from 91 to 38 kJ.mol<sup>-1</sup> due to the vitrification of the system (that appears in TOPEM<sup>®</sup> at about 135°C). The overall reaction rate decreases sharply; in the same interval viscosity reaches a plateau. Then, between 200 to 220°C chemical reactions restart (insert in **Figure IV.43**:  $E_a \sim 170$  kJ.mol<sup>-1</sup>) probably after a first devitrification near 160°C. In agreement with TOPEM<sup>®</sup> results, the activation energy dependency shows a very sharp increase of  $E_a$  at 220°C corresponding to the melting of still unreacted BTDA. In the temperature range between 200 and 275°C,  $E_a$  is quite constant to about ≈150 kJ.mol<sup>-1</sup>. This high  $E_a$  value is generally associated with side-reaction as homopolymerization.<sup>13</sup> In this temperature range, we observe a constant increase of complex viscosity from 2.5 to 3.5 MPa.s<sup>-1</sup>. Then, the viscosity starts to decrease near 250°C, in good agreement with TOPEM<sup>®</sup> exploitation that show a  $C_{p0}$  decrease at 256°C that was attributed to a possible devitrification of the material.

#### IV.4. Thermo-mechanical characterisations and structure-properties relationship

Molecular dynamics in polymers are characterized by localized and cooperative chains motions that are reflected in DMA analysis by  $\alpha$ ,  $\beta$  or  $\gamma$  relaxations in the order of decreasing temperature. A consequence of these relaxations is the viscoelastic behavior, the material showing properties between an elastic solid and a viscous liquid. Depending on its structure and temperature some events can occur during mechanical sollicitation like energy dissipation and mechanical transitions.

##### IV.4.1. Glass and sub-glass transitions studies by dynamic mechanical analysis

Few data are reported about the thermo-mechanical properties of biobased thermosets and fewer on ELO based thermosets.<sup>11</sup> An example of the DMA curves obtained over the interval temperature range -150 to 300°C is given in **Figure IV.44** and the main parameters are listed in **Table IV.7**.



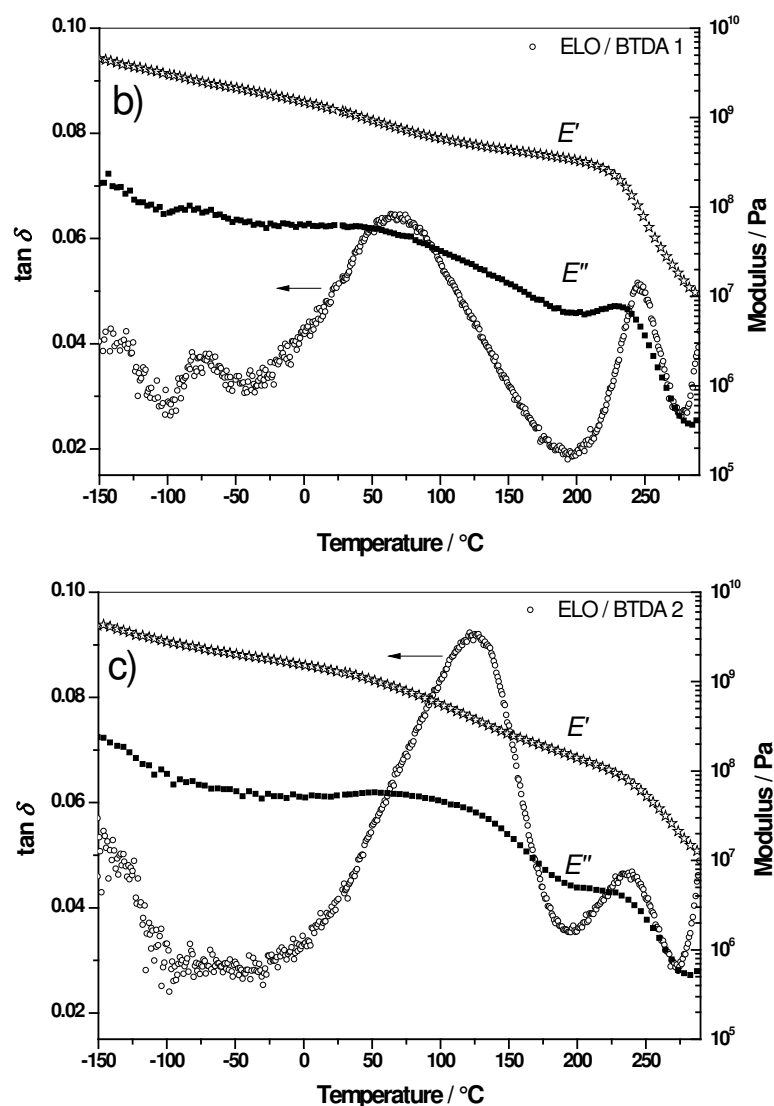


**Figure IV.44.** DMA plot for ELO/MHHPA (a), ELO/BTDA1 (b) and ELO/BTDA2 (c) systems from -150 to 230°C and 280°C respectively, at 1°C min<sup>-1</sup> and 1 Hz; o = loss factor (tan  $\delta$ ), \* = storage modulus ( $E'$ ), ■ loss modulus ( $E''$ )

**Table IV.7.** Values of tan  $\delta$  and temperatures of sub-glass transitions for ELO/MHHPA, ELO/BTDA1 and ELO/BTDA2 cured systems

	$T_{\gamma}/$ °C	$T_{\beta}/$ °C	$T_{\alpha}/$ °C	Peak height tan $\delta_{\max}$	$T_{\alpha'}$ /°C
ELO / MHHPA	-140	-50	134	0.27	-
ELO / BTDA 1	-140	-75	68	0.03	245
ELO / BTDA 2	-140	-75	127	0.01	240

The values of maximum of  $\tan \delta$  for all systems are assigned to the  $\alpha$  relaxation ( $T_\alpha$ ) phenomenon related to cooperative chain motions and associated with the macroscopic  $T_g$ .

By comparing the two anhydride systems, the ELO/MHHPA network shows a more symmetric Gaussian  $\tan \delta$  peak with a maximum centered at around 134°C ( $T_\alpha$ ). The ELO/MHHPA gaussian shape of  $\tan \delta$  peak is an indication of homogeneous distribution of relaxation times in polymers motions. The fact that this system has higher amplitude of damping, i.e. higher peak height ( $\tan \delta_{\max}$ ) could be a proof of the ease of chain motions; MHHPA acts as a sort of plasticizer between triglyceride chains to increase the energy dissipation by internal frictions. In consequence, the impact strength increases because of better dissipation of vibrational energy during impact.

In the case of ELO/BTDA1 system (partial crosslinked networks, reactions stopped after the first DSC peak) is important to note that homopolymerisation (intra-epoxy network still unfinished at this stage) occurs during the DMA heating experiment (**Figure IV.44**), leading to a decrease of the distance between the triglycerides of the network. Two  $\alpha$  relaxations appear around 68°C ( $T_\alpha$ ) and 245°C ( $T_{\alpha'}$ ). A possible explanation of this behaviour could be the creation of a two phase copolymer due to a change in solubility of polymerization mixture during crosslinking. Similar with the core-shell systems, the network could contain two kinds of phase: a flexible, rubbery one belonging to triglyceride chains (improving the free space allocated to the chains movement) and a rigid one from BTDA anhydride inter-connections clusters.

DMA results of ELO/BTDA2 tend to confirm this hypothesis, also two  $\alpha$  relaxations could be observed if the curing was completed by a high stage reaction (i.e. for ELO/BTDA2 system):  $T_\alpha \sim 127^\circ\text{C}$  and  $T_{\alpha'} \sim 240^\circ\text{C}$  in Table 2.

It seems that the post-cure of the system ELO/BTDA enhances the  $T_\alpha$  values from 68 to 127°C, this increase being attributed to side-reactions that mainly occur during this post-cure stage. That means the formation of a reinforced network by epoxies inter-connections characterized also by high modulus values in the rubbery region. This could be explained by a very dense architecture due to a higher crosslink density also with the segregation between rigid phase and rubbery network.

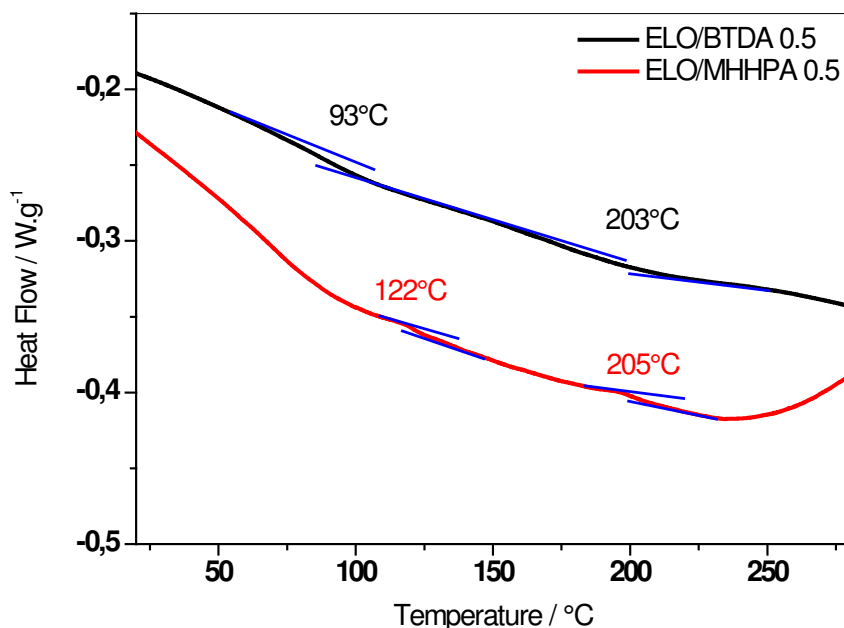


**Figure IV.45.** DSC thermograms at  $10^{\circ}\text{C}\cdot\text{min}^{-1}$  of ELO/MHHPA 1/0.5 and ELO/BTDA 1/0.5 (curing protocols: ELO/BTDA : 2h at  $120^{\circ}\text{C}$ , 2h at  $160^{\circ}\text{C}$  and 1h at  $230^{\circ}\text{C}$ ; ELO/MHHPA : 2h at  $120^{\circ}\text{C}$ , 2h at  $160^{\circ}\text{C}$  and 1h at  $230^{\circ}\text{C}$ )

This assertion is corroborated with the comparison between  $T_g$  measured by DSC for ELO/MHHPA 0.5, which also shows the existence of two glass transitions at around  $122^{\circ}\text{C}$  and  $205^{\circ}\text{C}$  (illustrated in **Figure IV.45**). An explanation of this result could be that the out of stoichiometry (epoxy excess) could favoured a phase separation. The higher  $T_g$  values obtained in the ELO/MHHPA system, relative to the ELO/BDTA system, could be explained by the cyclic structure of MHHPA, which contains a substituent methyl group that can inhibit the rotational movements and result in a higher  $T_g$  value.

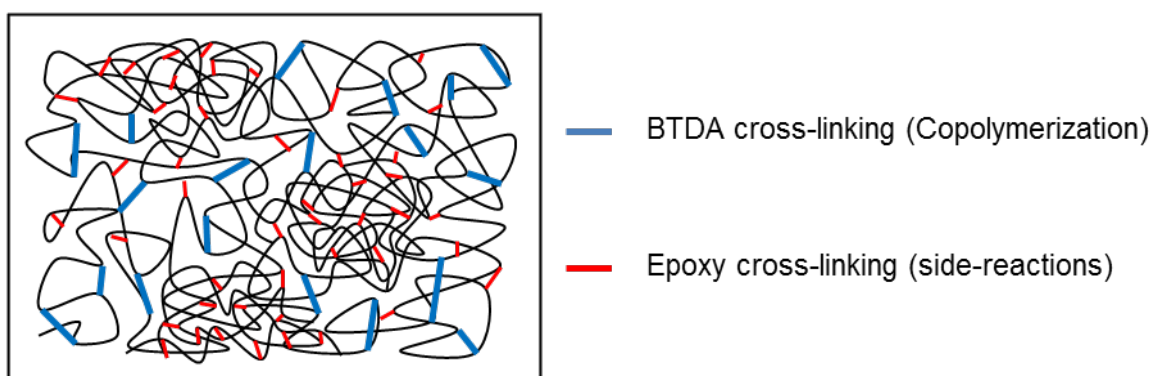


**Figure IV.46.** Schematic view of ELO/BTDA 2 proposed architecture

At temperatures below  $T_a$ , mechanical behavior from sub-glassy state to the glassy region is compared. As seen in **Figure IV.44** and reported in **Table IV.7**, obtained thermosets are characterized by two secondary transitions in the glassy state (sub-glass transitions):  $\beta$  and  $\gamma$

relaxations. In the glassy state, the physical behavior depends on cohesion and local molecular mobility. These relaxations appear due to residual segmental mobility at temperature below  $T_g$ . The localized motions related to these secondary transitions involve rotation, chair-chair isomerization in cycloaliphatic rings or crankshaft motions of short chains segments. The  $\beta$  relaxations can be correlated to fracture properties. Two categories of polymers can be described in function of position of  $T_\beta$  value reported to ambient temperature. Polymers with  $T_\beta$  values above ambient temperature are characterized by low intensity  $\beta$  dissipation peak, being more brittle. The second category is correlated to polymers with  $T_\beta$  below the ambient temperature. This is the case of polymers with relatively low moduli ( $< 3$  GPa) that can display a ductile or semiductile behavior.<sup>17</sup> In these networks  $\beta$  relaxations are highly active. ELO/anhydrides form networks of the second category,  $\beta$  relaxations being depicted by a dissipation peak due to the crankshaft motions of the branching diester segment  $-\text{CH}_2-\text{CH}(\text{R})-\text{O}-\text{CH}(\text{R})-\text{O}-$ . It is particularly clear with the intensity of  $\beta$  relaxations for ELO/BDTA1 and ELO/BDTA2. In ELO/BDTA1, numerous triglyceride chains did not react, ergo the network was not totally cross-linked and the aliphatic chains had greater degrees of freedom, and thus, intense  $\beta$  relaxations. On the other hand, the  $\beta$  relaxation was very weak for the full cured network on ELO/BDTA2.

#### IV.4.2. Thermogravimetric analysis (TGA)

Thermogravimetric analyses were carried out to measure the thermal stability of full cured materials under inert ( $\text{N}_2$ ) or oxidant (air) flows. Thermosets thermal degradations involve complex chemical or thermo-oxidative mechanisms.<sup>18</sup> In spite of a great number of works regarding the study of the epoxy/amine systems, literature data on epoxy/anhydride thermosets is relatively reduced.

Generally, the thermal stability of DGEBA/amines cured systems are around 300-370°C under air, being slightly superior under nitrogen. TG curves of proposed cured systems are reported in **Figure IV.47**. The temperature of degradation was considered at 10% of the weight loss,  $T_{10\%}$ . These thermograms curves reveal a high thermal stability of ELO/MHHPA and ELO/BDTA systems, under air and nitrogen. The degradation process is quite complex, with two or three stages of degradations which starts above temperatures of 333-337°C, superior to the degradation temperature of DGEBA/anhydride networks. The first degradation step shows a same shape in air and nitrogen atmosphere, and it is currently associated with the network degradation by scission of ester links. This result indicates that at this stage occur non-oxidative degradation reactions of thermolysis.

Under oxidative conditions, three successive steps of degradation process occur for both

systems, more evident for system containing dianhydride. This degradation behavior could be attributed to decomposition of BTDA aromatic moieties that occurs at high temperature (590°C). This phenomenon was previously observed when aromatic anhydride has been used as curing agent.<sup>19</sup>

For the thermogravimetric analysis conducted under non-oxidative atmosphere (N<sub>2</sub>) **Figure IV.47** shows that ELO/MHHPA and ELO/BTDA networks have different weight-loss behaviors. The ELO/MHHPA networks decompose integrally, maybe due to a less thermoresistant cycloaliphatic MHHPA structure. In contrast, a residual weight of about 20% is observed in the case of ELO/BTDA decomposition. So the degradation process produces less organic volatiles in comparison with ELO/MHHPA that degrades completely. This behavior of ELO/BTDA network could be correlated with a more homogenous structure, also with the presence of increased thermal stability of aromatic moieties of BTDA structure. This observation is in good agreement with high  $T_{\alpha}$  temperatures of ELO/BTDA networks. However, to obtain a scenario of thermal scissions of networks, a deeper study of mechanism of degradation is needed.

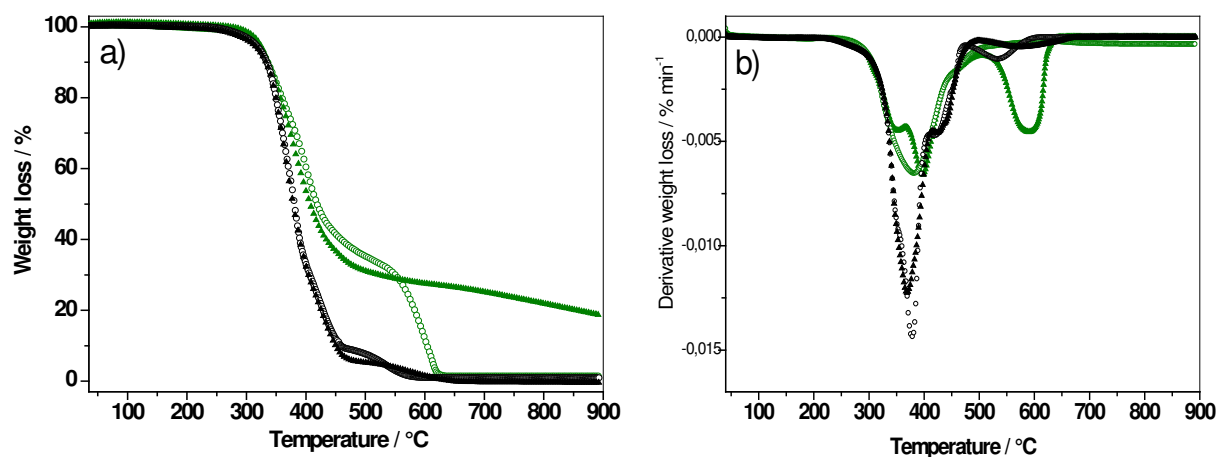


**Figure IV.47.** Thermogravimetric analysis of ELO/MHHPA (black symbols) and ELO/BTDA (green symbols) systems at 10 °C min<sup>-1</sup> under N<sub>2</sub> (triangles) or air (circles) flows: relative weight loss (a) and derivative weight loss (b)

## IV.5. Conclusions

The epoxy/acid anhydrides curing systems are widely used in electronic applications as circuit boards, encapsulating material for integrated circuits, or insulators in power current components. This study brings some insights into vegetable oil based epoxy/anhydrides networks as excellent biosourced alternatives to elaborate green thermosets. In the selected ELO/anhydride thermosets the bio-renewable ratio was increased by over 60 % for ELO/MHHPA to 70% for ELO/BTDA systems. A deeper insight in the cure mechanism of ELO/anhydride reactions has been gained. The relationships between structure and properties of these emergent materials have been

highlighted. Firstly, the cure behavior is very different when the ELO is reacted with MHHPA or with BTDA. The DSC thermoanalytical curves show the presence of a single reaction exotherm for ELO/MHHPA systems, at about 150°C. In comparison, ELO/BTDA presents a supplementary exotherm, at about 250°C which could correspond to the completion of side-reactions of polyetherification (homopolymerization). These results have been corroborated with TOPEM<sup>®</sup> and chemorheological analysis to quest more understanding by thermodynamic-viscoelastic properties correlation. As the reaction become diffusion controlled at vitrification, the crosslinking process must be conduct at  $T > T_{g\infty}$  ( $T_g$  of the completely cured network).

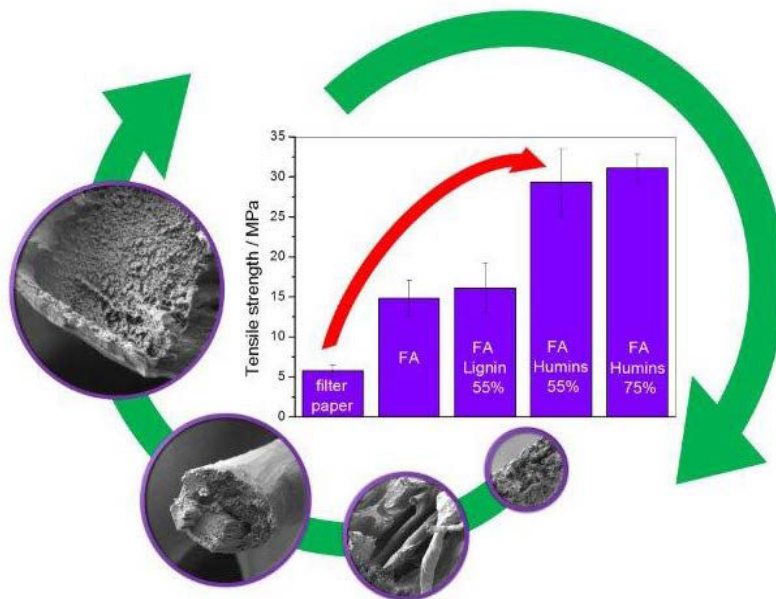
Concerning physico-chemical characteristics, the DMA measurements revealed important results that meant semi ductile networks with good impact strength were achieved. It seemed that phase separation occurred during crosslinking conduct to form a toughened network. Depending on the type of anhydride hardener and the curing program (i.e. considering or not side-reactions of polyetherification), different behaviors have been observed. Therefore, the  $\beta$  relaxations occur at negative temperatures ( $\sim -75^\circ\text{C}$  and  $-50^\circ\text{C}$ , respectively) that is an important indication about the resistance of these materials to fracture dissipation. The obtained results translate a semi-ductile behaviour, very important property because one of the most embarrassing defects of epoxides is their brittleness. Then,  $\alpha$  relaxation is active on a large range of temperatures for the two networks. This relaxation appears at about  $\sim 134^\circ\text{C}$  for ELO/MHHPA network but ELO/BTDA manifests two  $\alpha$  relaxations: about around  $\sim 127^\circ\text{C}$  and  $\sim 240^\circ\text{C}$ , respectively. This difference between  $\alpha$  relaxations behavior of networks developed with mono- or di-anhydride could be a consequence of the stiffness and toughness of connections in the vicinity of crosslinking bridges. A comparison of the materials obtained after anionic copolymerization without side-reactions (i.e. using low cure temperature), lead to the conclusion that the crosslinking density is increased when BTDA hardener is used instead of MHHPA. This is consistent with the results of dynamic mechanical testing (higher  $T_{\alpha'}$  value) and should correspond to a decrease of macromolecular mobility. This decrease could be associated with an increase of other structural properties as for example the thermal stability. Thermogravimetric studies revealed high temperatures of degradations under air or nitrogen, at about 340°C. Correlated with other thermo-mechanical properties this reflects a good thermal stability of backbone structures for both ELO/MHHPA and ELO/BTDA networks.

1. Fenollar, O.; Garcia-Sanoguera, D.; Sanchez-Nacher, L.; Lopez, J.; Balart, R., Effect of the epoxidized linseed oil concentration as natural plasticizer in vinyl plastisols. *J Mater Sci* **2010**, *45* (16), 4406-4413.
2. Supanchaiyamat, N.; Shuttleworth, P. S.; Hunt, A. J.; Clark, J. H.; Matharu, A. S., Thermosetting resin based on epoxidised linseed oil and bio-derived crosslinker. *Green Chemistry* **2012**, *14* (6), 1759.
3. Matějka, L.; Lövy, J.; Pokorný, S.; Bouchal, K.; Dušek, K., Curing epoxy resins with anhydrides. Model reactions and reaction mechanism. *Journal of Polymer Science: Polymer Chemistry Edition* **1983**, *21* (10), 2873-2885.
4. Leukel, J.; Burchard, W.; Krüger, R.-P.; Much, H.; Schulz, G., Mechanism of the anionic copolymerization of anhydride-cured epoxies – analyzed by matrix-assisted laser desorption ionization time-of-flight mass spectrometry (MALDI-TOF-MS). *Macromolecular Rapid Communications* **1996**, *17* (5), 359-366.
5. Ham, Y. R.; Kim, S. H.; Shin, Y. J.; Lee, D. H.; Yang, M.; Min, J. H.; Shin, J. S., A comparison of some imidazoles in the curing of epoxy resin. *Journal of Industrial and Engineering Chemistry* **2010**, *16* (4), 556-559.
6. Dušek, K.; Luňák, S.; Matějka, L., Gelation in the curing of epoxy resins with anhydrides. *Polymer Bulletin* **1982**, *7* (2-3), 145-152.
7. Mauri, A.; Galego, N.; Riccardi, C.; Williams, R., Kinetic model for gelation in the diepoxide-cyclic anhydride copolymerization initiated by tertiary amines. *Macromolecules* **1997**, *30* (6), 1616-1620.
8. Steinmann, B., Investigations on the curing of epoxides with phthalic anhydride. *Journal of applied polymer science* **1990**, *39* (9), 2005-2026.
9. Trappe, V.; Burchard, W.; Steinmann, B., Anhydride-cured epoxies via chain reaction. 1. The phenyl glycidyl ether/phthalic acid anhydride system. *Macromolecules* **1991**, *24* (17), 4738-4744.
10. Galy, J.; Sabra, A.; Pascault, J. P., Characterization of epoxy thermosetting systems by differential scanning calorimetry. *Polymer Engineering & Science* **1986**, *26* (21), 1514-1523.
11. Boquillon, N.; Fringant, C., Polymer networks derived from curing of epoxidised linseed oil: influence of different catalysts and anhydride hardeners. *Polymer* **2000**, *41* (24), 8603-8613.
12. Barie Jr, W. P.; Franke, N. W., High-Temperature Epoxy Resins Based on 3, 3', 4, 4'-Benzophenonetetracarboxylic Dianhydride (BTDA). *Industrial & Engineering Chemistry Product Research and Development* **1969**, *8* (1), 72-76.
13. Sbirrazzuoli, N.; Mititelu-Mija, A.; Vincent, L.; Alzina, C., Isoconversional kinetic analysis of stoichiometric and off-stoichiometric epoxy-amine cures. *Thermochimica acta* **2006**, *447* (2), 167-177.
14. Vyazovkin, S.; Sbirrazzuoli, N., Mechanism and Kinetics of Epoxy–Amine Cure Studied by Differential Scanning Calorimetry. *Macromolecules* **1996**, *29* (6), 1867-1873.
15. Hutchinson, J. M.; Shiravand, F.; Calventus, Y.; Fraga, I., Isothermal and non-isothermal cure of a tri-functional epoxy resin (TGAP): A stochastic TMDSC study. *Thermochimica Acta* **2012**, *529*, 14-21.
16. Sbirrazzuoli, N.; Vyazovkin, S.; Mititelu, A.; Sladic, C.; Vincent, L., A Study of Epoxy-Amine Cure Kinetics by Combining Isoconversional Analysis with Temperature Modulated DSC and Dynamic Rheometry. *Macromolecular Chemistry and Physics* **2003**, *204* (15), 1815-1821.
17. Pascault, J.-P.; Sautereau, H.; Verdu, J.; Williams, R. J., *Thermosetting polymers*. CRC Press: 2002; Vol. 64.
18. Vincent, L.; Mija, A.; Sbirrazzuoli, N., Liquid crystalline and isotropic epoxy thermosets: Mechanism and kinetics of non-isothermal degradation. *Polymer Degradation and Stability* **2007**, *92* (11), 2051-2057.
19. Jain, R.; Choudhary, V.; Narula, A. K., Curing and thermal behaviour of epoxy resin in the presence of pyromellitic dianhydride and imidazole. *Journal of Applied Polymer Science* **2007**, *106* (4), 2593-2598.



## Chapter V

Valorization of bio-refinery side-stream products:  
combination of humins with polyfurfuryl alcohol for  
composites elaboration



**Keywords:** bio-refinery, humins, polyfurfuryl alcohol, composites, mechanical properties



<b>V.1. Humins and furfuryl alcohol: the design of a furanic architecture .....</b>	<b>124</b>
V.1.1. From humins structure to green furanic strategy.....	124
V.1.2. Lignin organosolv as heterogeneous macromolecules of reference.....	125
<b>V.2. Resin formulation, composite elaboration and processability.....</b>	<b>126</b>
V.2.1. Materials.....	126
V.2.2. Humins/FA reactivity investigation by DSC.....	127
V.2.3. Elaboration of humins/FA cellulosic composite .....	128
V.2.4. Optimization parameters for resin and composite elaboration.....	129
V.2.4.1. <i>Effect of the pre-curing temperature</i> .....	129
V.2.4.2. <i>1 step vs 2 steps strategy</i> .....	130
V.2.4.3. <i>Importance of resin viscosity for impregnation</i> .....	131
<b>V.3. Structural characterization by FT-IR .....</b>	<b>132</b>
<b>V.4. Multi-comparative mechanical and morphological studies of cellulosic composite ...</b>	<b>136</b>
V.4.1. Mechanical characterization .....	136
V.4.2. Morphological characterization.....	138
<b>V.5. An opening toward industry.....</b>	<b>140</b>
V.5.1. Reduction of polymerization temperature .....	140
V.5.2. Application fields .....	141
<b>V.6. Conclusions .....</b>	<b>142</b>

## **V. Valorization of bio-refinery side-stream products: combination of humins with polyfurfuryl alcohol for composites elaboration**

### **V.1. Humins and furfuryl alcohol: the design of a furanic architecture**

#### V.1.1. From humins structure to green furanic strategy

This study proposes new applications domains for humins and aims to develop for the first time bio-based polymeric materials from which substantial parts are made on these recalcitrant by-products. Van Zandvoort proposed that humins have mainly an aromatic character consisting of essentially furanic moieties.<sup>1</sup> Intrinsically, this would suggest a good compatibility and peculiar chemical affinity with furanic compounds such as furfuryl alcohol. We therefore studied the inclusion of humins as macro-monomer into a polyfurfurylalcohol network as a good strategy to generate homogeneous and efficient materials. In this case, humins addition into a polyfuranic formulation can also reduce the resin cost price.

The furfuryl alcohol (FA) is indirectly issued from lignocellulosic biomass conversion via hydrogenation of furfural, and its production has largely increased since the last 20 years.<sup>2</sup> As depicted in **Figure V.48**, this furfural derivative has a high tendency to polymerize under acidic condition leading to the PolyFurfuryl Alcohol (PFA). This polymerization proceeds via a complex mechanism which can be mostly discriminated in two steps.<sup>3,4</sup> The first one corresponds to acid-induced polycondensation leading to the formation of linear furanic oligomers. Then, tridimensional amorphous networks are generated subsequently by cross-linking both via Mickael addition and Diels-Alder cycloadditions as illustrated in **section II.2.2.2**.<sup>5,6</sup> Indeed the phenomenon of reticulation includes an important transition on the physical state of the reaction medium: from a liquid to a viscoelastic solid.<sup>7</sup>

The PFA bio-based thermosetting resin is largely used in some applications such as foundry resins, composites, but also for wood adhesives<sup>8</sup> and impregnation, in particular, with its strong efficiency in term of biological degradation resistance.<sup>9</sup> The major drawback of the PFA network is its high brittleness so modification of thermomechanical properties are important issues that need to be addressed.

Combination with bio-based compounds modifies advantageously the PFA thermomechanical behavior such as introduction of triglyceride flexible moieties (**Chapter VI**).<sup>10</sup> Moreover, it has

been proven that the PFA can interact with heterogeneous macromolecular compounds such as tannin<sup>11</sup> or lignins<sup>12,13</sup> which are also well-known biorefinery by-products.<sup>14</sup>

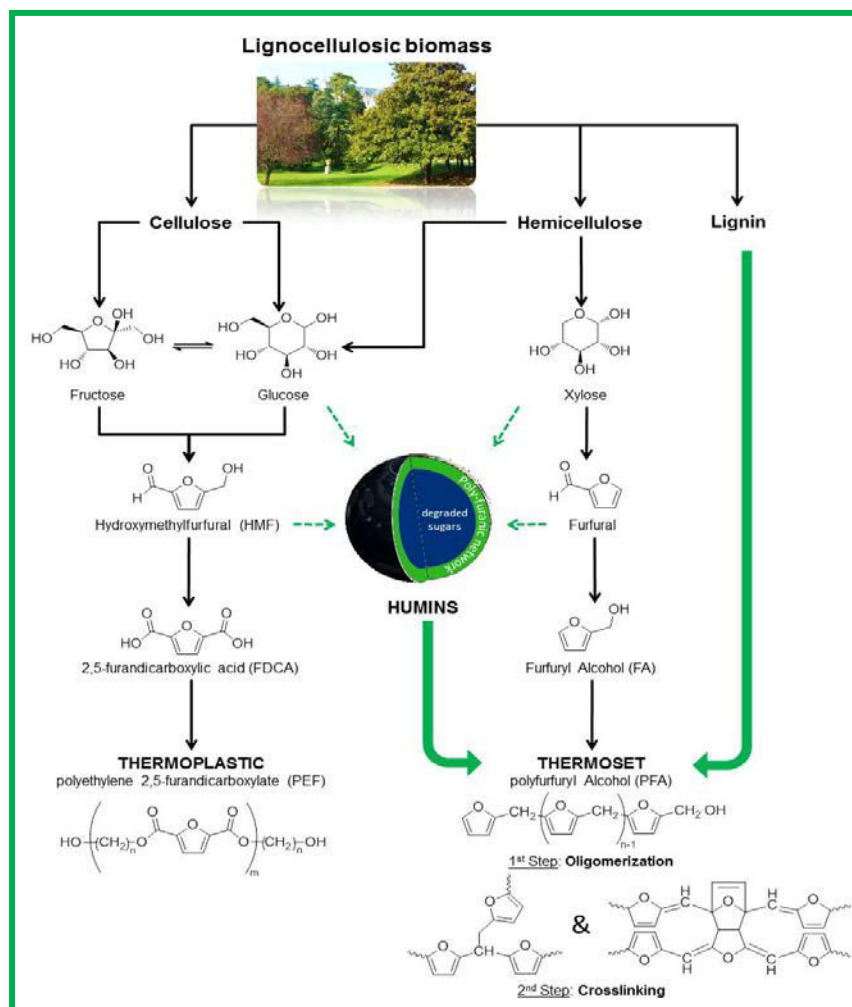


**Figure V.48.** Representative scheme of biorefinery key molecules for furanic based polymer

According to the above mentioned features, the polyfurfuryl alcohol (PFA) was logically chosen for being combined with humins for three main reasons: (i) the PFA is a bio-based polyfuranic so combination with humins leads to fully bio-based furanic resins, (ii) The PFA network develops under acid-induced polycondensation which is also one of the postulated routes for the humins growth<sup>15,16</sup>, (iii) regarding composite applications, introduction of humins into the dense cross-linked PFA network could modify the thermomechanical properties.

### V.1.2. Lignin organosolv as heterogeneous macromolecules of reference

As specified in **section II.2.2.1**, the native lignin is strongly linked to cellulose and hemicellulose, which will explain the drastic solutions proposed to selectively isolate it.

Historically, the main feedstock of isolated lignin was associated to side-stream product issued from the pulp of paper industry. However, the growing interest and development of biofuels allow lignin to be recovered from bio-refinery processes.<sup>17</sup> The principal raw material in papermaking industry is the chemical pulp obtained by the digestion of wood chips under various conditions of pH. This process has the particularity to remove lignin without degradation of polysaccharides, which is an important issue considering the necessity to preserve the hydrogen bondings between fibres, restricting the swelling and making them stiff, in order to produce high quality white paper.<sup>18</sup>

As depicted in **Figure V.49**, the entire chemical pulping method can be divided into two processes: sulphur, and sulphur-free.<sup>19</sup> Herein, organosolv process presents the double advantages to produce lignin without utilization of sulphur compounds. The resulting organosolv pulp has comparable properties in regard to alkaline Kraft pulp issued from a sulphur process. The organosolv technology consists in the treatment of wood chips under heat and pressure with liquor containing water and an organic solvent. The organic solvent is used as vector to promote plant tissues impregnation in order to release acetyl groups present on hemicellulose accompanied to the formation of acetic acid. These soft acidic conditions are enough to allow delignification and partial hemicellulose hydrolysis.<sup>20,21</sup> However, an addition of formic or acetic acid can improve the delignification process.<sup>22</sup>

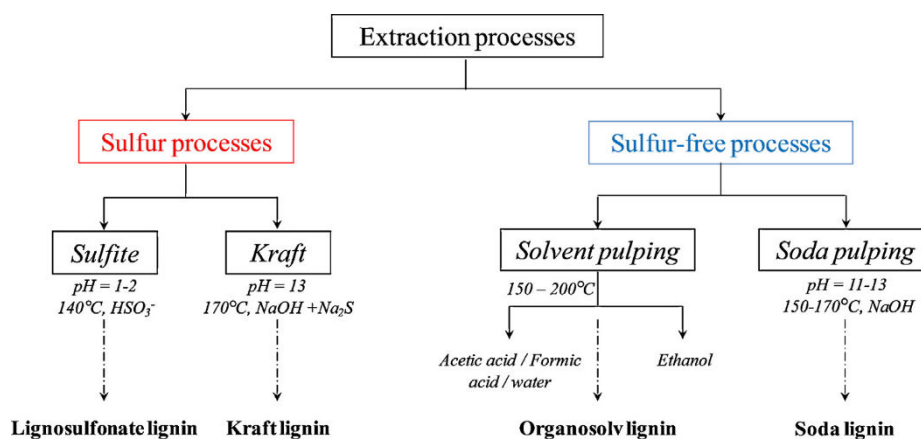


**Figure V.49.** Different extraction processes to separate lignin from lignocellulosic biomass.<sup>19</sup>

## V.2. Resin formulation, composite elaboration and processability

### V.2.1. Materials

Furfuryl alcohol (FA) (purity:  $\geq 98\%$ ) as monomer and maleic anhydride (MA) (purity:  $\geq 99\%$ ) as polymerization catalyst, were purchased from Sigma-Aldrich and were used as received. Humins are directly produced by Avantium Chemicals at their Pilot Plant in Geleen, the Netherlands, by conversion of fructose in methanol. These humins were distilled under high vacuum to reach low 5-hydroxymethylfurfural (HMF) and 5-methoxymethylfurfural (MMF) content ( $< 5\%$  by weight). The humins composition obtained by elemental analysis is approximately of 60 wt% C, 32 wt% O and 5 wt% H being in good correlation with other reported values.<sup>1,23</sup> Their heating value is around 23 MJ/kg. Humins have the appearance of very viscous, shiny black bitumen. Organosolv Lignin was provided by ECN.<sup>24</sup> A precise description of this lignin can be found in de Wild et al. paper.<sup>25</sup> The brown solid was finely crushed and passed through a sieve in order to have a good dispersion into the FA monomer. PFA/humins/cellulose and also PFA/lignin/cellulose composites were made with filter papers Whatman 40 having a diameter of 110 mm and a weight of 900 mg.

### V.2.2. Humins/FA reactivity investigation by DSC

On the basis of DSC investigations, introduction of viscous condensed humins into the FA/MA system decreases the overall reactivity and shift the polycondensation peak to a higher temperature compared to the pure FA/MA mixtures. The thermograms of **Figure V.50** show an exothermic event at 135°C for 40/55H/5, while the 40/58/2 formulation doesn't show any major event at this temperature but at a higher one. This result explains the necessity of a higher catalyst amount. For the sake of comparison the exothermic peak of PFA cross-linking is exhibited in the insert of **Figure V.50**.

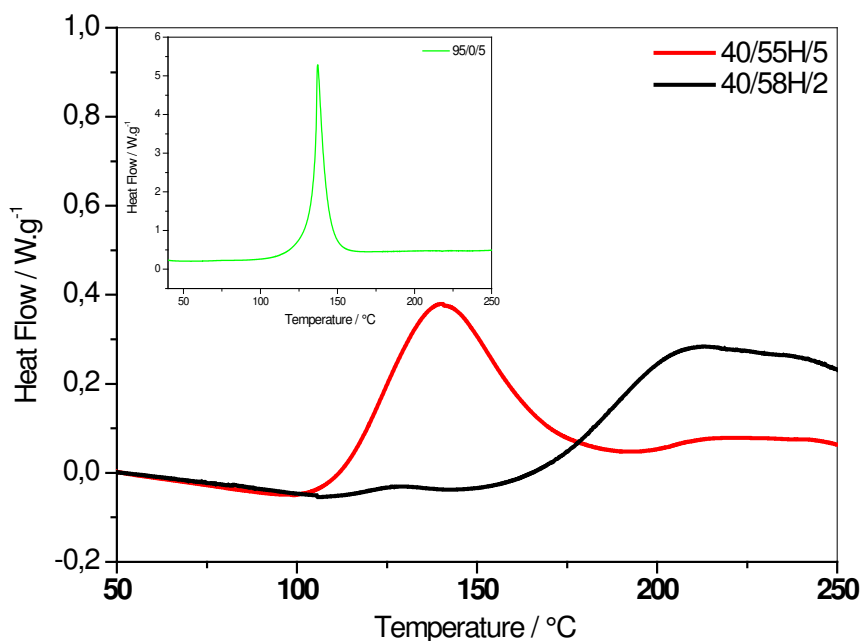


**Figure V.50.** DSC thermograms of reactivity studies for the two FA/Humins/MA formulations, and for the pure PFA (in insert).

### V.2.3. Elaboration of humins/FA cellulosic composite

Cellulose filter papers were impregnated with the different above-mentioned thermosetting resins, in order to achieve a 1:1 weight ratio between cellulose reinforcement and the cured thermosetting resin. In each case, the resin was spread homogeneously on the surface of cellulose filter. Then, these impregnated filters were protected by two sheets of kapton films and placed between two aluminium blocks to ensure uniform repartition of the resin during the curing. The system was placed into a ventilated oven and was cured at 160°C during 3 hours. This curing protocol was elaborated in good agreement with DSC investigation previously presented to reach a maximal conversion. All the process is described in **Figure V.51**.

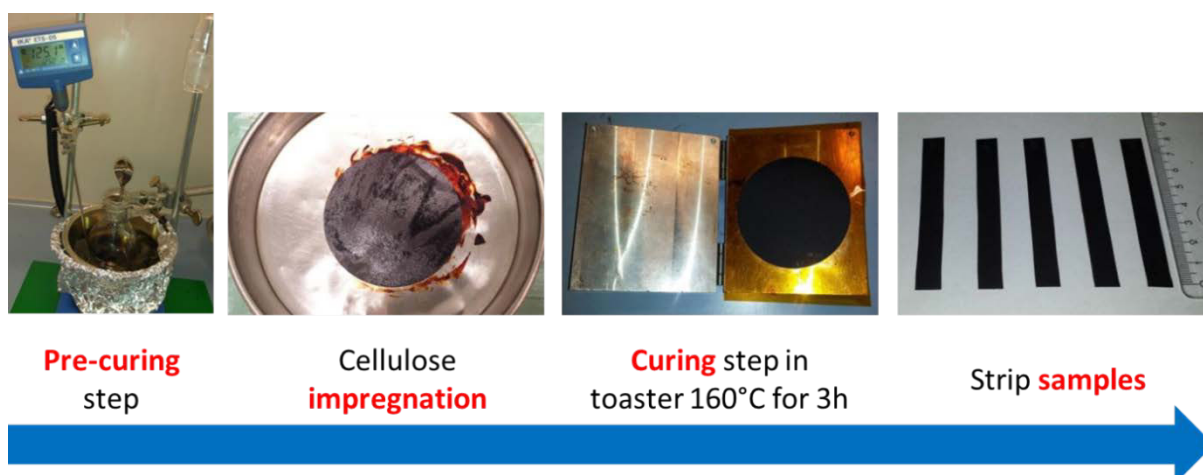


**Figure V.51.** Composite elaboration protocol

#### V.2.4. Optimization parameters for resin and composite elaboration

The optimization of parameters has been investigated for a representative medium ratio of 40/55H/5.

##### V.2.4.1. Effect of the pre-curing temperature

A first optimization has been investigated on the resin pre-curing. Firstly a mixture of humins (55% by weight) and FA (40% by weight) was heated at 105°C during 20 min in order to obtain a homogeneous black mixture. Then, the maleic anhydride (MA) (5% by weight) has been added as catalyst in the mixture. After that, two pre-curing temperatures have been chosen to measure the influence on oligomerization i.e. resinification. As result, the 40/55H/5 mixture has been heated at 85°C and 105°C during 10 min. After resin cooling, it was impregnated on cellulose filters, as presented below in **section V.2.3**. The **Figure V.52** shows the tensile test results for these two cellulosic composites after curing.

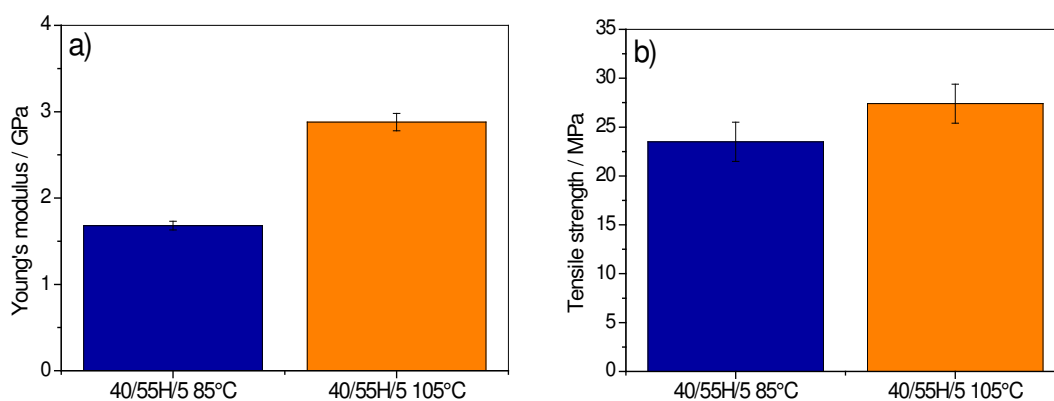


**Figure V.52.** Pre-curing temperature influence: Young's modulus (a), tensile strength (b).

A higher pre-curing temperature leads to generate composites with better mechanical properties: the Young modulus has double value ( $\approx 1.6$  vs 3 GPa). This result basically explains a better stress transfer between the matrix and the cellulose fibres. Furthermore, if we compare these two pre-curing temperatures, at lower temperature the extent of polymerization is inferior to that obtained at higher pre-curing temperature. That means a shorter length of linear furanic chains, less potentially connections with humins, and more free FA. According to the DSC results and to our knowledge on FA polymerisation, a very high isothermal curing temperature, such as 160°C, favours the cross-linking instead of polycondensation and thus oligomerization.<sup>26</sup> However, the first step of FA polymerization i.e. polycondensation is very important and determines Michael and Diels-Alder reactions cross-linking. So, this established fact can be reliable to the network density and homogeneity. For the resin pre-cured at 85°C, the network is probably more heterogeneous, with shorter polymer chains, and thus less cross-linking. This result could explain the tensile test results.

Herein, the solution to improve properties is to have a better resinification i.e. oligomerization. Concretely it means a longer isotherm or a higher pre-curing temperature. Unfortunately, a higher temperature cannot be reached because of the cross-linking and of the very quick gelation/vitrification process which is achieved at lower temperature due to the high concentration of catalyst (MA 5% by weight). The same problem occurs with a longer isotherm, even at lower temperature. For this reason, a catalyst addition strategy in two steps has been proposed.

### *V.2.4.2. 1 step vs 2 steps strategy*

To confirm the above mentioned supposition that a better pre-curing leads to generate composites with higher properties, the introduction of maleic anhydride in two steps has been investigated. The protocol of pre-curing, after the initial mixing of FA and humins at 105°C during 20 min, consists on a first addition of MA (2.5% by weight), then a heating at 120°C during 30min and at 130°C during 30 min. After that the mixture was cooled to 85°C, and the other 2.5% by weight of MA has been added. Then, the mixture has been stirred during 5 min and cooled down to room temperature for impregnation. The resulting “2 steps” cured composite has been confronted to the “1 step”: the experimental data has been resumed on **Figure V.53**.

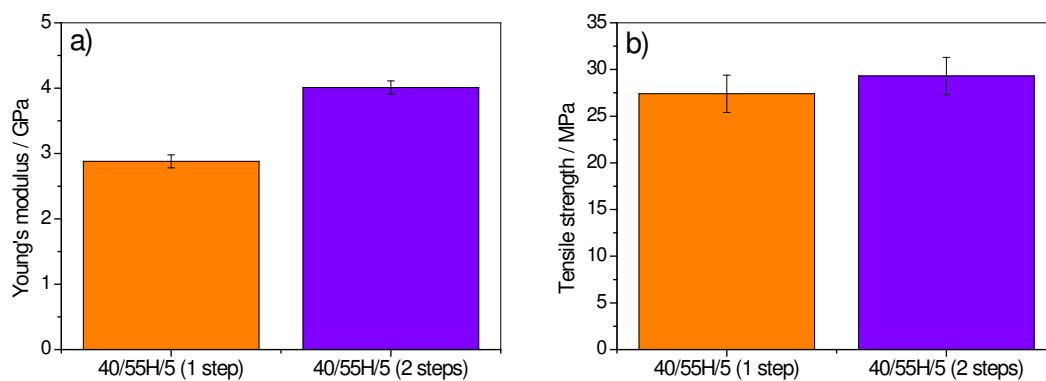


**Figure V.53.** 1 step vs 2 steps strategy: Young's modulus (a) and tensile strength (b) results.

As expected, the Young modulus of the “2 steps” procedure is higher, potentially due to the higher oligomerization. The tensile strength is slightly increased, but in the same range, which seems to impute that the tensile strength result mostly reflects the humins effect. Also, it shows a good stress transfer from cellulose to resin, and thus to humins. In the light of these results, the “2 steps” strategy has been adopted to develop the other resins for comparative studies.

#### V.2.4.3. Importance of resin viscosity for impregnation

Resins formulations were designed in order to reach approximately the same viscosity for each sample so to achieve similar impregnation conditions. The weight ratio of the different formulations, the procedures of resinification and the final viscosities of each resin are summarized in **Table V.8**. Note that it was necessary to adapt the pre-curing time and temperatures for each composition, due to their different reactivities and viscosities. Four formulations were prepared:

- ◆ The reference PFA resin consisted of 95% of FA and 5% of MA on weight. The catalyst quantity was chosen as optimal concentration, considering that potential interactions between MA and humins will consume a part of MA and thus will decrease the intrinsic FA reactivity. This assumption was confirmed by DSC studies, performed with the classical catalyst amount, i.e. 2% of MA (seen on section V.2.2).<sup>7</sup> As seen in **Table V.8**, the acidic catalyst (MA) was added in two steps to allow formation of a homogeneous viscous PFA resin and to reach a higher pre-curing temperature in the first step. Then, the reactive mixture was cooled to 80°C and the second addition of 2.5% of MA was done. This reference resin is reported as 95/0/5.
- ◆ Two formulations containing humins were prepared with FA/humins/MA weight ratios being respectively 40/55H/5 and 20/75H/5 (**Table V.8**). Prior to the addition of the acidic initiator, the FA (either 40 or 20% w/w) was mixed with the humins (either 55 or 75%

w/w) at 105°C for 20 min under mechanical stirring until a homogeneous, viscous black liquid was formed. Then, the maleic anhydride (5% w/w) was introduced in two equal steps of 2.5% w/w MA. The first pre-curing step was performed slightly longer and at a higher temperature range in the presence of humins (**Table V.8**). After cooling to 80°C, the last addition of 2.5% w/w MA was done. Subsequently, the mixture was stirred for another 5 min and cooled down to room temperature. A homogeneous viscous shiny black resin was obtained in each case. The resins were stored in the fridge and no phase separation was observed after several weeks.

- ◆ A resin was also prepared with an Organosolv lignin. The FA/lignin/MA weight ratio was 40/55L/5. First, FA was mixed with 55% of the Organosolv lignin and heated to 105°C for 20 min under mechanical stirring. Then the mixture was cooled to 80°C and 5% of MA was added. In this case MA was introduced in one single step. Otherwise, the viscosity which is already very high due to introduction of the lignin powder rose rapidly during the pre-polymerization (**Table V.8**).

**Table V.8.** Conditions of two pre-curing steps

Initial w/w ratios FA/Humins/MA FA/Lignin/MA	1 <sup>st</sup> pre-curing step	2 <sup>nd</sup> pre-curing step	Final resin viscosity at 25°C (Pa.s)	Final resin viscosity at 50°C (Pa.s)
95/0/5	40min at 110°C	80°C for 5min	515	13
40/55H/5	30min at 120°C and 30min at 130°C	80°C for 5min	627	28
40/55L/5	-	80°C for 5min	3900	530
20/75H/5	30min at 120°C	80°C for 5min	2240	59

### V.3. Structural characterization by FT-IR

The ATR-IR spectra of the neat FA monomer and of the raw humins are shown in **Figure V.54** together with the spectra of the 95/0/5 resins and the 40/55H/5 resins. The assignment of major bands, in good agreement with of literature,<sup>27,28</sup> is also summarized in **Table V.9**. At first sight, the four spectra do not exhibit major differences which would indicates that similar functional groups are present in the different systems under study.

**Table V.9.** Assignment of major bands on FT-IR spectra

Assignment	Wavenumber cm <sup>-1</sup>	In spectrum of
C-H wagging furan ring	728	FA
C-H wagging furan ring	738	40/55H/5

C-H wagging 5-sub furan ring	790	95/0/5
C-H wagging furan ring	798	40/55H/5
C-H wagging furan ring	812	FA
C-H wagging methylene group / C-O stretching D-A adduct	868	40/55H/5
C-C-C in-plane bending furan ring	886	FA
C-O stretching hydroxymethyl group	1000	FA
C-O stretching	1020	humins
C-O stretching furan ring and met C-H wagging and OH wagging	1146	FA
C-C/C-O stretching furan ring / C-C stretching hydroxymethyl group	1220	FA
C=C stretching furan ring	1505	FA
C=C stretching HMF's furan ring	1515	humins
C=C stretching 2,5-sub furan ring	1559	95/0/5
C=C stretching conjugated with C=O	1600	humins
C=O stretching MMF/HMF's aldehyde	1665	humins
C=O stretching	1690	95/0/5
C=O stretching conjugated with C=C	1712	humins
C=O stretching	1714	40/55H/5
C=O stretching	1720	95/0/5
C=O stretching	1735	40/55H/5

The spectrum of the FA monomer contains many peaks which can be assigned to vibrations respectively associated with the furan ring or with the hydroxymethyl group.<sup>27</sup> The furan C=C stretching vibration appears at 1505 cm<sup>-1</sup> while the peaks around 812 and 728 cm<sup>-1</sup> can be assigned to the C-H out of plane deformation of the furan ring (**Figure V.54**). The strong peak around 1000 cm<sup>-1</sup> corresponds to the C-O stretching of the hydroxymethyl group. The strong peak at 1146 cm<sup>-1</sup> is commonly attributed to the C-O stretching of the furan ring collectively associated with C-H and OH wagging.<sup>27,28</sup> Thus, this peak in association with two other FA characteristic peaks at 1220 and 884 cm<sup>-1</sup> (assigned in **Table V.9**) can be an indication of the free FA in the pre-cured resin composition. Indeed, this peak is also visible in the 95/0/5 and in the 40/55H/5, in quite the same intensity that means that the pre-cured step has been conducted approximately in the same conditions.

When the FA is prepolymerized into PFA, new bands are developing while others are shifting. The spectrum of 95/0/5 shows a new peak at 1559 cm<sup>-1</sup> which is assigned to C=C stretching in a 2,5-disubstituted furan ring. The red-shift of the C-H out of plane deformation from 812 to around 790 cm<sup>-1</sup> is taken as another proof of the furan substitution in the C<sub>5</sub> position. Moreover, the appearance of a composite peak between 1720 and 1690 cm<sup>-1</sup> indicates that carbonyl moieties could have been created through hydrolytic opening reactions of the furan ring. These peaks could also correspond to Diels Alder cyclo-adducts which are thought to be formed during PFA crosslinking.<sup>5</sup> All the above-mentioned features are consistent with previous IR studies on FA polymerization.<sup>7,28,29</sup>

The fructose-based humins spectrum shown in **Figure V.54** is consistent with previous FT-IR studies conducted on such complex poly-aromatic structures.<sup>1,15,16</sup> The molecular structure of

humins is mainly derived from HMF and 5-methoxymethylfurfural (MMF). The peak at  $1515\text{ cm}^{-1}$  is assigned to C=C stretching in furan rings while the peak at  $1020\text{ cm}^{-1}$  corresponds to C-O stretching. As for the PFA, the composite peaks between  $800$  and  $750\text{ cm}^{-1}$  are attributed to the out of plan C-H bending of the different substituted furans. According to Lund et al.<sup>15</sup> the peak at  $1712\text{ cm}^{-1}$  together with the peak around  $1600\text{ cm}^{-1}$  in humins are characteristic of carbonyl group conjugated to an alkene group. Finally, it should be mentioned that the feature at  $1665\text{ cm}^{-1}$  could arise from the C=O stretch of the MMF and HMF's aldehyde group.

The spectrum of the prepolymerized 40/55H/5 resin corresponds approximately to the superposition of the signals from the 95/0/5 PFA resin and those from the humins. However, some features can be attributed to specific interactions between the PFA network and the humins. A new band develops at  $868\text{ cm}^{-1}$  which is neither visible in the spectrum of PFA resin or in the spectrum of humins. The peaks appearing within this wavenumber region are generally attributed either to C-H wagging of methylene linkages or C-O stretching from Diels-Alder cycloadducts.<sup>28</sup> This might indicate that novel kinds of interactions were created between the side chain oxygen groups of the humins and the furanic rings from the PFA. Moreover, clear-cut shoulders appear at  $1714$  and  $1735\text{ cm}^{-1}$  in the carbonyl stretching region. The chemical environment of the carbonyl groups present in the aliphatic parts of the humins has been modified probably due to new interactions with the polyfurfuryl alcohol network. It should also be mentioned that the C-H out of plane bending of the furan rings appears at  $798$  and  $738\text{ cm}^{-1}$  for the 40/55H/5 resin. These peaks are broader and slightly shifted to higher wavenumbers compared to the PFA resin. It denotes a more complex network of furan rings due to interconnections between the two systems.

A putative chemical structure of the humins surface based on literature<sup>1,16</sup> and FTIR measurements is proposed on **Figure V.55** to highlight its possible covalent interactions with FA oligomers.

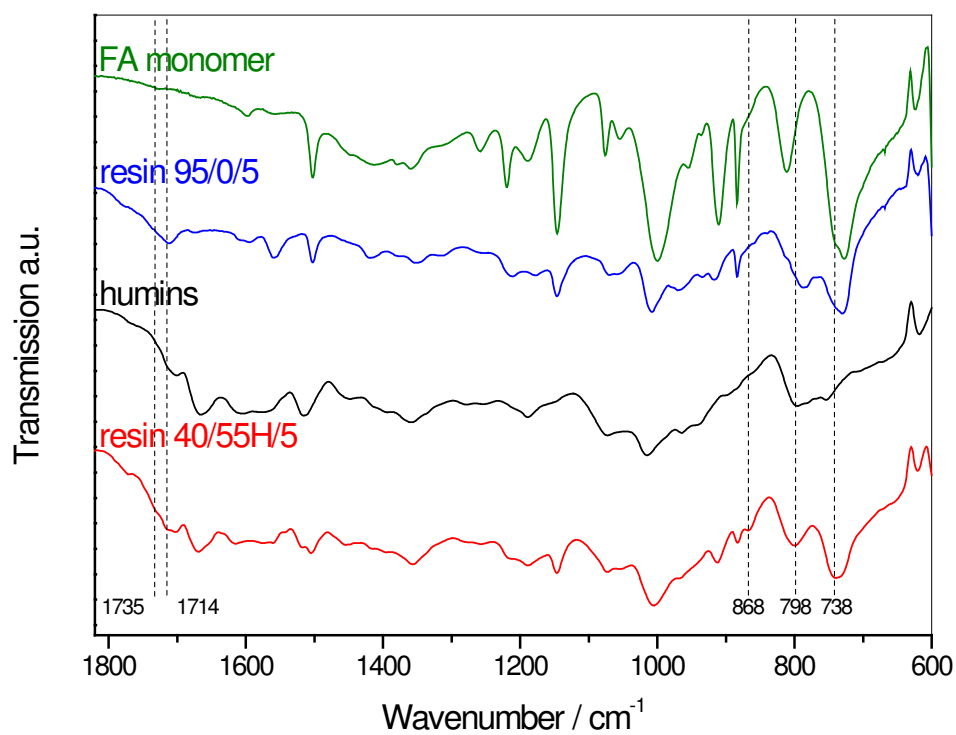


**Figure V.54.** IR spectra of FA monomer (green), humins (black), pre-cured resins 95/0/5 (blue) and 40/55H/5 (red).

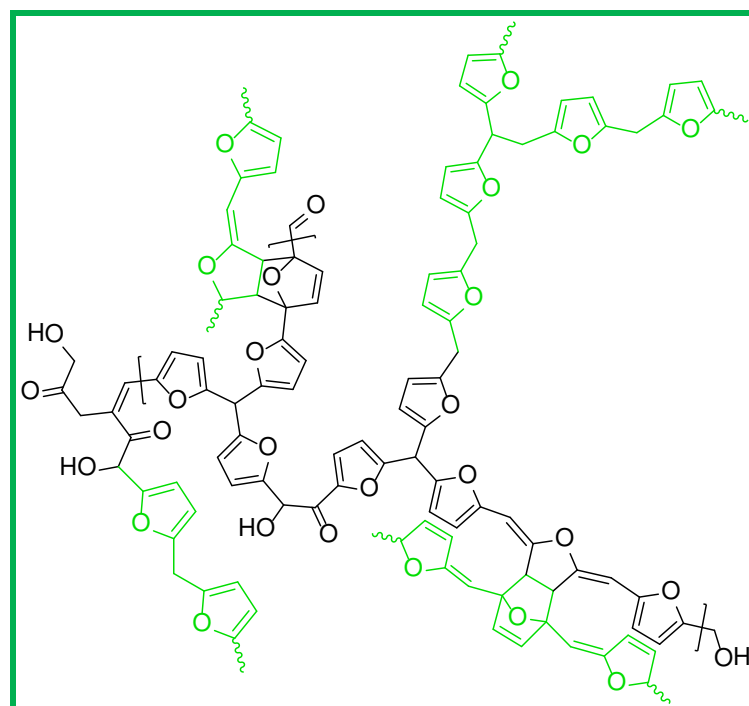


**Figure V.55.** Putative cross-links between humins structure taken from literature (black) and FA oligomers (green).<sup>1,16</sup>

#### V.4. Multi-comparative mechanical and morphological studies of cellulosic composite

This section focus on a multi-comparative study between cellulosic composites, impregnated with different furanic resins, in term of mechanical properties and morphologies of fracture surfaces. In order to highlight the effect of humins on the impregnation quality, humins cellulosic composites will be compared with those of pure PFA and lignin composites.

##### V.4.1. Mechanical characterization

**Figure V.56** shows the stress–strain curves of the non-impregnated cellulose paper together with those of the different cellulose/thermosets composites. The obtained curve for the cellulose paper sample reveals a succession of fractures which can be attributed to the progressive disentanglement of the fibers during the tensile test.<sup>30</sup> As observed on the SEM micrographs (**Figure V.56 E**), the fracture surface of the cellulose paper confirms the loosening of fibers. In comparison with the stress-strain test, the behavior of the thermoset composites impregnated cellulose fibers are very different and can be characterized in first approximation to a straight line of the tensile strength which is characteristic of an elastic response, leading to a brittle fracture. Such behavior reveals an uniform impregnation with an adhesion between the cellulose fibers and the matrix. These results were corroborated with the SEM micrographs presented in **Figure V.56**. Compared with the cellulose filter, the impregnated composites present a sharper fracture surface.

The Young modulus and tensile strength at failure obtained for the different composites are gathered in **Figure V.57**. As all the cellulose filters have similar mechanical behavior, the differences in the mechanical responses of the composites are only linked to the matrix and its abilities to generate a good adhesivity with the fibers reinforcement. When the PFA resin is used, the resulting composite exhibits a Young modulus of about 3.5 GPa, the tensile strength approaches 15 MPa while the strain at failure do not exceed 0.5% (**Figure V.56**). It denotes an extremely brittle behavior generated by the PFA network which is characteristic for this peculiar thermosetting resin.<sup>31</sup> The incorporation of Organosolv lignin within the PFA matrix does not dramatically change the mechanical properties of the composite. Similar tensile modulus and strength compared to the PFA resin indicates that Organosolv lignin does not modify the

brittleness of the composite and interfacial adhesion between the furanic matrix and cellulose fibers. Like the PFA resin, the lignin also exhibits a rigid aromatic structure which is not able to sufficiently flexibilize the cross-linked network.

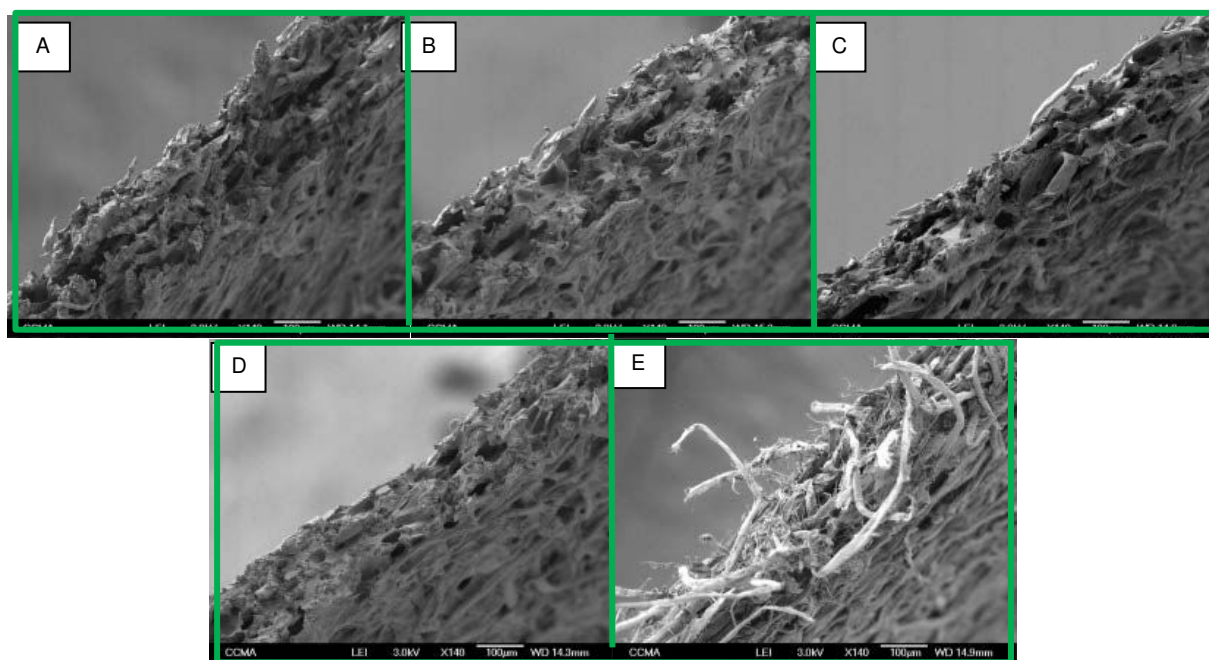
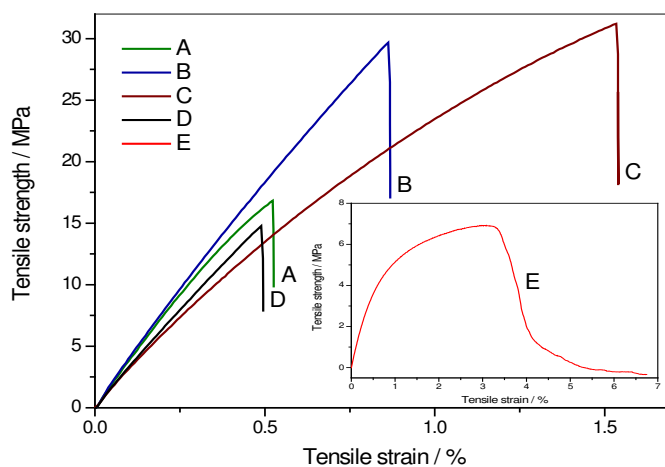


**Figure V.56.** Stress–strain curves and SEM fracture surface (A: 40/55L/5; B: 40/55H/5; C: 20/75H/5; D: 95/0/5; E: filter paper)

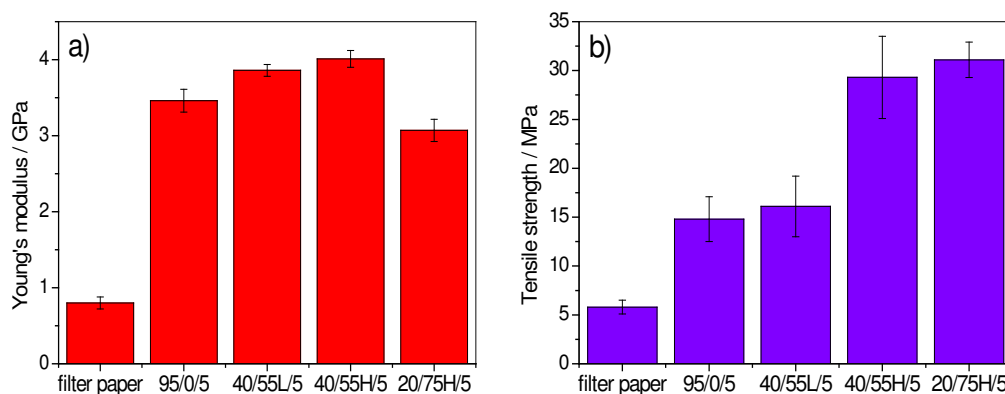


**Figure V.57.** Young's modulus (a) and tensile strength (b) histograms

On the other hand, the incorporation of humins into the matrix leads to a significant improvement of the composite mechanical properties. When the 40/55H/5 resin is used as matrix, the Young modulus reaches ~ 4 GPa and the tensile strength (~ 28 MPa) increases by a factor two compared to PFA based composite. Such behavior could result from better stress transfer between the matrix and the cellulose fibers. Moreover, the incorporation of humins unambiguously changes the mechanical behavior of the matrix itself which is likely to become more ductile and flexible compared to the rigid PFA network. This is particularly reflected in **Figure V.56** which highlights a plastic contribution on stress-strain curve when the amount of humins in the matrix increases to 75 % w/w. Consequently, the composite prepared with the 20/75H/5 resin has a tensile modulus of about 3 GPa which is lower compared to the other composites. However, it should be outlined here that the tensile strength of the 20/75H/5 composite is reaching ~ 32 MPa which is significantly higher compared the values obtained with the PFA and the PFA/lignin resins. The higher ductility of the humins-based matrix allows reaching a higher level of strength without sacrificing interfacial bonding with the cellulose fibers.

The humins micro-architecture can be schematically considered as a core-shell rubber. Several studies have demonstrated that the humins surface present a rigid aromatic structure while the ductile core is mostly constituted by non-aromatic moieties derived from degraded sugar.<sup>32,33</sup> Then, the incorporation of humins into the PFA matrix will induce higher flexibility. Such behavior is also observed when core-shell rubber microparticles are incorporated into a brittle matrix.<sup>34,35</sup>

#### V.4.2. Morphological characterization

The SEM micrographs shown in **Figure V.58** exhibit the fracture surface of the different composites. Each picture reveals, in good agreement with the stress-strain curves, a homogeneous resin impregnation which partly fills the empty spaces present between the cellulosic fibers of the filter paper. The fracture surface of the PFA composite (**Figure V.58 D**) highlights fibers that are embedded within the matrix but do not show fibers fracture or dislocation. The fracture seems to originate from the matrix itself. It corroborates the tensile measurements which denote the brittle behavior of the composite.

The presence of scattered resin fragments at the surface of the PFA/lignin-based composite (**Figure V.58 A**) also confirms the brittleness of this type of resin. The matrix appears in the form of fragmented and brittle mortar. A pulled-out single fiber can be clearly seen which would be the consequence of moderate interfacial bonding between the PFA/lignin matrix and the cellulosic fibers.

Interestingly, the fracture surface of the composites containing humins in the matrix reveals more fibers dislocation or rupture (**Figure V.58 B and C**). It would attest for higher interfacial bonding and more efficient stress transfer between the matrix and the fibers. Moreover, the matrix appears more ductile with fewer striations compared to the neat PFA and the PFA/lignin resins. These observations are correlating well with the higher tensile strength obtained for the PFA/humins-based composites. The pictures in **Figure V.59** are obtained for the composite processed with the 40/55H/5 based-resin and focus on the fibers/matrix interface. At higher magnitude, the formation of a homogeneous resin coating is distinctly highlighted at the surface of the fibers. No voids or cracks were observed which indicative of a good interfacial bonding. These observations confirm that the humins plays a positive role on the resin ductility and on the cellulose/matrix interface. These additional features underline the great potential to use the humins as raw component into the PFA resins.

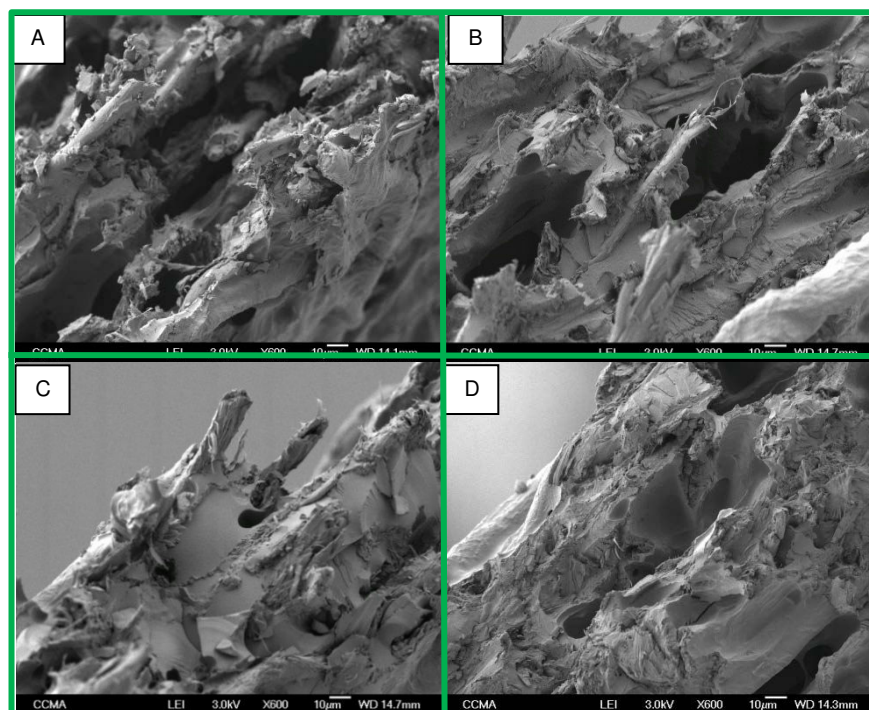


**Figure V.58.** SEM micrographs on fractures composites after tensile test (x600) A: 40/55L/5; B: 40/55H/5; C: 20/75H/5; D: 95/0/5

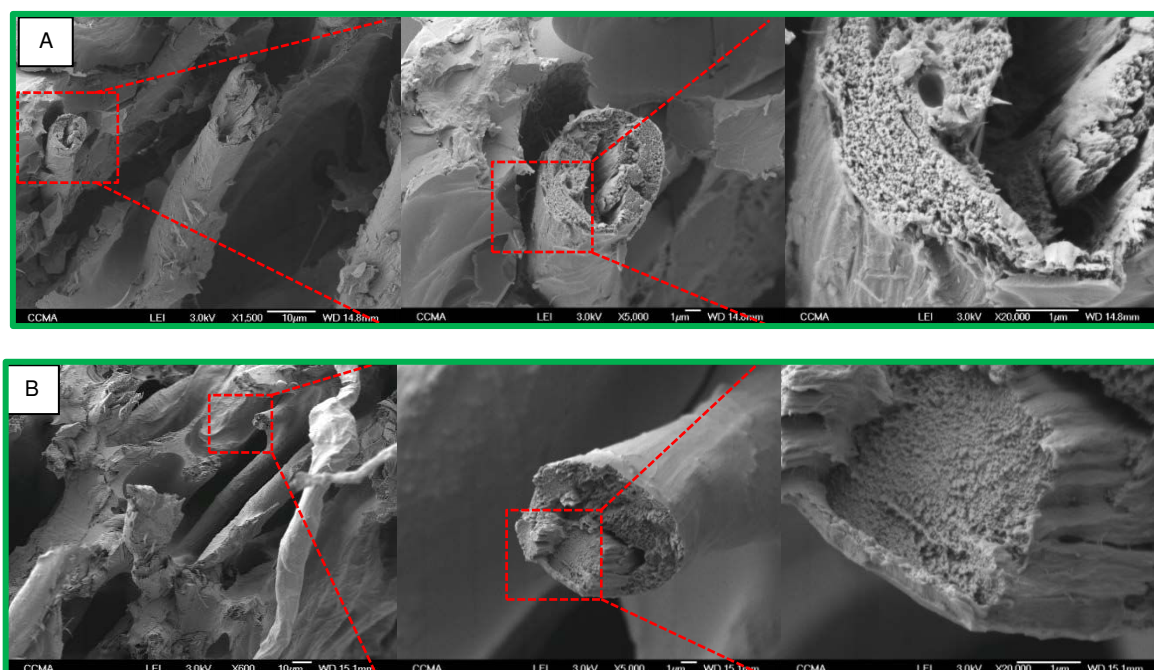


**Figure V.59.** SEM micrographs focused on fiber/matrix interfaces on PFA/lignin (A) or PFA/humins (B) composites

## V.5. An opening toward industry

### V.5.1.Reduction of polymerization temperature

The temperature of resin curing is a key issue for industrial assumption. Herein, a work on co-catalysis with a strong acid has been developed to reduce the temperature of curing. This investigation is particularly adapted for the “2 steps” strategy. Indeed, after the first introduction of 2.5% by weight of MA and the pre-heating, the resin was cooled down and then the co-catalyst was added at room temperature.

The quantity of sulfuric acid has been fixed for this first experience to 1 % by weight in an aqueous solution at 20 % (w/w). The quantity of sulfuric acid should be tailored in function of the reached curing temperature. The final composite after impregnation and curing at 160°C for 3h has been compared to the pure PFA and 40/55H/5 as reference in **Figure V.60**.

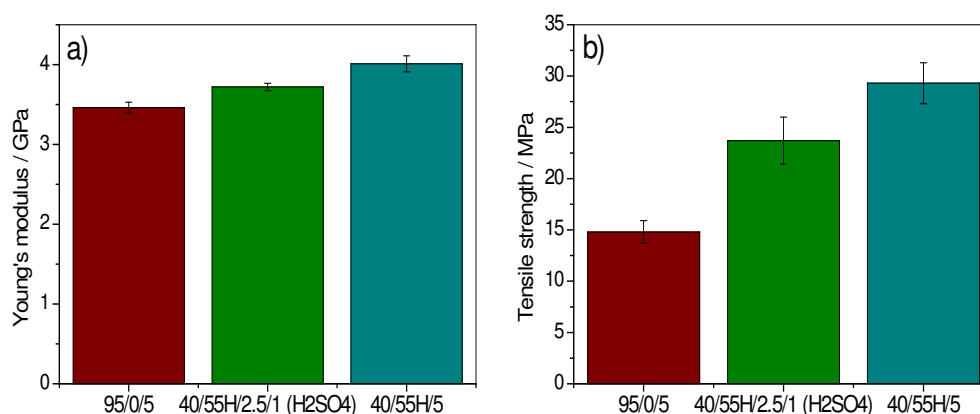


**Figure V.60.** Mechanical test results when using sulfuric acid as co-catalyst for curing: Young's modulus (a), tensile strength (b).

The composite obtained with the resin 40/55H/2.5/1 (H<sub>2</sub>SO<sub>4</sub>) exhibits an average mechanical behaviour between the two references of pure PFA and humins resins. The Young modulus is very close to the 40/55H/5 composite which confirms the very important first pre-curing step with the 2.5% of MA. The tensile strength is quite lower at around 24 MPa. The final result is better than pure PFA, and thus good omen for several applications. Furthermore, some qualitative tests with a higher content of sulphuric acid have been realized and reveal a good potential for curing for these kinds of resins, at room temperature.

### V.5.2. Application fields

As proof-of-concept, this precursory work opens gates to further develop reactive PFA/humins-based resins both for wood adhesion (plywood, fiberboards) and for wood durability as an example. Indeed, another advantage of cellulosic composite is that it is a good model study for textile and wood impregnation.<sup>36</sup> After several impregnation tests as depicted on **Figure V.61 (A)**, PFA/humins resin has proven to be efficient to elaborate textile composite and then design object like the presented hat in **Figure V.61 (B)** elaborated by NPSP company in Netherland. The success of these impregnation works has been the basis for the elaboration of a patent by the Avantium Company presented in **Annexe section**.

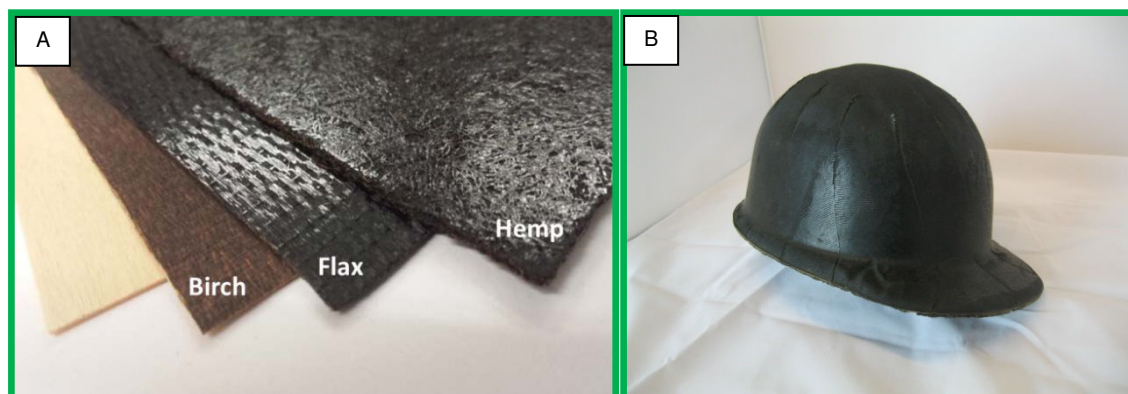


**Figure V.61.** Impregnation tests on textile fibers and wood (A) and hat made by NPSP Company in PFA/humins impregnated fibers (B).

## V.6. Conclusions

This study shows that large quantities of humins (either 55 or 75% w/w) can be successfully included into a polyfuranic thermosetting network which is a good solution to obtain lower cost price resins. Homogeneous systems comprising polyfurfuryl alcohol (PFA) and humins have been prepared via acid-induced polymerizations. FT-IR measurements confirm that potential interactions have been developed between the PFA and the humins network. The PFA/humins resins exhibit reasonably low viscosities for being impregnated onto cellulose filter and lead to cross-linked composites after final curing. The tensile strength of the PFA/humins based composites is two times higher than those obtained either with the neat PFA composites or the PFA/lignin composites. Incorporation of humins allows to decrease the brittleness of the furanic matrix and to increase the interfacial bonding with cellulose fibers. In agreement with the tensile test data, the SEM observations reveal that the PFA/humins composites present more fibers fractures than the other composites. It confirms that incorporation of humins impacts positively the mechanical properties of the thermosetting composites. This study demonstrates

that humins can be valorized as an active component into PFA and in the meantime decreases its brittleness which is one major drawback of the pure polyfurfuryl alcohol bio-based thermoset.

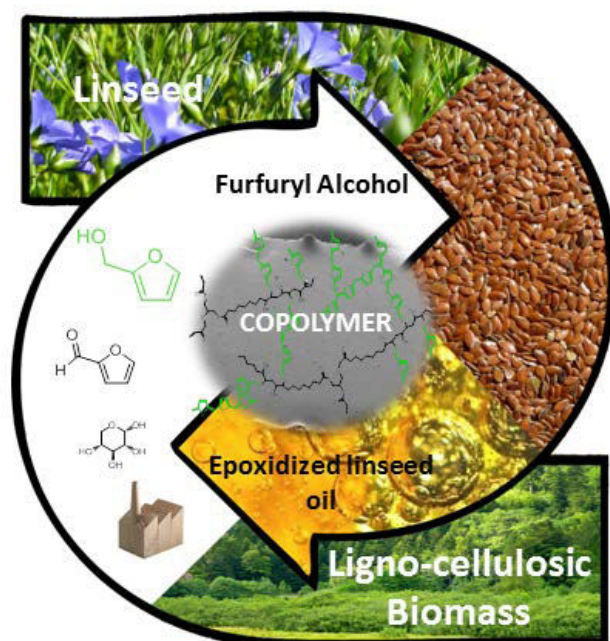
1. van Zandvoort, I.; Wang, Y.; Rasrendra, C. B.; van Eck, E. R.; Bruijninx, P. C.; Heeres, H. J.; Weckhuysen, B. M., Formation, molecular structure, and morphology of humins in biomass conversion: influence of feedstock and processing conditions. *ChemSusChem* **2013**, *6* (9), 1745-58.
2. Hoydonckx, H.; Van Rhijn, W.; Van Rhijn, W.; De Vos, D.; Jacobs, P., Furfural and derivatives. *Ullmann's Encyclopedia of Industrial Chemistry* **2007**.
3. Milkovic, J.; Myers, G. E.; Young, R. A., Interpretation of curing mechanism of furfuryl alcohol resins. *Cellulose chemistry and technology* **1979**.
4. Gandini, A.; Belgacem, M. N., Furans in polymer chemistry. *Progress in Polymer Science* **1997**, *22* (6), 1203-1379.
5. Choura, M.; Belgacem, N. M.; Gandini, A., Acid-Catalyzed Polycondensation of Furfuryl Alcohol: Mechanisms of Chromophore Formation and Cross-Linking. *Macromolecules* **1996**, *29* (11), 3839-3850.
6. Montero, A. L.; Montero, L. A.; Martínez, R.; Spange, S., Ab initio modelling of crosslinking in polymers. A case of chains with furan rings. *Journal of Molecular Structure: THEOCHEM* **2006**, *770* (1-3), 99-106.
7. Guigo, N.; Mija, A.; Vincent, L.; Sbirrazzuoli, N., Chemorheological analysis and model-free kinetics of acid catalysed furfuryl alcohol polymerization. *Physical chemistry chemical physics : PCCP* **2007**, *9* (39), 5359-66.
8. Belgacem, M. N.; Gandini, A., Furan-based adhesives. *Handbook of Adhesive Technology* **2003**, 615-634.
9. Lande, S.; Westin, M.; Schneider, M., Properties of furfurylated wood. *Scandinavian Journal of Forest Research* **2004**, *19* (sup5), 22-30.
10. Gandini, A., Polymers from Renewable Resources: A Challenge for the Future of Macromolecular Materials. *Macromolecules* **2008**, *41* (24), 9491-9504.
11. Li, X.; Nicollin, A.; Pizzi, A.; Zhou, X.; Sauget, A.; Delmotte, L., Natural tannin-furanic thermosetting moulding plastics. *RSC Advances* **2013**, *3* (39), 17732.
12. Guigo, N.; Mija, A.; Vincent, L.; Sbirrazzuoli, N., Eco-friendly composite resins based on renewable biomass resources: Polyfurfuryl alcohol/lignin thermosets. *European Polymer Journal* **2010**, *46* (5), 1016-1023.
13. Nordstierna, L.; Lande, S.; Westin, M.; Karlsson, O.; Furó, I., Towards novel wood-based materials: Chemical bonds between lignin-like model molecules and poly(furfuryl alcohol) studied by NMR. *Holzforschung* **2008**, *62* (6).
14. Thakur, V. K.; Thakur, M. K.; Raghavan, P.; Kessler, M. R., Progress in Green Polymer Composites from Lignin for Multifunctional Applications: A Review. *ACS Sustainable Chemistry & Engineering* **2014**, 140407122637003.
15. Patil, S. K. R.; Lund, C. R. F., Formation and Growth of Humins via Aldol Addition and Condensation during Acid-Catalyzed Conversion of 5-Hydroxymethylfurfural. *Energy & Fuels* **2011**, *25* (10), 4745-4755.
16. Patil, S. K. R.; Heltzel, J.; Lund, C. R. F., Comparison of Structural Features of Humins Formed Catalytically from Glucose, Fructose, and 5-Hydroxymethylfurfuraldehyde. *Energy & Fuels* **2012**, *26* (8), 5281-5293.
17. Lora, J. H.; Glasser, W. G., Recent industrial applications of lignin: a sustainable alternative to nonrenewable materials. *Journal of Polymers and the Environment* **2002**, *10* (1-2), 39-48.
18. Rinaudo, M., *les polymères naturels: Structure, Modifications, Applications*. GFP ed.; 2006; Vol. 13.
19. Laurichesse, S.; Avérous, L., Chemical modification of lignins: Towards biobased polymers. *Progress in Polymer Science* **2014**, *39* (7), 1266-1290.
20. Goyal, G. C.; Lora, J.; Pye, E., Autocatalyzed organosolv pulping of hardwoods: effect of pulping conditions on pulp properties and characteristics of soluble and residual lignin. *Tappi journal* **1992**, *75* (2), 110-116.
21. Glasser, W. G.; Barnett, C. A.; Muller, P. C.; Sarkanen, K. V., The chemistry of several novel bioconversion lignins. *Journal of Agricultural and Food Chemistry* **1983**, *31* (5), 921-930.
22. Pye, E. K.; Lora, J., The Alcell™ process: a proven alternative to kraft pulping. *Tappi journal* **1991**, *74* (3), 113-118.
23. Hoang, T. M.; Lefferts, L.; Seshan, K., Valorization of humin-based byproducts from biomass processing-a route to sustainable hydrogen. *ChemSusChem* **2013**, *6* (9), 1651-8.

24. Eerhart, A. J. J. E.; Huijgen, W. J. J.; Grisel, R. J. H.; van der Waal, J. C.; de Jong, E.; de Sousa Dias, A.; Faaij, A. P. C.; Patel, M. K., Fuels and plastics from lignocellulosic biomass via the furan pathway; a technical analysis. *RSC Advances* **2014**, *4* (7), 3536-3549.
25. De Wild, P.; Huijgen, W.; Heeres, H., Pyrolysis of wheat straw-derived organosolv lignin. *Journal of Analytical and Applied Pyrolysis* **2012**, *93*, 95-103.
26. Zavaglia, R.; Guigo, N.; Sbirrazzuoli, N.; Mija, A.; Vincent, L., Complex Kinetic Pathway of Furfuryl Alcohol Polymerization Catalyzed by Green Montmorillonite Clays. *The Journal of Physical Chemistry B* **2012**, *116* (28), 8259-8268.
27. Barsberg, S.; Berg, R. W., Combined Raman Spectroscopic and Theoretical Investigation of Fundamental Vibrational Bands of Furfuryl Alcohol (2-furanmethanol). *The Journal of Physical Chemistry A* **2006**, *110* (30), 9500-9504.
28. Barsberg, S.; Thygesen, L. G., Poly(furfuryl alcohol) formation in neat furfuryl alcohol and in cymene studied by ATR-IR spectroscopy and density functional theory (B3LYP) prediction of vibrational bands. *Vibrational Spectroscopy* **2009**, *49* (1), 52-63.
29. Conley, R. T.; Metil, I., An investigation of the structure of furfuryl alcohol polycondensates with infrared spectroscopy. *Journal of Applied Polymer Science* **1963**, *7* (1), 37-52.
30. Nishino, T.; Arimoto, N., All-Cellulose Composite Prepared by Selective Dissolving of Fiber Surface. *Biomacromolecules* **2007**, *8* (9), 2712-2716.
31. Pranger, L. A.; Nunnery, G. A.; Tannenbaum, R., Mechanism of the nanoparticle-catalyzed polymerization of furfuryl alcohol and the thermal and mechanical properties of the resulting nanocomposites. *Composites Part B: Engineering* **2012**, *43* (3), 1139-1146.
32. Sevilla, M.; Fuertes, A. B., The production of carbon materials by hydrothermal carbonization of cellulose. *Carbon* **2009**, *47* (9), 2281-2289.
33. Sevilla, M.; Fuertes, A. B., Chemical and structural properties of carbonaceous products obtained by hydrothermal carbonization of saccharides. *Chemistry-A European Journal* **2009**, *15* (16), 4195-4203.
34. Pearson, R. A.; Yee, A. F., Influence of particle size and particle size distribution on toughening mechanisms in rubber-modified epoxies. *J Mater Sci* **1991**, *26* (14), 3828-3844.
35. Giannakopoulos, G.; Masania, K.; Taylor, A. C., Toughening of epoxy using core-shell particles. *J Mater Sci* **2010**, *46* (2), 327-338.
36. Hautala, M.; Pasila, A.; Pirilä, J., Use of hemp and flax in composite manufacture: a search for new production methods. *Composites Part A: Applied Science and Manufacturing* **2004**, *35* (1), 11-16.



## Chapter VI

Combination of epoxidized linseed oil and furfuryl alcohol to design tailored fully bio-based material



**Keywords:** 2D correlation NMR, copolymerization, epoxidized vegetable oils, polyfurfuryl alcohol, mechanical properties.



<b>VI.1. Epoxidized linseed oil and furfuryl alcohol: a green cationic marriage.....</b>	<b>150</b>
VI.1.1. A cationic copolymerization strategy .....	151
<b>VI.2. Investigation on ELO/FA copolymerization reactivities.....</b>	<b>152</b>
VI.2.1. Materials.....	152
VI.2.2. Investigation of reactivities by DSC.....	152
VI.2.3. FT-IR analysis of structural evolution during copolymerization .....	153
VI.2.3.1. Monomers and ELO50/FA50 unreacted mixture.....	154
VI.2.3.2. Structural evolution during ELO50/FA50 copolymerization .....	154
VI.2.4. Structural polymerization investigation by multi-dimensional NMR .....	158
VI.2.4.1. Study of ELO50/FA50 system at $t=0$ in regard with comonomers signals.....	158
VI.2.4.2. Study of ELO50/FA50 system at $t=60$ min in regard with homopolymers signals..	
<b>VI.3. Thermo-mechanical study of ELO50/FA50 thermoset material.....</b>	<b>167</b>
VI.3.1. Elaboration of resin bulk for mechanical analysis.....	167
VI.3.2. ELO/FA bio-based thermoset characterization by dynamic mechanical analysis.....	167
VI.3.3. Tensile test experiments and fracture analysis by SEM .....	169
VI.3.4. Thermogravimetric analysis (TGA) .....	171
<b>VI.4. Conclusions .....</b>	<b>172</b>

## VI. Combination of epoxidized linseed oil and furfuryl alcohol to design tailored fully bio-based material

### VI.1. Epoxidized linseed oil and furfuryl alcohol: a green cationic marriage

The aim of this study, illustrated in the **Figure VI.62**, is to generate a new type of green thermosets, with a maximum content of renewable carbon, by the combination of epoxies based on vegetable oils and furfuryl alcohol as biomass derivatives. The copolymer obtained by the strategic association of these two monomers might combine the advantages of both structures, i.e. the flexibility of triglyceride and the mechanical properties also with the high thermal stability of polyfurfuryl chains. The literature reports the work of Vilela et al.<sup>1</sup> who have successfully synthesized monomers that combine fatty acids and furanic derivatives.

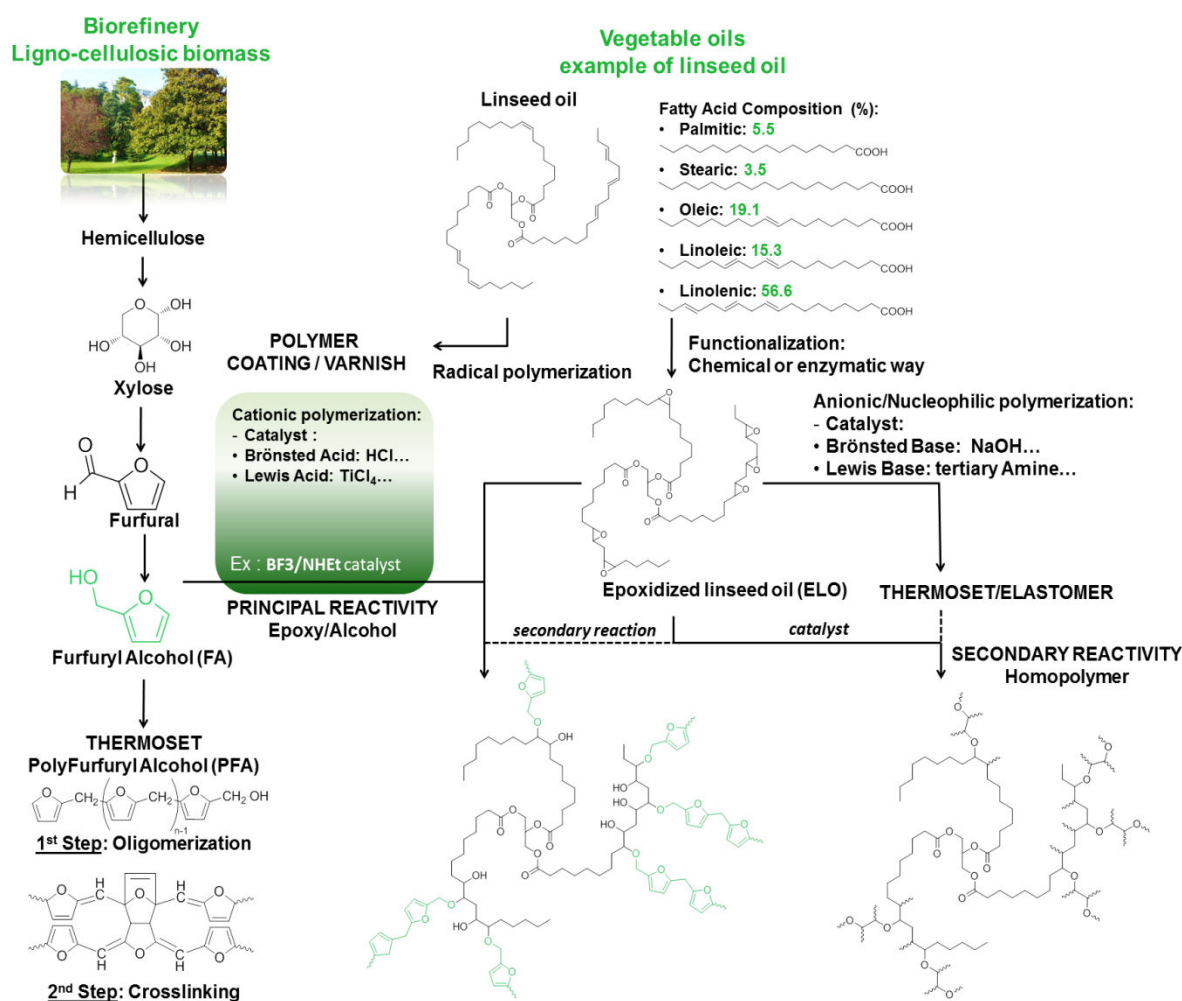


**Figure VI.62.** Scheme of biomass derivatives to design ELO/FA polymers

## VI.1.1. A cationic copolymerization strategy

Our purpose in the present work is to use a way which requires the utilization of minimum steps and/or chemicals. Thus, copolymerization between ELO and FA has been done in presence of a small amount of cationic initiator, without other chemicals or solvent. It is important to notice the good compatibility between ELO and FA in term of miscibility. In order to promote covalent interactions between these two comonomers, a cationic copolymerization has been investigated, with the utilization of a latent Lewis acid as catalyst, the boron trifluoride ethylamine complex ( $\text{BF}_3\text{NHEt}$ ). The main starting hypothesis of this work is that the FA hydroxyl could open the ELO oxiran ring as suggested in the literature<sup>2,3,4</sup> (**Figure VI.63 (a)**). Several secondary reactions could theoretically occur as: the catalyzed/uncatalysed (thermally induced) homopolymerization of ELO (**Figure VI.63 (b)**); the transesterification of glycerol moieties by FA; the epoxy opening ring or glycerol moieties hydrolysis with the water released by FA polycondensation and also, the ELO inter-cross-linking etherification by reaction of hydroxyl derived from an ELO opened ring and another oxiran ring.

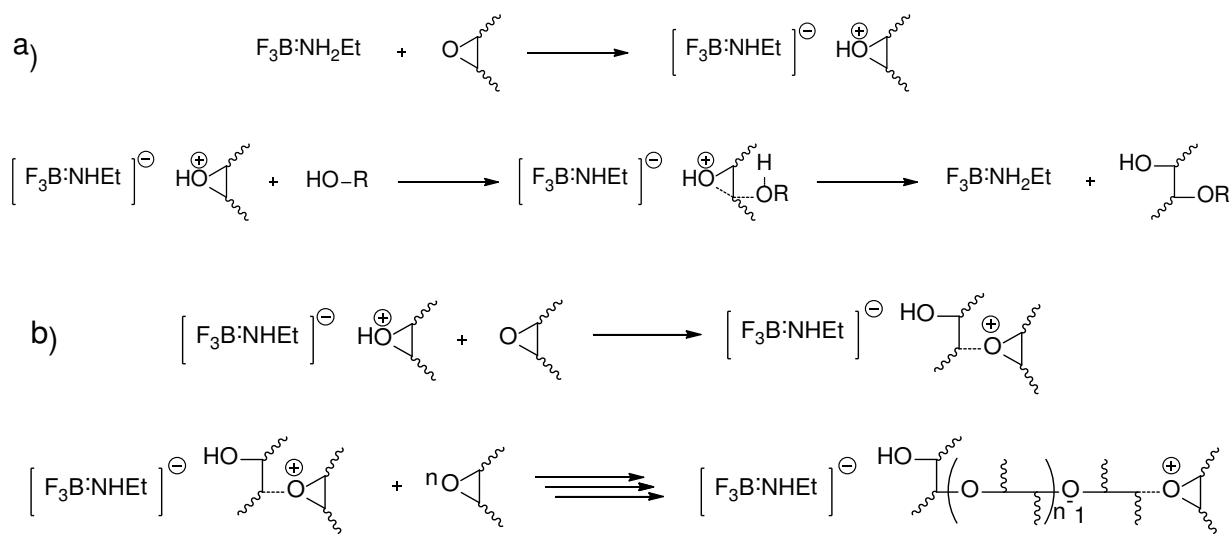


**Figure VI.63.** Epoxy/alcohol (a) and epoxy homopolymerization (b) cationic mechanism catalyzed by boron trifluoride ethylamine complex.<sup>2</sup>

To highlight the principal reactivities, after an initial investigation by differential scanning calorimetry (DSC), complementary studies by FT-IR and 1D/2D NMR were realized carefully. The thermoset homogeneity and mechanical properties have been discussed through the prism of dynamic mechanical analysis (DMA), tensile test and scanning electronic microscopy (SEM) results. Finally the thermal resistance of these materials has been evaluated by thermogravimetric analysis (TGA).

## VI.2. Investigation on ELO/FA copolymerization reactivities

### VI.2.1. Materials

Epoxidized linseed oil (ELO) was obtained from Akcros Chemicals Ltd. It is a viscous-liquid at room temperature with a viscosity of about 1,200 Pa.s. ELO has a molecular weight of about 980 g.mol<sup>-1</sup> and contains on average 5.5 epoxy groups per molecule. Furfuryl alcohol (FA) (purity: ≥ 98%) as monomer and boron trifluoride ethylamine complex as polymerization catalyst, were purchased from Sigma-Aldrich.

### VI.2.2. Investigation of reactivities by DSC

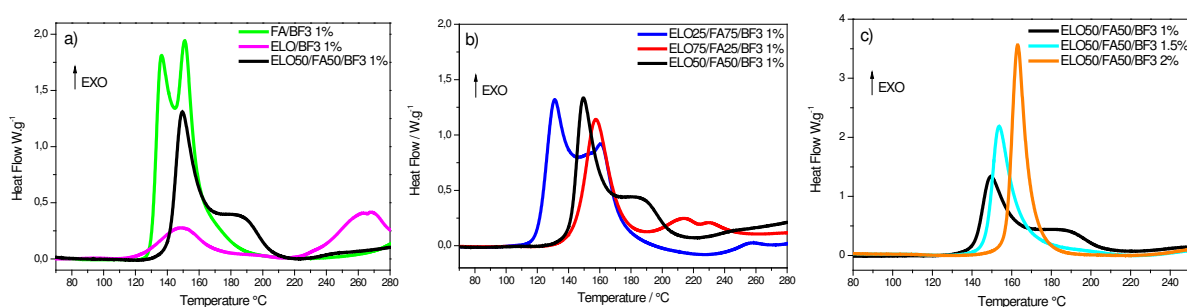


**Figure VI.64.** Nonisothermal DSC data at 6 °C.min<sup>-1</sup>

DSC investigations were conducted to study the thermally induced ELO/FA cationic polymerizations. **Figure VI.64** gathers all the DSC curves. **Figure VI.64 a)** aims to present the DSC measurements corresponding to cationic homopolymerizations of ELO and of FA alone in comparison with ELO and of FA mixtures (ELO50/FA50 50:50, w:w ratio) copolymerization (each of these three formulations contains a ratio of 1% in weight of catalyst). For FA/BF<sub>3</sub> system, we could notice a strong exothermic peak ( $\approx 500 \text{ J.g}^{-1}$ ) with two overlapped thermal events attributed to the condensation of furanic rings accompanied with water release<sup>5</sup>, followed by the cross-linking via Diels-Alder reactions.<sup>6,7</sup> In comparison, polymerization of ELO/BF<sub>3</sub> is less exothermic ( $96 \text{ J.g}^{-1}$ ) with a slower reaction rate as shown by the lower slope of the peak. However, we can distinguish two exothermic peaks (at 150°C and 265°C) that can be respectively attributed to the catalyzed homopolymerization reaction of ELO ( $96 \text{ J.g}^{-1}$ ), and to the uncatalysed one which generally occurs at high temperature range ( $81 \text{ J.g}^{-1}$ ).<sup>8</sup> Copolymerization of ELO with FA seems to have an intermediary trend, with a higher reaction enthalpy ( $\approx 360 \text{ J.g}^{-1}$ ) in comparison of that of ELO homopolymerization. The peak of ELO50/FA50 reaction is slightly shifted to higher temperature compared to those of neat ELO or FA homopolymerizations. The comparison of these 3 systems leads to the conclusion that the first thermal event occurs at higher temperature when both FA and ELO are present.

**Figure VI.64 b)** represents the reactivity of different ELO/FA ratios for a same concentration of catalyst (1%). **Table VI.10** gives the functionalities between the reactive groups of ELO (epoxy) and FA (alcohol) for each ELO/FA ratio that has been investigated. These ratios have been determinate in order to have a functionality of one site epoxy to one alcohol function, in concordance with the literature on epoxy/alcohol reactivity.<sup>9,2</sup> The increasing of ELO ratio shifts the polymerization to higher temperature and progressively decreases its enthalpy. This is in good agreement with the previously formulated hypothesis that addition of ELO decreases the reactivity of the system. This effect could be explained by a steric hindrance of the triglyceride chains that hinder the furanic polycondensation. The ELO/FA ratio of 75/25 presents a deficit on FA (**Table VI.10**), so consequently favors side reactions of epoxies in excess, like homopolymerization/etherification, as described above. It could correspond to exothermic peaks at around 240-260°C with  $\Delta_r H \sim 41 \text{ J.g}^{-1}$ . Thus, in the following studies, the polymerization reactivity will be investigated for an ELO/FA ratio 50/50 in order to obtain a deeper understanding of reaction mechanism occurring between these two monomers.

The **Figure VI.64 c)** highlights the influence of the catalyst concentration on ELO/FA reactivity. Surprisingly, the increase of catalyst amount shifts the peak maximum temperature to higher values. Indeed, the FA polycondensation is initiated after the catalyst decomplexation with the release of NHEt. As results, the pH increases, and in consequence the cationic intrinsic polycondensation of FA is shifted to higher temperature. The reaction enthalpies for 1, 1.5 and 2% catalyst content have similar values, around  $360 \text{ J.g}^{-1}$ , indicating that 1% is sufficient to catalyze the reaction. Herein, the system with 1% of catalyst has been retained in the following studies.

**Table VI.10.** Functionality and ELO/FA molecules ratios with 1% of initiator

Matrix ratio (w/w)	Functionality ratio Epoxy/alcool	Molecules ratio
ELO/FA 25/75	1:5.28	1:29.1
ELO/FA 50/50	1:1.76	1:9.7
ELO/FA 75/25	1:0.59	1:3.2

### VI.2.3. FT-IR analysis of structural evolution during copolymerization

The 50/50 ELO/FA w/w ratio has been chosen to investigate the reactivity between these two comonomers. For this purpose, a mixture of ELO50/FA50/BF3NHEt1% was heated to 120°C for 90 min on an opened system. Samples were taken every 15 min and immediately quenched, leading to a total of seven samples at a time from t=0 to t=90 min. The spectrum of air was

recorded as background. A total of 120 scans with a resolution of  $1\text{cm}^{-1}$  were accumulated for each sample.

### VI.2.3.1. Monomers and ELO50/FA50 unreacted mixture

To highlight the copolymerization of ELO with FA, FTIR spectra of neat FA and ELO were first recorded and compared to the spectrum of ELO50/FA50 at  $t = 0$ . Peaks assignment has been summarized in **Table VI.11** and the corresponding spectra are presented in **Figure VI.65**. The peak at  $1503\text{ cm}^{-1}$  is currently associated to C=C furan stretching, while the peak at  $884\text{ cm}^{-1}$  corresponds to the C-C bending of the furan ring. The C-H out of plane vibrations of furan ring peaks are generally assigned at  $812$  and  $728\text{ cm}^{-1}$ . The peak at  $1220\text{ cm}^{-1}$  and the intense band at  $1446\text{ cm}^{-1}$  are also characteristic from neat FA, with for the last one, a collective vibration between C-O stretching of furan ring associated with C-H and OH wagging. These bands are in good agreement with the IR data reported in the literature for furanic rings and hydroxymethyl groups.<sup>10,11,12</sup>

The IR peaks characteristics for ELO are less intense in ELO50/FA50 spectrum because of the ratio corresponding to ELO molecules into ELO/FA mixture is around 1/9.7 (**Table VI.10**). Anyway, principals ELO peaks could be assigned according to the literature.<sup>13,14,15</sup> The intense peak at  $1736\text{ cm}^{-1}$  corresponds to the C=O stretching of the triglyceride ester groups, while the large band at  $1152\text{ cm}^{-1}$  is generally associated to its C-O stretching from glycerol moiety. The ether C-O stretching in  $\alpha$ -position of the ester group could be associated to the peaks at around  $1116/1096\text{ cm}^{-1}$ . The epoxy functions are revealed by the bands at  $1245\text{ cm}^{-1}$  and  $820\text{ cm}^{-1}$  which respectively correspond to the C-O-C stretching and the C-H wagging from oxiran ring.

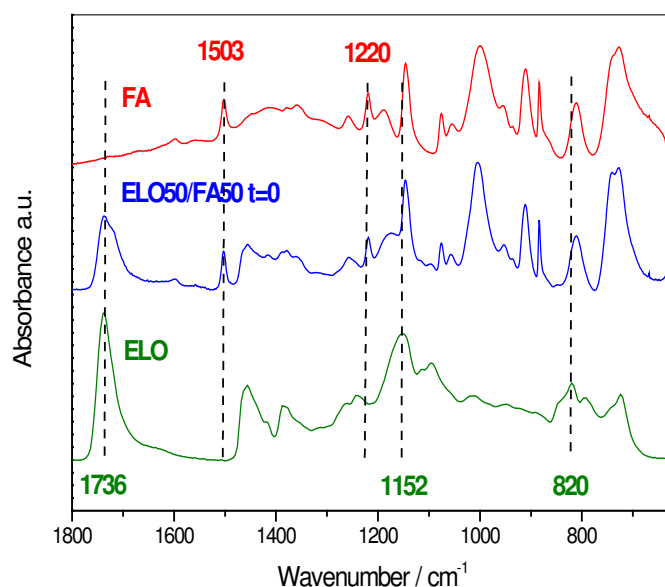


**Figure VI.65.** FTIR spectra of neat monomers and the mix ELO50/FA50 at  $t = 0$

### VI.2.3.2. Structural evolution during ELO50/FA50 copolymerization

**Figure VI.66** shows the evolution of IR bands of formed structures during the copolymerization of ELO50/FA50. The IR spectra were recorded on isothermal polymerized samples at 120°C from  $t = 0$  to  $t = 90$  min. The insert shows the isothermal DSC thermogram associated with its corresponding conversion curve. It is important to notice that this isothermal program reaches the same maximal extent of conversion in regard to the value of measured enthalpy (**Figure VI.64**).

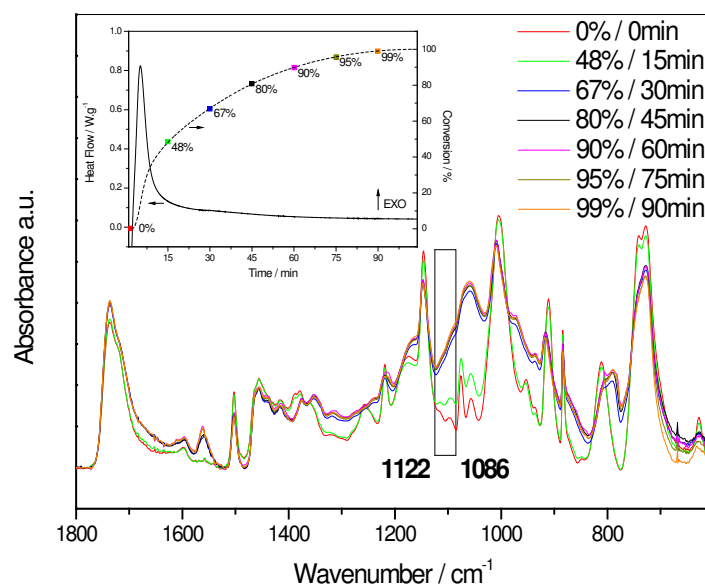


**Figure VI.66.** FT-IR evolution of ELO50/FA50 pre-cured resins coupled with the extent of conversion obtained from isothermal DSC at 120 °C.

$0 < \alpha < 0.48$ : the spectra at  $t = 0$  and  $t = 15$  min are approximately similar, with differences in the diminution and small shifts of peaks from free FA such as 1503, 1220, 1004, 884, 812 and 728  $\text{cm}^{-1}$ , that highlight the occurring of condensation reactions and the apparition of a new chemical environment. The major modifications are the increase of some bands between 1125 and 1040  $\text{cm}^{-1}$ . Barsberg et al.<sup>11</sup> observed into these ranges peaks associated with neat FA and PFA at 1076  $\text{cm}^{-1}$  and 1057  $\text{cm}^{-1}$ . The increasing absorbance in the interval from 1122 to 1086  $\text{cm}^{-1}$  (**Figure VI.66**) could be attributed to the stretching of linear ether C-O-C bonding of oxiran opened by the alcohol function of FA/FA oligomer.<sup>13</sup> Indeed, there are no characteristic bands in this wavenumber range for the PFA thermoset.<sup>6,11</sup> As we discussed above, some peaks of C-O stretching from glycerol part of ELO are present here, however these bands should be invariant with the polymerization.

In order to assess the credibility of our hypothesis, a theoretical investigation inspired by the work of Barsberg et al.<sup>11</sup> has been realized. The choice of the structure fragment model has been associated to the main concern of statistical oligomer predominance that means the utilization of

the most accessible oxiran of the linolenic moieties of ELO, opened by FA monomer. The computed spectrum presented in **Figure VI.67** exhibits a major band vibration at  $1127\text{ cm}^{-1}$  corresponding to the C-O-C stretching which connect FA to ELO. This result is in a good accordance with the monitored infrared data. Obviously, several approximations have been considered: for instance the fragment models considering only one epoxy and one furan monomer, without presence of oligomers, under vacuum medium. This approach gives substantial results which could be considerate in corroboration with the proposed ELO/FA connectivity.

$0.48 < \alpha < 0.99$ : this conversion range presents major modifications associated with oligomer chains growing. However, the same peak evolution of the spectrum of  $t = 15\text{ min}$  is noticed. It is particularly the case with the peak at around  $1730\text{ cm}^{-1}$  which usually corresponds to the stretching of C=O bonding. Its increase could be explained by the presence of ketones, probably due to some opened furan rings.<sup>6</sup> The shifted peaks of the neat FA also give information about a new furanic environment. For instance, the shift from  $1004\text{ cm}^{-1}$  to  $1009\text{ cm}^{-1}$  could correspond to hydroxylated furanic oligomer; also the peak at  $911\text{ cm}^{-1}$  usually associated to collective motions of neat FA, appears shifted to  $916\text{ cm}^{-1}$ . News peaks appeared, linked to the formation of PFA network, in agreement with the bands prediction for furanic dimers and trimers as shown by Barsberg et al.<sup>11</sup> Herein, the constant increase of the band at  $1559\text{ cm}^{-1}$  could be associated with the C=C stretching of two 2,5-substitued furan rings linked by a methylene. This information has been visually confirmed by the dark coloration of the mixture during heating, sign of chromophores apparition.<sup>5</sup> Bands around  $1318\text{ cm}^{-1}$  are commonly associated with the C-H wagging of methyne link between furanic dimers or trimers. The band at  $974\text{ cm}^{-1}$  corresponds to the 2,5-substitued furan pattern, more precisely to the C-C-C bending associated to the C-O stretching. The new band at  $936\text{ cm}^{-1}$  could correspond to the C-O stretching associated with the C-C bending and C-H in plane wagging of the terminal 2-substitued furan dimer or trimer.

Some evidences of Diels-Alder (DA) cross-linking have been highlighted by the apparition of news peaks at  $1352\text{ cm}^{-1}$ ,  $1314\text{ cm}^{-1}$  and shoulders at  $1235\text{ cm}^{-1}$  (assignments summarized in **Table VI.11**).

The cross-linking between FA oligomers and ELO is confirmed by the increase of absorbance in interval between  $1122$  and  $1086\text{ cm}^{-1}$  associated to C-O stretching provided by different environments issued from epoxy ring opening. Interesting peak evolution is observed in  $775\text{ cm}^{-1}$  to  $840\text{ cm}^{-1}$  range. A decrease of peaks at  $820\text{ cm}^{-1}$  and  $812\text{ cm}^{-1}$  reveals the consumption of neat FA and ELO epoxy ring. Indeed, the decrease of the epoxy ring wagging is correlated with the

decrease of the  $1245\text{ cm}^{-1}$  peak. It would indicate that the epoxy groups have been opened through covalent interaction with hydroxyl group of FA/FA oligomer.

Finally, the apparition of peaks at  $807\text{ cm}^{-1}$  and  $792\text{ cm}^{-1}$  could respectively be associated with the C-H wagging of 2- and 2,5-substituted furan rings oligomers.

**Table VI.11.** Assignment of major bands of ELO/FA on FT-IR spectra

Assignment	Wavenumber $\text{cm}^{-1}$	Corresponded entities
C-H wagging furan ring	728	FA
C-H wagging 2,5-sub furan ring	792	PFA
C-H wagging 2-sub furan ring	807	PFA
C-H wagging furan ring	812	FA
C-H wagging oxiran ring	820	ELO
C-C-C in-plane bending furan ring	884	FA
C-O stretching C-C-C bending CH in plane wagging deloc + 2-sub furan ring	936	PFA
C-C-C bending and C-O stretching 2,5-sub furan ring	974	PFA
C-O stretching hydroxymethyl group	1004	FA
C-O stretching in $\alpha$ -position of ester group	1116/1096	ELO
C-O-C stretching ELO ether	1122-1086	ELO/FA
C-O stretching furan ring and met C-H wagging and OH wagging	1146	FA
C-O stretching ester group	1152	ELO
C-C/C-O stretching furan ring / C-C stretching hydroxymethyl group	1220	FA
C-H wagging	1235	PFA
C-O-C stretching oxiran ring	1245	ELO
C-H wagging C-C stretching : DA link	1314	PFA
C-H wagging linkage dimer/trimer furan ring	1318	PFA
C-H wagging C-C stretching + $\text{CH}_2$ segment : DA link	1352	PFA
C=C stretching furan ring	1503	FA
C=C stretching 2,5-sub furan ring	1559	PFA
C=O stretching ester group	1736	ELO

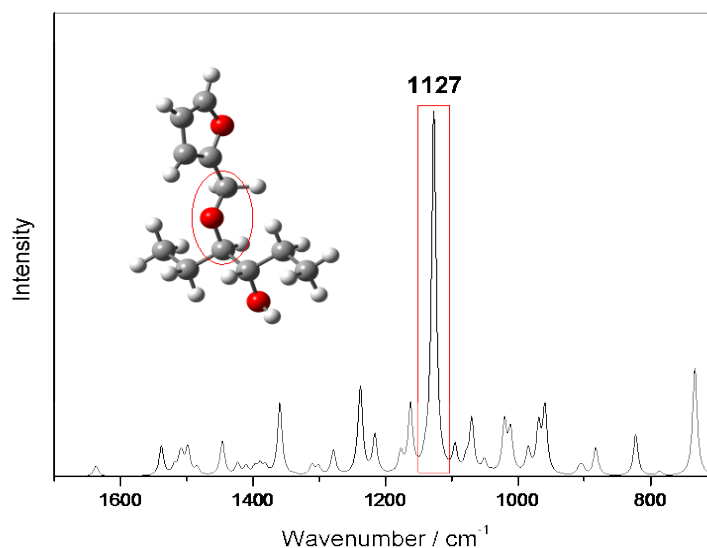


**Figure VI.67.** Theoretical IR spectrum of linolenic fragment, obtained at the B3LYP//6-311++G(d,p) level of theory. Maximum of intensity appears clearly at  $1127\text{ cm}^{-1}$ , the vibration associated with the connection between ELO and FA monomer (modelling chemical structure inserted)

### VI.2.4. Structural polymerization investigation by multi-dimensional NMR

The NMR investigations are presented in two parts. In the first part, the aim is to characterize the monomers (ELO, FA) and the initial mix of ELO50/FA50 at  $t=0$ . The second part focuses on the covalent interconnections developed between the triglyceride and the furanic network. For this purpose, multi-comparative studies between ELO50/FA50, PFA and ELO homopolymer at  $t=60$  min have been done. Samples preparation was proceeded by heating at 120 °C under stirring during 60 min. The NMR assignments are presented on **Table VI.12**.

**Table VI.12.** Molecules assignments correlated with NMR spectra

Molecules	Structure with atoms assignment	Correlated spectra/figure
Epoxidized linseed oil (ELO)		Figure 7, 8, 9, 11, 15
Furfuryl alcohol (FA)		Figure 7, 8, 9, 15
Furanic branched chain of polyfurfuryl alcohol (PFA)		Figure 10, 13, 14, 16
Cross-links between epoxy of ELO and FA oligomers ELO/FA connection		Figure 13, 16, 17

#### VI.2.4.1. Study of ELO50/FA50 system at $t=0$ in regard with comonomers signals

The  $^1\text{H}$  NMR and  $^{13}\text{C}$  NMR spectra of ELO, FA and ELO50/FA50 at  $t=0$  are given in **Figure VI.68** and **Figure VI.69**, respectively. The signals of ELO50/FA50 system at  $t=0$  corresponds only to the contribution of FA and ELO shifts. No other signal was detected in the initial ELO/FA mixture which indicates that no interaction occurs before polymerization. Characteristic NMR signals of FA<sup>5</sup> are associated with 7.58 ppm ( $\text{H}_\epsilon$ ); 6.39 ppm ( $\text{H}_\delta$ ); 6.29 ppm ( $\text{H}_\gamma$ ); 4.40 ppm ( $\text{H}_\alpha$ ) for  $^1\text{H}$  shifts and 155.8 ppm ( $\text{C}_\beta$ ); 142.4 ppm ( $\text{C}_\epsilon$ ); 110.6 ppm ( $\text{C}_\gamma$ ); 107.2 ppm ( $\text{C}_\delta$ ); 56.0

ppm ( $C_\alpha$ ) for the  $^{13}\text{C}$  shifts. The assignments of NMR signals of ELO molecule is in agreement with those reported for vegetable epoxidized oils<sup>13,14,16</sup>: the methyne proton at  $\delta= 5.2$  ppm ( $H_k$ ) and the methylene proton at  $\delta= 4.0-4.3$  ppm ( $H_j$ ) were associated with glycerol moiety. Epoxy ring proton signals are between  $\delta= 3.1$  and  $2.8$  ppm ( $H_g$ ); the methylene protons in  $\alpha$ -position of the ester carbonyl have a signal at  $\delta= 2.3$  ppm ( $H_f$ ) and in  $\beta$ -position at around  $1.7$  ppm ( $H_e$ ). The methylene bridge between two epoxy rings has a signal at around  $\delta= 1.8$  ppm ( $H_h$ ), while the methylene protons next to oxiran ring present signals at around  $\delta= 1.5$  ppm ( $H_d$ ). The methylene protons corresponding to alkyl backbones of triglycerides have signals around  $\delta= 1.2$  and  $1.4$  ppm ( $H_c$ ). The terminal methyl groups have signals around  $\delta= 1$  ppm for the linolenic methyl in  $\beta$ -position of the oxiran ring ( $H_b$ ), and  $0.86$  ppm for the methyl from alkyl chain ( $H_a$ ). For the ELO characterization by  $^{13}\text{C}$  NMR, the assignment of peaks signals at  $172.5$  ppm ( $C_i$ ) corresponds to the carbon of the carbonyl from ester moieties. Resonances at  $69.1$  ppm ( $C_k$ ) and  $62.1$  ppm ( $C_j$ ) correspond respectively to carbons of the methyne and methylene from glycerol moieties. The carbons from oxiran rings ( $C_g$ ) could be found between  $53.6$  and  $57.5$  ppm.

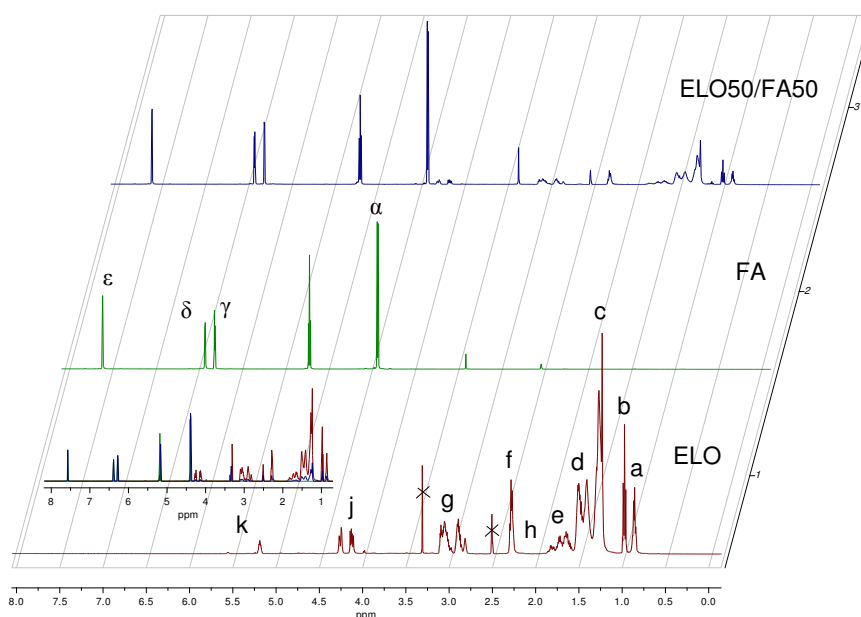


**Figure VI.68.**  $^1\text{H}$  NMR of ELO, FA and the ELO50/FA50 mixture at  $t=0$

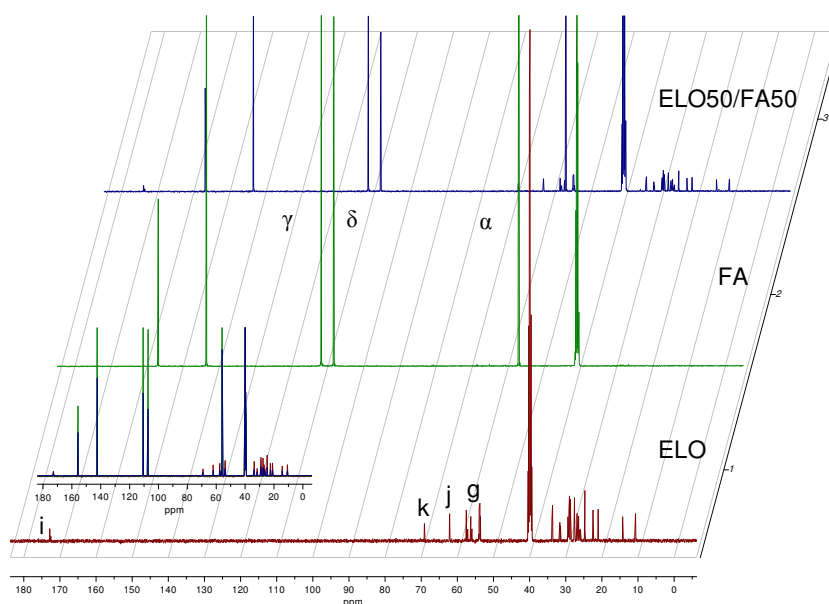


**Figure VI.69.**  $^{13}\text{C}$  NMR of ELO, FA and the ELO50/FA50 mix at  $t=0$

#### VI.2.4.2. Study of ELO50/FA50 system at $t=60$ min in regard with homopolymers signals

Chemical structures resulting from the ELO/FA reaction after 60 min at  $120^\circ\text{C}$  was investigated by multidimensional NMR techniques. First,  $^1J_{\text{CH}}$  correlations were investigated by HSQC NMR experiment as shown in **Figure VI.74**. The  $^1\text{H}$  sub-spectrum of the ELO/FA mix at  $t=60$  min is illustrated on the  $x$ -axis of the HSQC spectrum. To assign these protons to the corresponding carbons, a DEPT-135 sequence was used, presented on the  $y$ -axis of the spectrum.

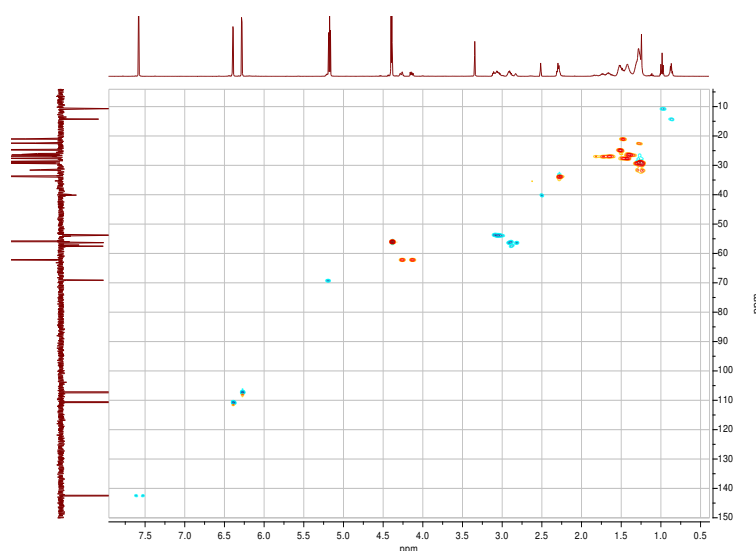


**Figure VI.70.** HSQC NMR of ELO50/FA50 at  $t = 0$ .

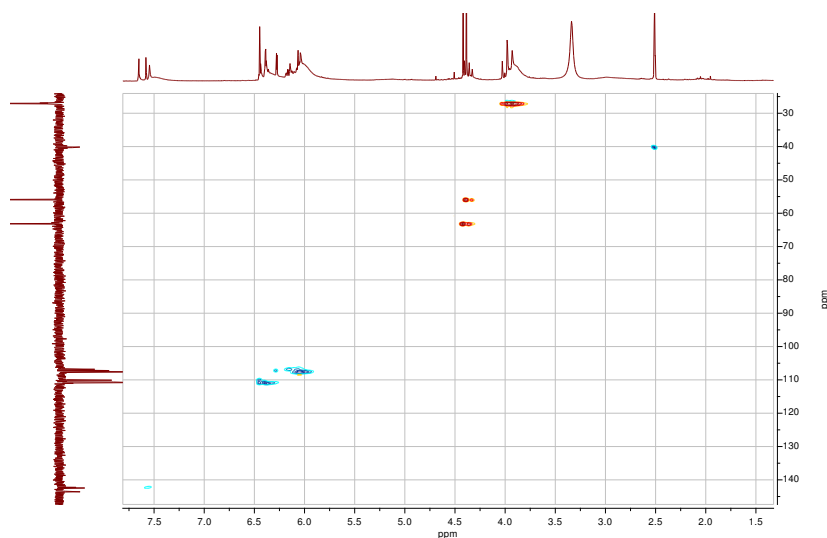


**Figure VI.71.** HSQC NMR of PFA at  $t = 60$  min.

The HSQC spectra of ELO/FA mix at  $t=0$  (**Figure VI.70**) and  $t=60$  min have been confronted in first time. A first notable difference is the complete disappearance of  $-CH-$  from oxiran signal (cross-peak at 53-58 ppm ( $C_g$ )), which is the sign of oxiran ring opening (**rounded dot line on HSQC  $t= 60$  min**). Cross-peaks from the HSQC  $t= 60$  min in **Figure VI.74** could be exploited as a multi-comparative interpretation confronted with the HSQC spectra of neat ELO (**in green**), neat FA (**in pink**), PFA oligomers (**in red**) and ELO homopolymer oligomers (**rounded dot line in black**). Herein, **Figure VI.72** shows the  $^1H$  NMR of ELO monomer and ELO homopolymer, the first observation is the strong similarity of these two spectra, however the represented signals are less thin and defined, which is related to the increase of the molecular weight during the formation of ELO oligomers.

The **Figure VI.73** exhibits the HSQC NMR of ELO homopolymer. Cross-peaks at around  $^1H$ , 2.8 ppm /  $^{13}C$ , 55 ppm correspond to the methyne in oxygen  $\alpha$ -position. These peaks group should correspond to the methyne reliable to epoxy groups from unreacted ELO, but also reliable to the methyne issued from ELO homopolymer as illustrated in the scheme **Figure VI.73**. Indeed, these methynes groups have respectively the same atomic environment and thus present quite the same chemical shift. Now if we confront these results with ELO50/FA50 HSQC in **Figure VI.74**, we observe the total disappearance of cross-peaks associated to ELO oxiran methyne, and don't noticed the appearance of cross-peaks at the same chemical shift of around  $^1H$ , 2.8 ppm /  $^{13}C$ , 55 ppm for ELO homopolymer: that suggests the non-occurrence of ELO homopolymerization.

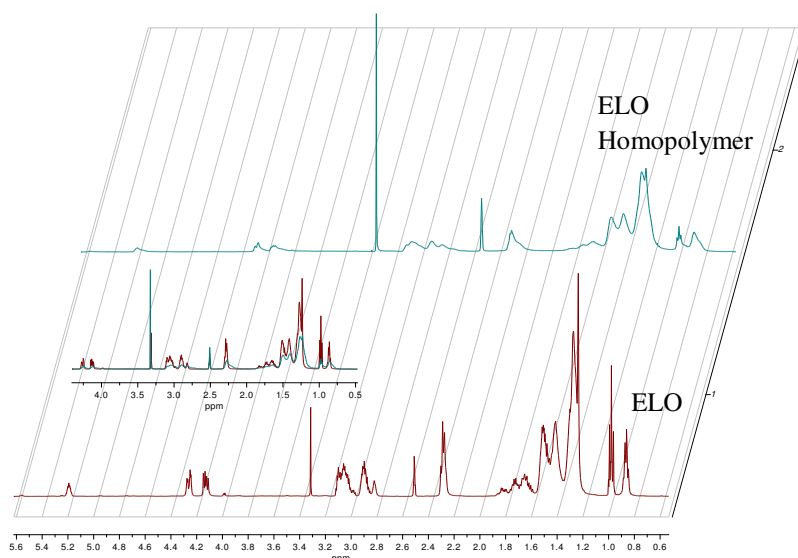


**Figure VI.72.**  $^1\text{H}$  NMR of ELO and ELO homopolymer at  $t = 60$  min.

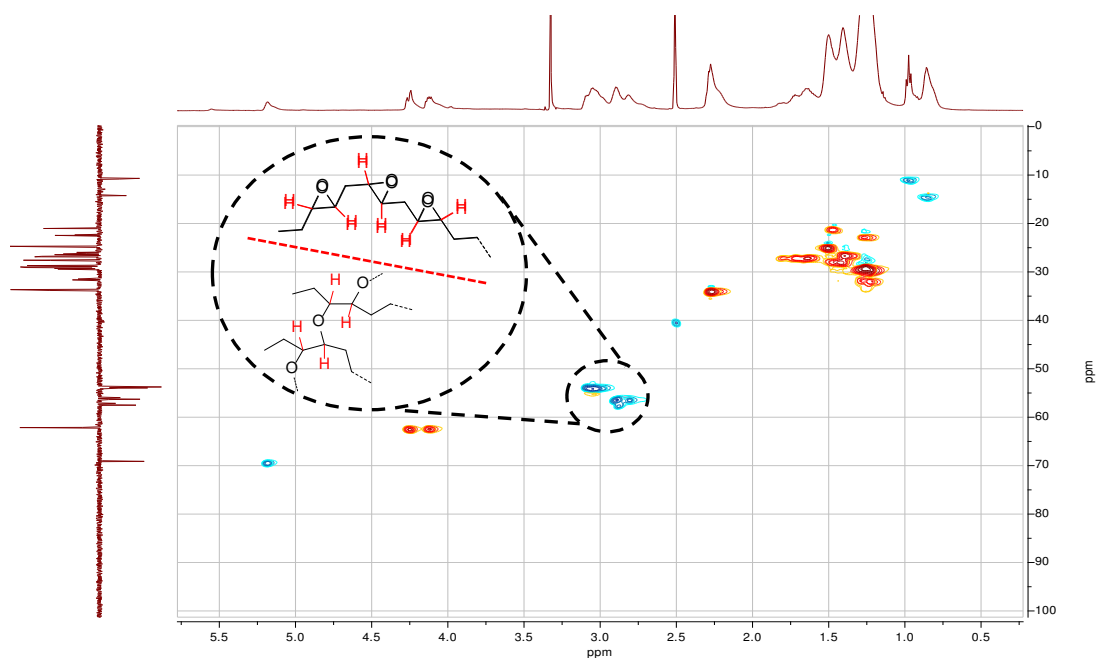


**Figure VI.73.** HSQC NMR of ELO homopolymer at  $t = 60$  min with associated methyne groups from ELO and ELO polymer fragment structure of linolenic moieties.

$^{13}\text{C}$  spectrum (**Figure VI.75**) and cross-peaks from HSQC for PFA (**Figure VI.71**) are present also in ELO50/FA50 copolymer signifying the presence of FA oligomer chains in the copolymer network. The characteristic peaks of PFA network have been assigned in agreement with the literature.<sup>17,18</sup> The  $^{13}\text{C}$  spectra reveal essentially two quaternary carbons due to the new environment of the furanic oligomer chains: the peak at 151.7 ppm ( $\text{C}_2'$ ), correlated with the terminal substituted furan ring, and the signal at around 150.6 ppm ( $\text{C}_2/\text{C}_5$ ) attributed to the 2,5-disubstituted furan rings. Cross-peaks from HSQC for PFA could be assigned to furanic

oligomer: 142.2 ppm ( $C_5$ ); 110.1 ppm ( $C_4$ ); around 107.6 ppm ( $C_4/C_3$ ) and 106.8 ppm ( $C_3$ ). Cross-peaks at 63.2 ppm could correspond to the methylene of (fu- $\underline{CH_2}$ -O- $\underline{CH_2}$ -fu), and the signal at 27.1 ppm attributed to the  $CH_2$  bridge between two furan rings. The main evolution of signal has been accompanied with the apparition of methynes cross-peaks detectable within the black square on ELO50/FA50 HSQC (**Figure VI.74**): between 70.5 and 84.4 ppm for 135 DEPT  $^{13}C$  signals correlated with the  $^1H$  spectrum signals between 3.1 and 4.6 ppm. The shifts of these signals are generally associated with methyne ether. A methylene cross-peak signal at 63.8 ppm for the  $^{13}C$  and 4.45 ppm for  $^1H$  are also new and is missing on PFA spectra. This can be associated with the furan methylene ( $C_{11}$ ) cross-linked to ELO by an ether link: fu- $\underline{CH_2}$ -O-CH-ELO, (**Figure VI.74 small black square**). This correlation confirmed by the weak intensity of  $^{13}C$  signal suggests the presence of linkage between the furanic methylene and ELO moieties.

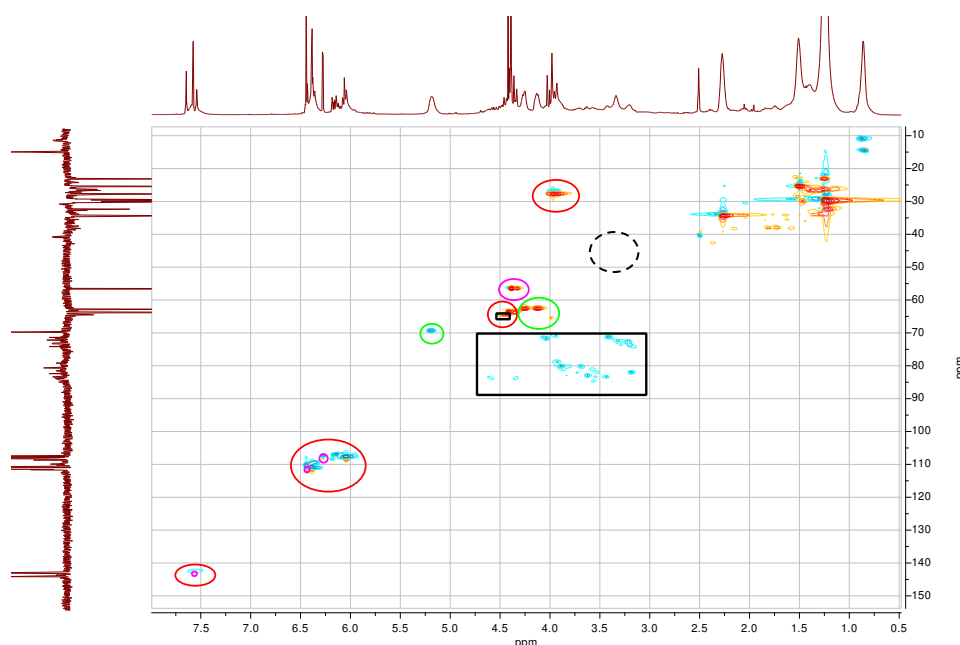


**Figure VI.74.** HSQC NMR of ELO50/FA50 at  $t = 60$  min with cross-peaks attributed to ELO (green), FA (pink), PFA (red), ELO/FA interaction (black) and disappearance of ELO epoxies signals (dash black)

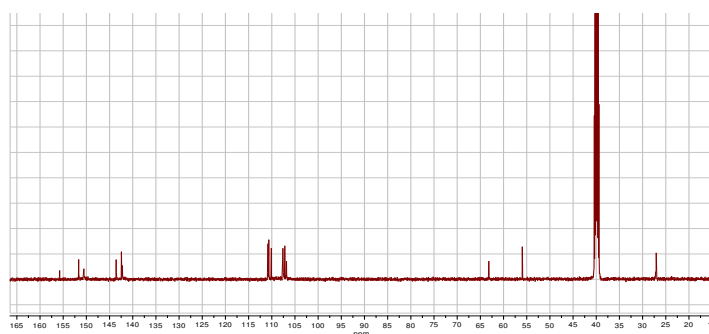


**Figure VI.75.**  $^{13}C$  NMR of PFA at  $t = 60$  min.

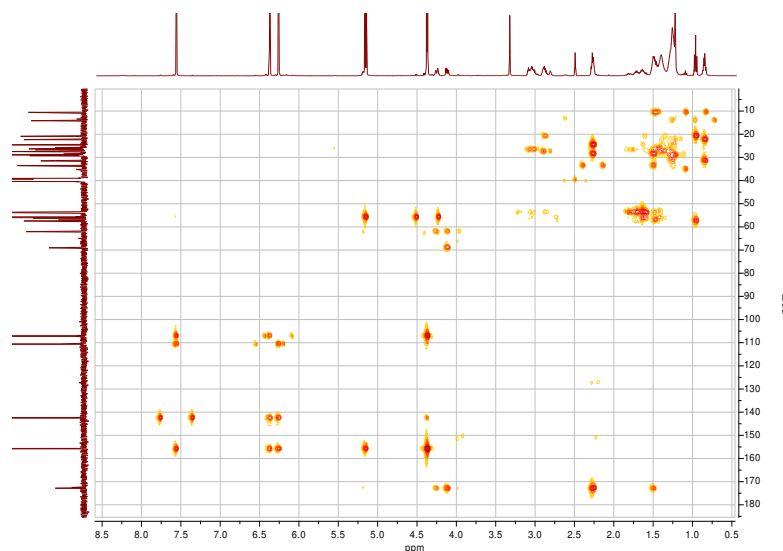


**Figure VI.76.** HMBC NMR of ELO50/FA50 at t=0.

To confirm the connectivity between FA and ELO, the different bonds linkage correlated with the  $J_{CH}$  has been established by HMBC NMR experiments. The HMBC spectrum of ELO50/FA50 t= 60 min is illustrated in **Figure VI.77 (purple zone)** and shows that no transesterification occurs between FA and the tri-ester part of ELO, at this polymerization stage. The cross-peaks of ester quaternary carbon presents the same environment in ELO50/FA50 HMBC at t=0 (**Figure VI.76**) and at t= 60 min suggesting the non-alteration of glycerol moieties from triglyceride (hydrolysis could be avoid or at least not significant at this extent of conversion). Indeed, in agreement with the molecule model investigated by Choura et al.<sup>5</sup>, the methylene proton (fu- $\underline{CH_2}$ -O-CO- $\underline{CH_3}$ ) having a signal at 4.5 ppm, is not present here (**Figure VI.77**), also in correlation with  $^{13}C$  ester signal. Moreover, furanic quaternary carbon could be found in a range of 150-160 ppm, not present in the PFA  $^{13}C$  (**Figure VI.75**), confirming the new environment of FA oligomer provided by the covalent bonding with ELO moieties. It is also important to notice the low probability of epoxy ring-opening by the water generated by the FA polycondensation, because of its volatilization in the opened system during isotherm cross-linking at 120°C.

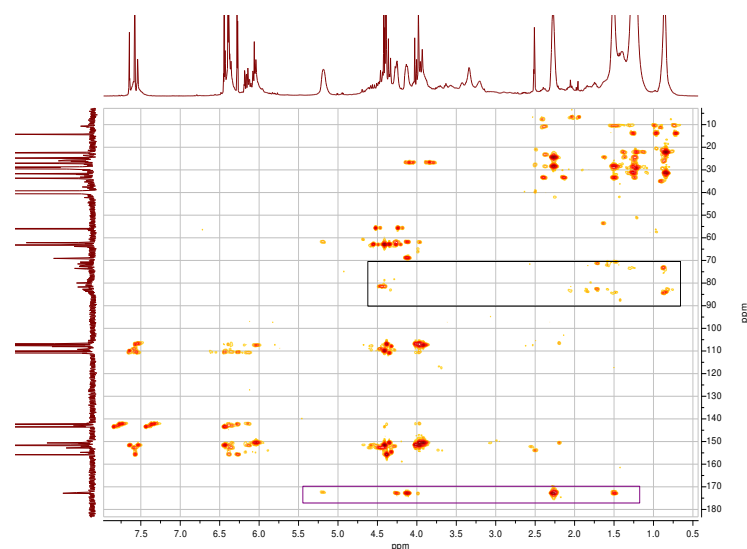


**Figure VI.77.** HMBC NMR of ELO50/FA50 at  $t = 60$  min (black zone) (purple zone of glycerol quaternary carbon)

The **Figure VI.78** emphasizes the HMBC spectrum in the range of interest that could correspond to the chemical interactions between ELO and FA. **Figure VI.78 (1)** highlights the environment of methyne carbon in ELO/FA network between 70 and 85 ppm, essentially correlated to  $^3J_{CH}$ . The postulated ELO / FA linking are emphasized with the structure presented in **Table VI.12**. Indeed, the  $^3J_{CH}$  correlation of methyne cross-peaks ( $C_8$ ) at around 81,8 ppm with the proton from the methylene  $H_{11}$  at 4.45 ppm is a proof that the  $CH_2-OH$  of FA opens the oxiran ring of ELO. This information, reliable with the literature<sup>13</sup>, explains the shift of the methyne link of furanic ether moieties (between 79 and 85 ppm), and those corresponding to the shift range of methyne link of the hydroxyl part (between 70 and 75 ppm), respectively, represented in zone B and A in HSQC spectrum in **Figure VI.78 (2)**. The zones (A1 et B1) on **Figure VI.78 (1)** could correspond to the methyl cross-peaks of linolenic epoxidized moiety, highly present on the linseed oil (in average 56.6 %)<sup>19</sup>. In the A1 zone, only one cross-peak is observed at 73.5 ppm ( $C_9$ ) and could be related with the hydroxy-methyne associated in  $^3J_{CH}$  to the methyl at 0.86 ppm ( $H_6$ ). Meanwhile, we can observe several cross-peaks in B1 zone, corresponding to the  $^3J_{CH}$  correlation between furanic methyne-ether and the linolenic methyl group. The presences of these peaks could be explained by different environments, probably providing by oligomers from FA polycondensation. The methylene cross-peaks located in the A2 and B2 zone are also correlated in  $^3J_{CH}$  to the hydroxy-methyne and ether methyne, respectively. The concerned atoms are mostly associated with isomers  $H_7/H_{7'}$  and  $H_{10}/H_{10'}$  (**Table VI.12**), with generally a more important shielding for  $H_{10}/H_{10'}$ .

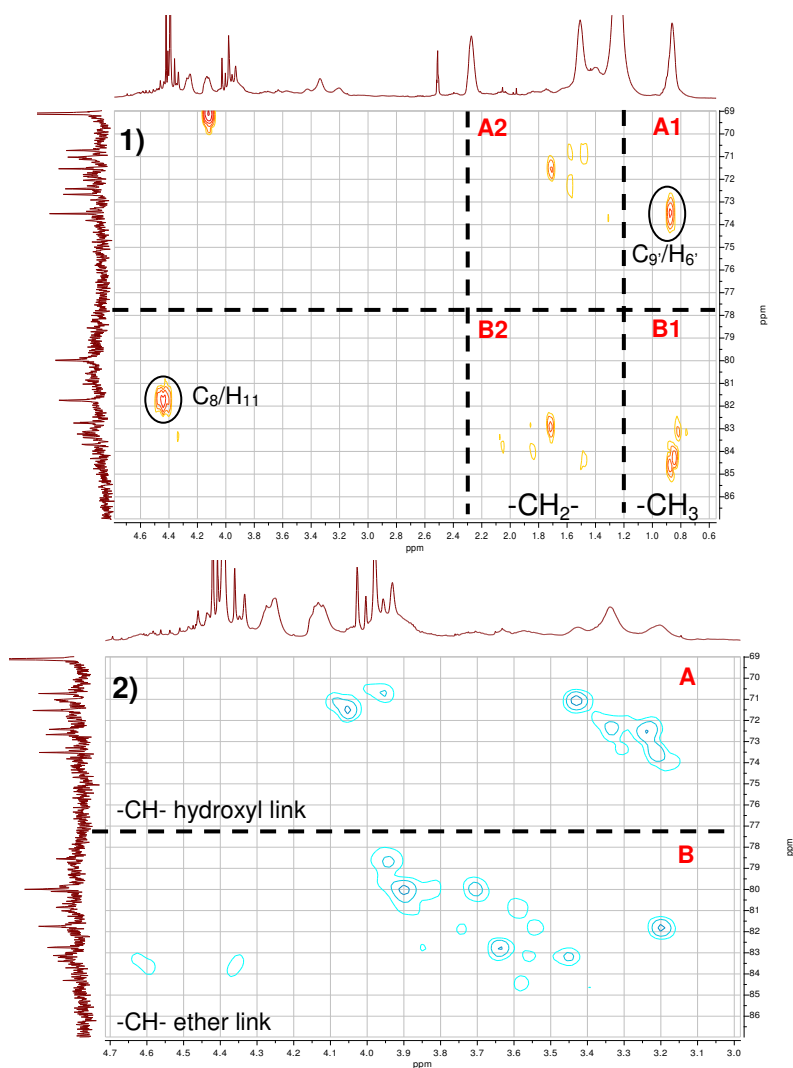


**Figure VI.78.** Zoom of HMBC (1) and HSQC (2) NMR ELO50/FA50  $t = 60$  min (black square in figure 72 and 75)

In the light of FT-IR and NMR studies, the **Figure VI.79** proposes a structural model for the ELO50/FA50 network where the principal reaction of copolymerization between ELO and FA/FA-oligomer also with FA polycondensation and Diels Alder reactions are highlighted.

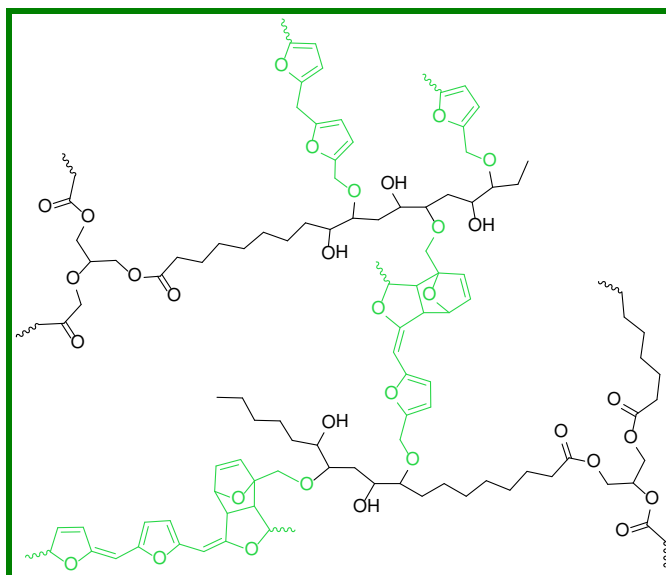


**Figure VI.79.** Putative structure for ELO50/FA50 copolymer fragment network in agreement with the structural investigations (in black chains from ELO and in green from FA)

### VI.3. Thermo-mechanical study of ELO50/FA50 thermoset material

#### VI.3.1. Elaboration of resin bulk for mechanical analysis

Thermoset bulk preparation for tensile tests and dynamic mechanical analysis (DMA) occurred in two steps. The first one consists in a pre-curing as oligomerization/prepolymerization, and the second is the resin curing into a mold. The PFA used as reference material is elaborated with a mix of FA and BF<sub>3</sub>:NH<sub>2</sub>Et as Lewis acidic initiator with respectively a ratio of 100/1 in weight. This solution was stirred and heated to 120°C during 80 min to reach a high viscosity (gel state). Then, the pre-polymer has been transferred into a mold of 80 x 25 x 30 mm (length x width x thickness) and heated at T=160 °C during 120 min under a pressure at 10 bars to avoid any eventual ununiformities of the material due to water releases during the FA polycondensation. Then the sample has been heated to 180°C for 180 min in an oven, to ensure cure completion. To measure the influence of the ELO co-monomer in the PFA network, a resin of ELO/FA/BF<sub>3</sub> has been elaborated with a ratio of (50/50/1). This copolymer was prepared in the same condition as PFA following a temperature program of 130°C for 120 min, 160°C for 120 min under 10 bars and finally at 180°C for 120 min. Experimental details are described on **section III.2.6**.

#### VI.3.2. ELO/FA bio-based thermoset characterization by dynamic mechanical analysis (DMA)

Amorphous polymers comport different molecular motions which depend on the time-temperature scale and can be easily discriminated by DMA. At low temperatures (or short time),

the so-called secondary relaxations are associated with local motions such as rotation of lateral groups (referred as  $\gamma$  relaxation) or motions of main chain segment ( $\beta$  relaxation). At higher temperatures (or longer time), the so-called  $\alpha$  relaxation corresponds to the cooperative motions of main chains. This  $\alpha$  relaxation is expressed in DMA as  $\tan \delta$  and causes very large changes in the mechanical properties of the material being known as the glass transition.<sup>20</sup> The **Figure VI.80** shows the evolution of storage modulus ( $E'$ ) and  $\tan \delta$  for the neat PFA and the ELO50/FA50 network.

The PFA presents a main relaxation peak at  $T_\alpha \approx 145^\circ\text{C}$  which is typical for highly cross-linked thermosets. Nevertheless, the very small amplitude of the  $\tan \delta$  peak attests a very low damping capacity of the material and thus indicates that PFA is a brittle thermoset. Moreover the range of the  $\alpha$  relaxation peak is very broad ( $\approx 150^\circ\text{C}$ ) indicating a large distribution of relaxation times. This can be associated with an heterogeneity of cross-linking within the neat PFA. The insert graphic in **Figure VI.80** helps to highlight a very small relaxation peak at  $T_\beta \approx -75^\circ\text{C}$  which could correspond to very local motions of few furanic entities.

The DMA results for ELO50/FA50 thermoset are very different in comparison with the PFA reference network. It presents a major peak relaxation at around  $20^\circ\text{C}$  which could be associated with the main  $\alpha$  relaxation process of the copolymer network. Compared to the neat PFA, a relaxation at such low temperature is the consequence of a much more flexible network due to the triglyceride aliphatic contribution. The  $\alpha$  relaxation process exhibits higher intensity that indicates higher damping capacity through energy dissipation for this flexibilized network. Above  $100^\circ\text{C}$ , a second and rather small relaxation shoulder (i.e. short decrease in  $E'$ ) is observed and could correspond to the cooperative motions of furanic entities that aren't flexibilized by ELO frame. Indeed, the relaxation occurs within the same temperature range of neat PFA. At lowest temperatures (from  $-150^\circ\text{C}$  to  $-25^\circ\text{C}$ ), the  $\tan \delta$  peak exhibits complex variations and shoulders which could attest for local motions of the copolymer. Thus, in contrast with the PFA, the ELO50/FA50 thermoset presents a small  $\gamma$  relaxation at around  $T_\gamma \approx -140^\circ\text{C}$  which could be associated with the rotation of methyl or hydroxyl groups, mostly generated by the epoxy-alcohol opening reaction<sup>2</sup>, and the sub-motion of methylene groups from ELO alkyl part.<sup>21</sup> At  $T_{\beta 1} \approx -75^\circ\text{C}$  and  $T_{\beta 2} \approx -40^\circ\text{C}$  other relaxations are observed which could correspond to local motions of copolymer. The free moving dangling of alkyl chains present in the network after cross-linking as well as the local breathing of furanic entities could be the origin and are related with these relaxations. More precisely, the  $\beta_1$  relaxation is in the same temperature range as  $\beta$  relaxation exhibited in neat PFA, and thus could be mostly attributed to motion issued from

furanic moieties. The  $\beta_2$  relaxation is on the same range temperature of that observed for ELO/anhydride thermoset network (see **Chapter IV**), and thus potentially associated with the alkyl chain motions from ELO.

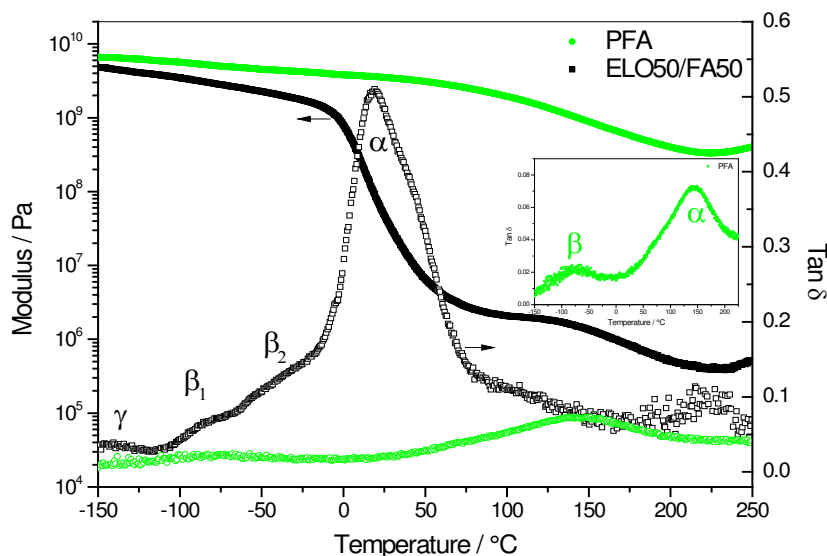


**Figure VI.80.** Storage modulus ( $E'$ ) and  $\tan \delta$  evolutions of ELO/FA thermoset (black) compared with PFA network (green); the insert represent a zoom of PFA curve.

### VI.3.3. Tensile test experiments and fracture analysis by SEM

**Figure VI.81** shows the tensile tests results on stress-strain curves of PFA and ELO50/FA50 thermosets. For ELO/FA the ELO contribution of 50% in weight in the PFA matrix gives a copolymer with a very different mechanical response. The PFA curve is characteristic to a brittle and fragile material, with mostly an elastic response and a small deformation of about 5%. In comparison, the ELO50/PFA50 curve exhibits a more ductile behavior with a higher deformation of about 40%. In agreement with the DMA results, the ELO50/FA50 copolymer thermoset presents higher flexibility which gives as outcomes a lower  $T_\alpha$  and a higher ductility. The values of Young's modulus and the tensile strength at break are summarized in **Table VI.13**. The mechanical properties of the PFA material are in agreement with those found by Pranger et al.<sup>22</sup> Thus, a modulus of around 1 GPa has been obtained for the PFA and around 44 MPa for ELO50/FA50 copolymer. For the tensile strength values at break, the PFA value is around 40 MPa vs. 7 MPa for ELO50/FA50. These differences could be explained by different viscoelastic states. In good agreement with the DMA experiment, at the tensile test experiment temperature ( $\approx 20^\circ\text{C}$ ), the PFA is in the glassy state, while ELO50/FA50 is in the leathery region. The SEM micrographs on **Figure VI.81** exhibit the fracture surface of PFA and ELO50/FA50 thermosets. The difference between these two materials is highlighted by the surface morphology. In good

agreement with stress-strain curves, the **Figure VI.81 (A)** for the PFA, shows a surface with a lot of asperities, characteristic of a brittle material.<sup>23</sup> In contrast as shown in **Figure VI.81 (B)**, ELO50/FA50 fracture reveals a sharp cutting and a very homogeneous and smooth surface: no phase separation was observed. This last result is very important for ELO50/FA50 characterization and corroborates with the precedent structural investigations and with the thermo-mechanical results as consequences of the presence of covalent linkages between FA/FA oligomers and ELO on building the frame of ELO/FA copolymer network.

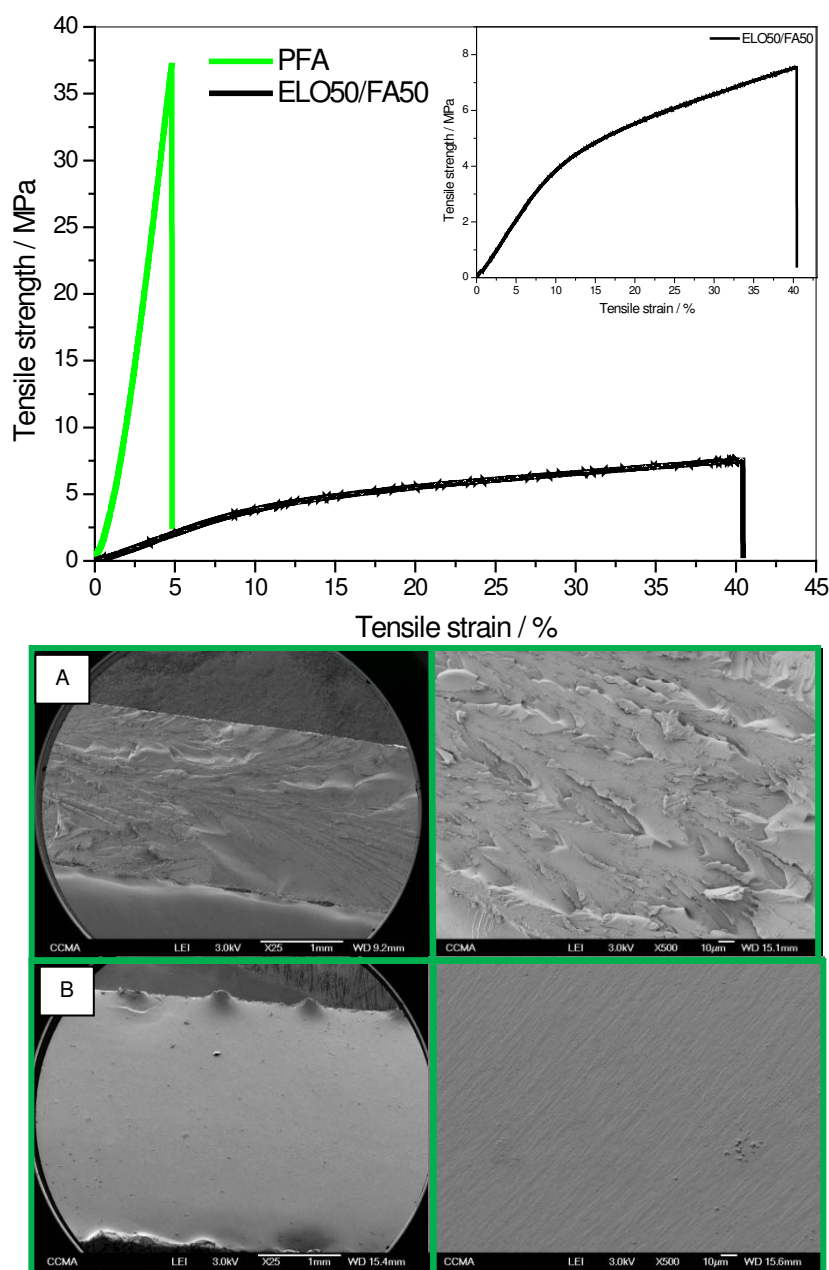


**Figure VI.81.** Stress–strain curves and SEM fracture surface (A: PFA; B: ELO50/FA50)

**Table VI.13.** Young's modulus and tensile strength at break for cured thermosets

	Young's modulus (MPa)	Tensile strength at break (MPa)
ELO50/FA50	$44.34 \pm 4.45$	$7.33 \pm 0.93$

### VI.3.4. Thermogravimetric analysis (TGA)

The thermal stabilities of PFA and ELO/FA thermosets have been studied with the help of thermogravimetric analyses. As shown in TGA curves presented in **Figure VI.82**, below 300°C no mass loss is observed on the two materials. This observation indicates that the materials didn't exhibit significant volatilization of unreacted monomers or oligomers, thus we could conclude to an optimal cross-linking. The TGA result for PFA network presents a remarkable thermal resistance,  $T_{d,10\%} = 402^\circ\text{C}$  while that of the ELO50/FA50 has an inferior temperature of decomposition  $T_{d,10\%} = 364^\circ\text{C}$ . These thermal decomposition temperatures are comparable with that of conventional thermosets such as epoxy resins.<sup>24</sup> ELO50/FA50 copolymer also exhibits a higher degradation rate in a smaller temperature range (typically 300 to 600°C) compared to PFA.

The complex degradation mechanism of ELO50/FA50 network can be divided in three main steps (centered at 400, 450 and 550°C) according to the peaks of derivative weight loss. Thus the first step of degradation could probably be attributed to the breaking of C-O ether issued from ELO/FA linkage, i.e. the connection of ELO with furanic moieties, followed by the thermolysis of ester part from glycerol moieties. The third step is due to final carbonization and oxidation. Neat PFA network shows a slower degradation rate between 300 and 550°C followed by a more complex degradation from 550 to 900°C. As stated in a previous study,<sup>25</sup> the chain scissions occur first on methylene and methyne extra-ring linkages and then on furanic rings.

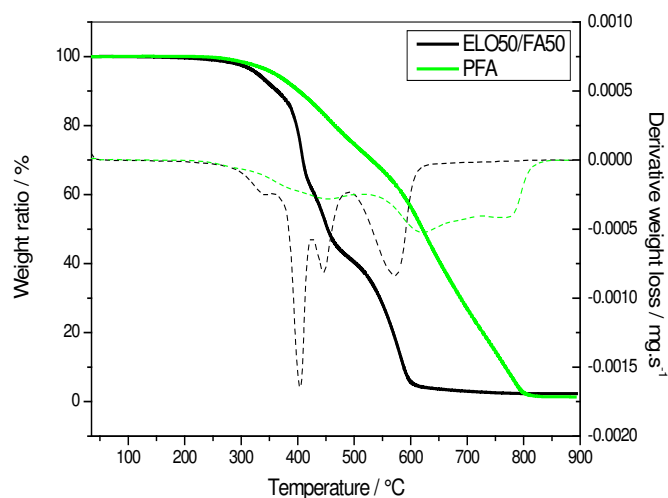


**Figure VI.82.** TGA of cured bio-resins under air flow ( $50 \text{ mL}\cdot\text{min}^{-1}$ ) at  $10^\circ\text{C}\cdot\text{min}^{-1}$ .

#### **VI.4. Conclusions**

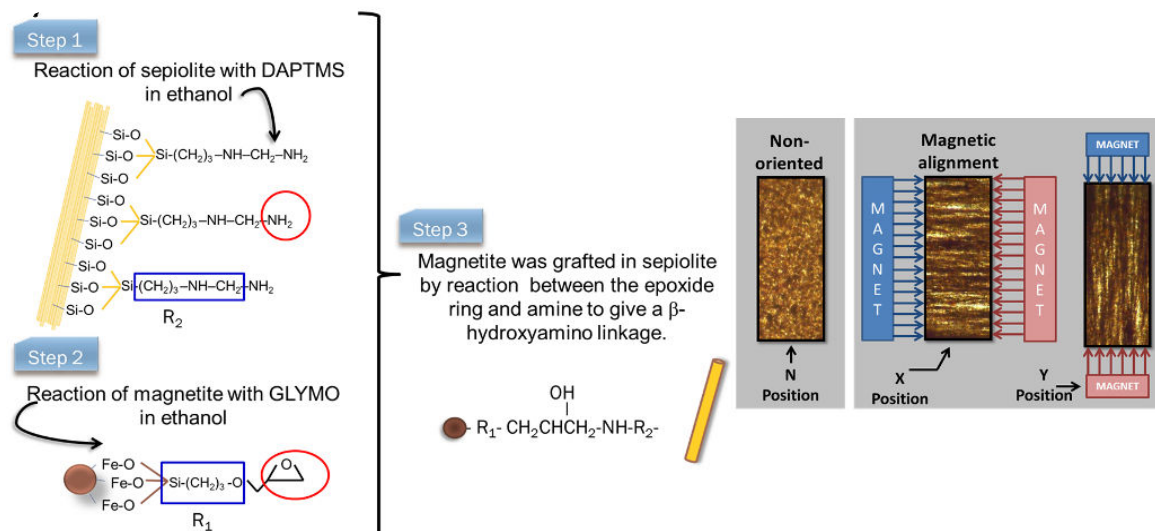
This study reveals a successful combination of two bio-based monomers, ELO and FA, to design fully biobased material through a cationic copolymerization. This cationic reactivity has been fruitfully investigated by IR and NMR spectroscopies with the relevant proof that covalent bonds were created between alcohol functions of neat FA/FA oligomers and epoxy functions of ELO. The DMA and SEM observations confirm the macroscopic homogeneity of the bulk cross-linked materials. The mechanical properties of ELO50/FA50 exhibit a semi-ductile behavior with a strain of about 40 %, while the PFA presents a strain of about 5%, characteristic to brittle materials. Herein, this study tackles out the main issues regarding the development of furanic thermosets which are limited by their brittleness. Smart incorporation of triglyceride networks through the dense furanic counterpart disturbs the cross-linking density of PFA. The combined material is more flexible without sacrificing the thermal performance, which could expand the range of potential applications as semi-ductile biobased thermosets.

1. Vilela, C.; Cruciani, L.; Silvestre, A. J.; Gandini, A., A Double Click Strategy Applied to the Reversible Polymerization of Furan/Vegetable Oil Monomers. *Macromol Rapid Commun* **2011**.
2. Henry Lee, K. N., *Handbook of epoxy resins*. Mc Graw-Hill Book Company ed.; 1982.
3. Raghavachar, R.; Sarnecki, G.; Baghdachi, J.; Massingill, J., Cationic, thermally cured coatings using epoxidized soybean oil. *J Coat Technol Res* **2000**, 72 (909), 125-133.
4. Park, S.-J.; Jin, F.-L.; Lee, J.-R.; Shin, J.-S., Cationic polymerization and physicochemical properties of a biobased epoxy resin initiated by thermally latent catalysts. *European Polymer Journal* **2005**, 41 (2), 231-237.
5. Choura, M.; Belgacem, N. M.; Gandini, A., Acid-Catalyzed Polycondensation of Furfuryl Alcohol: Mechanisms of Chromophore Formation and Cross-Linking. *Macromolecules* **1996**, 29 (11), 3839-3850.
6. Guigo, N.; Mija, A.; Vincent, L.; Sbirrazzuoli, N., Chemorheological analysis and model-free kinetics of acid catalyzed furfuryl alcohol polymerization. *Physical chemistry chemical physics : PCCP* **2007**, 9 (39), 5359-66.
7. Montero, A. L.; Montero, L. A.; Martínez, R.; Spange, S., Ab initio modelling of crosslinking in polymers. A case of chains with furan rings. *Journal of Molecular Structure: THEOCHEM* **2006**, 770 (1-3), 99-106.
8. Montserrat, S.; Flaqué, C.; Calafell, M.; Andreu, G.; Málek, J., Influence of the accelerator concentration on the curing reaction of an epoxy-anhydride system. *Thermochimica Acta* **1995**, 269-270 (0), 213-229.
9. Shechter, L.; Wynstra, J., Glycidyl Ether Reactions with Alcohols, Phenols, Carboxylic Acids, and Acid Anhydrides. *Industrial & Engineering Chemistry* **1956**, 48 (1), 86-93.
10. Barsberg, S.; Berg, R. W., Combined Raman Spectroscopic and Theoretical Investigation of Fundamental Vibrational Bands of Furfuryl Alcohol (2-furanmethanol). *The Journal of Physical Chemistry A* **2006**, 110 (30), 9500-9504.
11. Barsberg, S.; Thygesen, L. G., Poly(furfuryl alcohol) formation in neat furfuryl alcohol and in cymene studied by ATR-IR spectroscopy and density functional theory (B3LYP) prediction of vibrational bands. *Vibrational Spectroscopy* **2009**, 49 (1), 52-63.
12. Pin, J.-M.; Guigo, N.; Mija, A.; Vincent, L.; Sbirrazzuoli, N.; van der Waal, J. C.; de Jong, E., Valorization of bio-refinery side-stream products: combination of humins with polyfurfuryl alcohol for composite elaboration. *ACS Sustainable Chemistry & Engineering* **2014**.
13. Luo, Q.; Liu, M.; Xu, Y.; Ionescu, M.; Petrović, Z. S., Thermosetting Allyl Resins Derived from Soybean Oil. *Macromolecules* **2011**, 44 (18), 7149-7157.
14. Adhvaryu, A.; Erhan, S. Z., Epoxidized soybean oil as a potential source of high-temperature lubricants. *Industrial Crops and Products* **2002**, 15 (3), 247-254.
15. Okieimen, F. E.; Pavithran, C.; Bakare, I. O., Epoxidation and hydroxylation of rubber seed oil: one-pot multi-step reactions. *European Journal of Lipid Science and Technology* **2005**, 107 (5), 330-336.
16. Lathi, P. S.; Mattiasson, B., Green approach for the preparation of biodegradable lubricant base stock from epoxidized vegetable oil. *Applied Catalysis B: Environmental* **2007**, 69 (3-4), 207-212.
17. Chuang, I. S.; Maciel, G. E.; Myers, G. E., Carbon-13 NMR study of curing in furfuryl alcohol resins. *Macromolecules* **1984**, 17 (5), 1087-1090.
18. Principe, M.; Ortiz, P.; Martínez, R., An NMR study of poly(furfuryl alcohol) prepared with p-toluenesulphonic acid. *Polymer International* **1999**, 48 (8), 637-641.
19. Xia, Y.; Larock, R. C., Vegetable oil-based polymeric materials: synthesis, properties, and applications. *Green Chemistry* **2010**, 12 (11), 1893.
20. Pascault, J.-P.; Sautereau, H.; Verdu, J.; Williams, R. J., *Thermosetting polymers*. CRC Press: 2002; Vol. 64.
21. Dammont, F. R.; Kwei, T. K., Dynamic mechanical properties of aromatic, aliphatic, and partially fluorinated epoxy resins. *Journal of Polymer Science Part A-2: Polymer Physics* **1967**, 5 (4), 761-769.
22. Pranger, L. A.; Nunnery, G. A.; Tannenbaum, R., Mechanism of the nanoparticle-catalyzed polymerization of furfuryl alcohol and the thermal and mechanical properties of the resulting nanocomposites. *Composites Part B: Engineering* **2012**, 43 (3), 1139-1146.
23. Guigo, N.; Mija, A.; Vincent, L.; Sbirrazzuoli, N., Eco-friendly composite resins based on renewable biomass resources: Polyfurfuryl alcohol/lignin thermosets. *European Polymer Journal* **2010**, 46 (5), 1016-1023.

24. Vincent, L.; Mija, A.; Sbirrazzuoli, N., Liquid crystalline and isotropic epoxy thermosets: Mechanism and kinetics of non-isothermal degradation. *Polymer Degradation and Stability* **2007**, 92 (11), 2051-2057.
25. Steinmann, B., Investigations on the curing of epoxides with phthalic anhydride. *Journal of applied polymer science* **1990**, 39 (9), 2005-2026.

## Chapter VII

# Anisotropic Reinforcement of Epoxy-Based Nanocomposites with Aligned Magnetite-Sepiolite Hybrid Nanofiller



**Keywords:** Polymer-matrix composites (PMCs), short-fiber nanofillers, magnetic properties, mechanical properties.



<b>VII.1. Orientation of hybrid magnetic nanofiller into the epoxy thermoset .....</b>	<b>178</b>
VII.1.1. Strategy of hybrid nanofiller preparation and elaboration of nanocomposite. ....	178
<b>VII.2. Elaboration and characterization of the sepiolite hybrid nanofiller.....</b>	<b>179</b>
VII.2.1. Materials.....	179
VII.2.2. Synthesis of amino-modified sepiolite .....	180
<i>VII.2.2.1. Synthesis of SEP/DAPTMS.....</i>	<i>180</i>
<i>VII.2.2.2. Characterization by FT-IR, TGA and solid-NMR .....</i>	<i>180</i>
VII.2.3. Synthesis and structural characterization of glymo-modified magnetite particles .....	181
<i>VII.2.3.1. Synthesis of MAG/GLYMO.....</i>	<i>181</i>
<i>VII.2.3.2. Characterization by FT-IR and TGA.....</i>	<i>182</i>
VII.2.4. Preparation and characterization of magnetite-sepiolite hybrid nanofiller.....	183
<i>VII.2.4.1. Preparation of m-SEP .....</i>	<i>183</i>
<i>VII.2.4.2. Characterization by AAS, DSC, TEM and magnetization.....</i>	<i>183</i>
<b>VII.3. Thermomechanical anisotropy of epoxy nanocomposite .....</b>	<b>185</b>
VII.3.1. Preparation of m-sepiolite oriented fibers epoxy nanocomposite .....	185
VII.3.2. Morphologies alignment of m-sepiolite into the epoxy matrix .....	185
VII.3.3. Anisotropic thermomechanical properties of hybrid nanocomposite.....	186
<i>VII.3.3.1. Nanocomposite mechanical properties as a function of frequency.....</i>	<i>187</i>
<i>VII.3.3.2. Nanocomposite mechanical properties as a function of temperature .....</i>	<i>189</i>
<i>VII.3.3.3. Thermal stability of hybrid epoxy nanocomposites .....</i>	<i>190</i>
<b>VII.4. Conclusions .....</b>	<b>190</b>

## VII. Anisotropic Reinforcement of Epoxy-Based Nanocomposites with Aligned Magnetite-Sepiolite Hybrid Nanofiller Orientation of hybrid magnetic nanofiller into the epoxy thermoset

The mechanical reinforcement of epoxy matrices is usually enhanced by using anisotropic nanoparticles such as nanotubes or nanofibers-like fillers because of their high aspect ratio and high surface area<sup>1</sup>. This morphology makes them susceptible to orientation, thus imparting additional improvement of the mechanical performance of the corresponding epoxy nanocomposite<sup>2</sup>. This approach has been employed for the development of carbon nanotubes<sup>3</sup> and graphite-based epoxy nanocomposites<sup>4</sup> with increased mechanical and electrical as well as with anisotropic properties. This work proposes an original way by orientation of functionalized sepiolite fibers into the epoxy matrix to reach an enhancement of mechanical properties.

### VII.1.1. Strategy of hybrid nanofiller preparation and elaboration of nanocomposite.

Sepiolite as presented in the **section II.3.3.1.**<sup>5</sup> possess an acicular morphology which makes this natural clay mineral as very promising reinforcing nanofiller for epoxy systems. As sepiolite does not present any magnetic or electric properties which could help its alignment by applying an external magnetic or electric field, it must be previously functionalized with magnetic nanoparticles. As seen in the bibliographic part (**section II.3.3.**), very few studies focus on highly oriented polymer/nanoclay systems. If the fibers are made by a ferromagnetic material they could be oriented by the application of a magnetic field before and during the curing process. Actually, a class of these materials called magnetorheological elastomers (MRE) are made by ferromagnetic particles aligned in a matrix before curing and present the particularity to change their mechanical or electrical properties by application of a magnetic field.<sup>6</sup> The increase of modulus in this way is usually of the order of 1MPa, so it can represent 100% of increase in an elastomeric matrix, but no more than  $10^{-3}$  if the matrix is a fully cross-linked polymer of modulus in the range of 1GPa. The aim of this work is to show that it is possible to improve the mechanical properties of an epoxy resin by aligning sepiolite fibers inside the matrix with the help of a magnetic field.

More in details, the present study describes a new method to incorporate magnetite onto sepiolite surface, based on the reaction between sepiolite and magnetite previously functionalized with [3-(2-aminoethylamino) propyl] trimethoxysilane (DAPTMS) and 3-glycidoxypropyl-

trimethoxysilane (GLYMO), respectively. The functionalization of both fibers and particles were performed by the known hydrolysis/condensation reactions between the organo-silanes and the hydroxyl groups located on both sepiolite and magnetite surfaces. Then, the amine and epoxy groups of the functionalized sepiolite/magnetite could react promoting a strong covalent anchorage (chemical grafting). The general scheme for the preparation of the m-SEP fibers is illustrated in **Figure VII.83**. Then, the mechanical properties of epoxy-based nanocomposites have been investigated by dynamic mechanical analysis (DMA) for aligned and non-aligned materials to appreciate the efficiency of the alignment on the reinforcing of the epoxy matrix containing different amounts of magnetic grafted sepiolite.

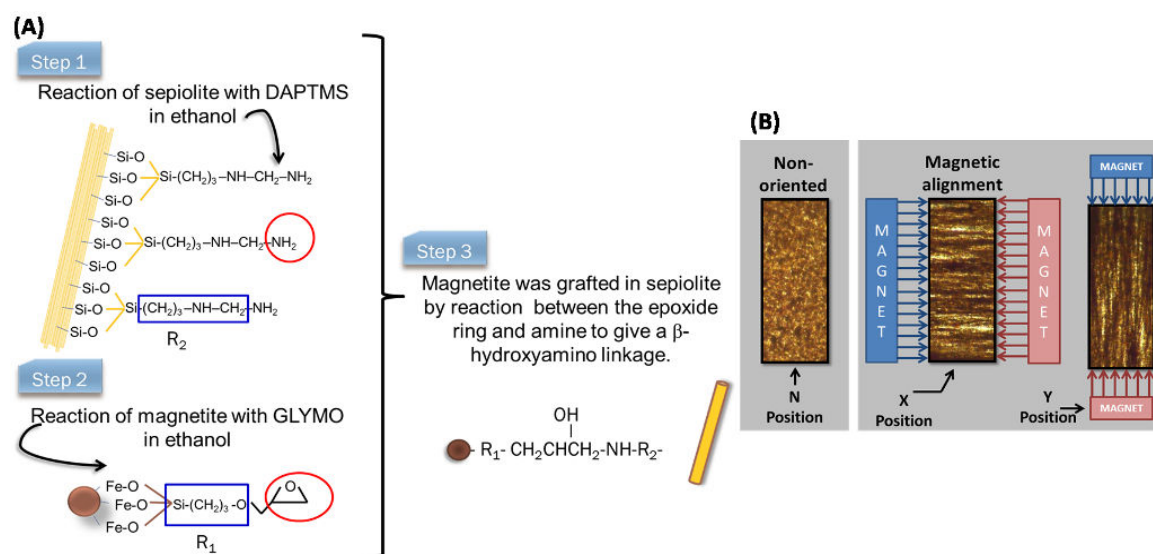


**Figure VII.83.** Procedure for grafting the magnetite particles onto the sepiolite fibers (A) scheme and optical microscopy for the non-oriented and two magnetically aligned m-SEP/epoxy composites (B)

## VII.2. Elaboration and characterization of the sepiolite hybrid nanofiller

### VII.2.1. Materials

Ferric chloride ( $FeCl_3 \cdot 6H_2O$ ; Aldrich, 97%), ferrous sulfate ( $FeSO_4 \cdot 7H_2O$ ; Aldrich, 99%), [3-(2-Aminoethylamino) propyl] trimethoxysilane (DAPTMS; Aldrich,  $\geq 80\%$ ), 3-glycidoxypropyl-trimethoxysilane (GLYMO; Aldrich,  $\geq 98\%$ ), ammonium hydroxide aqueous solution (Aldrich,  $\geq 25\% NH_3$  in  $H_2O$ ) glacial acetic acid (Aldrich,  $\geq 99.85\%$ ) and sulfuric acid (Aldrich, 95-98%), were used as received without further purification. Poly (propylene glycol) bis (2-aminopropyl ether) samples, with molar mass of 230 (PPGA230) and 2000 (PPGA2000) g/mol were also supplied by Sigma Aldrich and used as the hardener for the epoxy resin. Diglycidyl ether of bisphenol A (DGEBA) – based epoxy prepolymer (EPON 828, EEW= 185-192 g/eq,  $\rho=1.16 g/cm^3$ ) was purchased by Shell Chemicals - Brazil. Sepiolite Pangel (S9 grade, Tolsa)

was used without purification ( $\rho = 2.362 \text{ g/cm}^3$ ). De-ionized water (18.2M $\Omega$ ) was used in all synthesis.

## VII.2.2. Synthesis of amino-modified sepiolite

### VII.2.2.1. Synthesis of SEP/DAPTMS

Sepiolite was firstly ultrasonicated for 20 min in water using a high power ultrasound wave – BIOBLOCK (20 kHz and 750 W) working at 180 W (24% amplitude), to disaggregate the bundles and to obtain isolated sepiolite fibers. Then, the isolated fibers were dried at 100 °C for 12 hours before used, as suggested in the literature.<sup>7</sup> The dried sepiolite fibers were silanized according to the literature<sup>7b</sup>. In a typical procedure, 5 g of sepiolite fibers were dispersed into 100 mL of ethanol using an ultrasound tip for 20 minutes. Then, 5g of DAPTMS were added and the medium was heated under reflux at 60°C using mechanical stirring at 600 rpm for 3 hours. The functionalized sepiolite fibers were centrifuged, washed with ethanol and dried under reduced pressure, at 80 °C for 8 h. (**Figure VII.83 (A)** - Step 1).

### VII.2.2.2. Characterization by FT-IR, TGA and solid-NMR

Sepiolite modified with DAPTMS has been characterized by FT-IR, TGA and NMR<sup>29</sup> Si/MAS solid-state nuclear magnetic resonance spectroscopy. **Figure VII.84 (A)** compares the FT-IR spectra of sepiolite (Fig. 2(a)), DAPTMS (Fig. 2(b)) and SEP/DAPTMS (Fig. 2(c)). The spectra of DAPTMS and the SEP/DAPTMS present the characteristic absorption bands at 2933 and 1476  $\text{cm}^{-1}$  which are respectively ascribed to  $-\text{CH}_2$  stretching vibration and CH bending vibration. The modified sepiolite fiber presents the absorption band at 1569  $\text{cm}^{-1}$ , attributed to the bending vibration of the  $-\text{NH}_2$  group. These bands are not present in the spectrum of the pure sepiolite, confirming the grafting reaction of the amino-silane onto the sepiolite surface. Notice that the band at 1012  $\text{cm}^{-1}$  in the spectra of sepiolite and SEP/DAPTMS fiber is attributed to the Si-O-Si network. The NMR spectrum of the sepiolite in the **Figure VII.84 (B)** presents the characteristics peaks at -85.25, -92.42, -94.76 and -98.5 ppm refer to Si-OH, Si near edge, Si center and edge, respectively.<sup>8</sup> The peak at 85 ppm disappears in the spectrum of the modified sepiolite, which is an indication of the condensation of amino-silane on the sepiolite surface. These results are in good agreement with the FT-IR spectrum. Thermogravimetric analysis was applied to SEP and SEP/DAPTMS systems in order to determine the amount of DAPTMS grafted onto the sepiolite fibers (**Figure VII.84 (C)**). The first decomposition step of both samples, occurs between 25 and 150°C and corresponds to the physical desorption of water

molecules on the sepiolite surface.<sup>7b, 8b</sup> Pure sepiolite also presents three well defined degradation steps, from 200 to 900°C, attributed to the structural water, dehydroxylation of silanol and magnesium hydroxide present in the clay mineral. These three steps are not well defined in the case of modified sepiolite (SEP/DAPTMS) because of the superposition of the amino-silane degradation which occurs during this range of temperature.<sup>8b</sup> From the values of mass loss observed for functionalized and non-functionalized sepiolite, it is possible to determine the amount of DAPTMS grafted onto the sepiolite fiber as around 6 wt%.

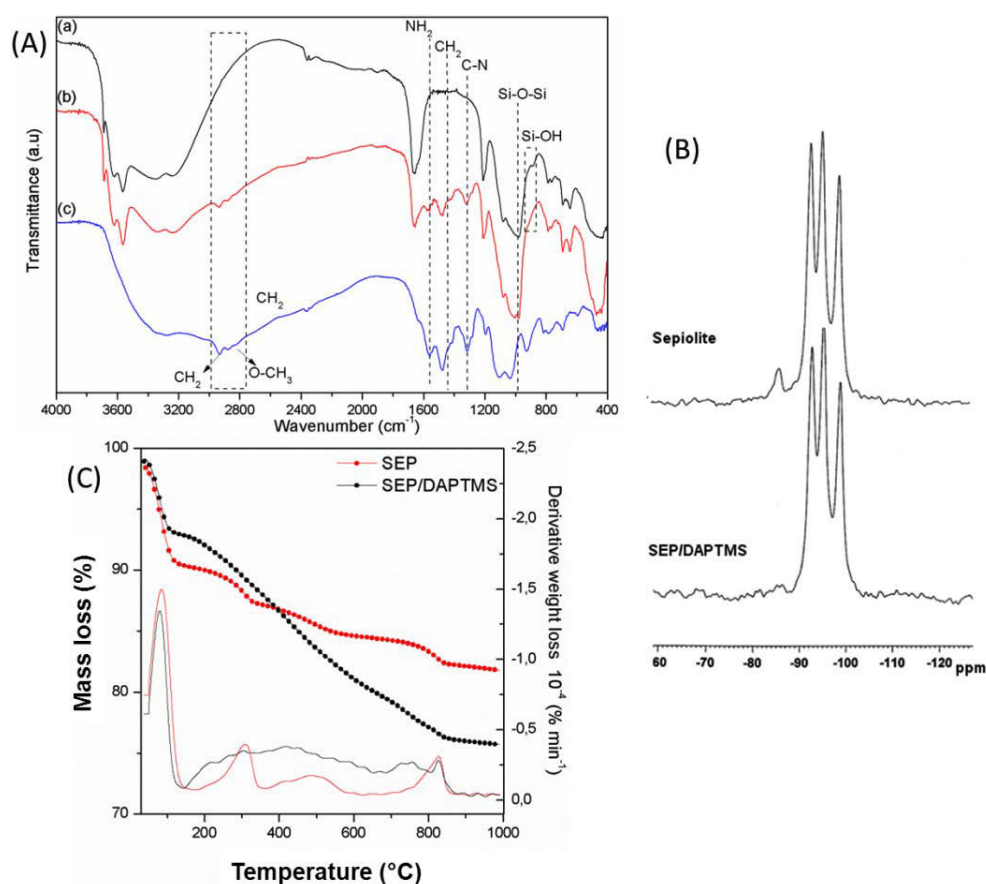


**Figure VII.84.** Characterization of sepiolite and SEP/DAPTMS grafted sample: (A) FT-IR patterns of sepiolite (a), sepiolite/DAPTMS (b) and DAPTMS(c). (B) NMR<sup>29</sup>Si/MAS spectra and (C) TGA curves of sepiolite and SEP/DAPTMS

### VII.2.3. Synthesis and structural characterization of glymo-modified magnetite particles

#### VII.2.3.1. Synthesis of MAG/GLYMO

For the synthesis of the magnetite particles, 4.250 g of FeCl<sub>3</sub> and 2.675 g of FeSO<sub>4</sub> were dissolved into 100 mL of water, under mechanical stirring at 70°C and 600 rpm ; then 10.5 mL

of  $\text{NH}_4\text{OH}$  aqueous solution (25vol%) were added and the stirring was kept for 5 min until the suspension became black. These formed magnetic particles were washed with distilled water to completely remove the  $\text{NH}_4\text{OH}$ , and with ethanol, five times, and finally kept in the ethanol medium (the pH of the medium was adjusted to 4 with glacial acetic acid). For the magnetic particles functionalization, 1.2 g of GLYMO was added to the ethanolic dispersion containing the magnetic particles and kept under mechanical stirring for 3 hours at 70° C. The unreacted GLYMO was removed from the medium by washing four times with ethanol. (**Figure VII.83 (A)** - Step 2).

#### VII.2.3.2. Characterization by FT-IR and TGA

Magnetite, functionalized with GLYMO (MAG/GLYMO), was characterized by FT-IR and TGA analysis. **Figure VII.85 (A)** compares the FT-IR spectra of magnetite, MAG/GLYMO and GLYMO. The absorption bands at 2921 and 2849  $\text{cm}^{-1}$ , correspond to C-H stretching, while the band at 1449  $\text{cm}^{-1}$  can be assigned to the  $\text{CH}_2$  bending, present in both GLYMO and MAG/GLYMO spectra confirming the grafting assumption of silane precursor on the magnetite surface.<sup>9</sup> The MAG/GLYMO hybrid particle exhibits several absorption bands at 619, 581 and 459  $\text{cm}^{-1}$ , which is usually associated to the Fe-O bond of magnetite nanoparticles, therefore this is a confirmation of the presence of magnetite in the hybrid particle.

The thermal decompositions of magnetite and MAG/GLYMO are illustrated in the **Figure VII.85 (B)**. Magnetite presents two main degradation events. A first one in the range of 200 – 450°C, related to the transformation of ferro-ferric oxide (magnetite) in ferric oxide (maghemite).<sup>10</sup> Then, a second one in the range of 600-800°C, assigned to the transformation of magnetite and maghemite in hematite ( $\alpha\text{-Fe}_2\text{O}_3$ ).<sup>11</sup> MAG/GLYMO hybrid particle presents a mass loss at 25-150°C, attributed to the evaporation of water and probably ethanol releases during the condensation process of GLYMO. The two other degradation steps are similar to pure magnetite previously described.

The third degradation step starts at around 500°C and could include the decomposition of the silane moiety. From the values of mass loss observed for functionalized and non-functionalized magnetite it is possible to determine the amount of GLYMO grafted onto the magnetite particles as around 5 wt%.

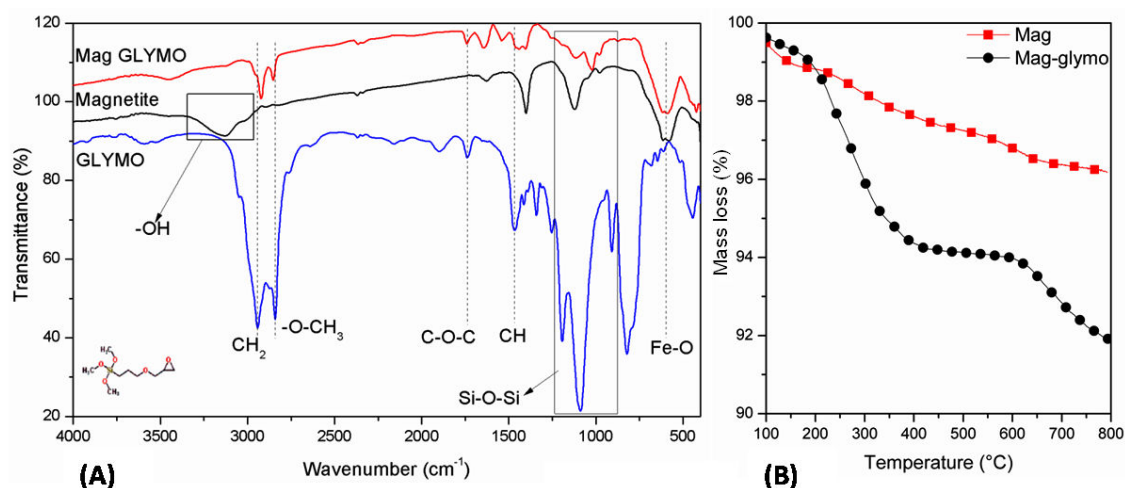


**Figure VII.85.** FT-IR patterns of magnetite and magnetite/GLYMO particles (A) and TGA curves of magnetite and MAG/GLYMO (B)

#### VII.2.4. Preparation and characterization of magnetite-sepiolite hybrid nanofiller

##### VII.2.4.1. Preparation of *m*-SEP

A dispersion of 5 g of SEP/DAPTMS in 100 mL of ethanol was mixed with an ethanolic dispersion containing 2 g of MAG/GLYMO. Then, 15 mL of an aqueous solution of sulfuric acid (0.228M) was added as catalyst of epoxy-amine reaction to form the  $\beta$ -hydroxyamino linkages. The resulting dispersion was kept under reflux and mechanical stirring at 70°C and 600 rpm for 3 hours. The dispersion containing *m*-SEP fibers (hybrid fibers) was washed with ethanol and kept in ethanol solution (**Figure VII.83 (A)** - step 3).

##### VII.2.4.2. Characterization by AAS, DSC, TEM and magnetization

The theoretical density of the magnetic sepiolite fiber was equal to 2.64 g/cm<sup>3</sup> and the volume fraction of magnetite in sepiolite of around 0.106 has been determined by atomic absorption spectrometry. To confirm the presumed reaction between the epoxy and amine groups, dry mixtures of SEP/DAPTMS and MAG/GLYMO have been prepared at the same conditions used for hybrid synthesis but without catalyst. This mixture was analyzed by DSC (**Figure VII.86 (A)**): the first run corresponds to the temperature program from 25°C to 250°C at 10 °C.min<sup>-1</sup>. An exothermic peak is present between 100°C and 150 °C ( $\Delta H \approx 8.62$  J/g), which is in general

the epoxy/amine temperature range of reaction. The second run did not show any exothermic peak, which means that all possible reactions at this temperature range were already completed. Herein, this experiment highlights the creation of covalent bonding between sepiolite and magnetite nanoparticles. Moreover, the transmission electron microscopy (TEM) image in **Figure VII.86 (B)** reveals a good anchorage of nanoparticle onto sepiolite surface. Similar results have been described in literature by González-Alforo et al.<sup>12</sup> for the preparation of dry ferrofluids. Their purpose was to immobilize the nanoparticles on the sepiolite surface by physical interactions with hydroxyl groups. They have shown that this immobilization is possible by thermal treatment at around 500°C in air flux, allowing a partial oxidation of magnetite to maghemite.

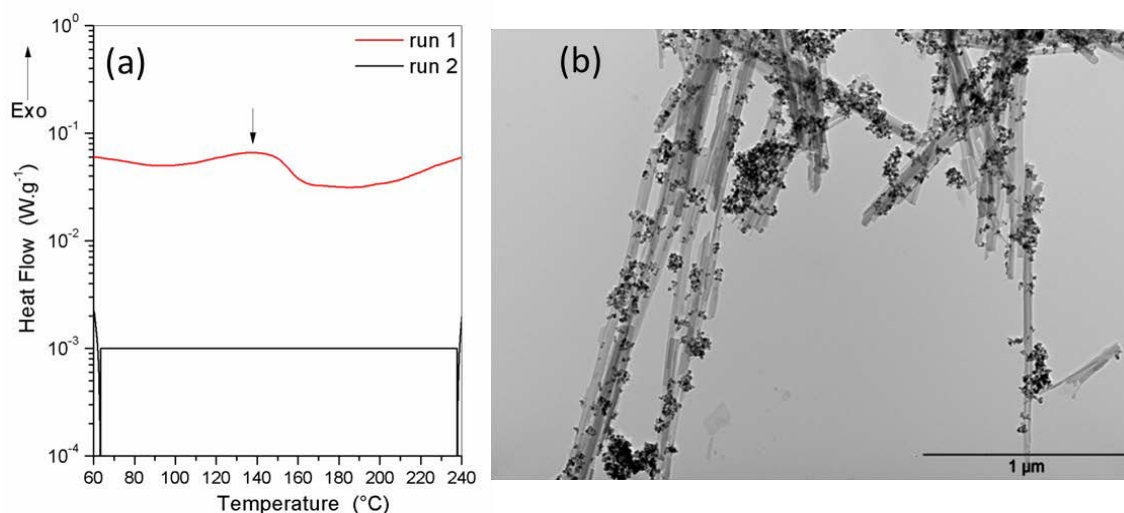


**Figure VII.86.** DSC curves for the reactions of a dry mixture of sepiolite with DAPTMS (run1) and MAG/GLYMO (run2) (A) and resulting TEM micrographs of hybrid directly obtained after reaction (B).

The saturation magnetization curves of the magnetite, the MAG/GLYMO and of the m-SEP hybrid in a powder form are illustrated in **Figure VII.87**. The saturation magnetization,  $M_s$ , of pure magnetite was found to be around 449 kA/m, which is comparable with the values reported in the literature.<sup>13</sup> The MAG/GLYMO and m-SEP hybrid fibers present superparamagnetic properties with  $M_{s(\text{MAG/GLYMO})} = 395$  kA/m and  $M_{s(\text{m-SEP})} = 53$  kA/m, respectively. The volume fraction,  $\phi_m$ , of magnetite in mixture can be obtained by the relationship  $\phi_m = M_{s(\text{m-SEP})} / M_s$ ;<sup>14</sup> thus  $\phi_m = 0.118$  which is close to the value of 0.106 that was determined by AAS. Also the organosilane volume fraction,  $\phi_{os}$ , in the magnetite is  $\phi_{os} = 1 - M_{s(\text{MAG/GLYMO})} / M_s = 0.12$ .

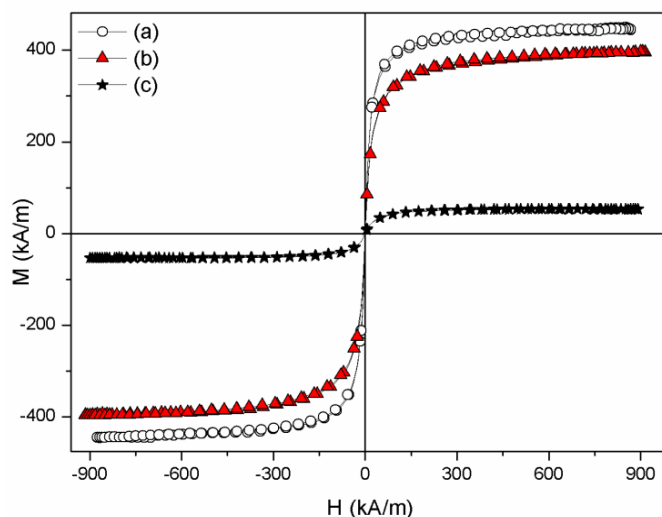


**Figure VII.87.** Magnetic curves at room temperature of pure magnetite (a), MAG/GLYMO (b) and m-SEP (c)

### VII.3. Thermomechanical anisotropy of epoxy nanocomposite

#### VII.3.1. Preparation of m-sepiolite oriented fibers epoxy nanocomposite

The m-SEP fibers in ethanol solution were dispersed into the DGEBA matrix with the help of a sonication using a Branson Sonifier® S-450D digital ultrasound apparatus operating at 40 W for 20 min. Separately, the polyetheramines (PEA230 and PEA2000), in a proportion of 90:10 wt%, were mechanically mixed at room temperature for 5 min, and a stoichiometric amount of this mixture (related to the epoxy resin) was added to the epoxy m-SEP fibers dispersion. The system was then degassed under reduced pressure and transferred into silicone molds. Samples of  $25 \times 11.5 \times 3.2 \text{ mm}^3$  were cured using a temperature program, which consisted of heating at  $80^\circ\text{C}$  for 2 hours then at  $125^\circ\text{C}$  for 3 hours. For the aligned composites, the samples were put between two permanent magnets with lateral dimensions corresponding to  $35 \times 8 \text{ mm}^2$ , under a magnetic field of around  $H = 0.13 \text{ Tesla}$ , and polymerized using the same curing protocol. The magnetic field was applied in two different positions, longitudinal and orthogonal, as shown in **Figure VII.83 (B)**.

#### VII.3.2. Morphologies alignment of m-sepiolite into the epoxy matrix

The morphologies of m-SEP/epoxy resin hybrid were investigated by optical microscopy and TEM. **Figure VII.88** illustrates the morphology of the dispersion without (non-oriented) and with (oriented) the application of a magnetic field.

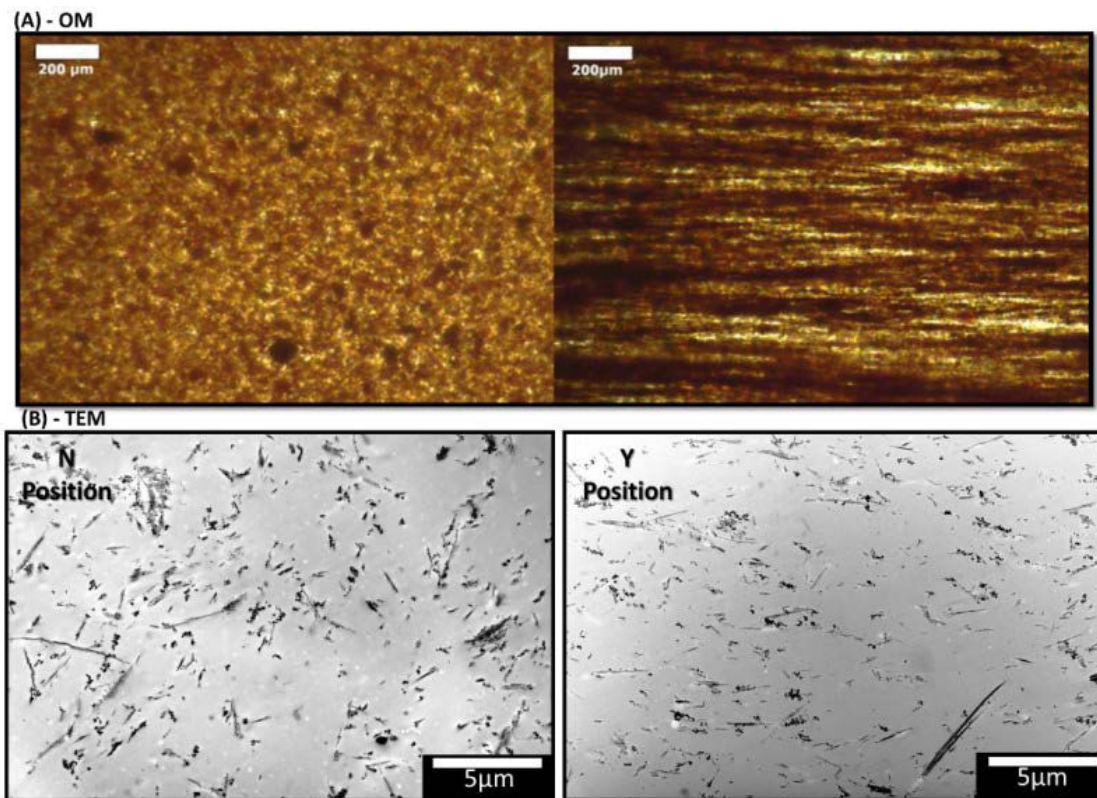


**Figure VII.88.** Optical microscopies of the m-SEP /epoxy resin dispersion: non-oriented and oriented particles (A). TEM micrographs of the m-SEP/epoxy networks (10 wt%): without (N position) and under (Y position) the applied magnetic field (B)

The optical microscopy in **Figure VII.88 (A)** clearly shows the alignment of the hybrid fibers under the magnetic field, establishing different macrostructures. Such alignment is not evident in TEM micrographs, shown in **Figure VII.88 (B)**, probably because of the higher magnification and very small observation area employed by this technique. However, the TEM micrographs suggest a better dispersion state of the sepiolite fibers for the aligned system.

### VII.3.3. Anisotropic thermomechanical properties of hybrid nanocomposite

The effect of the m-SEP alignment on the dynamic mechanical properties of the m-SEP/epoxy nanocomposites was evaluated isothermally (25°C) as a function of frequency or isochronally (1 Hz) as a function of temperature.

## VII.3.3.1. Nanocomposite mechanical properties as a function of frequency

For the aligned samples, the test in bending mode was applied in the parallel (X position) and perpendicular (Y position) directions of m-SEP alignment. **Figure VII.89** displays the variation of flexural modulus with frequency for the m-SEP/epoxy nanocomposites, as a function of the amount of nanofiller and alignment. **Table VII.14** also summarizes the flexural modulus values at 1 Hz and the glass transition temperature.

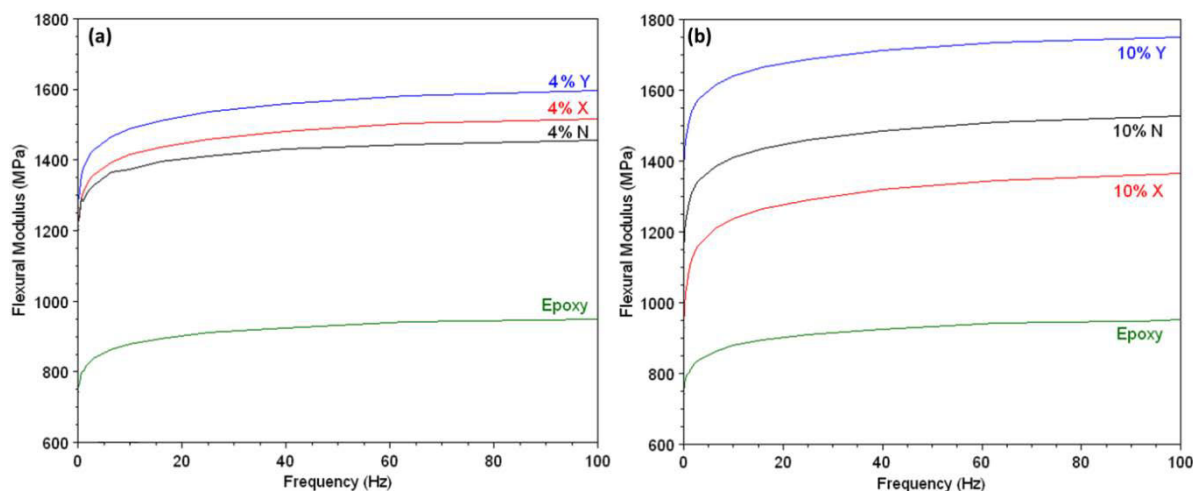


**Figure VII.89.** Dependence of flexural modulus with frequency taken at 25 °C, for m-SEP/epoxy nanocomposites as a function of the amount of nanofiller and alignment.

**Table VII.14.**  $T_{\alpha}$  and flexural modulus of epoxy and nanocomposites N: non-oriented fibers, X: oriented perpendicular to the long axis of the sample; Y: oriented parallel to the long axis;  $E_{th}$  is the prediction of the Halpin-Tsai model

Sample	$T_{\alpha}$ (°C) <sup>a</sup>	E (GPa) <sup>b</sup>	$E_{th}$ (GPa)
cEpoxy	67.2	0.93 ± 0.01	---
4% N	64.4	1.43 ± 0.03	1.22
4% X	64.4	1.48 ± 0.05	0.98
4% Y	63.6	1.56 ± 0.04	1.62
10% N	54.3	1.48 ± 0.02	1.69
10% X	58.2	1.32 ± 0.04	1.06
10% Y	64.1	1.71 ± 0.03	2.14

The presence of non-oriented and oriented m-SEP provoke an increase of flexural modulus in all frequency range studied, confirming the reinforcing effect of the magnetic sepiolite nanofibers. The alignment in the X position results in a slightly increase of modulus for sample containing

4wt% of m-SEP and a decrease of this property for sample containing 10wt% of m-SEP. On the other hand, the alignment in Y position reveals an important increase of the modulus, being the highest value observed for the sample containing 10wt% of m-SEP fibers. These results are reliable to an anisotropic material in terms of mechanical properties.

An estimation of the Young modulus (E) of the composite, for fibers with high aspect ratio, is given by the Halpin-Tsai model. For a disordered orientation, the modulus is given by:<sup>15</sup>

$$E = \frac{3}{8}E_L + \frac{5}{8}E_T, \text{ where } E_L \text{ and } E_T \text{ are the moduli for fibers aligned parallel (X) or perpendicular (Y)}$$

to the direction of traction, respectively. The  $E_L/E_m$  ratio is defined by the equation:

$$\frac{E_L}{E_m} = \frac{1+2f\eta_L\phi}{1-\eta_L\phi}, \text{ where } \phi \text{ is the volume fraction of fibers, } f \text{ is shape factor based on the length and}$$

$$\text{diameter of the fiber and } \eta_L = \frac{\frac{E_f}{E_m} - 1}{\frac{E_f}{E_m} + 2f}, \text{ where } E_f \text{ is the modulus of the fiber and } E_m \text{ the modulus of}$$

the matrix. For transverse orientation relatively to the traction, we have:  $\frac{E_T}{E_m} = \frac{1+2\eta_T\phi}{1-\eta_T\phi}$ , with

$$\eta_T = \frac{\frac{E_f}{E_m} - 1}{\frac{E_f}{E_m} + 2}. \text{ We could use } E_f=180 \text{ GPa for typical modulus of the sepiolite fiber}^{16} \text{ and } f=25 \text{ for}$$

the inferior estimation of the shape factor (based on aspect ratio - length of 1  $\mu\text{m}$  and the diameter of 40 nm for sepiolite). Lowe et al.<sup>17</sup> have found that a value of  $f=20$  fit their results, but the shape factor depends on the sepiolite batch and on the disaggregation process. The modulus of the pure epoxy at the intermediate frequency of 20Hz is around  $E_m=0.93\text{GPa}$ . For the weight fractions of 4% and 10% with the respective densities of the hybrid fibers ( $\rho_f=2.64\text{g/cm}^3$ ) and of the epoxy resin ( $\rho_m=1.16 \text{ g/cm}^3$ ), we obtain respectively  $\phi= 1.8\%$  and  $\phi= 4.65\%$  for the volume fraction.

The prediction for the ratio of the moduli for the three different orientations is compared to the experimental values in **Table VII.14**. We have the right order of magnitude, which is an indication that the fibers are well dispersed in the matrix and also that they are well linked with the epoxy matrix, but obviously the alignment effect is not so strong as predicted by the theory. For instance, for 10wt% fibers aligned along the main dimension of the sample, we have an increase of modulus of 84% instead of 200% predicted by the model. Also for fibers oriented perpendicular to the main axis and 10wt%, the modulus is well below the one for aligned fibers but too high compared to the prediction. It is still inferior at 4wt% where modulus of non-oriented fibers is slightly lower to the one of the perpendicular alignment. An explanation could be, as observed in **Figure VII.88 (B)**, that the alignment of fibers is quite imperfect. For non-

oriented fibers, we observe that there is practically no increase of modulus between 4wt% and 10wt%. Nevertheless, the increase of 84% observed for nanocomposite contained 10wt% of aligned fibers is quite successful, once in previous works using sepiolite, the maximum increase in modulus was around 20-30% at a weight fraction of 3-5%, which decreased at higher concentration.<sup>15a, 18</sup> These are the first results obtained with permanent magnets (**Figure VII.83 (B)**) and weak values of the field. In the future, we plan to use an electromagnet with higher field and a controlled ramp of magnetic field in order to get a better alignment of the fibers; also the magnetization of the fibers can be improved by increasing the magnetite proportion relatively to the one of sepiolite.

### VII.3.3.2. Nanocomposite mechanical properties as a function of temperature

Concerning the  $\alpha$ -relaxation temperature ( $T_\alpha$ ) presented in **Figure VII.90** and summarized in **Table VII.14**, the addition of m-SEP decreased the  $T_\alpha$  of the non-aligned nanocomposites. This result is more significant for the nanocomposites containing 10wt% of m-SEP fibers and could be attributed to the presence of free amino groups in the sepiolite surface, which also could react with the epoxy monomer, causing a perturbation of the stoichiometric balance. Furthermore, the presence of free volume in the filler-matrix interfaces, caused by the roughness of inorganic particles, may also contribute to the increase in mobility of the polymer chains and therefore to a reduction in  $T_\alpha$ . Both effects are more important for systems containing 10% of m-SEP because of the greater amount of amino groups and higher free volume concentration caused by the higher filler-matrix interface. The alignment of composite with 10% m-SEP increases the  $T_\alpha$ , which may be attributed to the increase in the interaction among the fibers. For nanocomposite containing 4wt% of m-SEP, the alignment does not influence the  $T_\alpha$  probably because the system is more diluted so resulting in a lower interaction with the fibers.

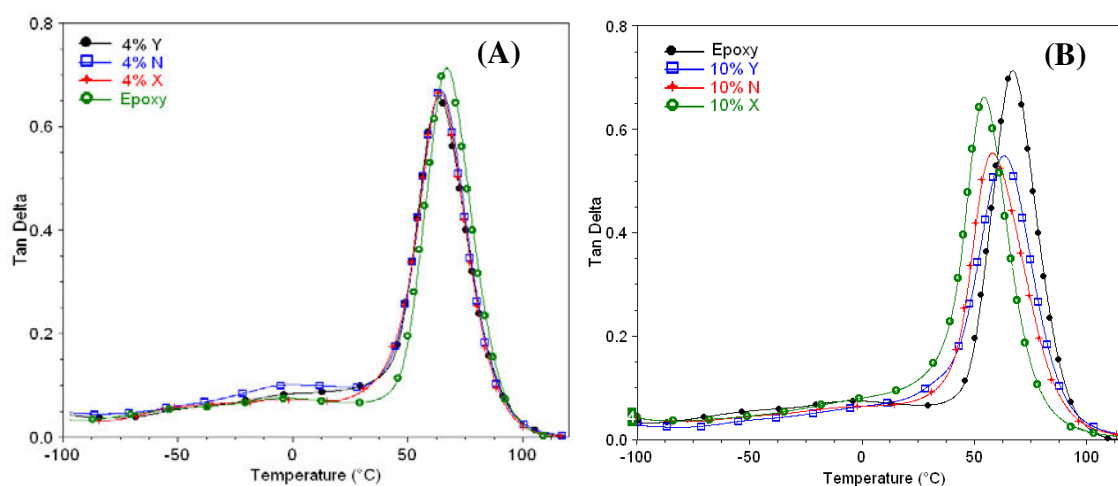


**Figure VII.90.** Tan delta as a function of temperature for epoxy resin and the nanocomposites with 4 (A) and 10% wt (B) of the hybrid in different orientations

### VII.3.3.3. Thermal stability of hybrid epoxy nanocomposites

The thermal stability of the epoxy systems was evaluated by TGA in **Figure VII.91**. The presence of the m-SEP fibers produces a slight decrease of the onset and maximum degradation temperatures of the nanocomposites in comparison with those of the neat epoxy resin. Some authors also observed similar results, which were attributed to the catalytic action of sepiolite for the degradation process of epoxy resin, which is minimized by the surface functionalization.<sup>19</sup> As expected, the percentage of final mass loss decreases with the amount of filler introduced in the nanocomposite.

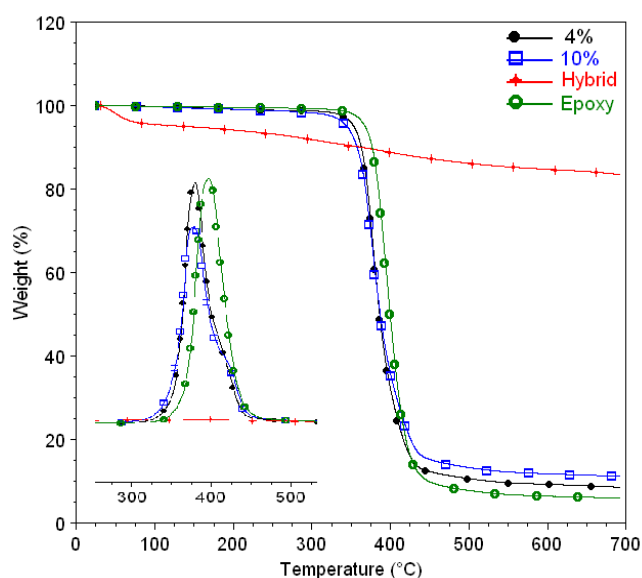


**Figure VII.91.** TGA of neat epoxy resin (green), m-Sep hybrid particles (red) and of the nanocomposites with 4 (black) and 10% wt (blue) of m-Sep hybrid particles.

## VII.4. Conclusions

A new route for the chemical grafting of magnetite nanoparticles on sepiolite fibers has been successfully established by reacting epoxy-silylated magnetite particles with amino-silylated sepiolite fibers. The corresponding m-SEP hybrid contains 12 vol% of magnetite attached on sepiolite and present superparamagnetic behavior. The epoxy-based nanocomposites containing this hybrid were prepared in the presence of a magnetic field, displaying significant orientation along the field as observed by optical microscopy. The aligned nanocomposites in the longitudinal direction present superior flexural modulus, characterizing the anisotropic property of these nanocomposites. Finally, the results presented in this work highlight the importance of the chemical reaction between magnetite particles and sepiolite fibers to create strong covalent

bonds. This allows the development of aligned reinforcing epoxy network without magnetite separation during the application of an external magnetic field.

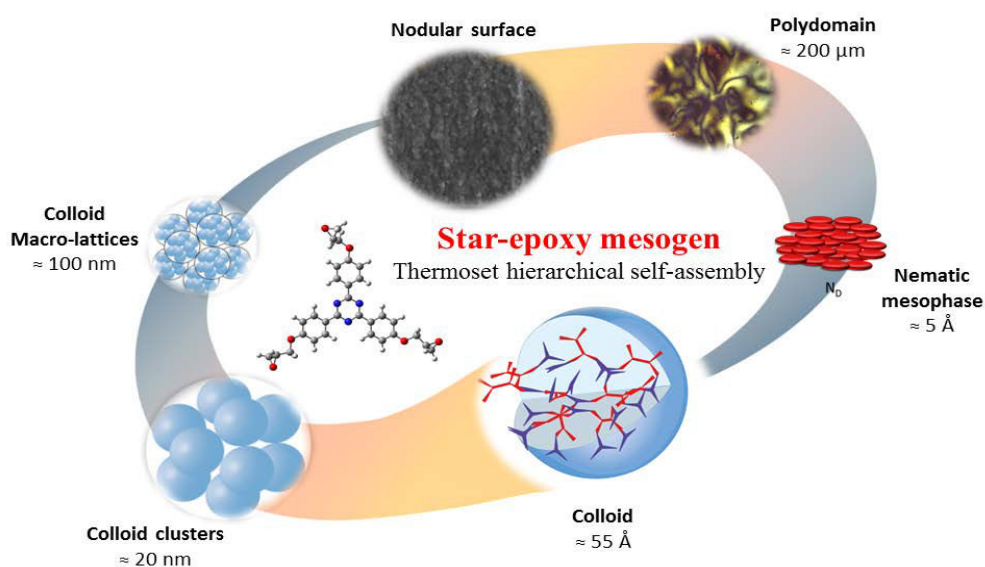
1. Azeez, A. A.; Rhee, K. Y.; Park, S. J.; Hui, D., Epoxy clay nanocomposites - processing, properties and applications: A review. *Composites Part B-Engineering* **2013**, *45* (1), 308-320.
2. Moniruzzaman, M.; Winey, K. I., Polymer nanocomposites containing carbon nanotubes. *Macromolecules* **2006**, *39* (16), 5194-5205.
3. (a) Kim, I. T.; Tannenbaum, A.; Tannenbaum, R., Anisotropic conductivity of magnetic carbon nanotubes embedded in epoxy matrices. *Carbon* **2011**, *49* (1), 54-61; (b) Shen, J.; Qin, C.; Hu, Y.; Li, N.; Ye, M., Facile Synthesis of Magnetic Nanoparticle-Coated Single-Walled Carbon Nanotubes and Its Functional Modification in Epoxy Resin. *Polymer Composites* **2010**, *31* (12), 2035-2041; (c) Prolongo, S. G.; Meliton, B. G.; Del Rosario, G.; Urena, A., New alignment procedure of magnetite-CNT hybrid nanofillers on epoxy bulk resin with permanent magnets. *Composites Part B-Engineering* **2013**, *46*, 166-172; (d) Monti, M.; Natali, M.; Torre, L.; Kenny, J. M., The alignment of single walled carbon nanotubes in an epoxy resin by applying a DC electric field. *Carbon* **2012**, *50* (7), 2453-2464; (e) ALDAJAH, S.; CHATTERJEE, J.; ALRAWADEH, M.; KOSURI, A.; HAIK, Y., Alignment of carbon nanotubes using magnetic nanoparticles. **2009**, *8* (3), 251-259.
4. Zhao, W.; Wang, H.; Tang, H.; Chen, G., Facile preparation of epoxy-based composite with oriented graphite nanosheets. *Polymer* **2006**, *47* (26), 8401-8405.
5. (a) Serna, C.; Ahlrichs, J. L.; Serratos, J. M., FOLDING IN SEPIOLITE CRYSTALS. *Clays and Clay Minerals* **1975**, *23* (6), 452-457; (b) Rautureau, M.; Tchoubar, C., STRUCTURAL-ANALYSIS OF SEPIOLITE BY SELECTED AREA ELECTRON-DIFFRACTION - RELATIONS WITH PHYSICOCHEMICAL PROPERTIES. *Clays and Clay Minerals* **1976**, *24* (1), 43-&.
6. (a) Carlson, J. D.; Jolly, M. R., MR fluid, foam and elastomer devices. *Mechatronics* **2000**, *10* (4-5), 555-569; (b) Bellan, C.; Bossis, G., Field dependence of viscoelastic properties of MR elastomers. *International Journal of Modern Physics B* **2002**, *16* (17-18), 2447-2453.
7. (a) Volle, N.; Challier, L.; Burr, A.; Giulieri, F.; Pagnotta, S.; Chaze, A.-M., Maya Blue as natural coloring fillers in a multi-scale polymer-clay nanocomposite. *Composites Science and Technology* **2011**, *71* (15), 1685-1691; (b) Volle, N.; Giulieri, F.; Burr, A.; Pagnotta, S.; Chaze, A. M., Controlled interactions between silanol groups at the surface of sepiolite and an acrylate matrix: Consequences on the thermal and mechanical properties. *Materials Chemistry and Physics* **2012**, *134* (1).
8. (a) Delacaille, J. B. D.; Fripiat, J. J., A REASSESSMENT OF THE SI-29 MAS-NMR SPECTRA OF SEPIOLITE AND ALUMINATED SEPIOLITE. *Clay Minerals* **1994**, *29* (3), 313-318; (b) Weir, M. R.; Kuang, W. X.; Facey, G. A.; Detellier, C., Solid-state nuclear magnetic resonance study of sepiolite and partially dehydrated sepiolite. *Clays and Clay Minerals* **2002**, *50* (2), 240-247.
9. Yamaura, M.; Camilo, R. L.; Sampaio, L. C.; Macedo, M. A.; Nakamura, M.; Toma, H. E., Preparation and characterization of (3-aminopropyl) triethoxysilane-coated magnetite nanoparticles. *Journal of Magnetism and Magnetic Materials* **2004**, *279* (2-3), 210-217.
10. (a) Durdureanu-Angheluta, A.; Ardeleanu, R.; Pinteala, M.; Harabagiu, V.; Chiriac, H.; Simionescu, B. C., Silane covered magnetite particles. Preparation and characterisation. *Digest Journal of Nanomaterials and Biostructures* **2008**, *3* (1), 33-40; (b) Durdureanu-Angheluta, A.; Stoica, I.; Pinteala, M.; Pricop, L.; Doroftei, F.; Harabagiu, V.; Simionescu, B. C.; Chiriac, H., Glycidoxypropylsilane-functionalized Magnetite as Precursor for Polymer-covered Core-shell Magnetic Particles. *High Performance Polymers* **2009**, *21* (5), 548-561.
11. Colombo, U.; Gazzarri, F.; Lanzavec, G.; Sironi, G., MAGNETITE OXIDATION - A PROPOSED MECHANISM. *Science* **1965**, *147* (3661), 1033-&.
12. Gonzalez-Alfaro, Y.; Aranda, P.; Fernandes, F. M.; Wicklein, B.; Darder, M.; Ruiz-Hitzky, E., Multifunctional Porous Materials Through Ferrofluids. *Advanced Materials* **2011**, *23* (44), 5224-5228.
13. (a) Wang, Y.; Zhu, Z.; Xu, F.; Wei, X., One-pot reaction to synthesize superparamagnetic iron oxide nanoparticles by adding phenol as reducing agent and stabilizer. *Journal of Nanoparticle Research* **2012**, *14* (4); (b) Xu, Z.; Shen, C.; Hou, Y.; Gao, H.; Sun, S., Oleylamine as Both Reducing Agent and Stabilizer in a Facile Synthesis of Magnetite Nanoparticles. *Chemistry of Materials* **2009**, *21* (9).
14. Galindo-Gonzalez, C.; de Vicente, J.; Ramos-Tejada, M. M.; Lopez-Lopez, M. T.; Gonzalez-Caballero, F.; Duran, J. D. G., Preparation and sedimentation behavior in magnetic fields of magnetite-covered clay particles. *Langmuir* **2005**, *21* (10), 4410-4419.
15. (a) Sabzi, M.; Jiang, L.; Atai, M.; Ghasemi, I., PLA/sepiolite and PLA/calcium carbonate nanocomposites: A comparison study. *Journal of Applied Polymer Science* **2013**, *129* (4), 1734-1744; (b) Agarwa, B. D. I.; Broutman, L. J.; Chandrashekhara, K., *Analysis and Performance of Fiber Composites*. 3rd ed.; John Wiley & Sons: New Jersey, 2006; p 576.

16. Chen, B. Q.; Evans, J. R. G., Elastic moduli of clay platelets. *Scripta Materialia* **2006**, *54* (9), 1581-1585.
17. Lowe, D. J.; Chapman, A. V.; Cook, S.; Busfield, J. J. C., Micromechanical Models of Young's Modulus of NR/Organoclay Nanocomposites. *Journal of Polymer Science Part B-Polymer Physics* **2011**, *49* (22), 1621-1627.
18. (a) Verge, P.; Fouquet, T.; Barrere, C.; Toniazzi, V.; Ruch, D.; Bomfim, J. A. S., Organomodification of sepiolite clay using bio-sourced surfactants: Compatibilization and dispersion into epoxy thermosets for properties enhancement. *Composites Science and Technology* **2013**, *79*, 126-132; (b) La Tegola, S.; Terenzi, A.; Martini, R.; Barbosa, S.; Torre, L.; Kenny, J., Processing and Final Properties Improvement of Polyolefin-Sepiolite and Carbon Nanofibre Nanocomposites. *Eurofillers* **2011**, *301*, 128-135; (c) Bilotti, E.; Deng, H.; Zhang, R.; Lu, D.; Bras, W.; Fischer, H. R.; Peijs, T., Synergistic Reinforcement of Highly Oriented Poly(propylene) Tapes by Sepiolite Nanoclay. *Macromolecular Materials and Engineering* **2010**, *295* (1), 37-47.
19. Ahmetli, G.; Deveci, H.; Soydal, U.; Seker, A.; Kurbanli, R., Coating, mechanical and thermal properties of epoxy toluene oligomer modified epoxy resin/sepiolite composites. *Progress in Organic Coatings* **2012**, *75* (1), 97-105.



## Chapter VIII

# Star-epoxy mesogens to design multifunctional materials: polymerization kinetics and fractal self-assembly



**Keywords:** Star-shape monomer, polymerization kinetics, fractal self-assembly, liquid-crystal, mechanical properties.



<b>VIII.1. Investigations on a new family of epoxy monomers .....</b>	<b>198</b>
VIII.1.1. Star-epoxy mesogens as potential platform monomers to design hierarchical materials .	198
<b>VIII.2. Synthesis and characterization of a star-epoxy mesogen monomer .....</b>	<b>199</b>
VIII.2.1. Materials.....	199
VIII.2.2. Synthesis and characterization of a star-epoxy monomer with 1,3,5-triazine core ....	199
VIII.2.2.1. 2,4,6-Tris( <i>p</i> -hydroxyphenyl) triazine: TriaOH .....	199
VIII.2.2.2. 1,3,5-Triazine,2,4,6-tris[4-(2-oxiranylmethoxy)phenyl]: TriaEP.....	200
VIII.2.3. Investigations on star-epoxy monomer's mesogeneity .....	202
<b>VIII.3. Influence of supramolecular interactions on the polymerization kinetic: an example of anionic living copolymerization.....</b>	<b>203</b>
VIII.3.1. An epoxy/anhydride anisotropic network.....	203
VIII.3.2. Influence of supramolecular interactions on the polymerization kinetic.....	206
<b>VIII.4. Network morphological investigations correlated with thermomechanical properties: an example of A<sub>4</sub>B<sub>3</sub> epoxy/amine architecture .....</b>	<b>209</b>
VIII.4.1. TriaEP/2,7-DAF system: generation of an A <sub>4</sub> B <sub>3</sub> network .....	209
VIII.4.2. Morphological and thermomechanical investigations of TriaEP/2,7 DAF .....	211
VIII.4.2.1. TriaEP/2,7 DAF: a fractal polymerization.....	211
VIII.4.2.2. Relationship between anisotropic architecture and thermomechanical properties .....	214
<b>VIII.5. Conclusions .....</b>	<b>216</b>

## VIII. Star-epoxy mesogens to design multifunctional materials: polymerization kinetics and fractal self-assembly

### VIII.1. Investigations on a new family of epoxy monomers

#### VIII.1.1. Star-epoxy mesogens as potential platform monomers to design hierarchical materials

Three-arms mesogens, also called star-shaped mesogens, with an idealized  $C_3$ -symmetry are fascinating platform for the exploration of self-assembly process permitting the design of complex hierarchical and functional soft materials.<sup>1</sup> As exposed on **section II.3.5.1.**, compared with the conventional core design mesogens such as rod-like<sup>2</sup> or disc-like<sup>3</sup> shapes, the multi-arms mesogens extended to dendrons, dendrimers<sup>4</sup> or supramolecular mesogens as metallo-mesogens<sup>5</sup>, are driven by the nanosegregation of building blocks also by the proclivity to fill efficiently the space in condensed matter.<sup>6</sup>

Star-mesogens can also be self-organized in nematic, lamellar, columnar or cubic phases.<sup>3,7</sup> This study focuses on octopolar 1,3,5-triazine derivatives which are well known for the development of organic light emitting diodes (OLEDs)<sup>3,8</sup> and for its various biocide properties.<sup>9,10</sup> Herein, the design of a star-epoxy monomer has been primarily investigated to explore its self-assembly ability to form a tridimensional architecture, starting from its three-armed macromonomers, at the pre-gel state, obtained during the first stages of polymerization, until the macromolecule and infinite network formation at the post-gel state.<sup>11,12,13</sup>

This work emphasis on the elaboration of a liquid-crystalline thermoset (LCT)<sup>14,15</sup> through an overall study from the influence of supramolecular interactions on the polymerization reactivity to the elaboration of the tridimensional architecture, in relationship with the thermomechanical properties. To explore all this aspects of cross-linking, after a section which presents the star-epoxy monomer synthesis (1,3,5-triazine,2,4,6-tris[4-(2-oxiranylmethoxy)phenyl] called TriEP), a first example of monomer cross-linking through an anionic living copolymerization will be presented, highlighting the influence of the liquid-crystalline phase fade-in/fade-out on the polymerization kinetics. The second example exhibits an uncommon  $A_4B_3$  architecture, provided by the polymerization of TriEP with an aromatic di-amine cross-linker having a rod-like geometry: 2,7-diaminofluorene (2,7-DAF). In this case, the discussion will be oriented around morphological aspects with the evidence of a nodular surface on the fully cured polymer, which could be associated to a fractal expansion during polymerization.

## VIII.2. Synthesis and characterization of a star-epoxy mesogen monomer

### VIII.2.1. Materials

Products were purchased from Sigma Aldrich: 4-cyanophenol 95%, trifluoromethanesulfonic acid  $\geq 99\%$ , ( $\pm$ )-epichlorohydrin  $\geq 99\%$ , benzyltrimethylammonium bromide 97%, 2,7-diaminofluorene  $\geq 97\%$ , succinic anhydride  $\geq 99\%$  and 2-methylimidazole 99%.

### VIII.2.2. Synthesis and characterization of a star-epoxy monomer with 1,3,5-triazine core

The **Figure VIII.92** resumes the two steps synthesis strategy to obtain the star-epoxy monomer 1,3,5-Triazine,2,4,6-tris[4-(2-oxiranylmethoxy)phenyl] called TriaEP that will be presented and characterized in details in the following sections.

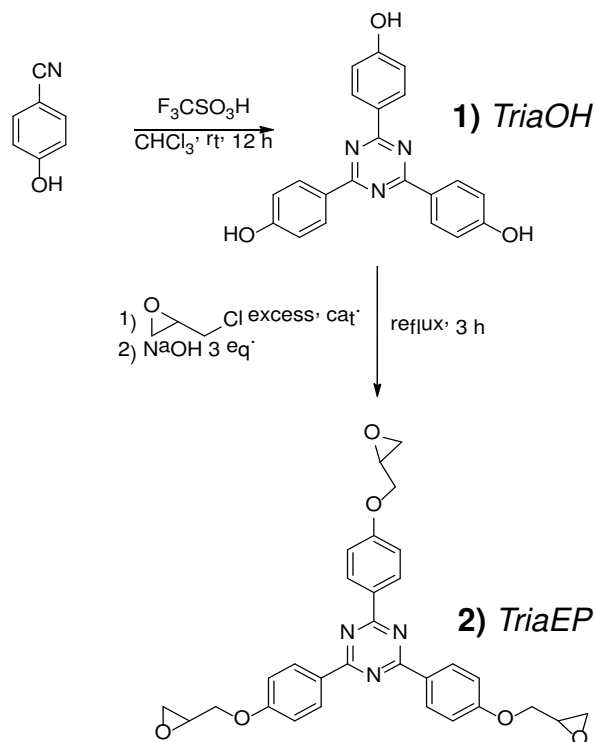


**Figure VIII.92.** Star-epoxy monomer synthesis yields: (1) *TriaOH* 91%, (2) *TriaEP* 95%.

#### VIII.2.2.1. 2,4,6-Tris(*p*-hydroxyphenyl) triazine: *TriaOH*

500 mg of 4-cyanophenol (4.197 mmol) were dissolved in 10 mL of dry chloroform. The cyclotrimerization proceeds in triflic acid ( $CF_3SO_3H$ ) media with the addition of 1.9 mL of acid (20.98 mmol) at  $0^\circ C$ . The mixture was stirred at  $0^\circ C$  for 10 min and then kept under nitrogen at room temperature during 12 h. Then, the reaction mixture was quenched with a dilute solution of ammonia until neutralization. The reaction mixture was filtered and washed with water. The

reaction product was recrystallized from acetone to obtain 455 mg of pure compound as a colorless solid, yield 91%.

- ◆ NMR characterization : (**Figure VIII.93**)  $^1\text{H}$  NMR (500 MHz, DMSO- $d_6$ )  $\delta$  10.30 (s, 3H, OH), 8.56 (d,  $J = 8.8$  Hz, 6H, Ar-H), 6.98 (d,  $J = 8.8$  Hz, 6H, Ar-H).  $^{13}\text{C}$  NMR (50 MHz, DMSO- $d_6$ )  $\delta$  170.0 (C=N), 161.7 (Ar-C), 130.6 (Ar-C), 126.5 (Ar-C), 115.5 (Ar-C). NMR analysis of this precursor is in good agreement with the literature<sup>16</sup> confirming the synthesized structure.

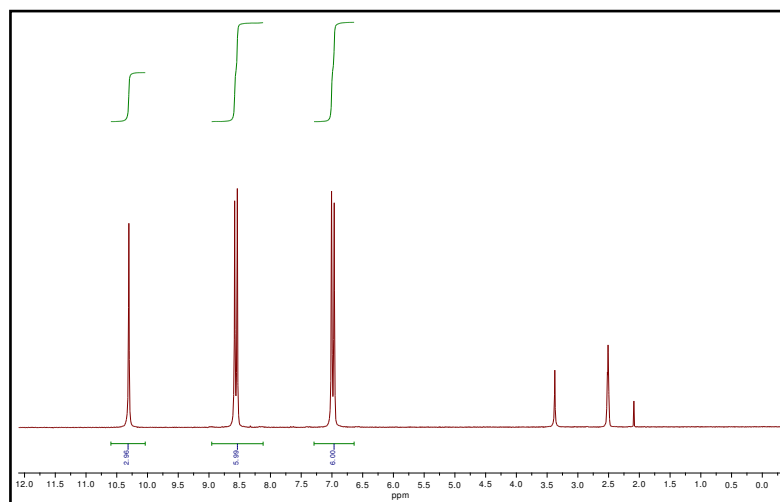


**Figure VIII.93.** TriaOH  $^1\text{H}$  NMR at 500 MHz in DMSO- $d_6$

#### VIII.2.2.2. 1,3,5-Triazine,2,4,6-tris[4-(2-oxiranylmethoxy)phenyl]: TriaEP

1g on 2,4,6-tris(*p*-hydroxyphenyl) triazine (2.798 mmol), 20mL of epichlorohydrin and 0.05g of benzyltrimethylammonium bromide as catalyst were charged into a two-necked flask. The mixture was stirred and refluxed for 120 min. Then, 0.370g of sodium hydroxide (9.250 mmol) (more than stoichiometric 10 wt.-%) were added as 15 wt.-% of aqueous solution. After refluxing for another 60 min, the mixture was allowed to cool at room temperature. The epichlorohydrin was then removed under vacuum and the residue was water washed. Finally the product was recrystallized from toluene to give 1.34g of a white powder, yield 95%.

- ◆ NMR characterization: (**Figure VIII.94**)  $^1\text{H}$  NMR (500 MHz, DMSO- $d_6$ )  $\delta$  8.65 (d,  $J = 8.9$  Hz, 6H, Ar-H), 7.19 (d,  $J = 8.9$  Hz, 6H, Ar-H), 4.49 (dd,  $J = 11.4, 2.5$  Hz, 3H, CH<sub>2</sub> of glycidyl), 3.97 (dd,  $J = 11.4, 6.6$  Hz, 3H, CH<sub>2</sub> of glycidyl), 3.39 (m, 3H, CH of epoxy), 2.89 (dd, 3H, CH<sub>2</sub> of epoxy), 2.78 (dd,  $J = 5.0, 2.6$  Hz, 3H, CH<sub>2</sub> of epoxy).  $^{13}\text{C}$  NMR (50 MHz, DMSO- $d_6$ )  $\delta$  170.1 (C=N), 162.1 (Ar-C), 130.5 (Ar-C), 128.2 (Ar-C), 114.7 (Ar-C), 69.2 (CH<sub>2</sub> of glycidyl), 49.5 (CH of epoxy), 43.7 (CH<sub>2</sub> of epoxy). The classical glycidyl NMR shifts are in good agreement with the literature.<sup>17</sup>

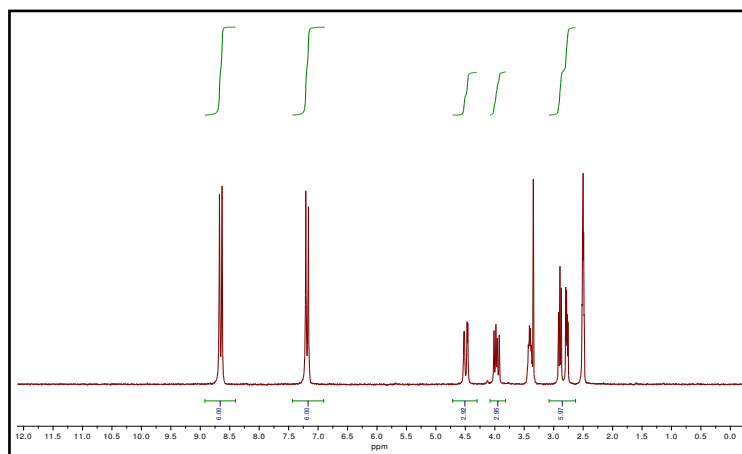


**Figure VIII.94.** TriaEP  $^1\text{H}$  NMR at 500 MHz, in DMSO- $d_6$

- ◆ **MS analysis:** as seen on **Figure VIII.95** the TriaEP molecular mass and structure have been confirmed through fragmentation with:

$m/z$  482:  $[\text{M} + \text{H} - 44]$ : loss of  $\text{C}_2\text{H}_4\text{O}$  :

$m/z$  470:  $[\text{M} + \text{H} - 56]$ : loss of  $\text{C}_3\text{H}_4\text{O}$  :

$m/z$  176: corresponds to the following substructure  $\text{C}_{10}\text{H}_{10}\text{NO}_2^+$  :

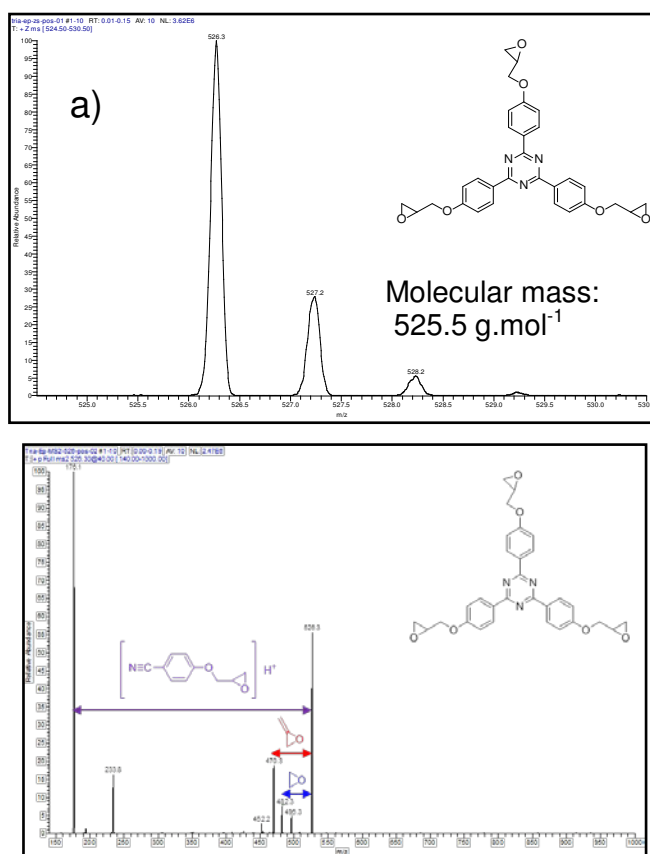


**Figure VIII.95.** a) TriaEP spectrum of ESI-MS:  $[\text{M} + \text{H}]^+ = 526.3\text{g.mol}^{-1}$  quasi molecular mass; enhanced resolution experiment (zoom scan) confirms isotropy; b) MS/MS experiment under CID condition (isolation width: 1.5  $m/z$ ; NCE: 40%).

## VIII.2.3. Investigations on star-epoxy monomer's mesogeneity

The DSC thermogram of TriaEP monomer exhibits two endothermic peaks at around 130-140°C and close to 150°C as shown in **Figure VIII.96 (a)**. These phenomena are respectively associated with the succession of transitions from a solid crystal to a liquid-crystal phase and then to an isotropic liquid phase.<sup>18</sup> The liquid-crystalline phase stability, in agreement with the polarized light optical microscopy (POM) observations, corresponds to a temperature range from around 130 to 152°C. The TriaEP birefringence at 140°C visible by POM on **Figure VIII.96 (b)** reveals a dense texture, that could be a characteristic of a very ordered organization<sup>15</sup>, such as smectic or columnar mesophases which are currently observed in the case of mesogens built from 1,3,5-triazine core<sup>3</sup> but deeper SAXS investigations would be necessary to confirm the mesophase type. In **Figure VIII.96 (d)** the WAXS profile shows the diffraction peak at around 4.4 Å for TriaEP molecule at 140°C, in liquid-crystal state. This distance typically corresponds to the  $\pi$ - $\pi$  stacking space between two TriaEP discs in this case. Furthermore, the POM birefringence patterns could also suggest a long range order that is not observable by the WAXS experiment.<sup>19</sup>

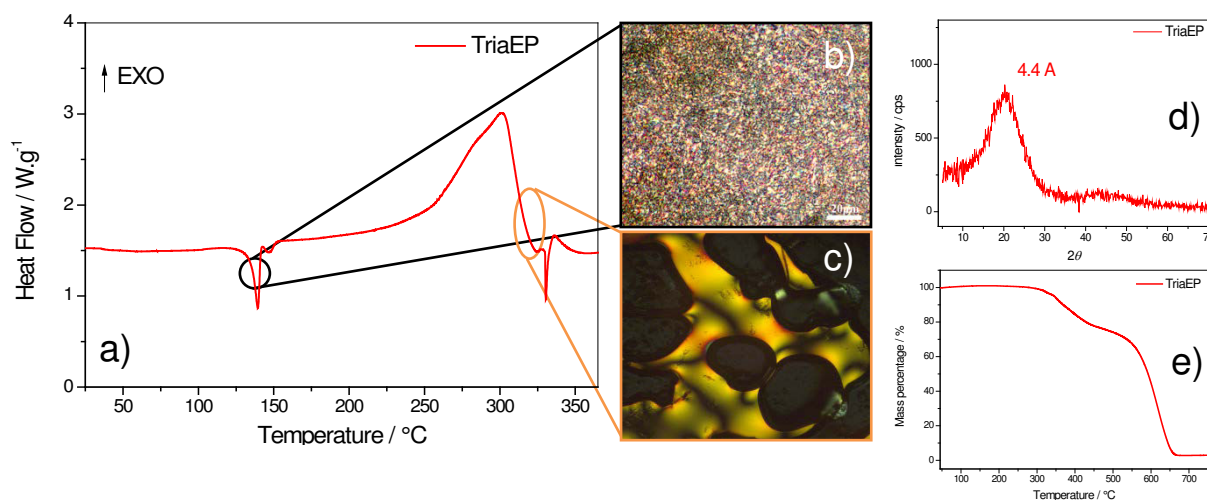


**Figure VIII.96.** TriaEP DSC at 5 °C.min<sup>-1</sup> a), TriaEP mesophases textures obtained by POM at 140 °C b) and 310 °C c), TriaEP WAXS pattern at 140 °C d), TG thermogram of TriaEP at 10 °C.min<sup>-1</sup> under air flow of 50 mL.min<sup>-1</sup> e).

The DSC thermogram exhibits also an exothermic peak ranging from 160 to 320°C (with a maximum at around 300°C) which can be associated with the thermally induced homopolymerization that can typically occur in this temperature range as seen on **Chapter II**. The resulting polymer is birefringent as seen in **Figure VIII.96 c)**, which confirms the formation of a liquid-crystalline thermoset (LCT) network (**section II.3.5.**). However, this

homopolymerization reaction occurs at high temperature and is concomitant with the beginning of the thermal degradation (**Figure VIII.96 e**)), thus several secondary reactions provided by formed radicals could also occur. Finally the thin endothermic peak at 330 °C has been assigned to the isotropization of the liquid-crystalline phase, according with POM observations.

### **VIII.3. Influence of supramolecular interactions on the polymerization kinetic: an example of anionic living copolymerization**

This section is dedicated to the evaluation of the role of supramolecular interactions on the formation of a thermoset network. To reach this objective, the anionic living copolymerization between TriaEP and succinic anhydride (SA), in stoichiometric ratio in regard to functionalities, and catalyzed by 2-methylimidazole (2MI) (1% by weight) has been retained. Indeed, this kind of polymerization presents the advantage to have a unique and well-known mechanism of propagation, instead of epoxy/amine cross-linking that intrinsically exhibits a competition between primary and secondary amine (**section II.1.1.2.**). Furthermore, the reactivity of epoxy/SA monoanhydride system catalyzed by 2MI has been thoroughly investigated in an isotropic system case in the **Chapter IV**, and thus could be a base for comparison.

#### **VIII.3.1. An epoxy/anhydride anisotropic network**

The **Figure VIII.97 a**) exhibits the DSC heating thermogram of TriaEP/SA reaction system, catalyzed by 2MI. It is important to notice that this tri-component formulation has been prepared by grounding the monomers and catalyst mixture followed by a re-crystallization from acetone for a better homogeneity. A first observation allows to associate the endothermic peak that appears at 109 °C to the melting of reacting components, immediately followed by an exothermic peak at 145 °C, corresponding to the epoxy/anhydride polymerization, catalyzed by 2MI: the mechanism has already been presented in **section IV.1.2.1.**

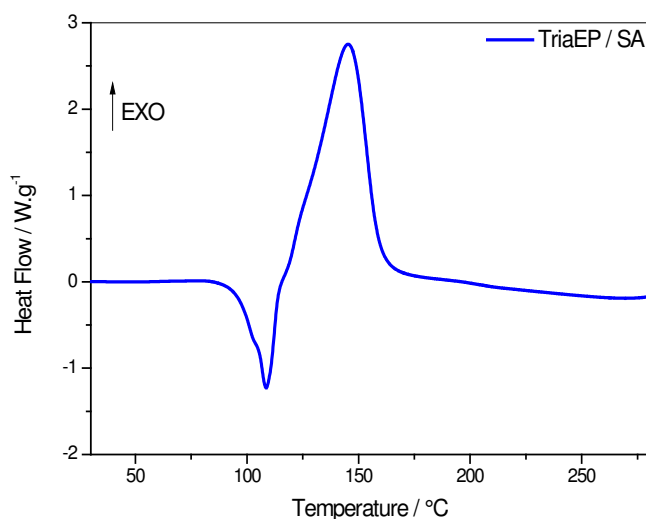


**Figure VIII.97.** DSC thermogram during heating the TriaEP/SA mixture at  $10\text{ }^{\circ}\text{C}\cdot\text{min}^{-1}$

Epoxy/anhydride cross-linking has been followed by FT-IR investigations, to highlight the structural variations of the epoxy group from TriaEP/SA uncured formulation with those of ester group from thermoset network (**Figure VIII.98 a**). The major evolution concerns the consumption of anhydride and epoxy groups which can be respectively reliable to the disappearance of absorption peaks at  $1860$  and  $1780\text{ cm}^{-1}$  (carbonyl axial deformation) and at  $916\text{ cm}^{-1}$  (internal oxiran ring stretching). We can also notice the apparition of a peak at  $1730\text{ cm}^{-1}$  that could be associated with the carbonyl stretching from the ester moieties provided by the anionic living copolymerization reaction.

The resulting material exhibits structural and optical anisotropies as seen on WAXS pattern and POM micrographs (**Figure VIII.98 b**), **c**) and **d**)), characteristic of liquid-crystalline epoxy resins (LCER) as seen on **section II.3.5.2**. The attribution of the type of mesophase in this kind of polymers is difficult due to the amorphous matrix character and to the presence of polydomains. However certain indications could allow us to formulate hypothesis. Indeed, the micrographs on **Figure VIII.98 c**) and **d**) exhibit a Schlieren texture which is characteristic of all nematic phases ( $N$ ,  $N_D$ ,  $N_C$ ) because they have the same symmetry with only an orientational order.<sup>3</sup> On another hand, the micrographs **c**) and **d**) exhibit some texture differences with the apparition of strongly birefringent “droplet” at later stage of polymerization that could be potentially be associated with the apparition of a new kind of mesophase. A recent study of Harada et al.<sup>20</sup> explains that in the case of LCER an incubation period, implying the achievement of certain critical nematic volume ( $\alpha > 0.8$ ), is necessary for a phase transition from nematic to smectic phase. The resulting volume of smectic phase depends on several parameters such as cross-linker nature. This observation could be generalized in the case of our system, considering

the phase transition from  $N_D$  to  $N_C$  mesophase. The WAXS pattern on **Figure VIII.98 b)** supplies some indications to support this hypothesis. A diffraction peak at 4.5 Å can be observed, similar to the distance found for TriaEP  $\pi$ - $\pi$  stacking in its liquid-crystalline phase ( **Figure VIII.96 d)**). An unusual break in the diffraction peak slope is observable at 6.0 Å, highlighting a broad amorphous diffraction peak from around 6.0 to 17.0 Å. This distance interval could be associated with the inter-columnar distance of  $N_C$  mesophase, with the minimal distance of around 6.0 Å that could be reliable to the short length of SA cross-linker between two inter-columnar TriaEP discs.

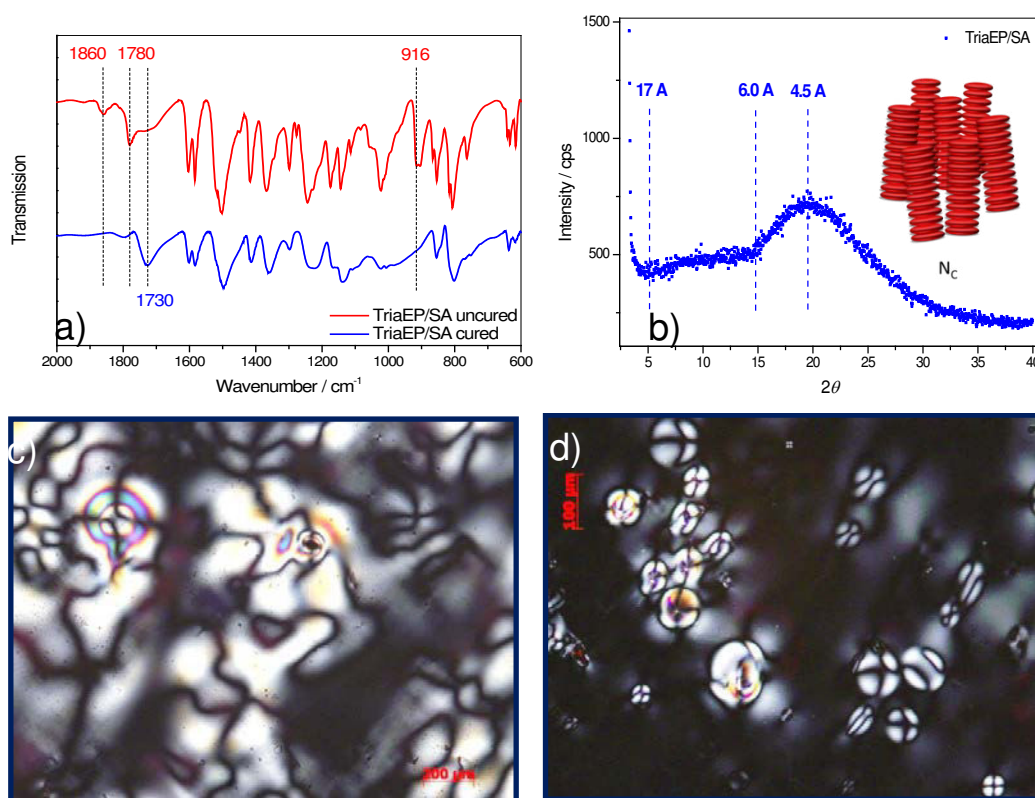


**Figure VIII.98.** FT-IR spectra of TriaEP/SA uncured mix (in red) and the resulting cured polymer (in blue) a), WAXS pattern of fully cured polymer at 160°C (1h) and at 180 °C (1h) b), and the corresponding mesophases textures obtained by POM at 160°C after 30 min c) and after curing during 1h at 160°C and 1h at 180 °C d).

After this evidence of anisotropic network formation, we will interest in details to how this network has been formed, from the reactive mixture to the generation of the tridimensional architecture. And also on how the occurrence and the supramolecular interactions can influence the cross-linking process.

### VIII.3.2. Influence of supramolecular interactions on the polymerization kinetic

To respond to this problematic, an advanced isoconversionnal method (seen **section III.1**) has been applied on the TriaEP/SA system using non-isothermal data (DSC thermograms at 8, 10, 12 °C.min<sup>-1</sup>): the results are represented in **Figure VIII.99 a**). The computed apparent activation energy ( $E_a$ ) superimposed to the DSC thermogram exhibits an unexpected complex behavior. In order to simplify and clarify the scientific approach, we have segmented the overall cross-linking process in four zones. The following discussion will focus on the variation of  $E_a$  reliable to our measurements and observations with that proposed in the literature. The summarized interpretations are available on **Figure VIII.100**.

- ◆ Zone 1: As seen on DSC thermogram and POM micrograph, this zone is mostly associated with the melting of SA and the transition from crystal to liquid-crystalline state for TriaEP monomer as we seen on **section VIII.2.3**.
- ◆ Zone 2: the thermogram exhibits a strong exothermy, reliable with the anionic living copolymerization, with the characteristic  $E_a \approx 70 \text{ kJ.mol}^{-1}$  generally associated with the chemical control on the early stage of polymerization during sol formation.<sup>21</sup> Notice that in this zone the SA is on isotropic liquid state and TriaEP in liquid-crystalline state.
- ◆ Zone 3: this zone is delimited by gelation and vitrification phenomena (**section II.1.2**) highlighted by rheological measurement, respectively associated with the cross between  $G'/G''$  and the plateau of  $G'$  modulus on **Figure VIII.99 b**). Notice that rheological measurements has been done at 4 °C.min<sup>-1</sup>, for technical reason, instead of kinetics data which are computed for a reaction rate average of 10 °C.min<sup>-1</sup>. Hence, the comparison is done by considering that these phenomena are shifted to higher temperature when a higher heating rate is used. Thus, gelation and vitrification phenomena can be superimposed to the  $E_a$ -dependency by taking into account this temperature shift. After gelation the viscosity of the medium increases dramatically which is reflected by a high decrease of the apparent activation energy  $E_a$  until the system vitrification. Indeed, at this stage of the epoxy/anhydride reaction, the diffusion of molecules into the media becomes rate-limiting, thus the  $E_a$ -dependency decrease can be attributed to a transition from chemical to diffusion control.<sup>22</sup> This decrease is characteristic of a transition from chemical ( $E_a \sim 70 \text{ kJ.mol}^{-1}$  for pure chemical control) to diffusion ( $E_a \sim 10 \text{ kJ.mol}^{-1}$  for pure diffusion control) regimes and

has been reported for various epoxy systems under curing including epoxy-amine and epoxy-anhydride.<sup>21,23</sup> In our case,  $E_a$  decreases reaching negative values of  $E_a$  ( $-70 \text{ kJ}\cdot\text{mol}^{-1}$ ). Such behavior has already been reported for crystallization of semi-crystalline polymers from the melt,<sup>24,25,26,27</sup> but it is uncommon for a chemical reaction. These negative values of  $E_a$  are not to be considered as negative energetic barrier, but as an anti-Arrhenian behavior which signifies that the reaction rate decreases with the increase of temperature, as observed for melt crystallization. This phenomenon can be related to TriaEP beginning of isotropization as seen on DSC thermogram

- ◆ **Figure VIII.96 a)** and on POM micrograph in **Figure VIII.100**. Thus the anti-Arrhenian behavior could be associated to a global decrease of order with the extent of polymerization. In another term, we could consider that the propagation of anionic living copolymerization is favored in LC state, because of a higher number of effective collisions due to a lower distance between reactive entities. Thus, the TriaEP isotropization leads to a decrease of the polymerization reaction rate. This conclusion is in good agreement with the results reported by Nunez et al.<sup>28</sup> who observed an anti-Arrhenius behavior for the isomerization reaction in LC solvent as a consequence of nematic-smectic A-reentrant nematic phase transitions. This was explained because the transition from smectic A to nematic phase is associated with a decrease of order. At  $T > 150^\circ\text{C}$ ,  $E_a$  exhibits a sharp peak with an amplitude from around  $-70$  to  $300 \text{ kJ}\cdot\text{mol}^{-1}$  which is the signature of a first order transition and could correspond to the transition of TriaEP from LC to isotropic phase<sup>29</sup> (as observed for BTDA melting in **section IV.2.2.**)
- ◆ **Zone 4:** In this zone, the unreacted monomer and cross-linker are in isotropic liquid phase and the material is in the glassy state. As seen on **section II.1.2.1.**, vitrification has the particularity to drastically decrease the reaction rate.<sup>21</sup> Thus, the apparent activation energy reaches the positive low values ( $25 \text{ kJ}\cdot\text{mol}^{-1}$ ) characteristic of diffusion of unreacted monomers in the glassy state. Starting from negative values, another transition regime from anti-Arrhenian to Arrhenian behavior is thus observed ( $-70$  to  $25 \text{ kJ}\cdot\text{mol}^{-1}$ ). In this case, the global order of the system increases (micrograph in **Figure VIII.100**) and corresponds to the organization of the macromolecule in polydomains. The transition from anti-Arrhenian to Arrhenian behavior leads to the more common behavior characterized by an increase of the reaction rate when the temperature increases.

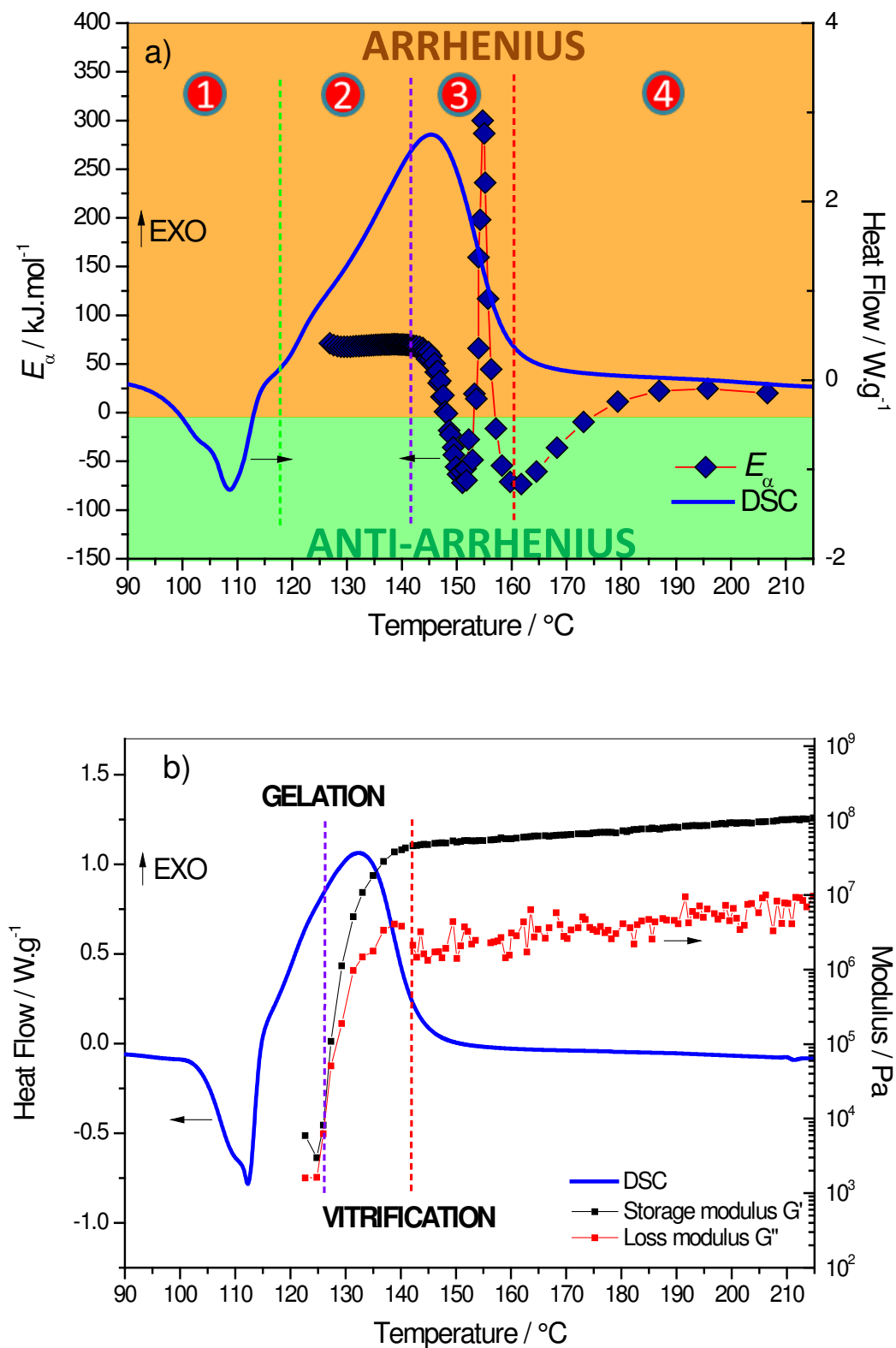


**Figure VIII.99.** TriaEP/SA apparent activation energy from DSC curves at 8, 10, 12 °C.min<sup>-1</sup> vs DSC curve at 10 °C.min<sup>-1</sup> with the corresponding 1/2/3/4 zones present on **Figure VIII.100 a)** and DSC vs  $G'/G''$  modulus at 4 °C.min<sup>-1</sup> b).

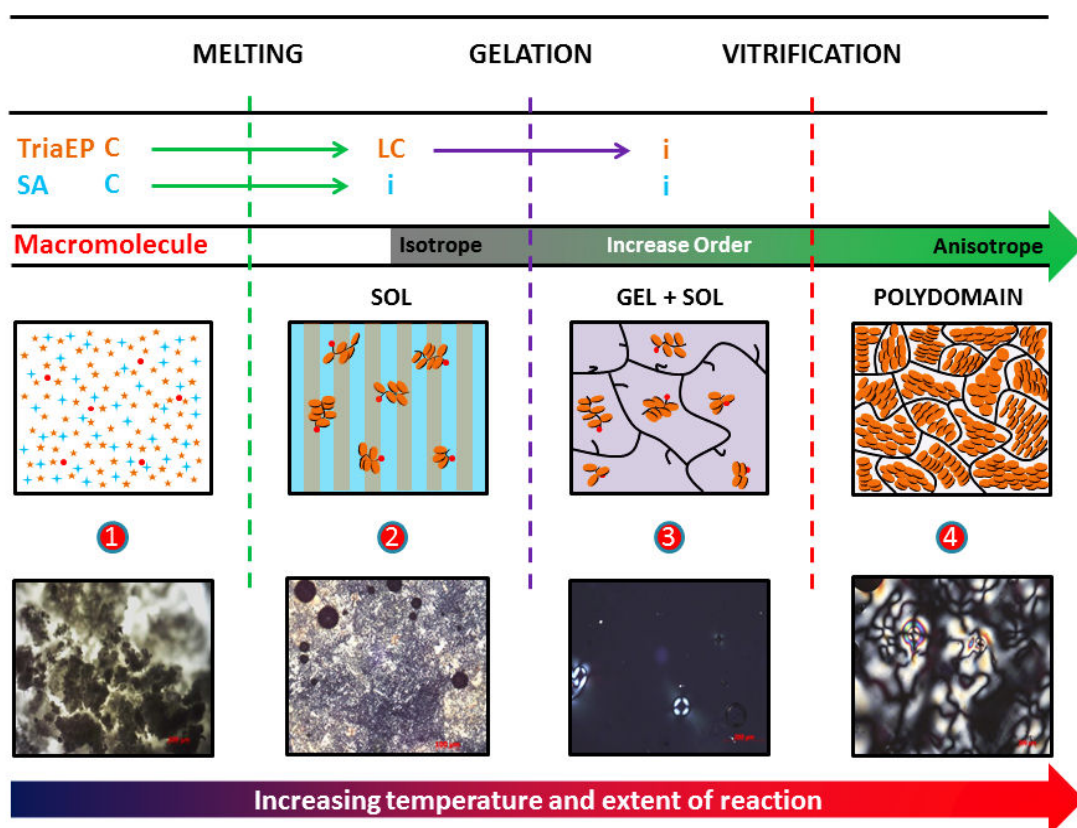


**Figure VIII.100.** Recapitulative scheme of physico-chemical phenomena which occurs during TriaEP/SA polymerization in dynamic heating mode.

#### VIII.4. Network morphological investigations correlated with thermomechanical properties: an example of $A_4B_3$ epoxy/amine architecture

##### VIII.4.1. TriaEP/2,7-DAF system: generation of an $A_4B_3$ network

The TriaEP/2,7-DAF polymer exhibits an  $A_4B_3$  structure (**Figure VIII.101**), with a stoichiometric ratio in regard to monomer and cross-linker functionalities, that are three for the epoxy monomer and four for the diamine (**section II.1.1.2.**)<sup>11</sup> These reactants, in the form of solid powders, have been finely crushed together and put in the DSC pan to measure the heat flow evolution in dynamic scanning temperature. An endothermic peak at around 123°C is initially observed and reliable to TriaEP/2,7-DAF mixture melting (**Figure VIII.102**). This phenomenon is immediately followed by an exothermal event corresponding to the epoxy-amine reaction.<sup>11</sup> As soon as a part of components became more reactive by transition into liquid phase, the polymerization reaction starts. This appears as an exothermic peak ranging between 120 and 200°C, with a maximum at around 150°C, with a very steep slope which is characteristic for

epoxy-amine cross-linking in a liquid-crystal media. As seen above for TriaEP/SA, we can highlight that the ordered state should favour the crosslinking reaction.<sup>14</sup> This order could also have an influence on polymerization reactivity, with the secondary amine attack favoured than primary one, due to a proximity of electrophile site.<sup>30,31</sup> In the present study the network anisotropy was confirmed by the birefringence of Schlieren texture observed by POM (**Figure VIII.102**).

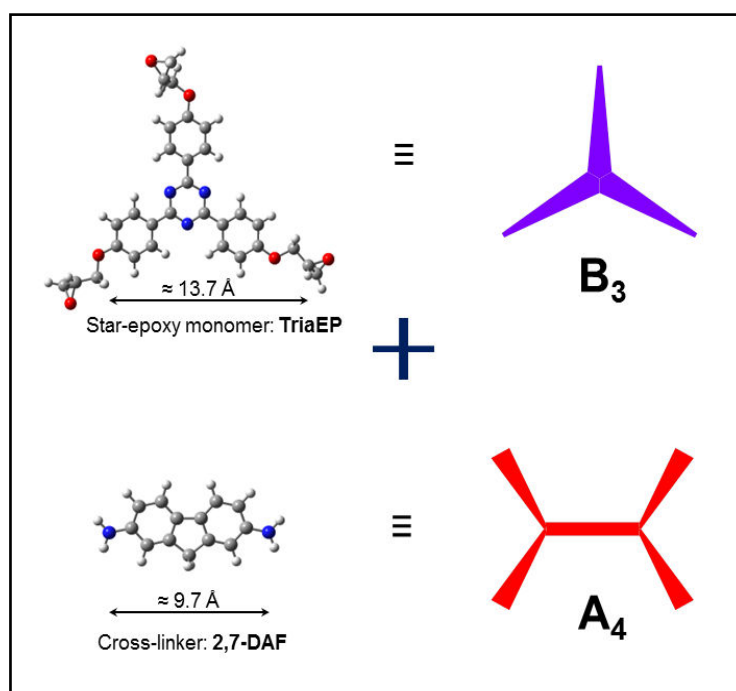


**Figure VIII.101.** Epoxy monomer and cross-linker to design A<sub>4</sub>B<sub>3</sub> TriaEP/2,7-DAF polymer. Distances were calculated with Gaussian03 software<sup>32</sup> with DFT method at the B3LYP/6-311G+ level of theory.

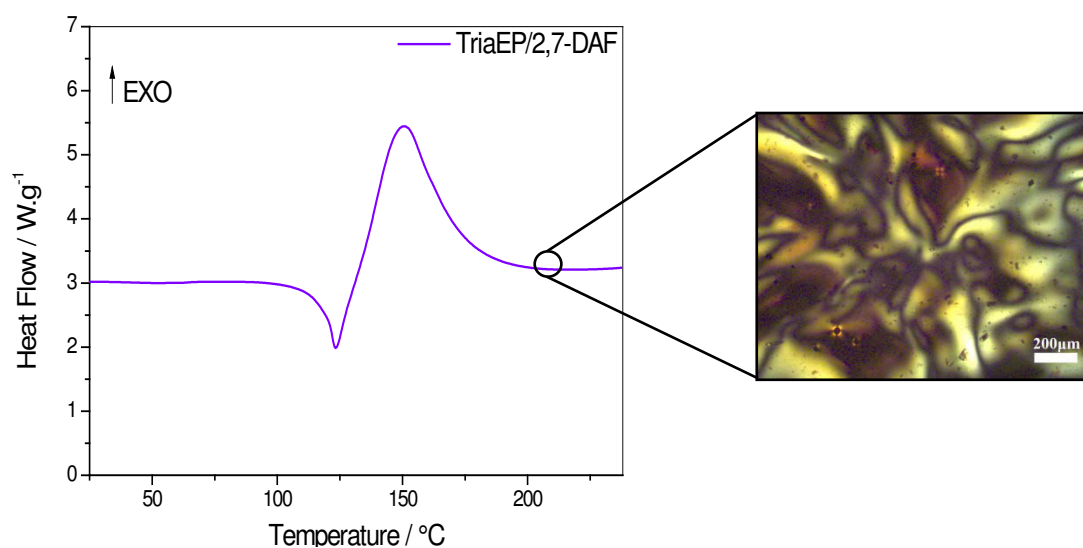


**Figure VIII.102.** TriaEP / 2,7-DAF DSC thermogram at 20 °C.min<sup>-1</sup> and the corresponding thermoset texture observed by POM

The epoxy/amine reactivity has been confirmed by FT-IR investigations, presented in **Figure VIII.103**, with the decrease of the peak at  $916\text{ cm}^{-1}$  sign of oxiran ring consumption and the peak apparition at  $1217\text{ cm}^{-1}$  which could be attributed to the aromatic C-N stretching of tertiary amine groups. The shift at  $1360\text{ cm}^{-1}$  could also be correlated with C-N stretching of the secondary amine groups.

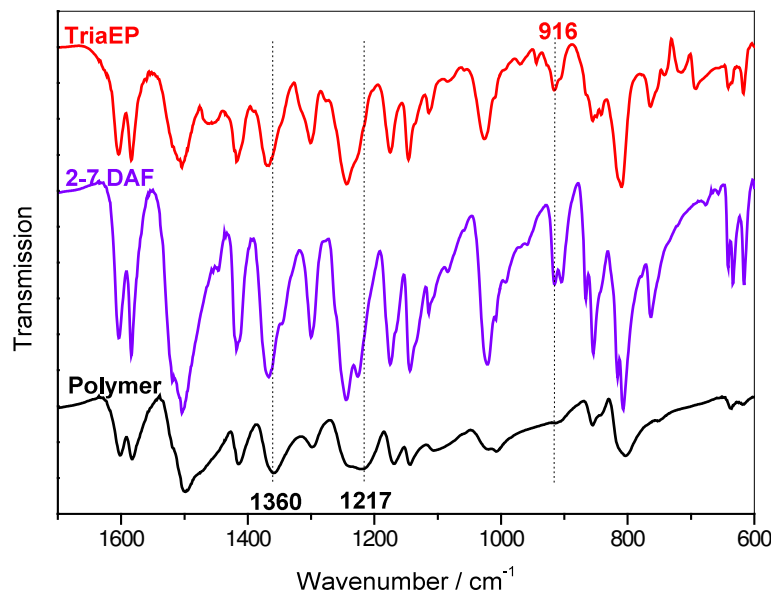


**Figure VIII.103.** FT-IR spectra of TriaEP monomer, 2,7 DAF cross-linker associated with the resulting polymer.

## VIII.4.2. Morphological and thermomechanical investigations of TriaEP/2,7 DAF

### VIII.4.2.1. TriaEP/2,7 DAF: a fractal polymerization

As seen in **Figure VIII.104 a**), the polymer TriaEP/2,7-DAF cured during 1h at  $170^\circ\text{C}$  exhibits a major diffraction peak at  $5.0\text{ \AA}$ . This diffraction could be associated with the distance between two  $\pi$ -delocalized systems, including the 2,7-DAF cross-linker. The presence of a second peak at  $55.2\text{ \AA}$  indicates a long range order which could be associated with the length of columnar mesophase and/or to the diameter of dendritic-like shape as fractal hyper-branched polymer colloids. This hypothesis could be reliable to the morphology of cryo-fracture of the fully cured polymer observed in SEM (**Figure VIII.104 b**)). The nodular surface structure is characteristic for fractal polymers (FPs) generally associated with a molecular structure of three-arms connector with rigid rod-like spacer<sup>15</sup> which corresponds to the situation here with TriaEP and

2,7-DAF structures. Indeed, Aharoni et al.<sup>33</sup> explained that primary structural unit of FPs is formed by dense colloidal particles of diameter of around 50 Å. To support this assumption, the dependence of intensity  $I(q)$  on  $q$  (**Figure VIII.105**) has been calculated from **Equation (1)**, with the momentum transfer  $q$ , also called the scattering vector, defined as:

$$q = 4\pi\sin(\theta/2)\lambda \quad (1)$$

and characterized by the scattering angle  $\theta$  and the wavelength  $\lambda$  of the scattered beam.<sup>34</sup> An exponent power between 3 and 4 is an indication of the fractal nature of the thermoset network (**Equation (2)**)<sup>35,36,37</sup> with the mass fractal dimension ( $D_f$ ) between 3 and 4 and the surface fractal dimension ( $D_s$ ) between 2 and 3 (**Equation (3)**).

$$I(q) \propto q^{-D_f}; 3 < D_f \leq 4 \quad (2)$$

With

$$6 - D_s = D_f; 2 \leq D_s < 3 \quad (3)$$

The results summarized on **Table 1** confirm the supposition of a fractal growing nature of the mesomorphic epoxy-amine network with a high  $D_s$  value of 2.8. A  $D_s = 2$  corresponds to a smooth surface, and  $D_s$  increases toward 3 for a corrugated surface<sup>34</sup>, which is in our case in good agreement with the tri-dimensional hyper-branched cross-linking assumption.<sup>38</sup> The calculated dimensions of monomer and cross-linker, presented in **Figure VIII.101**, are also in good correlation with the colloid dimensions, taking into account the steric hindrance generated by the high functionality in balance with the proclivity of self-assembly into mesophase. This information is reliable to the unusual reactivity of epoxy/amine crosslinking in liquid-crystalline media, where the first stage of polymerization favour the 3D branching (promoted by secondary amine) compare to 2D linear growing (reaction with primary amine).

From a geometrical point of view, a model of fractal growing based on the Voronoi tessellation concept<sup>39</sup> has been already proposed to build two-dimensional networks, and could be extended for the description of three-dimensional systems.<sup>33</sup> Another approach of biological mimics self-assembly is illustrated in **Figure VIII.104 c)** with a model of aggregation from a fractal development of primary dendrimer units, assimilated here to a colloid, to explain the formation of covalent bonded nanostructures.<sup>40,41</sup> This model is also in a good accordance with the classical network morphology described by Dusek<sup>42</sup> considering a microgel agglomeration into clusters and theirs coalescence as seen on **section II.1.2.1**.

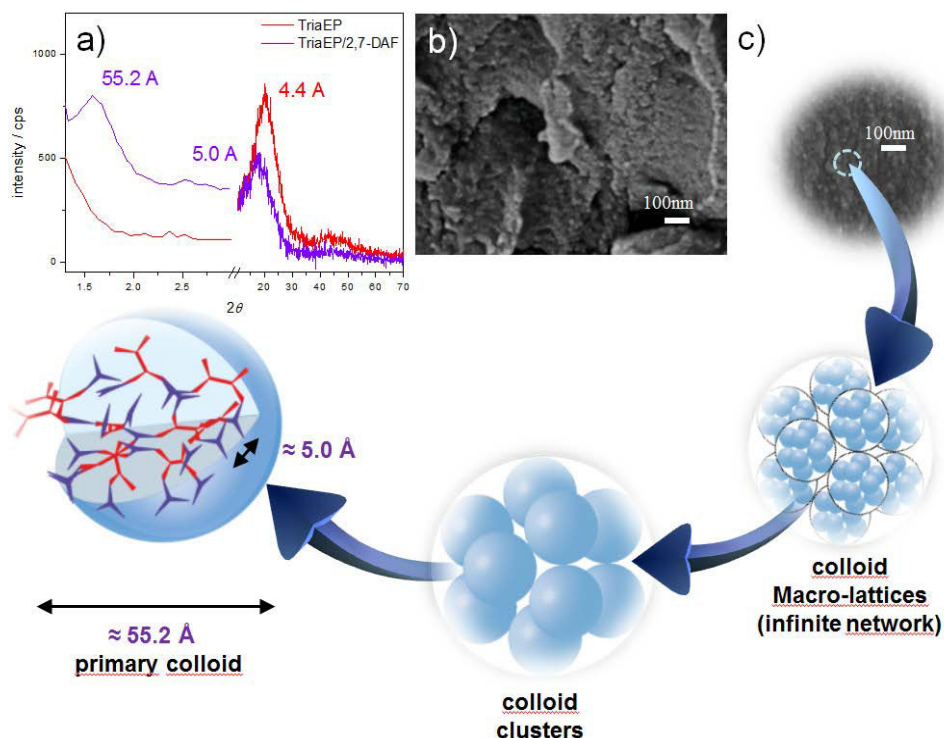


**Figure VIII.104.** WAXS patterns for TriaEP monomer at 140°C and for TriaEP/2,7-DAF polymer cured at 170°C for 1h (a); SEM fracture surface of fully cured network (b); model of dendrimer self-assembly extend to colloids from “Genealogically Directed Synthesis” in analogy with biological systems (c).<sup>43</sup>

As specify by Baer et al.<sup>44</sup> information concerning the self-organization of biological hierarchical structures can be useful to have an overview of the nanoscopic complexity, to be able to envision desired spectrum of functional properties. Thus, this biomimetic model could be a good approximation in regard to the fractal development which is a recurrent scheme to describe the great variety of natural structures.<sup>45</sup>

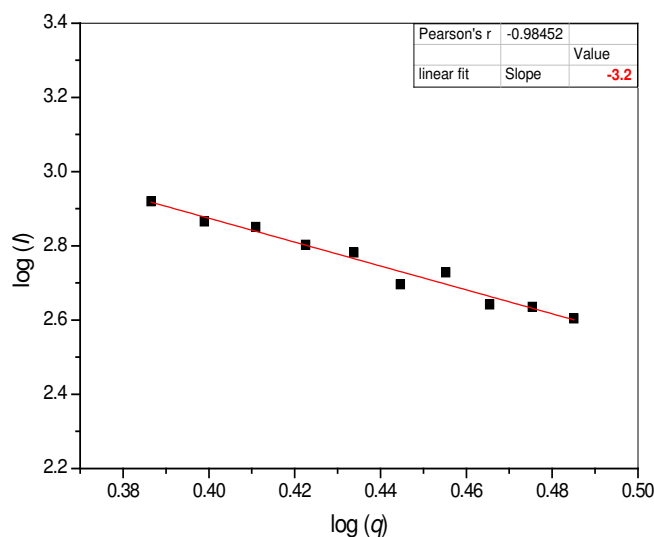


**Figure VIII.105.** Intensity of WAXS versus  $q$  of highly cross-linked TriaEP/2,7-DAF thermoset plotted on log-log scale.

**Table VIII.15.** X-ray d-spacing and scattering exponents.

Polymer	X-ray d-spacing (Å)		mass fractal dimensions $D_f$	surface fractal dimensions $D_s$
	short range	long range		
	TriaEP/2,7-DAF	5.0	55.2	3.2

#### VIII.4.2.2. Relationship between anisotropic architecture and thermomechanical properties

Tan  $\delta$  curves of **Figure VIII.106** make the distinction between three relaxations commonly called  $\gamma$ ,  $\beta$ ,  $\alpha$ , in an ascending temperature range order, and associated with polymer chains part motions.<sup>38</sup> Indeed, TriaEP/2,7-DAF polymer is characterized by a main cooperative  $\alpha$  transition at 220°C for a curing temperature of 160°C for 3h. This very high transition temperature is usually found for dense aromatic cross-linked networks.<sup>14,46</sup> The weak amplitude of  $\alpha$  relaxation peak could be explained by a very dense network due to a high functionality but also by the mesogenic network character. Herein, Ortiz et al.<sup>47</sup> explain the molecular constraint by a restriction of cross-link motions from all directions, imposed by the supramolecular self-assembly associated with the randomly oriented mesophases in poly-domains. The residual segmental mobility in an interval temperature below  $T_\alpha$ , such as  $\beta$  transition at 85°C, is correlated on the epoxy-amine networks with the crankshaft motions of the -N-CH<sub>2</sub>-CH(OH)-CH<sub>2</sub>- segments. The polymer exhibits a modulus of  $E' = 2.41$  GPa at room temperature which corresponds to a highly cross-linked network.<sup>47</sup> However the most notable result concerns the extremely high value of  $E' = 690$  MPa in the rubbery region, above  $T_\alpha$ , even for liquid-crystalline epoxy networks. For the sake of comparison, for a very ordered smectic epoxy thermoset network Ortiz et al.<sup>47</sup> measured a modulus on the rubbery plateau of  $E' = 115$  MPa. This unusual high value of modulus plateau above  $T_\alpha$ , is characteristic of mesogenic tri-dimensional networks, where the deformation is mostly dominated by the entropic response and by the mobility of the aliphatic part provided by opened epoxy rings.<sup>47</sup> Due to the dense ordered mesophase the crosslinks aren't free to move in all directions, even above  $T_\alpha$ , which explains the very high value of  $E'$  and the presence of rubbery plateau. This particularity favours the integrity of architecture until the thermal degradation.

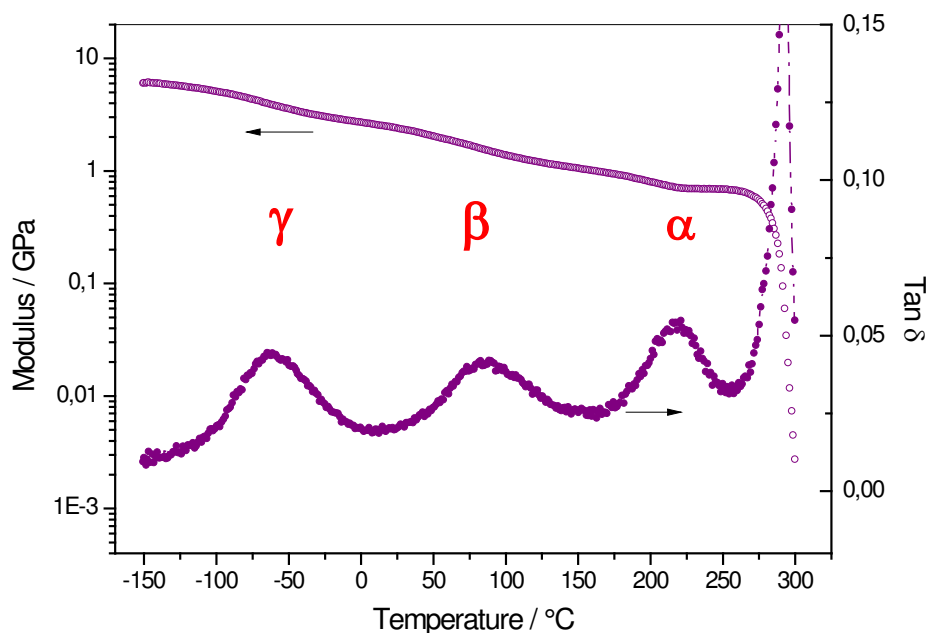


**Figure VIII.106.** Tan  $\delta$  and  $E'$  modulus curves from DMA experiments in traction mode for TriEP/2,7-DAF polymer at 1 Hz and  $1^{\circ}\text{C}\cdot\text{min}^{-1}$

The TGA thermogram of the crosslinked material is presented in **Figure VIII.107**. A two steps thermal decomposition mechanism could be observed in 250-800°C temperature range. A first thermal degradation reaction, the cleavage of network, occurs at high temperatures, around 350°C, highlighting a good thermal resistance of LCT.<sup>48</sup> The 10% of mass loss of the material is observed at around  $T_{d\ 10\%} = 393^{\circ}\text{C}$ .

As observed in **Figure VIII.107** the slope of the degradation curve is very slow, the material being stable against temperature. At around 500°C, the mass loss is only 30%. This peculiar behavior underlines a high thermal stability of the material.<sup>49</sup> The starting temperature range of degradation of the polymeric network is well correlated with the DSC results. The first degradation step at 354°C reveals a small exotherm in DSC curve, which could correspond to a small amount of thermal decomposition reactions with the generation of some radicals.

Another exothermic peak observed in DSC at around 621 °C could be correlated with the thermo-oxidation and carbonization of the aromatic moieties. This second degradation mechanism occurs very fast, with a complete degradation of material, i.e. without any residual products starting from 700°C.

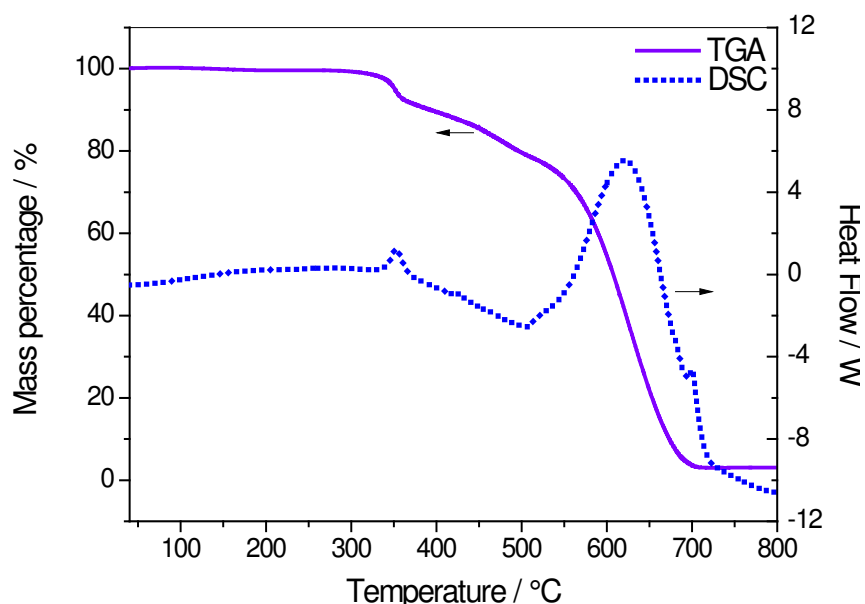


**Figure VIII.107.** Mass percentage and heat flow curves from TGA/DSC measurement at  $10^{\circ}\text{C}\cdot\text{min}^{-1}$  under air.

### VIII.5. Conclusions

In this chapter we report, up to our knowledge, the first study of a star-shaped epoxy mesogen molecule, called TriaEP which was successfully synthesized, with a very good yield. In addition to its potential importance as precursor for  $C_3$ -symetric supramolecules, we have been interested in this present work to explore it's reactivity as monomer through two examples. In the first example, the TriaEP/SA polymer seems to reveal an anisotropic potential to form nematic columnar mesophases that were for the first time frozen in a tridimensional architecture. The reactivity by anionic living copolymerization in liquid-crystalline media has been carefully analyzed, exhibiting a strong influence of the monomer and macromolecule mesogenic character on the polymerization kinetic. This influence is expressed by a transition regime from Arrhenian to anti-Arrhenian behavior and *vice-versa* in correlation with the overall order variation during the polymerization. For the second example, TriaEP has been cross-linked with an aromatic diamine having a rod-like geometry (2,7-DAF), in order to generate an atypical  $A_4B_3$  polymer structure revealing a hierarchical self-organization through a nematic architecture with a fractal polymerization development. SEM nodular surface, characteristic of FPs has been confirmed by the surface fractal dimension of 2.8 calculated from WAXS experiment for a primary colloid diameter of around  $55.2 \text{ \AA}$ . This resulting material presents high  $T_g$  at about  $220^{\circ}\text{C}$  and also a very high thermal stability  $T_{d 10\%} \sim 393^{\circ}\text{C}$ .

1. Lehmann, M., Star mesogens (hekates)--tailor-made molecules for programming supramolecular functionality. *Chemistry* **2009**, *15* (15), 3638-51.
2. Demus, D.; Goodby, J. W.; Gray, G. W.; Spiess, H. W.; Vill, V., *Handbook of Liquid Crystals, Low Molecular Weight Liquid Crystals I: Calamitic Liquid Crystals*. John Wiley & Sons: 2011.
3. Laschat, S.; Baro, A.; Steinke, N.; Giesselmann, F.; Hagele, C.; Scalia, G.; Judele, R.; Kapatsina, E.; Sauer, S.; Schreivogel, A.; Tosoni, M., Discotic liquid crystals: from tailor-made synthesis to plastic electronics. *Angewandte Chemie* **2007**, *46* (26), 4832-87.
4. Percec, V.; Glodde, M.; Bera, T.; Miura, Y.; Shiyanovskaya, I.; Singer, K.; Balagurusamy, V.; Heiney, P.; Schnell, I.; Rapp, A., Self-organization of supramolecular helical dendrimers into complex electronic materials. *Nature* **2002**, *419* (6905), 384-387.
5. Cardinaels, T.; Ramaekers, J.; Guillon, D.; Donnio, B.; Binnemans, K., A Propeller-like Uranyl Metallomesogen. *Journal of the American Chemical Society* **2005**, *127* (50), 17602-17603.
6. Tschierske, C., Micro-segregation, molecular shape and molecular topology - partners for the design of liquid crystalline materials with complex mesophase morphologies. *Journal of Materials Chemistry* **2001**, *11* (11), 2647-2671.
7. Lehmann, M.; Jahr, M., Programming Star-Mesogens toward the Formation of Columnar or Cubic Phases. *Chemistry of Materials* **2008**, *20* (17), 5453-5456.
8. Pang, J.; Tao, Y.; Freiberg, S.; Yang, X.-P.; D'Iorio, M.; Wang, S., Syntheses, structures, and electroluminescence of new blue luminescent star-shaped compounds based on 1,3,5-triazine and 1,3,5-trisubstituted benzene. *Journal of Materials Chemistry* **2002**, *12* (2), 206-212.
9. Srinivas, K.; Srinivas, U.; Rao, V. J.; Bhanuprakash, K.; Kishore, K. H.; Murty, U., Synthesis and antibacterial activity of 2, 4, 6-tri substituted triazines. *Bioorganic & medicinal chemistry letters* **2005**, *15* (4), 1121-1123.
10. Srinivas, K.; Srinivas, U.; Bhanuprakash, K.; Harakishore, K.; Murthy, U.; Jayathirtha Rao, V., Synthesis and antibacterial activity of various substituted triazines. *European journal of medicinal chemistry* **2006**, *41* (11), 1240-1246.
11. Henry Lee, K. N., *Handbook of epoxy resins*. Mc Graw-Hill Book Compagny ed.; 1982.
12. Pascault, J.-P.; Williams, R. J., *Epoxy polymers*. John Wiley & Sons: 2009.
13. Aida, T.; Meijer, E. W.; Stupp, S. I., Functional Supramolecular Polymers. *Science* **2012**, *335* (6070), 813-817.
14. Carfagna, C.; Amendola, E.; Giamberini, M., Liquid crystalline epoxy based thermosetting polymers. *Progress in Polymer Science* **1997**, *22* (8), 1607-1647.
15. Shiota, A.; Ober, C. K., Rigid rod and liquid crystalline thermosets. *Progress in Polymer Science* **1997**, *22* (5), 975-1000.
16. Dash, B. P.; Satapathy, R.; Maguire, J. A.; Hosmane, N. S., Facile Synthetic Routes to Phenylene and Triazine Core Based Dendritic Cobaltabisdicarbollides. *Organometallics* **2010**, *29* (21), 5230-5235.
17. Li, Y.; Badrinarayanan, P.; Kessler, M. R., Liquid crystalline epoxy resin based on biphenyl mesogen: Thermal characterization. *Polymer* **2013**, *54* (12), 3017-3025.
18. Lu, M. G.; Shim, M. J.; Kim, S. W., Curing Reaction and Phase Change in a Liquid Crystalline Monomer. *Macromolecular Chemistry and Physics* **2001**, *202* (2), 223-230.
19. Lee, C. J.; Lee, S. J.; Chang, J. Y., Synthesis of a polymerizable discotic liquid crystalline compound with a 1,3,5-triazine core. *Tetrahedron Letters* **2002**, *43* (21), 3863-3866.
20. Harada, M.; Ando, J.; Hattori, S.; Sakurai, S.; Sakamoto, N.; Yamasaki, T.; Masunaga, H.; Ochi, M., In-situ analysis of the structural formation process of liquid-crystalline epoxy thermosets by simultaneous SAXS/WAXS measurements using synchrotron radiation. *Polymer Journal* **2012**, *45* (1), 43-49.
21. Vyazovkin, S.; Sbirrazzuoli, N., Kinetic methods to study isothermal and nonisothermal epoxy-anhydride cure. *Macromolecular Chemistry and Physics* **1999**, *200* (10), 2294-2303.
22. Vyazovkin, S.; Sbirrazzuoli, N., Isoconversional method to explore the mechanism and kinetics of multi-step epoxy cures. *Macromolecular rapid communications* **1999**, *20* (7), 387-389.
23. Vyazovkin, S.; Sbirrazzuoli, N., Mechanism and Kinetics of Epoxy-Amine Cure Studied by Differential Scanning Calorimetry. *Macromolecules* **1996**, *29* (6), 1867-1873.
24. Vyazovkin, S.; Sbirrazzuoli, N., Isoconversional analysis of the nonisothermal crystallization of a polymer melt. *Macromolecular rapid communications* **2002**, *23* (13), 766-770.

25. Vyazovkin, S.; Sbirrazzuoli, N., Isoconversional analysis of calorimetric data on nonisothermal crystallization of a polymer melt. *The Journal of Physical Chemistry B* **2003**, *107* (3), 882-888.
26. Bosq, N.; Guigo, N.; Persello, J.; Sbirrazzuoli, N., Melt and glass crystallization of PDMS and PDMS silica nanocomposites. *Physical Chemistry Chemical Physics* **2014**, *16* (17), 7830-7840.
27. Codou, A.; Guigo, N.; van Berkel, J.; De Jong, E.; Sbirrazzuoli, N., Non-isothermal Crystallization Kinetics of Biobased Poly (ethylene 2, 5-furandicarboxylate) Synthesized via the Direct Esterification Process. *Macromolecular Chemistry and Physics* **2014**, *215* (21), 2065-2074.
28. Nunez, A.; Hollebeek, T.; Labes, M. M., Chemical reactions in liquid crystalline solvents: anti-Arrhenius behavior as a consequence of nematic-smectic A-reentrant nematic phase transitions. *Journal of the American Chemical Society* **1992**, *114* (12), 4925-4926.
29. Chen, W.; Dadmun, M.; Zhang, G.; Boller, A.; Wunderlich, B., Isotropization of nematic liquid crystals by TMDSC. *Thermochimica acta* **1998**, *324* (1), 87-94.
30. Mititelu, A.; Hamaide, T.; Novat, C.; Dupuy, J.; Cascaval, C. N.; Simionescu, B. C.; Navard, P., Curing kinetics of liquid-crystalline epoxy resins with inverse reactivity ratios. *Macromolecular Chemistry and Physics* **2000**, *201* (12), 1209-1213.
31. Vyazovkin, S.; Mititelu, A.; Sbirrazzuoli, N., Kinetics of Epoxy–Amine Curing Accompanied by the Formation of Liquid Crystalline Structure. *Macromolecular Rapid Communications* **2003**, *24* (18), 1060-1065.
32. Frisch, A.; Frisch, M. J.; Trucks, G. W., *Gaussian 03 user's reference*. Gaussian, Incorporated: 2003.
33. Aharoni, S.; Edwards, S., Rigid Polymer Networks, volume 118 of Advances in Polymer Science. Springer, Berlin: 1994.
34. Aharoni, S. M., Gelled networks prepared from rigid fractal polymers. *Macromolecules* **1991**, *24* (1), 235-239.
35. Martin, J. E.; Hurd, A. J., Scattering from fractals. *Journal of Applied Crystallography* **1987**, *20* (2), 61-78.
36. Schmidt, P. W.; Höhr, A.; Neumann, H. B.; Kaiser, H.; Avnir, D.; Lin, J. S., Small-angle x-ray scattering study of the fractal morphology of porous silicas. *The Journal of Chemical Physics* **1989**, *90* (9), 5016-5023.
37. Aharoni, S. M.; Murthy, N. S.; Zero, K.; Edwards, S. F., The fractal nature of 1-step highly-branched rigid rodlike macromolecules and their gelled-network progenies. *Macromolecules* **1990**, *23* (9), 2533-2549.
38. Pascault, J.-P.; Sautereau, H.; Verdu, J.; Williams, R. J., *Thermosetting polymers*. CRC Press: 2002; Vol. 64.
39. Voronoi, G., Nouvelles applications des paramètres continus à la théorie des formes quadratiques. Premier mémoire. Sur quelques propriétés des formes quadratiques positives parfaites. *Journal für die reine und angewandte Mathematik* **1908**, *133*, 97-178.
40. Hawker, C. J.; Frechet, J. M., Preparation of polymers with controlled molecular architecture. A new convergent approach to dendritic macromolecules. *Journal of the American Chemical Society* **1990**, *112* (21), 7638-7647.
41. Tomalia, D. A.; Naylor, A. M.; Goddard, W. A., Starburst dendrimers: molecular-level control of size, shape, surface chemistry, topology, and flexibility from atoms to macroscopic matter. *Angewandte Chemie International Edition in English* **1990**, *29* (2), 138-175.
42. Dušek, K., Are cured thermoset resins inhomogeneous? *Die Angewandte Makromolekulare Chemie* **1996**, *240* (1), 1-15.
43. Tomalia, D.; Durst, H. D., Genealogically directed synthesis: Starburst/cascade dendrimers and hyperbranched structures. In *Supramolecular Chemistry I — Directed Synthesis and Molecular Recognition*, Springer Berlin Heidelberg: 1993; Vol. 165, pp 193-313.
44. Baer, E.; Hiltner, A.; Keith, H., Hierarchical structure in polymeric materials. *Science* **1987**, *235* (4792), 1015-1022.
45. Mandelbrot, B. B., The fractal geometry of nature/Revised and enlarged edition. New York, *WH Freeman and Co.*, 1983, 495 p. **1983**, *1*.
46. Ochi, M.; Shimizu, Y.; Nakanishi, Y.; Murata, Y., Effect of the network structure on thermal and mechanical properties of mesogenic epoxy resin cured with aromatic amine. *Journal of Polymer Science Part B: Polymer Physics* **1997**, *35* (2), 397-405.
47. Ortiz, C.; Kim, R.; Rodighiero, E.; Ober, C. K.; Kramer, E. J., Deformation of a Polydomain, Liquid Crystalline Epoxy-Based Thermoset. *Macromolecules* **1998**, *31* (13), 4074-4088.

48. Vincent, L.; Mija, A.; Sbirrazzuoli, N., Liquid crystalline and isotropic epoxy thermosets: Mechanism and kinetics of non-isothermal degradation. *Polymer Degradation and Stability* **2007**, *92* (11), 2051-2057.
49. Bellenger, V.; Fontaine, E.; Fleishmann, A.; Saporito, J.; Verdu, J., Thermogravimetric study of amine cross-linked epoxies. *Polymer Degradation and Stability* **1984**, *9* (4), 195-208.



## **Chapter IX**

General conclusion and perspectives



## IX. General conclusion and perspectives

### IX.1. General conclusion

After the conclusions relatives to each chapter, that expose the main results and interpretations, this general conclusion aims to cross the advances in thermosets field in the light of the objectives presented in the introductive **Chapter I**.

(4) *Upgrade the knowledge on monomers behavior as precursors for the elaboration of thermosets in terms of polymerization and structure-properties correlation* **Chapter IV, VI, VIII**

As presented in **section II.1.1.2.** in epoxies thermosets science, the nature of monomers governs the polymeric architecture which is driven by the functionality rules and determines also the reactivity. However, the physico-chemical characteristics of the monomers have a great impact in the network design:

- ◆ Indeed, as a first example, ELO and TriaEP are epoxy monomers both with three-arms geometry (star-shape), but they differ by several aspects, as illustrated in **Table IX.16**. These dissimilarities induce not only differences between the physico-chemical properties intrinsic of monomers but condition the overall polymerization reactivity and thus the construction of polymer architecture. This is particularly relevant in regard to the apparent activation energy ( $E_a$ ) of polymerization. Indeed, for a same epoxy/mono-anhydride polymerization reaction – i.e. the living anionic copolymerization – the systems ELO/MHHPA/2MI and TriaEP/SA/2MI present a very different evolution of  $E_a$  dependency. For ELO system this dependency presents a *classical* scenario with the successive chemical and diffusion controls, associated with characteristic values of  $E_a$ . In the case of TriaEP system, a very complex mechanism needs to be considerate in addition to the *classical* ELO behavior: the overlapping and evolution of supramolecular interactions of TriaEP monomer and TriaEP/SA polymer.

**Table IX.16.** ELO vs TriaEP physico-chemical characteristics

ELO	TriaEP
viscous liquid at <i>RT</i>	solid at <i>RT</i>
isotropic character	mesogenic character 135 °C < LC < 150 °C
aliphatic	aromatic
~ 5.5 epoxies	3 epoxies
internal epoxies	terminal epoxies

- ◆ With ELO/FA as a second example, the classical functionality associated to the epoxy/alcohol reaction is modified by the superimposition of two main reactions. The first one is the epoxy/alcohol reaction respecting the functionality rules. The second one corresponds to the FA self-condensation in C<sub>2</sub> position and cross-linking. The theoretical functionality of ELO50/FA50 is about 1:1.76 considering only epoxy/alcohol reactions, but is lower in reality, more close to a stoichiometric ratio (1:1) due to FA self-reaction consumption. Thus the overall polymerization and network formation are kinetically dependent on the competition between these two main reactions. This original example of combined cationic polymerizations represents well the advantages of thermosets science that allows to combine different kind of polymerizations with a selection of versatile monomers such as ELO or FA.

*(5) Elaboration of performant (fully) bio-based materials. Chapter IV, V, VI*

The transition to performant bio-based thermosets as alternative to petroleum-based resins is not evident because usually high  $T_g$  is associated with aromatic moieties (mostly phenyl moieties issued from petroleum) present on the polymer network. However, another way could be envisaged to reach high  $T_g$ . Our purpose has been to take advantage of the particular structure of ELO (with ~5.5 epoxy groups per triglyceride) by increasing the crosslink density to the maximum. So to reach a very dense network and thus an high  $T_g$ . This strategy has been relevant with a  $T_g$  of about 134 °C for the system ELO + mono-anhydride MHHPA, i.e. without aromatic moieties. The utilization of a cross-linker with a higher functionality, BTDA di-anhydride has also been successful. This kind of cross-linker is commonly used in industry in little quantity in the epoxy formulations to improve the  $T_g$ . In this context, as principal cross-linker, only a small quantity can be used for processability: our formulation was 1:0.5 in proportions of ELO and BTDA in regard to their functionalities. The large epoxy excess has been essential in regard with the final properties of thermoset material that exhibits two  $T_g$  at 127 and 240°C, with two kind of networks: respectively one copolymer network reinforced by homopolymer linkage, and one containing mostly the homopolymer. This last very high  $T_g$  highlights the great importance of homopolymerizations on the final targeted network properties.

Concerning the elaboration of fully bio-based thermosets, two strategies have been proposed in this manuscript. The first strategy has been to create resins from the association of FA and humins. This route represents the most logical choice, with the combination of two furanic

entities, provided by the same bio-based “family”, which means from carbohydrates catalytic conversion. This furanic combination confirmed to be very interesting in terms of structure and chemistry, more specifically, concerning the very good solubilization of humins in FA, and the multiple possible cross-linking ways between the FA/FA oligomer and the furanic structure of humins particles. The second strategy was based on the combination of different bio-resources: ELO and FA. The epoxidation of linseed oil contributes to increase the reactivity and also the hydrophilic character of triglycerides, which had permitted to easily mix ELO and FA without phase separation.

In term of monomeric contribution for the elaboration of tridimensional networks, these molecules possessing antagonist properties can polymerize together conducting on a network with hybrid properties. Indeed, FA/FA oligomers contribute to the network rigidity by aromatic furanic moieties, (in replacement of benzoic moieties currently provided by petroleum-based hardeners, as exposed above) while ELO contribution is reliable to a plasticization of the network by this intrinsic aliphatic moieties, but also because ELO provokes steric hindrances that reduce the PFA cross-links density. Both of these strategies lead to generate fully bio-based thermoset polymers with,  $T_g$  varying from 20 °C to 170 °C.

*(6) Proposes original strategies to improve classical thermosets properties or to develop new ones. Chapter V, VII, VIII*

The proposed strategy has been based on a bio-mimetic reflection around the hierarchical matter organization at different scales from micrometer to nanometer (illustrated in **Figure IX.108**). Herein, for the micro-scale, humins have been successfully used as core-shell particles, through a preliminary investigation on cellulose composites, to respond to the PFA major problem, i.e. the brittleness.

For the micro and nanoscale the utilization of oriented nanofillers (m-Sep) has proven to be efficient in the generation of a controlled anisotropy following the applied magnetic field orientation. Finally, the polymerization of a star-epoxy mesogen exhibited a self-assembly from nanoscale (liquid-crystalline phase) to microscale.

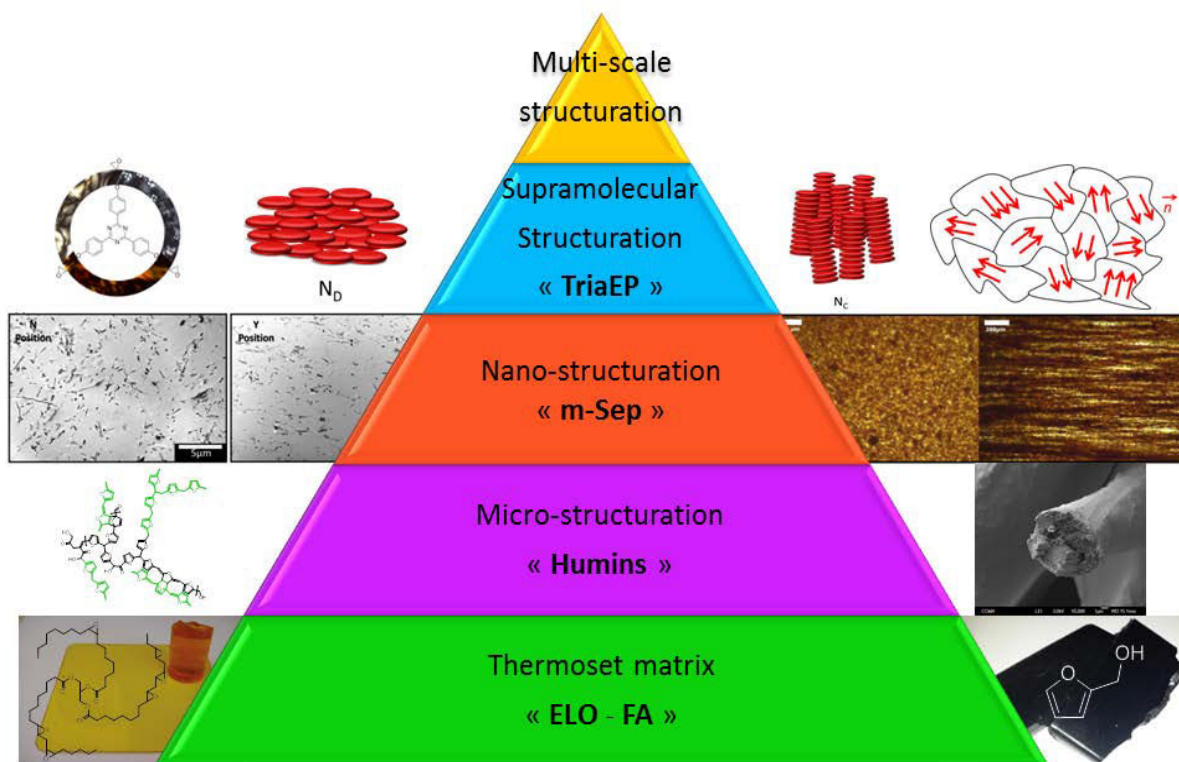


**Figure IX.108.** Thesis strategy of thermoset multi-scale organization

## IX.2. Perspectives

This last part of the thesis manuscript would like to expose some potential perspectives related to each chapter separately, by brief terms and finally to propose a general envision of the subject at long term.

- ◆ **Chapter IV:** after this fundamental work on reactivity with petroleum-based hardeners, possible investigations would be to develop formulations with green hardeners, favoring cross-linkages by 1-1 functionality, as carboxylic acids/anhydrides instead of amines, because of the inherent steric hindrance of the triglyceride network. An idea to reach high  $T_g$  could be to use the succinic anhydride (short linker) that is derived from lactic acid. Another proposition, could be to improve this ELO/anhydride matrix by the elaboration of copolymer/nanocomposite, as an example with epoxidized silica nanocage: octakis(dimethylsiloxypopyl)glycidylether)silsesquioxane called POSS-OG (seen [Pub 05] in Annexes).
- ◆ **Chapter V:** as a complementary work, after the study of cellulosic composite, a possible issue should be to investigate humins resin behavior in bulk, for another kind of application such as mold for instance. A first encouraging result is exhibited in the **Figure IX.109** with

the DMA of 40FA/55Hu/5MA in regard to pure PFA resins. The main result can be summarized to a less dense network for humins resin, with an higher  $T_{\alpha}$  in comparison with pure PFA material. The presence of a secondary transition at  $T = -20^{\circ}\text{C}$  could be reliable to the ductile part of humins structure. This behavior is in good agreement with composite mechanical test, highlighting an increase of both ductility and rigidity properties.

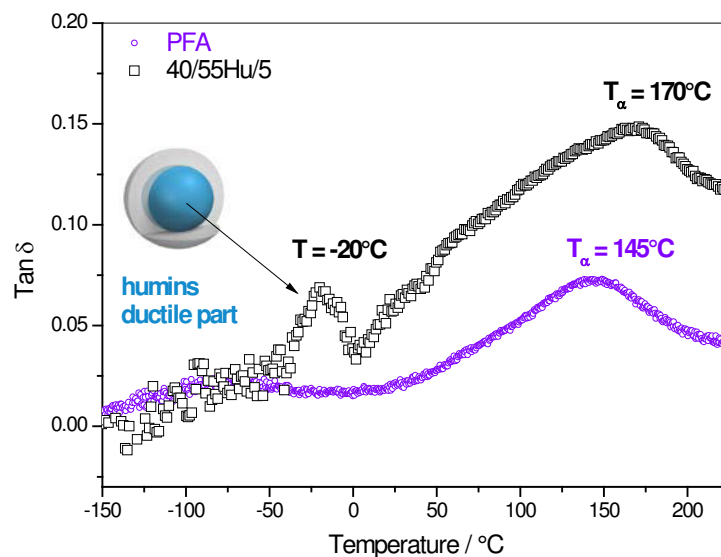


**Figure IX.109.** DMA of resin bulk for PFA and 40FA/55Hu/5MA in the same conditions as presented in **Chapter III**.

Concerning humins potential applications, in my opinion, one of an easier issue could be the use of humins as bitumen in additive or itself after modifications. Another higher added value application could be the utilization of humins for the elaboration of carbon material following the investigation on HTC materials.

- ◆ **Chapter VI:** after focusing on the principal ELO/FA reactivity, with the middle 50/50 ratio, the future works could be oriented to the study of side-reactions influence (higher ratios of ELO) such as homopolymerization/etherification, firstly on the reactivity and secondly on the network density reliable to mechanical properties.
- ◆ **Chapter VII:** nanofiller's orientation in DGEBA matrix has been proven to be efficient to provoke anisotropic magnetical and mechanical properties. Now we could consider the utilization of a greener matrix, like ELO, with the difficulty to choose an adapted cross-linker. Indeed, as shown on the **Chapter IV**, the utilization of aliphatic amines (as presented in the **Chapter VII** with DGEBA) for ELO cross-linking didn't reach a fully cured material. Another interesting issue could be to use an high frequency alternative magnetic field devise

to selectively heat locally magnetite particles in order to induce the polymerization from the m-Sep. This approach, illustrated in **Figure IX.110**, could lead to improve the compatibility between nanoparticles and matrix that could be the main challenge for the strategy to improve the mechanical properties.

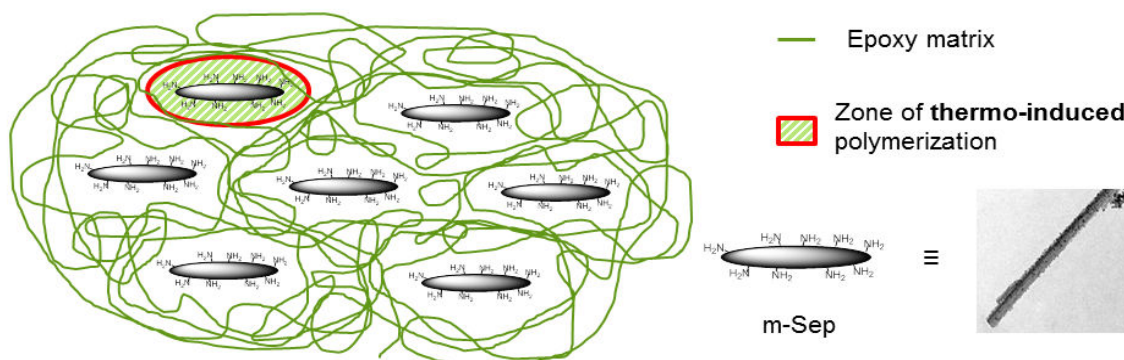


**Figure IX.110.** Strategy of thermo-induced polymerization by an alternative magnetic field

- ◆ **Chapter VIII:** Several issues could be considered to promote star-epoxy mesogens as high added value monomers for the conception of multi-functional materials. As a first example, this kind of mesogenic monomers should be interesting to generate self-healing materials by promoting supramolecular interactions that could induce a possible segregation in order to favor reversible reactions such as the di-sulfur metathesis for instance. As a second example, rigid star-epoxy mesogen like TriaEP could be a very interesting precursor for the elaboration of materials with a multi-scale porosity. Indeed, the generation of a controllable porosity (around 30-100 nm) is possible for an epoxy/amine resin system considering supramolecular interaction which could occur during the polymerization in a polar solvent. Recently, the research has focused on conjugated microporous polymers (CMPs) that exhibit tailored micropores (1-3 nm). The distribution and surface area of such thermoset generated is reliable to a rigid three-arm monomer linked to a rigid rod-like spacer. Thus, by the association of TriaEP monomer with a rigid cross-linker, using a functionality of 1-1, a material which presents two different scales of porosities could be obtained.

Since the classical tridimensional cross-linked amorphous polymers elaborated in the beginning of 20<sup>th</sup> century, thermosets science field has been continually enlarged in correlation with the major discoveries in chemistry field. Herein, as seen on **section II.3.5.1**, with the theoretical description of the liquid-crystal state, De Gennes initiated the great adventure of liquid-crystalline thermosets. In the same manner, Lehn's work on supramolecular chemistry and then

on dynamic adaptive chemistry, has contributed to extend the thermosets field by the creation of dynamic covalent polymers. These thermosets possess a network with reversible covalent cross-linked bonds that are able to respond to several stimuli such as pH or temperature, leading to self-healing properties for instance. As examples, these reversing covalent reactions could correspond to transesterification or disulfide metathesis reactions. Finally, in regard to the quest of the *universal dynamic nature* undertaken by Leonardo Da Vinci (**section II.3.**) through the precursory concept of bio-inspiration, the lowest common denominator of this motion could be the chemical bond, in all of its diversity. Thus, the elaboration of a future generation of adaptive biomimetic materials could be based on the association of bio-inspiration concept with the utilization of bio-based synthons and monomers. The building-blocks required to accomplish the “eco-design” of this kind of materials could be found in the richest diversity provided by the combination of different bio-resources that can derived from ligno-cellulosic biomass, lipids or 3<sup>rd</sup> biomass generation (algae and aquatic derived).



# ANNEXES

## Patent

- Ed de Jong, Jan Kees van der Waal, Nathanael Guigo, Jean-Mathieu Pin, *Composition comprising furfuryl alcohol*, **Dutch Patent Application, 2013**, P31679NL00.

## Publications

- **[Pub 01]:** Jean-Mathieu Pin, Nathanael Guigo, Alice Mija, Luc Vincent, Nicolas Sbirrazzuoli, Jan Kees van der Waal, Ed de Jong, *Valorization of bio-refinery side-stream products: combination of humins with polyfurfuryl alcohol for composite elaboration*, **ACS Sustainable Chem. Eng.** **2014**, 2(9), 2182-2190.

### **Abstract:**

A challenge of today's industry is to transform low-value side products into more value-added materials. Humins, a byproduct derived from sugar conversion processes, can be transformed into high value-added products. Thermosetting furanic composites were elaborated with cellulose filters. Large quantities of humins were included into a polyfuranic thermosetting network. Comparisons were made with composites generated with polyfurfuryl alcohol (PFA) and with PFA/lignin. It was concluded that new chemical interactions were created between the side-chain oxygen groups of the humins and the PFA network. Analysis of the fracture surface of the composites containing humins lead to the conclusion that higher interfacial bonding and more efficient stress transfer between the matrix and the fibers is present. The higher ductility of the humins-based matrix allows for a two-fold higher tensile strength in comparison with other composites tested. Incorporation of humins decreases the brittleness of the furanic composites, which is one major drawback of the pure PFA composites.

- **[Pub 02]:** Jean-Mathieu Pin, Nicolas Sbirrazzuoli, Alice Mija, *From epoxidized linseed oil to bio-resin: an overall approach of epoxy/anhydride cross-linking*, **ChemSusChem** **2015**, *8*, 1232–1243.

**Abstract:**

Biorenewable resources can be used as green monomers to design tailored structures for formulations that can play an important role as functional materials. The choice of optimal structures depends on the targeted properties and applications. This work focuses on the elaboration of biobased materials with toughened mechanical properties based on epoxidized linseed oil. This result was obtained by an overall approach of cross-linking process, that is, starting with the optimal choice of hardeners and finally favoring the side reactions of polymerization. Therefore, the anionic alternating copolymerization of epoxide with mono- and dianhydrides was investigated to tailor the parameters that led to maximal conversions and properties. The obtained highly cross-linked networks perform well, as demonstrated by good impact strengths, high glass transition temperatures, and excellent thermal stability, which opens up the possibility of using these emergent materials for industrial applications.

- **[Pub 03]:** Jessica Alves Marins, Alice Mija, Jean-Mathieu Pin, Françoise Giulieri, Bluma Guenther Soares, Nicolas Sbirrazzuoli, Pascal Lançon, Georges Bossis *Anisotropic Reinforcement of Epoxy-Based Nanocomposites with Aligned Magnetite-Sepiolite Hybrid Nanofiller*, **Composites Science and Technology** **2015**, *112*, 34–41.

**Abstract:**

Magnetic sepiolite fiber (m-SEP) was successfully prepared by chemical coupling of aminosilane- functionalized sepiolite with epoxysilane-functionalized magnetite, as confirmed by Fourier Transform Infrared Spectroscopy and Transmission Electron Microscopy. This hybrid material was magnetically aligned into an epoxy resin under the action of a relatively weak magnetic field and the resulting oriented dispersion was cured with a polyether amine. The addition of m-SEP increased the flexural modulus of the epoxy nanocomposites and the alignment in the longitudinal direction resulted in an additional reinforcement of the epoxy network, mainly for system containing 10wt% of m-SEP. These results confirm the anisotropic reinforcing effect of the aligned magnetic sepiolite fibers.

- **[Pub 04]:** Jean-Mathieu Pin, Nathanael Guigo, Luc Vincent, Nicolas Sbirrazzuoli, Alice Mija, *Combination of epoxidized linseed oil and furfuryl alcohol to design tailored fully bio-based material*, **submitted**.

**Abstract:**

Epoxidized Linseed Oil (ELO) and Furfuryl Alcohol (FA) are bio-resourced monomers with high potential in material science. This work proposes to copolymerize for the first time these monomers, under  $\text{BF}_3$  catalysis, with the aim to design fully green thermoset. Herein, the cationic polymerization reactivity has been investigated through DSC and obtained structures confirmed by IR spectroscopy and 2D NMR revealing the principals chains connections. Essentially, the interconnections between oxiran rings of ELO and the hydroxyl groups of furanic moieties are emphasized. Multi-ways possibilities of chemical connections, including copolymerization and cross-linking, lead to an homogeneous network confirmed by dynamic mechanical analysis (DMA) and scanning electron microscopy (SEM). Furthermore, the tensile test measurements show the creation of a copolymer with semi-ductile behavior (tensile strain at break:  $\approx 40\%$ ), which is a significant challenge for applications as very high potential thermoset material.

- **[Pub 05]:** Jean-Mathieu Pin, Nicolas Sbirrazzuoli, Alice Mija, *Bio-based nanocomposite with epoxidized linseed oil and POSS-OG: influence of hybrid architecture on epoxy/anhydride polymerization kinetics*, **submitted**.

**Abstract:**

Epoxidized linseed oil (ELO) and octakis(dimethylsiloxypolyglycidylether) silsesquioxane (OG) have been cross-linked with mono- and di-anhydride hardeners (methyltetrahydrophthalic anhydride and pyromellitic dianhydride). Apparent activation energies ( $E_a$ ) dependencies have been firstly determined for initially systems: ELO/anhydride and OG/anhydride. Further, a compared investigation has been done for ELO/OG/anhydride copolymer with increasing ratios of 2/5/10 % in weight of OG. The influences of cross-linkers and OG co-monomer nature have been evaluated on the polymerization kinetics in regard to chemical and diffusion regime controls. SEM and WAXD observations confirmed that ELO/OG/anhydride networks are homogenous, without exhibition of OG silica nano-cage aggregations. The final architecture reveals an improvement of  $T_g$  from 103 to 129 °C for an addition of 10 % OG by weight on the ELO/anhydride matrix.

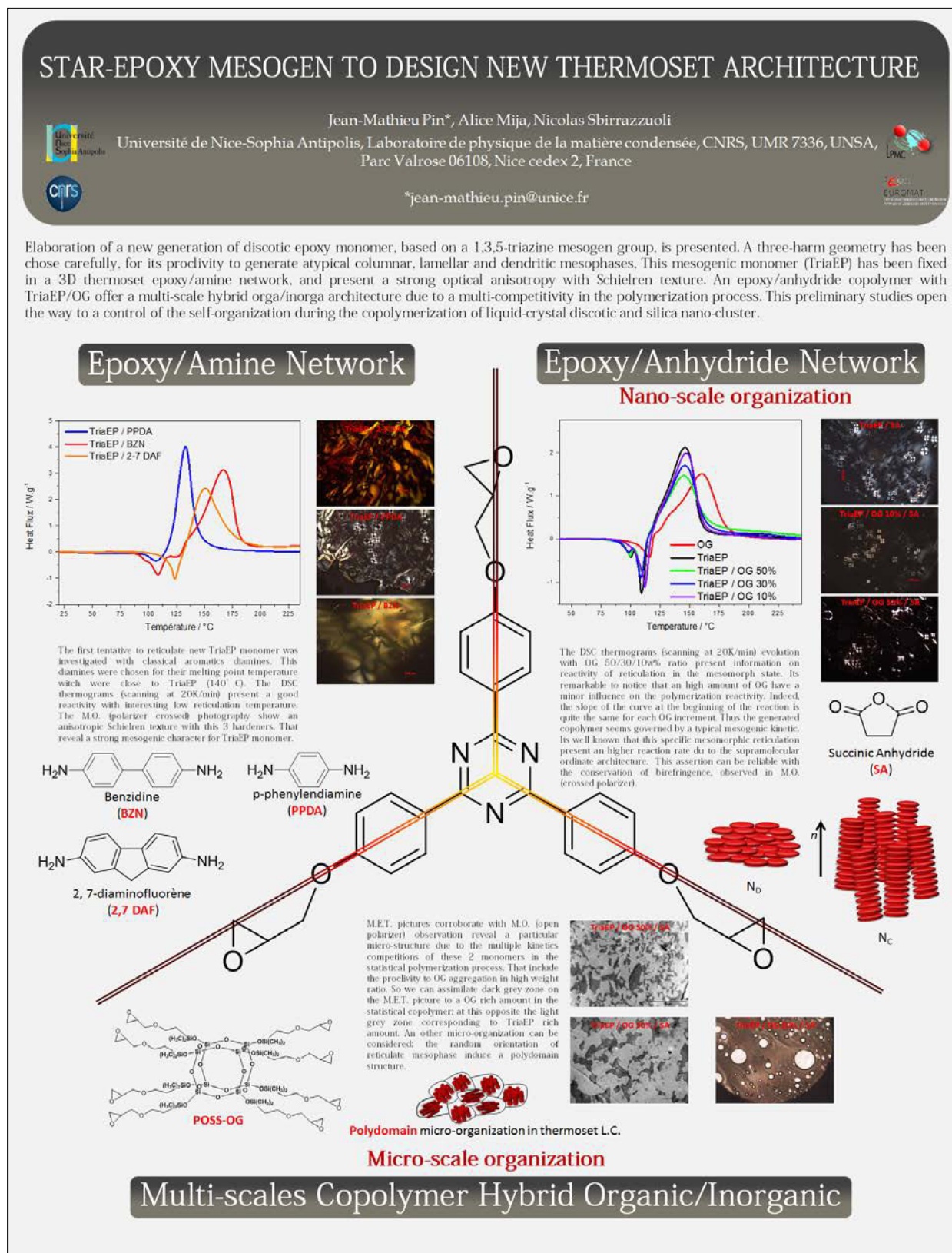
- [Pub 06]: Jean-Mathieu Pin, Nicolas Sbirrazzuoli, Alice Mija, *Star-epoxy mesogen with 1,3,5-triazine core: a model of  $A_4B_3$  fractal polymerization in a liquid-crystalline thermoset media*, **submitted**.

**Abstract:**

A Star-Epoxy monomer with intrinsic LC behavior has been synthesized by creation of a 1,3,5-triazine core. Combined with a rod-like crosslinker 2,7-DAF, a hierarchical self-assembly has been revealed. From the primary diameter colloid of around 55.2 Å to colloid cluster and to *in fine* “genealogically” generate colloid macro-lattice. The fractal development of thermoset morphology is associated to the formation of an anisotropic network through a self-organisation into nematic mesophase organized at micro-scale in polydomains. This hierarchical *multi* self-assembly has been highlighted by WAXS, SEM and POM investigations. The LC thermoset network presents high thermo-mechanical properties such as a high  $T_g$  at about 220°C and a very high thermal stability  $T_d \sim 393^\circ\text{C}$ .

## Posters

- **Jean-Mathieu Pin, Alice Mija, Nicolas Sbirrazzuoli, Star-epoxy mesogen to design new thermoset architecture, European Congress and Exhibition on Advanced Materials and Processes, EUROMAT 2013, Sep 2013, Seville, Espagne.**



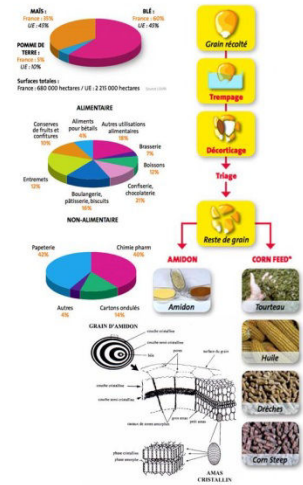
- Jean-Mathieu Pin, De la biomasse vers l'élaboration de matériaux "verts", dissemination for BIOFUR project on "Fête de la Science", Oct 2014, Parc Valrose, Nice, France.

# DE LA BIOMASSE VERS ... L'ÉLABORATION DE MATÉRIAUX "VERTS"

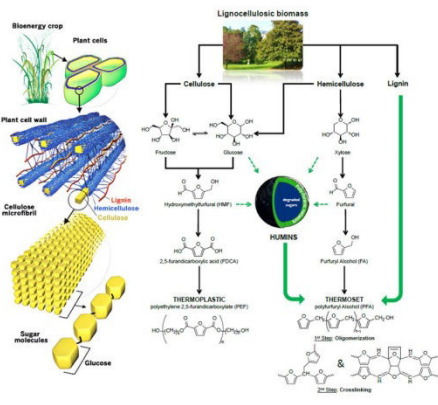
C. IEE. "A NEW POWER IS RISING" IOTR 2002



### 1ÈRE GÉNÉRATION AMIDON


### 2ÈME GÉNÉRATION BIOMASSE LIGNOCELLULOSIQUE

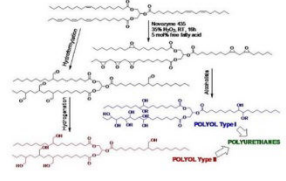
### THERMOPLASTIQUES



### THERMODURCISSEBLES



### HUILE VÉGÉTALE







**EQUIPE MATÉRIAUX ÉCO COMPATIBLES**



## Invited conferences

- Alice Mija, Jean-Mathieu Pin, Nicolas Sbirrazzuoli, **Vegetable oil based epoxy thermosets**, *European Congress and Exhibition on Advanced Materials and Processes, EUROMAT 2013*, **Sep 2013**, Séville, Espagne.
- Alice Mija, Jean-Mathieu Pin, Nicolas Sbirrazzuoli, **Polymères et matériaux issus de ressources végétales**, *Huitième Colloque Franco-Roumain de Chimie Appliquée*, **Sep 2014**, Montpellier, France

## Conferences

- Jean-Mathieu Pin, Alice Mija, Nicolas Sbirrazzuoli, **Du polymère amorphe au matériau auto-organisé, réactivité comparée**, *Colloque des doctorants de 2<sup>ème</sup> année – ED SFA*, **Mai 2013**, Amphithéâtre Valrose, Nice.
- Jessica Alves Marins, Alice Mija, Jean-Mathieu Pin, Françoise Giulieri, Bluma Guenther Soares, Nicolas Sbirrazzuoli, Pascal Lançon, Georges Bossis, **Mechanical properties of hybrid nano-composites based on sepiolite fibers aligned by a magnetic field**, *European Congress and Exhibition on Advanced Materials and Processes, EUROMAT 2013*, **Sep 2013**, Seville, Espagne.
- Alice Mija, Jean-Mathieu Pin, Luc Vincent, Nicolas Sbirrazzuoli, **Epoxidized linseed oil: a biosourced alternative to elaborate bisphenol A free thermosets**, *ACS Congress EPNOE 2013: "Polysaccharides and polysaccharide-derived products, from basic science to applications"*, **Oct 2013**, Nice, France.
- Jean-Mathieu Pin, Alice Mija, Nicolas Sbirrazzuoli, **Epoxidized linseed oil and Star-epoxy mesogen to design multi-scales thermoset architecture**, *ACS Congress EPNOE 2013: "Polysaccharides and polysaccharide-derived products, from basic science to applications"*, **Oct 2013**, Nice, France.
- Alice Mija, Jean-Mathieu Pin, Nicolas Sbirrazzuoli, **L'huile de lin époxydée : une nouvelle matrice biosourcée comme alternative aux monomères à base de bisphénol A**, *Congrès GFP-BPG 2013*, **Nov 2013**, Roubaix, France.
- Alice Mija, Jessica Alves Marins, Jean-Mathieu Pin, Nicolas Sbirrazzuoli, Georges Bossis, **Matériaux composites à base des nanofibres de sépiolite dispersées et alignées dans une matrice époxyde**, *XIème Colloque Franco-Roumain sur les Polymères*, **Août 2014**, Pitești, Romania.
- Jean-Mathieu Pin, Alice Mija, Nicolas Sbirrazzuoli, **Star-epoxy mesogène : une cinétique de réticulation conditionnée par l'ordre supramoléculaire**, *Huitième Colloque Franco-Roumain de Chimie Appliquée*, **Sep 2014**, Montpellier, France.
- Nathanael Guigo, Jean-Mathieu Pin, Alice Mija, Luc Vincent, Nicolas Sbirrazzuoli, Jan van der Waals, Ed de Jong, **Improved interfacial bonding in cellulosic biocomposites with humins-based furanic resins**, *249<sup>th</sup> ACS Meeting & Exposition, Chemistry of Natural Resources*, **March 2015**, Denver, CO, USA.

- Jean-Mathieu Pin, Alice Mija, Nicolas Sbirrazzuoli, **Star-epoxy mesogen to design multifunctional materials: polymerization kinetics and fractal self-assembly**, *European Polymer Federation EPF Dresden, June 2015*, Dresden, Germany.
- Jean-Mathieu Pin, Alice Mija, Nathanael Guigo, Luc Vincent, Nicolas Sbirrazzuoli, Jan C. van der Waals, Ed de Jong, **Fully green thermosets issued from bio-refinery: copolymerizations between furfuryl alcohol and epoxidized linseed oil or humins**, *European Polymer Federation EPF Dresden, June 2015*, Dresden, Germany.

## Honors

- **Prize for the best oral communication during COFrRoCA, SFC, Huitième Colloque Franco-Roumain de Chimie Appliquée, Sep 2014**, Montpellier, France.



- **Medal of Nice Sophia Antipolis University, researchers, PhD and post-doctoral students at the honor in 2014** *chercheurs, doctorants et post-doctorants à l'honneur en 2014*.



## ANNEXES - Français

### Introduction Générale:

La stratégie entreprise par la « recherche » internationale, dans le contexte de nos sociétés moderne, est orientée vers l'élaboration de matériaux possédant des propriétés originales, comme illustré dans la **Figure A.1**. La demande actuelle en matériaux à haute valeur ajoutées est considérable et exacerbé by un marché compétitif. La création de matériaux haute performances est devenue possible avec l'émergence des nanotechnologies. Ce domaine est le fruit d'une transversalité entre les sciences chimique et physique, le but étant le contrôle de l'auto-assemblage d'entités nanométriques. De plus, ce contrôle permettrait d'induire des propriétés spécifiques par modification de la matière à différentes échelles : les matériaux multifonctionnels sont nés.

La science macromoléculaire joue un rôle primordial dans le design et l'élaboration de matériaux multifonctionnels qui peuvent posséder des propriétés combinés comme la semi-conduction, l'adsorption de gaz ou la résistance au feu et de hautes propriétés mécaniques. Ces types de matériaux peuvent être trouvés dans des objets du quotidien comme les bouteilles plastiques, les batteries, les colles, ainsi que les matériaux utilisés pour le transport ou l'énergie par exemple.



**Figure A.1.** Omniprésence des polymères dans nos sociétés, pour les secteurs du transport, de l'énergie, du textile etc.

Aujourd'hui l'hégémonie pétrolière dans la conception de matériaux avancés est quasi-totale. Toutefois, la raréfaction de cette ressource, qui n'est pas renouvelable à l'échelle humaine,

impacte directement l'économie mondiale. En outre, l'usage immodéré des sous-produits pétrolier à causer d'importants dommages environnementaux. Pour toutes ces raisons économique, environnementale et géostratégique, de plus en plus de pays sont engagés pour une transition vers une bio-économie, comme décrit dans la **Figure A.2.**

Cette prise de conscience se matérialise concrètement à travers la ratification d'accords comme le protocole de Kyoto en 1997, qui engage les pays signataires à une régulation de l'émission de gaz à effets de serres d'origine anthropique. Dans le cadre de l'Union Européenne, la directive REACH (Registration, Evaluation and Authorization of Chemicals) a été ratifié par les pays membres, rendant la législation en termes de sécurité et de management des produits chimiques bien plus drastique, en accord avec les principes de « Chimie Verte », qui valorise une utilisation de produits chimiques et de processus éco-respectueux.<sup>3</sup>

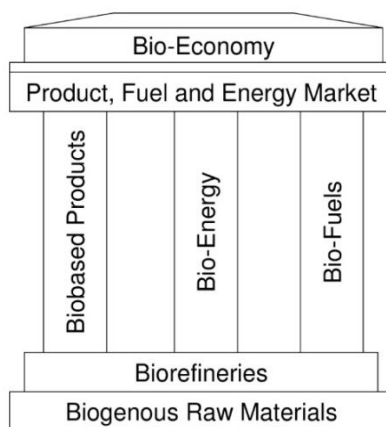


**Figure A.2.** les 3 piliers associés au modèle de bio-économie.

Comme observé dans la **Figure A.2.**, le concept de bio-économie est basé sur l'utilisation de matériaux issue de la biomasse. Deux bio-ressources sont reconnu comme ayant un grand potentiel pour substituer les « briques chimiques » issue du pétrole, ce sont les huiles biologiques et la biomasse ligno-cellulosique. Comme premier exemple, nous pouvons noter l'association Fimalin crée en 2009, qui vante l'utilisation des fibres et de l'huile de lin afin de concevoir des biomatériaux performants. Un autre exemple est celui de la société Avantium Chemicals qui développe de nouveau synthons et polymères à partir de la conversion de la biomasse ligno-cellulosique. En effet, Avantium développe une unité pilote ayant pour but de convertir les carbohydrates en Alkoxymethylfurfural (RMF), et ainsi générer une nouvelle classe de composés furaniques basée sur le FDCA, noté YXY.

<sup>3</sup> Anastas, P. T.; Warner, J. C., Green chemistry: theory and practice. Oxford university press: 2000.

Due à leurs grands potentiels et leur abondance, l'huile de lin et l'alcool furfurylique ont été choisis comme précurseurs à l'élaboration de matériaux bio-sourcés pour ce travail doctoral.

Cette thèse a été cofinancée par la région *Provence-Alpes-Côte d'Azur* (PACA) et la société Sicomin Composite qui travaille sur la formulation de résines époxydes depuis plus de vingt ans pour divers secteurs comme l'énergie et le transport. Ce financement a été concrètement supporté par le projet Région-APO BIOECOMAT. En accord avec le contexte international de transition d'une économie basée sur le pétrole à une bio-économie présenté précédemment, ce projet ambitionne le développement de nouveaux matériaux bio-sourcés.

Les objectifs du projet BIOECOMAT ont été étendus à un projet Européen appelé "BIOpolymers and BIOfuels from FURan" (BIOFUR) dans le cadre de "Marie Curie Industry-Academia Partnerships and Pathways" (IAPP) (FP7-PEOPLE-2012-IAPP). Ce projet est conduit par la société Avantium Chemicals, en collaboration avec le laboratoire CNRS à Nice, France, pour la partie polymère, et à l'université de Messine, Italie, pour la partie catalyse. Le travail principal de ce manuscrit en relation avec le projet BIOFUR a été d'étudier les possibilités de valorisation d'un sous-produit issu de la conversion de la biomasse destiné à l'élaboration de biopolymère et biocarburant : les humins. Ce travail a été essentiellement conduit dans la société Avantium à Amsterdam, Pays-Bas, sous la supervision du Dr. Ed de Jong, Dr. Jan C. Van der Wall et Dr. Nathanaël Guigo, durant mon détachement de quatre mois, du 22 juillet 2013 au 15 novembre 2013.

En accord avec les projets BIOECOMAT et BIOFUR, trois objectifs ont été définis pour cette investigation doctorale :

- (7) *Apporter de nouvelles connaissances sur le comportement de monomères pour l'élaboration de thermodurcissable en termes de polymérisation et de corrélation structure-propriétés. Chapitre IV, VI, VIII*
- (8) *Elaboration de matériaux (totalement) bio-sourcés performants. Chapitre IV, V, VI*
- (9) *Proposer des stratégies originales afin d'améliorer les propriétés d'un polymère thermodurcissable ou en développer de nouvelles. Chapitre V, VII, VIII*

En conformité avec ces objectifs, ce manuscrit a été organisé en 9 chapitres, avec 5 chapitres de résultats : **Chapitres IV, V, VI** pour les polymères issus de la biomasse et **Chapitres VII et VIII** pour les matériaux organisés.

- ◆ **Chapitre I:** présente une partie introductive, qui met en lumière les objectifs principaux de cette thèse en accord avec le contexte international actuel. La stratégie de recherche est présentée.
- ◆ **Chapitre II:** la partie bibliographique, ce chapitre présente les concepts principaux qui seront discutés dans les chapitres suivants. Le premier paragraphe présente les principales avancées dans la science des **polymères thermodurcissables**, à travers les différents phénomènes physico-chimiques qui se déroulent durant le processus de réticulation, lié à la création d'une **architecture tridimensionnelle**. Un deuxième paragraphe s'articulera autour de la chimie développée autour de la conversion de la biomasse, mettant en exergue **l'huile de lin époxydée**, **l'alcool furfurylique** et les **humins** comme précurseurs préférentiels pour l'élaboration de polymères bio-sourcés. Le dernier paragraphe présentera une approche fondamentale pour le développement de **matériaux hiérarchiquement organisés** à travers une approche bio-inspirée. Cette démarche concerne la conception de **nanocomposites** avec l'élaboration de nano-objets inorganico-hybrides (**sepiolite** et **magnétite**) ainsi que leurs combinaisons. Enfin, une autre stratégie présentée traitera de l'auto-assemblage de **monomère mésogène** en **polymères cristaux-liquides**.
- ◆ **Chapitre III:** décrit les différentes techniques, appareils et méthodes qui ont été utilisés pendant cette investigation, associées à chaque chapitre.
- ◆ **Chapitre IV:** ce chapitre se concentre sur l'élaboration de polymères à partir **d'huile de lin époxydée**, à travers une **étude comparative entre un mono- et di-anhydride** comme agent réticulant. Premièrement, les paramètres physico-chimiques de polymérisation ont été optimisés (par DSC, rhéométrie, analyse cinétique) afin d'obtenir un réseau tridimensionnel totalement réticulé. Deuxièmement, les propriétés thermomécaniques (DMA, TGA) ont été discutées en mettant en lumière les relations entre la réactivité et l'architecture du polymère obtenue i.e. l'influence des **réactions secondaires comme l'homopolymérisation ou l'étherification**.
- ◆ **Chapitre V:** l'objectif principal de ce chapitre est d'explorer les possibles applications concernant les **humins** qui sont un sous-produit récalcitrant. Pour cela, une **stratégie « furanique »** a été investie en utilisant les humins comme charge et co-monomère en association avec le **polyalcool furfurylique (PFA)**. Des **composites cellulose** ont alors été préparés comme modèle pour tester l'habileté des résines à base d'humins à imprégner le bois ou les textiles. Des tests en traction ont alors été effectués sur ces composites cellulose afin d'évaluer l'influence des humins par rapport à la résine PFA pure et d'un composite à base de lignine.

- ◆ **Chapitre VI:** ce chapitre rapporte l'élaboration d'un **polymère thermodurcissable totalement bio-sourcé** à travers la combinaison **d'huile de lin époxydée (ELO)** et **d'alcool furfurylique (FA)**. Le but de cette étude étant d'être capable d'avoir un matériau avec des propriétés modulable en fonction du ratio de monomères utilisés. La polymérisation cationique a été étudiée par FT-IR, RMN-2D et les propriétés mécaniques ont été mises en avant par DMA et machine à traction.
- ◆ **Chapitre VII:** propose une stratégie pour le **renforcement anisotropique** d'une résine époxyde à travers la création **originale d'un nano-objet hybride** composé de magnétite greffée sur la surface de la sépiolite. La nanoparticule résultante est **capable de s'orienté sous champs magnétique**. La première partie de cette étude présente l'élaboration de cette nanofibre par la double fonctionnalisation de **magnétite** et **sépiolite**, suivie par l'élaboration et la réticulation de la résine époxyde **nanocomposite** sous champ magnétique. La deuxième partie de l'étude se focalisera sur l'influence de l'orientation de ces nanofibres (parallèle, anti-parallèle ou isotrope) dans le composite, par rapport à une sollicitation mécanique unidirectionnelle (DMA). Ce travail a été fait en collaboration avec le Dr. Jessica Alves Marins, le Dr. Françoise Giulieri et le Dr. Georges Bossis.
- ◆ **Chapitre VIII:** se focalise sur le développement de résines époxydes possédant une **organisation multi-échelle**. Pour cela, un travail préliminaire a été entrepris avec la conception et l'étude d'une nouvelle classe d'époxyde monomère possédant une géométrie en forme d'étoile (star) et un caractère mésogène capable d'induire une auto-organisation en mésophase pendant la polymérisation. Après la synthèse et la caractérisation de ce **star-époxyde mésogène**, sa propension à générer des polymères réticulés a été explorée. Premièrement, avec la combinaison d'anhydride d'acide à travers une analyse de l'influence des **interactions supramoléculaires** sur la **cinétique de polymérisation** ; et deuxièmement avec l'association d'une diamine comme agent réticulant, mettant en exergue le **développement fractale** du réseau polymère crée (WAXS) en relation avec les propriétés thermomécaniques (TGA et DMA).
- ◆ **Chapitre IX:** présente la conclusion générale de ce travail doctoral, et ouvre la discussion sur des perspectives.

## Résumé des principaux résultats :

Les principaux résultats obtenus au cours des 5 chapitres de résultats vont être brièvement présenté ci-dessous. La valorisation de molécules plateformes issues des bio-raffineries est au

cœur de la stratégie de substitution des matériaux pétro-sourcés. Deux molécules à fort potentiel, que sont l'huile de lin époxydée et l'alcool furfurylique, ont été choisies afin d'élaborer de nouveaux matériaux biosourcés à hautes performances. De la chimie supramoléculaire (star-époxy mésogène) aux nanocomposites (sépiolite et magnétite fonctionnalisées), plusieurs voies de recherches ont été explorées afin d'obtenir des matériaux aux propriétés thermo-mécaniques intéressantes.

La première étude s'est intéressée à l'élaboration de copolymère ELO/anhydride à travers une étude globale qui va de la compréhension de la réactivité physico-chimique (copolymérisation anionique vivante) associée à la polymérisation et à la relation structure propriété de l'architecture polymère considérée. Cette étude s'est effectuée à travers le choix de deux durcisseurs anhydride (MHHPA et BTDA) présentant des fonctionnalités différentes, et donnant lieu à des réseaux et des réactivités bien particulières, mettant en avant une certaine propension à l'homopolymérisation dans le cas du di-anhydride. Ces principaux résultats peuvent être décrits par la **Figure A.3.** qui met en lumière la possibilité qu'a une matrice comme ELO de générer des propriétés thermomécanique semblable aux matrices pétro-sourcées.

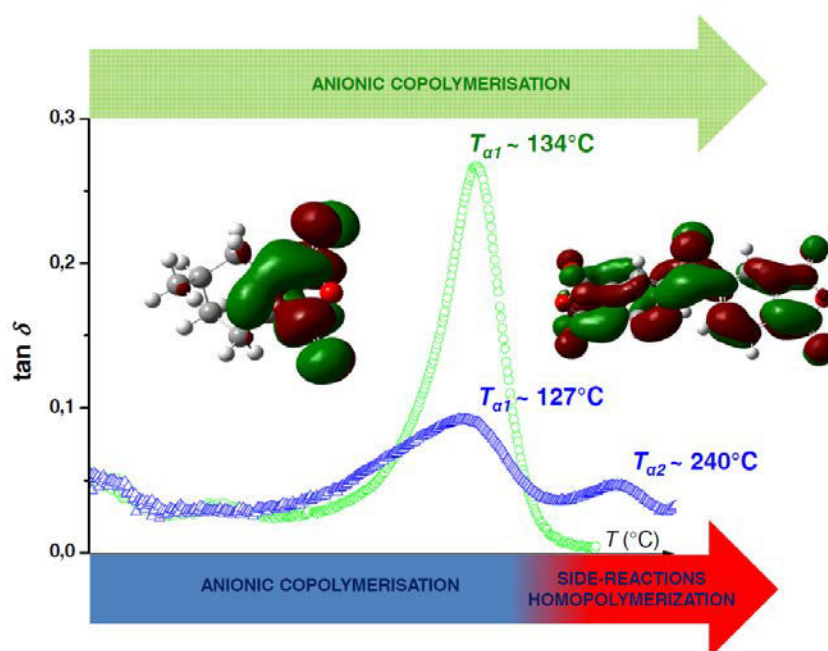


**Figure A.3.** Thermogrammes DMA des systèmes ELO/MHHPA/2MI (vert) et ELO/BTDA/2MI (bleu).

Une deuxième étude s'est focalisée sur l'élaboration de composite cellulosique à base de diverses résines furaniques PFA. Le principal but de cette étude a été de mettre en évidence l'influence d'une charge micrométrique appelée humins (sous-produit des bio-raffineries) sur la cohésion matrice-cellulose. Un résumé de ces résultats peut être observé sur la **Figure A.4.** où nous remarquons, qu'en plus de pouvoir ajouter une très grande quantité d'humins à la matrice PFA, les valeurs des modules, et du tensile strength en particulier, sont augmenté de manière drastique en comparaison de la matrice PFA pure.

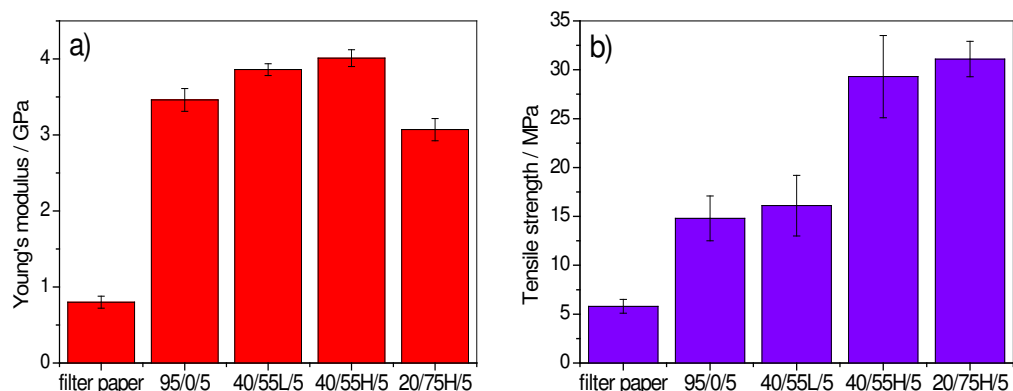


**Figure A.4.** Young's modulus (a) et tensile strength (b) histogrammes des composites cellulosique

L'étude suivante est le fruit de la combinaison de deux matrices totalement bio-sourcées et précédemment présentées, qui sont l'ELO et le FA. A travers une stratégie de copolymérisation cationique, des copolymères entièrement bio-sourcés et homogènes ont été créés. Après avoir mis en évidence les réactions principales qui régissent la copolymérisation (réaction epoxyde/alcool et la réaction de polycondensation/réticulation du FA) par FT-IR et RMN 2D, les propriétés mécaniques de du copolymère ELO50/FA50 ont été comparé à l'homopolymère PFA comme nous pouvons le voir ci-dessous dans la **Figure A.5.** Le résultat principal peut-être associé à la grande propension qu'à l'ELO à flexibiliser la matrice PFA de manière covalente i.e. avec 50% d'ELO dans la matrice PFA, on obtient une élongation à la rupture du matériau qui passe de 5 à 40 %.

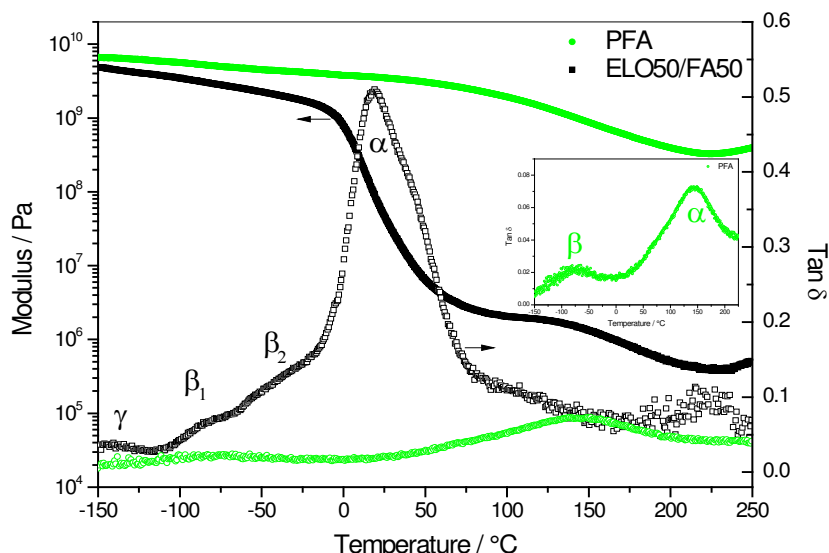


**Figure A.5.** Module ( $E'$ ) et  $\tan \delta$  évolutions pour ELO/FA polymère (noir) comparé au PFA (vert).

L'investigation suivante propose une stratégie originale afin de générer une anisotropie contrôlée dans une matrice époxyde. Cette stratégie passe par l'élaboration d'un nano-objet hybride par la double fonctionnalisation de sépiolite par un aminosilane et de magnétite par un époxyxilane. La nanofibre hybride résultante (greffage des nanoparticules de magnétite sur la surface de la sépiolite via réaction époxy/amine) possède la capacité de s'orienter sous champs magnétique (**Figure A.6**). Cette nanofibre a alors été mélangé à différent ratio dans une matrice époxyde DGEBA suivant différentes orientations (parallèle, antiparallèle et isotrope) afin de mesurer l'influence de l'orientation des fibres par rapport à une sollicitation mécanique unidirectionnelle en traction. Le résultat principal est associé à l'influence de la fréquence sur les mesures des modules, mettant en évidence un module plus élevé dans le cas d'une sollicitation qui est provoqué dans le sens de l'alignement des fibres.

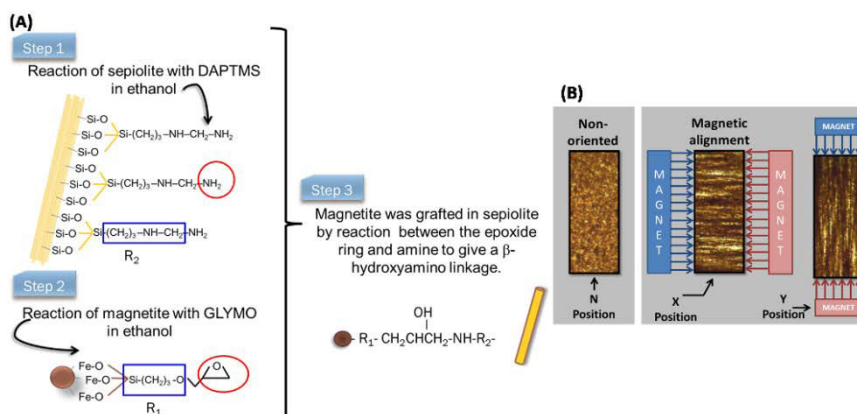


**Figure A.6.** Stratégie de synthèse de la nanofibre hybride magnétique-sépiolite (a) et son orientation sous champs magnétique (b).

La dernière étude s'est focalisée sur les résines époxydes mésomorphe, où l'état cristal-liquide est figé dans un réseau tridimensionnel. La chimie des monomères à géométrie bâtonnet ou « rod-like » dérivé de cœurs mésogènes biphenyle ou azométhine par exemple, ainsi que leur influence sur l'architecture supramoléculaire ont fait l'objet de nombreuses recherches. Certaines études se sont également intéressées à la cinétique de polymérisation à l'état anisotrope et ont révélé un comportement atypique où les liaisons faibles de type  $\pi$ -stacking, en particulier, jouent un rôle prépondérant sur la réactivité. Afin de poursuivre ces travaux, inspirés par une chimie supramoléculaire de plus en plus inventive, nous nous sommes proposé de synthétiser un monomère époxyde modèle à géométrie discotique, le 1,3,5-triazine,2,4,6-tris[4-(2-oxiranylmethoxy)phenyl] appelé TriaEP. Cette géométrie en tri-branche également appelé « Star » a été choisie pour sa propension à adopter un grand nombre de mésophases différentes et éclectiques (colonnaire, dendritique...). Une étude thermo-mécanique globale a été investie par calorimétrie différentielle à balayage (DSC), analyse mécanique dynamique (DMA) et thermogravimétrie (TGA). Les premiers résultats concernant le monomère TriaEP ont pu mettre en exergue un caractère cristal-liquide intrinsèque, sur une plage de température allant de 135 à 150°C. Par la suite, les premiers polymères thermodurcissables ont été élaborés avec des durcisseurs classiques de type di-amines, en particulier avec le 2,7-diaminofluorène (2,7-DAF) qui révèle un développement de type fractale au cours de la polymérisation. Ce réseau anisotrope très dense possède avec une transition  $\alpha$  à 220°C pour une température de réticulation de 160°C (Figure . A.7.)

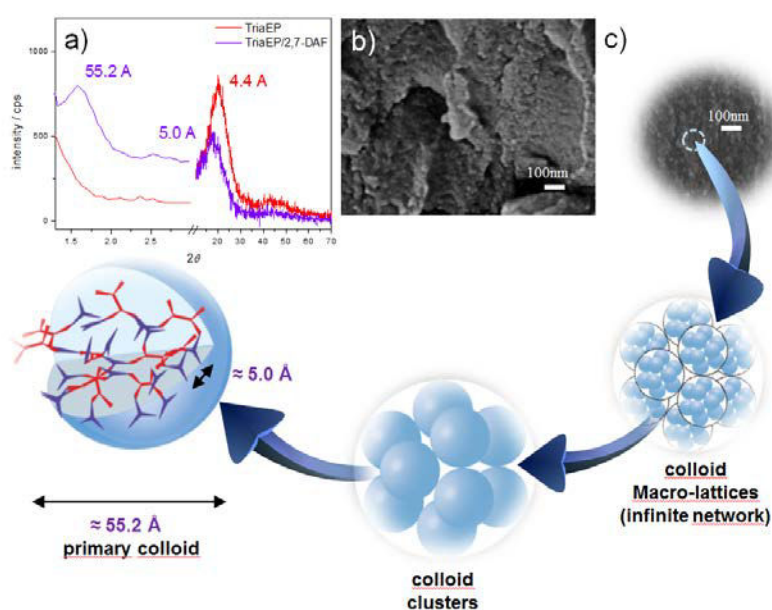


**Figure A.7.** WAXS diffractogramme pour le monomère TriaEP à 140°C et pour le polymère réticulé TriaEP/2,7-DAF à 170°C pendant 1h (a); MEB cryo-fracture du polymère TriaEP/2,7-

DAF (b); modèle d'auto-assemblage de dendrimères étendu aux colloïdes par analogie avec les systems biologiques "Genealogically Directed Synthesis" (c).

Une deuxième étude sur la cinétique de la réticulation via une copolymérisation anionique vivante avec l'anhydride succinique (SA) a été investie par les méthodes isoconversionnelles avancées en mode dynamique. Nous pouvons ainsi observer la variation d'énergie apparente de réaction ( $E_a$ ) de la polymérisation, de la fusion des réactifs jusqu'à la formation du réseau tridimensionnel. La dépendance de l'énergie d'activation apparente de réaction ( $E_a$ ) montre en effet un mécanisme de réticulation complexe, avec une variation de l'énergie qui passe du positif au négatif et vice-versa. Cette variation reflète la transition d'une vitesse de réaction suivant un comportement Arrhénien à anti-Arrhénien. Cela correspond respectivement au passage d'une vitesse de polymérisation qui croît à une vitesse qui décroît avec l'augmentation de la température. Ce résultat peut être interprété comme étant le reflet d'une polymérisation où l'ordre supramoléculaire évolue au cours de la réaction. Une étude menée par A. Numez et coll. sur une réaction d'isomérisation en présence d'un solvant cristal-liquide, a mis en évidence un changement d'ordre dans la mésogénie Nématique-Smectique-Nématique lorsque la température varie. La vitesse de polymérisation présente alors un comportement anti-arrhénien lorsque l'ordre diminue, au passage d'une organisation Smectique à Nématique : c'est le phénomène de ré-entrance. Dans notre cas, afin de mettre en exergue l'évolution de l'anisotropie optique durant la réticulation, un suivie par microscopie optique en lumière polarisée à la même vitesse de chauffe a été entrepris. Cela nous a permis de corrélérer les fluctuations de l'énergie d'activation apparente de réaction ( $E_a$ ) avec l'anisotropie optique, généralisé aux variations d'ordre au sein des chaînes oligomères puis polymère pendant la réticulation. Le phénomène global de polymérisation en phase crystal-liquide de TriaEP/SA est résumé dans la **Figure A.8**.

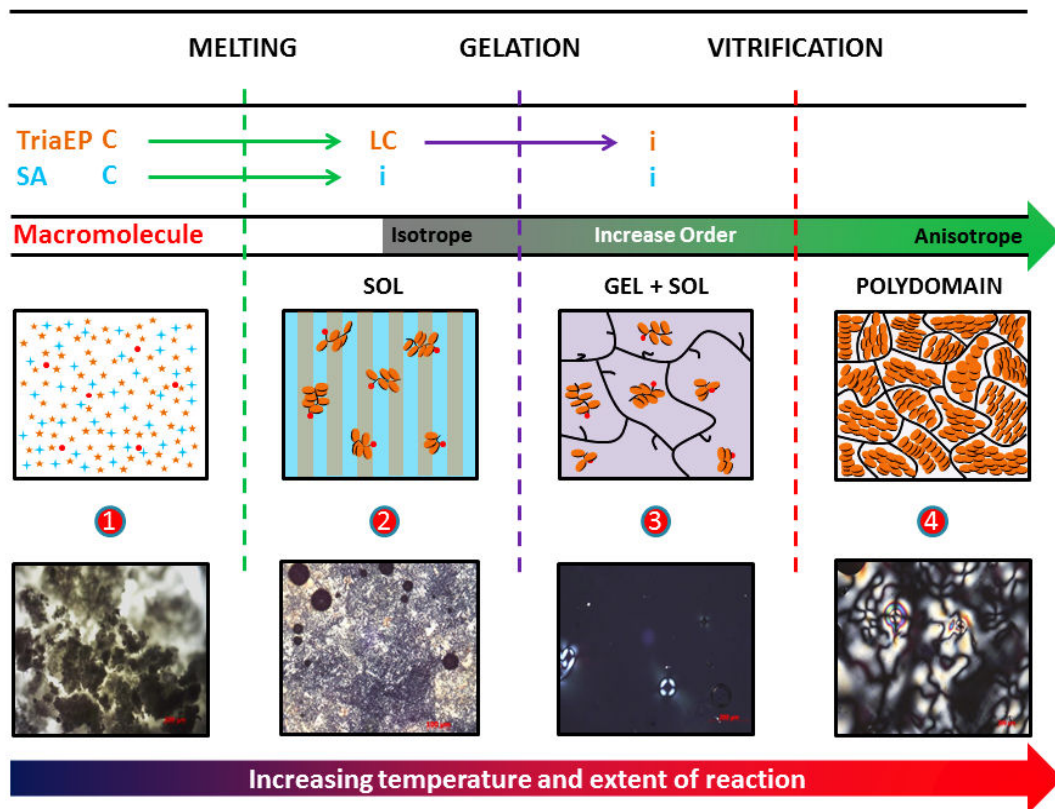


**Figure A.8.** Schéma récapitulatif des phénomènes physico-chimiques qui ont lieu durant la réticulation du système TriaEP/SA.

## Conclusion Générale et Perspectives:

Après les conclusions relatives à chaque chapitre, qui ont exposé les résultats et interprétations principales, cette conclusion générale veut croiser les différentes avancées dans la science des polymères thermodurcissables à la lumière des objectifs présentés dans la partie introductive (**Chapitre I**).

*(1) Apporter de nouvelles connaissances sur le comportement de monomères pour l'élaboration de thermodurcissable en termes de polymérisation et de corrélation structure-propriétés.*

**Chapter IV, VI, VIII**

Comme présenté en **section II.1.1.2.**, dans la science des polymères thermodurcissable, la nature des monomères gouvernent l'édification de l'architecture polymérique qui est conditionné par les règles de la fonctionnalité et déterminé par la réactivité. Toutefois, les caractéristiques physico-

chimiques du monomère peuvent avoir un grand impact sur la conception de l'architecture polymère :

- ◆ En effet, comme premier exemple, les monomères époxydes ELO et TriaEP, présentent tous deux une géométrie tri-branche (star-géométrie), mais diffère par différents aspects, comme illustré dans la **Table A.1**. Ces dissimilarités induisent non seulement des différences entre les propriétés physico-chimiques intrinsèques aux monomères, mais conditionnent tout le processus de polymérisation et donc les architectures résultantes. C'est particulièrement visible si nous comparons l'énergie d'activation apparente associée à chaque polymérisation. En effet, pour une même polymérisation époxyde/anhydride – i.e. copolymérisation anionique vivante – les systèmes ELO/MHHPA/2MI et TriaEP/SA/2MI présentent une évolution de  $E_a$  très différente. Pour le système avec ELO la dépendance de l'énergie présente un scénario d'évolution *classique* avec la succession des contrôles chimique et de diffusion de la polymérisation, associé à des valeurs caractéristique de  $E_a$  qui peuvent être retrouvés dans la littérature. Dans le cas du système avec le TriaEP, un mécanisme complexe est mis en évidence, en plus du comportement *classique* comme observé pour le système ELO : la superposition et l'évolution des interactions supramoléculaires du monomère TriaEP et du polymère TriaEP/SA.

**Table A.1.** ELO vs TriaEP: caractéristiques physico-chimiques

<b>ELO</b>	<b>TriaEP</b>
Liquide visqueux à <i>RT</i>	Solide à <i>RT</i>
Caractère isotrope	Caractère mésogène 135 °C < LC < 150 °C
aliphatique	aromatique
~ 5.5 époxydes	3 époxydes
époxyde interne	époxydes terminaux

- ◆ Avec ELO/FA comme second exemple, la fonctionnalité associée à la réaction époxyde/alcool est modifiée par la superposition de deux réactions principales. La première réaction est celle respectant une fonctionnalité déterminée : époxyde/alcool. La seconde correspond à la condensation du FA en position C<sub>2</sub> et la réticulation. La fonctionnalité théorique de ELO50/FA50 est 1 :1.76, considérant seulement la réaction époxyde/alcool, mais se trouve être moindre en réalité, plus proche d'un ratio stœchiométrique (1:1) dû à la consommation du FA par auto-condensation. Le processus global de polymérisation, et la

formation du réseau polymère sont donc cinétiquement dépendants, fruit de la compétition de ces deux réactions principales. Cet exemple original de polymérisation cationique combinée représente bien la versatilité de la science des thermodurcissables qui permet la combinaison de différents types de polymérisation par une sélection judicieuse de monomère comme ELO et FA.

## *(2) Elaboration de matériaux (totalement) bio-sourcés performants. Chapter IV, V, VI*

La transition vers l'élaboration de polymère thermodurcissable bio-sourcé comme alternative aux résines pétro-sourcé n'est pas forcément évidente, car les hautes  $T_g$  sont généralement associées aux résines contenant des noyaux aromatiques (principalement des phényles issus du pétrole). Toutefois, une autre voie peut être envisagée pour obtenir des matériaux à haute  $T_g$ . Notre proposition est de tenir compte de l'avantage que nous porte la structure de l'ELO (avec ~5.5 groupes époxydes par triglycérides) par augmentation de la densité de réticulation à son paroxysme, afin d'obtenir un réseau très dense et donc une  $T_g$  élevée. Cette stratégie s'est révélée efficace avec une  $T_g$  de 134 °C pour le système ELO + mono-anhydride (MHHPA), i.e. sans aromatique. L'utilisation d'un agent réticulant avec une fonctionnalité supérieure, un di-anhydride (BTDA) a été investie avec succès. Ce type de durcisseur est généralement utilisé dans l'industrie en petite quantité dans certaines formulations pour augmenter la  $T_g$ .

Dans ce contexte, comme principal agent réticulant, seulement une petite quantité peut être utilisée pour des raisons de processabilité : notre formulation est de 1:0.5 en proportion d'ELO et de BTDA, considérant leurs fonctionnalités respectives. Le large excès d'époxyde joue un rôle prépondérant dans les propriétés finales du matériau qui montre deux  $T_g$  à 127 et 240 °C, avec deux types de réseaux polymères : un réseau copolymère renforcé par certaines liaisons homopolymères, et un autre réseau contenant pour majorité un réseau homopolymère. Cette dernière très haute  $T_g$  met en évidence la grande importance des réactions d'homopolymérisation sur les propriétés finales du matériau.

Concernant l'élaboration de polymère thermodurcissable totalement bio-sourcé, deux stratégies ont été proposées dans ce manuscrit. La première stratégie a été de créer des résines par association de FA avec des humins. Cette voie représente le choix le plus logique, en combinant deux entités furaniques, provenant de la même bio-source, c'est-à-dire de la conversion catalytique de carbohydrate. Cette combinaison furanique s'avère très intéressante en termes de structure et de chimie, plus spécifiquement, concernant la bonne solubilisation des humins dans le FA, et les multiples connexions possibles entre FA/FA oligomère et la structure furanique des particules d'humins. La deuxième stratégie est basée sur la combinaison de différentes bio-ressources : ELO et

FA. L'époxydation de l'huile de lin contribuant à augmenter la réactivité et le caractère hydrophile des triglycérides, ce qui a permis de mélanger facilement ELO et FA sans séparation de phase.

Si nous considérons la contribution de chaque monomère pour l'élaboration de l'architecture polymère, ces molécules possèdent des propriétés antagonistes conduisant à l'édification d'un réseau polymère avec des propriétés hybrides. En effet, les oligomères de FA contribuent à la rigidité du réseau par la présence de chromophore furanique, (en remplacement des groupes phenyls que l'on peut retrouver dans les résines pétro-sourcées) alors que l'ELO apporte une contribution flexibilisante au réseau par ces groupes aliphatiques : l'ELO causant une gêne stérique qui a pour effet de réduire la densité de réticulation du PFA. Ces deux stratégies ont permis de concevoir des polymères thermodurcissables totalement bio-sourcés, possédant des  $T_g$  variant de 20 à 170 °C.

*(3) Proposer des stratégies originales afin d'améliorer les propriétés d'un polymère thermodurcissable ou en développer de nouvelles. Chapter V, VII, VIII*

La stratégie proposée ici a été basée sur une réflexion biomimétique autour de l'organisation hiérarchique de la matière à différentes échelles, du micromètre jusqu'au nanomètre (comme illustré dans la **Figure A.9**). Pour ce qui est de l'échelle micrométrique, les humins ont été utilisés comme core-shell particules avec succès, comme l'a montré l'étude préliminaire à travers l'élaboration de composite cellulosique pour répondre au problème majeur du PFA, qui est sa fragilité. Pour l'échelle micrométrique et nanométrique, l'utilisation de nanofibres orientables sous champs magnétique a prouvé être efficace pour générer une anisotropie contrôlée. Enfin, la polymérisation d'un star-époxyde mésogène a montré un auto-assemblage de l'échelle nanométrique (phase cristal-liquide) à l'échelle micrométrique.

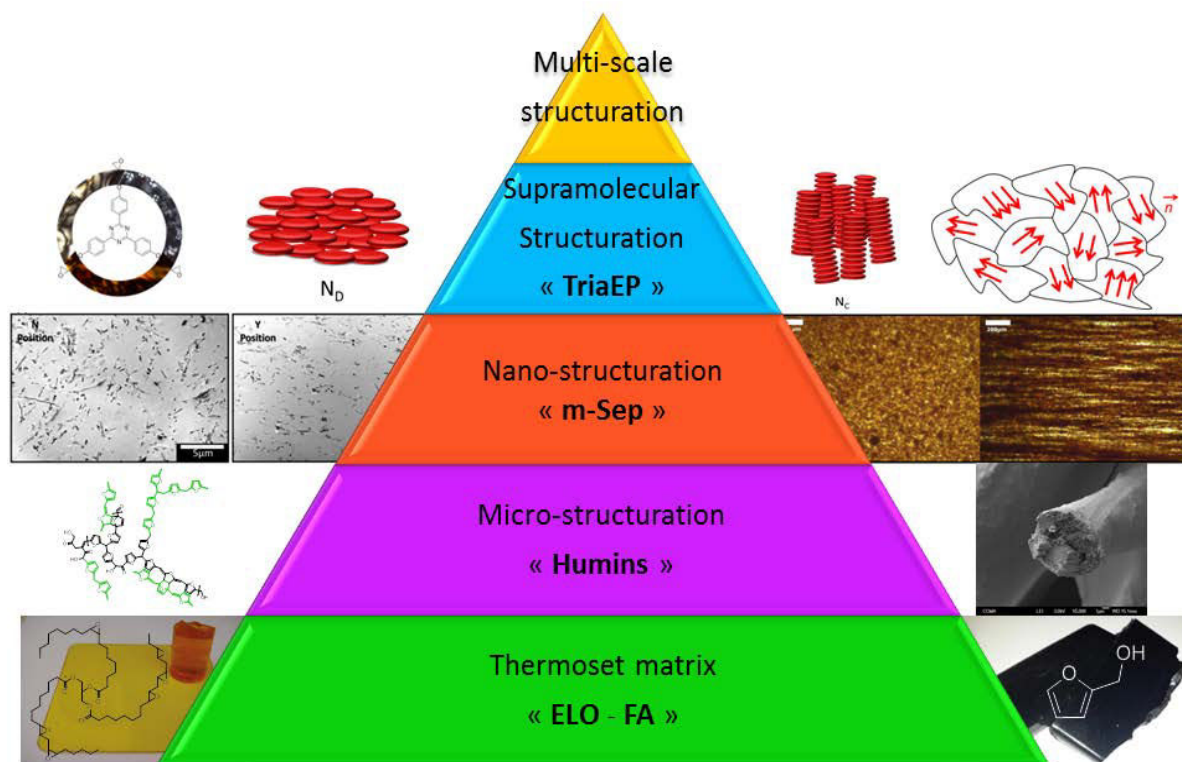


**Figure A.9.** Stratégie employé dans ce travail doctoral autour d'une l'organisation multi-échelle.

Cette dernière partie du manuscrit se focalise sur les potentielles perspectives associées à chaque chapitre de manière indépendante, et fini par proposer une vision générale du sujet à plus long terme.

- ♦ **Chapitre IV:** après le travail fondamental qui a été effectué sur la réactivité de la réticulation avec des durcisseur pétro-sourcé, des investigations peuvent être développer avec des agents réticulant bio-sourcés, favorisant une fonctionnalité 1-1 avec des durcisseurs comme des acides carboxyliques ou anhydrides à la place des classiques amines, dû au réseau triglycérider qui induit beaucoup de gêne stérique. Une idée pour avoir un matériau à haute  $T_g$  pourrait d'être d'utiliser l'anhydride succinique (espaceur court) qui est dérivé de l'acide lactique. Une autre proposition, pourrait d'être d'augmenter les propriétés de la matrice ELO/anhydride par l'élaboration de copolymer/nanocomposite avec, par exemple, l'utilisation de nanocages de silice époxydées : octakis(dimethylsiloxypopylglycidylether)silsesquioxane appelé POSS-OG (voir [Pub 05] dans Annexes).
- ♦ **Chapitre V:** Comme travail complémentaire, après l'étude de composite cellulosique, une investigation sur les propriétés mécaniques des résines humins en « block » peut être entreprise, pour étendre leur domaine d'application aux moules de fonderie par exemple. Un

premier résultat encourageant est présenté dans la **Figure A.10.** avec la DMA du mélange 40FA/55hu/5MA comparé au pure PFA. Le résultat principal peut être résumé par un réseau polymère moins dense pour le matériaux contenant les humins. La présence d'une transition secondaire à  $T = -20\text{ °C}$  peut être relié à la partie ductile de la structure des humins. Ce comportement est en bonne corrélation avec les propriétés mécaniques trouvés pour le composite cellulosique, mettant en évidence une augmentation de la ductilité et de la rigidité.

Concernant le potentiel des humins en termes d'application, de mon point de vue, une des plus évidentes pourrait être de les utiliser comme bitume, comme additif, ou en remplacement des actuels bitumes après modification. Une autre possible application à plus haute valeur ajoutée pourrait d'être d'utiliser les humins pour l'élaboration de matériaux carbonés suivant la stratégie opérée pour les matériaux HTC.

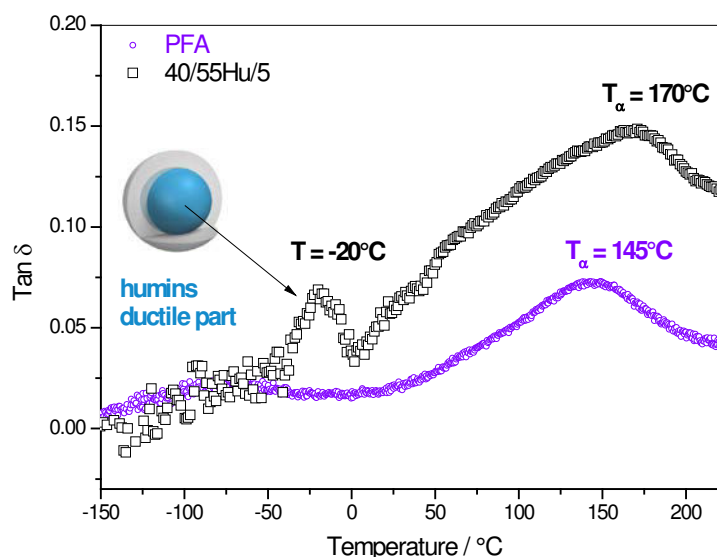


**Figure A.10.** Thermogrammes DMA pour les résines PFA et 40FA/55Hu/5MA.

- ◆ **Chapitre VI:** après s'être focalisé sur la réactivité principale entre ELO et FA avec le ratio un médian 50/50, le travail futur peut être orienté sur l'étude de l'influence des réactions secondaires (pour des haut ratios en ELO) comme l'homopolymérisation/éthérification, premièrement sur la réactivité et deuxièmement sur la densité du réseau polymère, lié aux propriétés mécaniques.
- ◆ **Chapitre VII:** l'orientation de nanofibers dans une matrice DGEBA à montrer de bons résultats dans la génération d'une anisotropie magnétique et mécanique. Nous pourrions considérer l'utilisation d'une matrice bio-sourcée, comme l'ELO, avec la difficulté de choisir

un agent réticulant adapté. En effet, comme montré dans le **Chapitre IV**, l'utilisation d'amine aliphatique (comme utilisé dans le **Chapitre VII** avec le DGEBA) pour la réticulation de l'ELO ne forme pas un réseau totalement réticuler. Une autre possible perspective serait d'utiliser un champ magnétique alternatif à haute fréquence pour selectivement chauffer localement les nanoparticules magnétiques afin d'induire une polymérisation qui s'initierais à partir de m-Sep. Cette approche, illustrée par la **Figure A.11.**, pourrait augmenter la compatibilité entre les nano-objets et la matrice, ce qui est le principal défi pour augmenter les propriétés mécaniques.

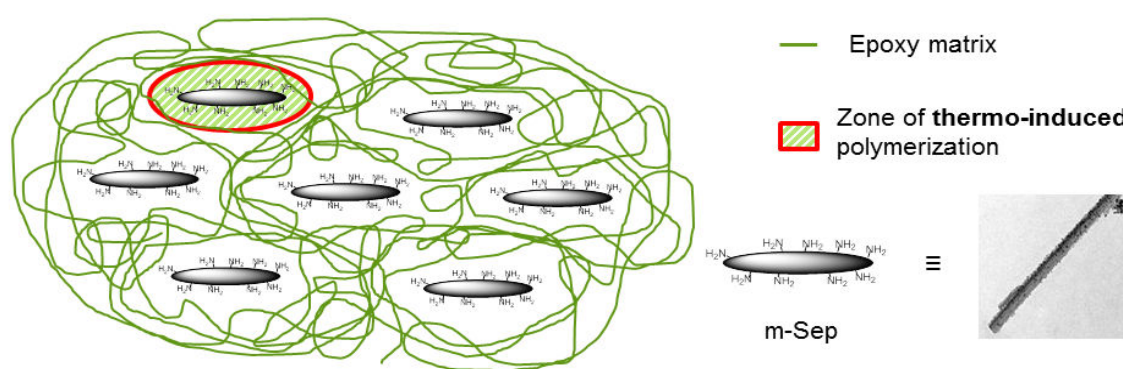


**Figure A.11.** Stratégie de polymérisation thermo-induite par un champ magnétique alternatif.

- ♦ **Chapitre VIII:** plusieurs stratégies peuvent être envisage afin de promouvoir les star-époxydes mésogène comme monomère à haute valeur ajouté pour la conception de matériaux multifonctionnel. Comme premier exemple, ce type de monomère mésogène pourrait s'avérer intéressant pour générer des matériaux auto-réparant, en favorisant les interactions supramoléculaires qui par ségrégation de phase favoriseraient des réactions réversibles comme la métathèse de ponts disulfures par exemple. Comme second exemple, les star-époxydes mésogène rigide comme le TriaEP pourrait être des précurseurs intéressant pour l'élaboration de matériaux présentant une porosité à différente échelle. En effet, il est possible de générer une porosité contrôlée (autour de 30-100 nm) pour une résine époxyde/amine, tenant compte des interactions supramoléculaires qui ont lieux durant la polymérisation dans un solvant polaire. Récemment, la recherche s'est focalisée sur les polymères conjugués microporeux (CMPs) qui présente des micropores de l'ordre de 1-3 nm. La distribution et l'aire de ces pores est reliées à la structure du polymère qui se présente sous forme d'un monomère rigide tri-branche associé à un espaceur di-fonctionnel

en forme de « bâtonnet ». Fort de ce constat, l'association du monomère TriaEP avec un agent réticulant rigide, possédant une fonctionnalité 1-1, pourrait générer un matériau qui présenterait deux différentes porosités.

Depuis l'élaboration des premiers polymères amorphes réticulés au début du 20<sup>ème</sup> siècle, la science des polymères thermodurcissables a été continuellement élargie en corrélation avec les découvertes majeures de la Chimie. En effet, comme nous l'avons vu dans la **section II.3.5.1.** avec la description théorique de l'état crystal-liquide, De Gennes initia la grande aventure des polymères thermodurcissables cristaux-liquides. De la même manière, le travail de Lehn sur la chimie supramoléculaire et puis, sur la chimie dynamique adaptative a contribué à étendre le champ des thermodurcissables par la création de polymère possédant des liaisons covalente dynamique. Ces polymères possèdent un réseau avec des liaisons covalentes réversibles qui sont capable de répondre a différent stimuli comme le pH ou la température, afin d'obtenir des propriétés d'autoréparation par exemple. Comme exemple de ces réactions covalentes réversible, nous pouvons citer la transestérification ou la métathèse de ponts disulfures. Pour finir, en ce qui concerne la quête de la *dynamique universelle de la nature* entreprise par Leonardo Da Vinci (**section II.3.**) à travers le concept précurseur de bio-inspiration, le plus petit dénominateur commun de cette dynamique pourrait être associé à la liaison chimique, dans toute sa diversité. En cela, l'élaboration d'une future génération de matériaux adaptatifs biomimétiques pourrait être basée sur l'association du concept de bio-inspiration associé à l'utilisation de synthons bio-sourcé. Les éléments « briques » requis pour accomplir « l'éco-design » de ce type de matériaux pourrait être trouvé parmi la richesse pourvoyé par la combinaison de différentes bio-ressources qui peuvent dériver de la biomasse ligno-cellulosique, les lipides, ou la biomasse de 3<sup>ème</sup> génération (algues et dérivés aquatique)



## RESUME:

Le travail de recherche présenté dans cette thèse s'est orienté vers l'élaboration de matériaux avancés et la conception de polymères/composites biosourcés. Ce dernier sujet a été entrepris à travers la combinaison de différentes matières premières biosourcées qui sont connues comme ayant un grand potentiel de substitution des monomères pétrosourcés. Tout d'abord, un travail fondamental a été exécuté en combinant l'huile de lin époxydée (ELO) avec des dérivés d'anhydrides d'acides comme agents de réticulation, afin de relier la réactivité chimique de polymérisation à la structure du réseau formé et aux propriétés thermomécaniques. Afin de devenir économiquement viable, les bio-raffineries doivent urgemment valoriser les sous-produits issus de la conversion de la biomasse. Fort de ce constat, une deuxième étude sur l'incorporation et la copolymérisation d'une quantité importante d'humins (résidu hétérogène obtenu durant la conversion des sucres en hydroxyméthylfurfural (HMF)) avec de l'alcool furfurylique (FA) a été réalisée avec succès afin de créer de nouvelles résines thermodures. Une autre voie proposée consiste en la combinaison de ELO et de FA à travers une polymérisation cationique, dans l'idée de créer de nouvelles résines totalement biosourcées, générant ainsi une gamme de matériaux aux propriétés mécaniques modulables. En ce qui concerne l'élaboration de polymères et composites aux propriétés avancées, une réflexion autour des matériaux naturels structurés de manière hiérarchique a été entreprise afin d'adapter les concepts d'auto-organisation et de structuration aux architectures polymères. Pour cela, un nano-objet hybride-inorganique orientable (m-Sep) a été synthétisé à travers le greffage covalent de nanoparticules de magnétite sur la surface de la sépiolite. L'hybride m-Sep ainsi obtenu a été « gelé » dans une matrice thermodure suivant différentes orientations, puis les réponses mécaniques de ces matériaux anisotropes ont été évaluées. Pour finir, la conception de matériaux organisés en multi-échelle a été explorée à travers la synthèse d'un monomère époxyde cristal-liquide présentant une géométrie en forme d'étoile. Par la suite, le processus de réticulation a été étudié en termes de cinétique de réticulation et d'auto-assemblage en corrélation avec les propriétés mécaniques des matériaux.

**Mots-clés:** alcool furfurylique, cristaux-liquides, huile de lin époxydée, humins, magnétite, nanocomposite, polymère biosourcé, sépiolite, thermodur.

## ABSTRACT:

The research work presented in this thesis was oriented on advanced thermoset materials and also on the conception of bio-based polymers and composites. This last topic has been investigated by the combination of different bio-based raw materials which are well-known to have a great potential to substitute the petroleum monomers. Firstly, a fundamental work has been done on the combination of epoxidized linseed oil (ELO) and anhydrides as cross-linkers, which links the polymerization reactivity with the network structure and thermomechanical properties. For being economically realistic, the bio-refineries are urged to valorize the side-stream products issued from biomass conversion. In that respect, a second study investigated successfully the incorporation and copolymerization of an important amount of humins (heterogeneous residues obtained during the sugar conversion into hydroxymethylfurfural (HMF)) with furfuryl alcohol (FA) in order to create new resins. Another proposed combination, focused on ELO and FA cationic copolymerization with the purpose to create new fully bio-based resins with tailored mechanical properties. Concerning the elaboration of advanced polymers and composites, a reflection around the hierarchically organized natural materials has been achieved in order to adapt the self-organization and structuration concepts to polymeric network. Herein, an inorganic-hybride orientable nanofiller (m-Sep) has been synthesized through the covalent grafting of magnetite nanoparticles under sepiolite surface. The obtained hybrid of m-Sep was ulterior "frozen" in different orientations in a thermoset matrix, and its anisotropic mechanical responses have been highlighted. Finally, the conception of multi-scale ordered materials has been explored through the synthesis of an epoxidized liquid-crystalline monomer with a star-shape geometry. Then, the cross-linking process of this monomer has been studied in terms of polymerization kinetics and self-organization in correlation with the mechanical properties.

**Keywords:** bio-based polymers, epoxidized linseed oil, furfuryl alcohol, humins, liquid-crystals, magnetite, nanocomposites, sepiolite, thermosets.